The Origins of Cosmic Dust: A Study of Dust in Galactic Supernova Remnants

by

Hannah Chawner

A Thesis submitted to Cardiff University
for the degree of Doctor of Philosophy

28 September 2020

Author: Hannah Chawner
Title: The Origins of Cosmic Dust:
A Study of Dust in Galactic Supernova Remnants
Date of submission: 28 September 2020

DEDICATION

'So much of me
Is made of what I learned from you
You'll be with me
Like a handprint on my heart
And now whatever way our stories end
I know you have rewritten mine
By being my friend'

WINNIE HOLZMAN, WICKED

When I moved to Cardiff all the way back in 2012 I never thought that I'd still be around 8 years later! I've had an incredible time and I've loved living in this city, despite all the seagulls...

I have to start by thanking my awesome supervisors Mikako and Haley. First, for thinking of me when this project started - my life would be very different if you hadn't sent me that email, and I'd have missed out on so many wonderful memories. Second, for giving me so many opportunities throughout my PhD - the trips that I've been on for conferences and observing have been extraordinary and they are happy memories that will stay with me for a long time! And of course, thank you for all of the support and guidance you've given me, both throughout my undergrad and PhD. You're both an inspiration to me of incredible women who can achieve their dreams and be so successful.

I wouldn't get those letters in front of my name if it weren't for my examiners, Matt Griffin and Aneurin Evans, who took the time to read this humongous book that is the last four years of my life! Thank you to them, and to Patrick Sutton,

for probing my work and making my viva as close to enjoyable as it could be!

I've met lots of incredible, super-intelligent people during my PhD and it's fair to say that the last four years wouldn't have been so fun without all of you. Being part of the Cosmic Dust group made the difference to my work on numerous occasions and helped create a clear direction for me to take, thank you for many interesting meetings, and for all of your advice and ideas. Thank you to everyone in the Galaxies office: Andy, Aris, Brad, Chris, Connor, Dan, Dan, Eleonora, Eve, Gayathri, James, Jeni, Lottie, Matt, Nikki, Phil, Rosie, Tom, Tom, Zoe. Thank you for the office golf, the crazy Christmas decorations, all of the chats, and all of the other little things that make work life that bit happier. You've made it a pleasure to go into work and I've learnt a lot from everyone along the way. All of you are amazing and I can't wait to see the incredible things you do in the future. A special thank you to Amber, who's been a great friend throughout undergrad and PhD. I'm so glad we got to share this journey together!

A big thank you to everyone in the physics girls chat for all of the uplifting and inspiring messages, and most importantly all of the pet photos! You made the last few months of doing a PhD in lockdown much more bearable, and all the supportive chats gave me the motivation to go out and be as awesome as all of you. To all of the physics coffee, cake, and special tea group: thank you for providing a much needed distraction, some awesome baking, and a great way to end each week (with some sometimes questionable contributions). It's fair to say there's been some interesting conversations, not all of which I've understood (e.g. all of the Star Trek chat)... Thank you to all of the 1st Year labs crew for providing that weekly distraction from real work and a reminder of how far I've come since the time that I was on the other side of those lab benches!

My time as a PhD student would have been very different without being involved in Cardiff University Korfball and Raptors Korfball Clubs. This weird sport gave me something to think about outside of PhD, and in the more difficult times provided a distraction to come back with a clear mind. So, thank you to everyone involved in running those clubs and everyone who was my teammate at any point. An especial thank you to Katie and Jordan for all of the work you do, for all of the lifts to training and matches, and for your constant upbeat enthusiasm!

To the family I've gained through Andrew: Val, Martin, Jon, and Lauren,

I'm so grateful for the times that we've had, and will have, to spend together. Thank you for welcoming me into the family: here's to many more curry and pub trips!

To my wonderful Mom and Dad, thank you for always believing in me. You've always helped me to believe that my journey is in my own hands and that I can achieve whatever I put my mind to if I work at it. You've always been an inspiration and an example of how to work hard and enjoy life too! I'm so grateful for all of your love and everything you've done for me, and I hope that I make you proud. Emma, Liz, and Chris, I love you loads and I love seeing everything that we all achieve as we get older. Thank you for all of your support and, at least feigned, interest!

Finally Andrew, thank you for making my life happier. I'm so grateful for all of the adventures we've had together and the happy memories we've made, and I'm excited to keep on exploring the world with you. Thank you for making my worries seem smaller; I love our little unit and that we can share in both of our successes and happinesses. Sharing it with you has made this chapter of my life all the happier: now let's go see what the next holds for us!

ACKNOWLEDGEMENTS

This work was made possible by support from the European Research Council (ERC) in the form of Consolidator Grant Cosmic Dust (ERC- 2014-CoG-647939, PI H L Gomez).

This work has made use of the Python packages Astropy[1] (The Astropy Collaboration et al., 2013, 2018), MatPlotLib[2] (Hunter, 2007), NumPy[3] (Oliphant, 2006; Van Der Walt et al., 2011), pandas[4] (McKinney, 2010), and SciPy[5] (Virtanen et al., 2020). This thesis made use of PPMAP (Marsh et al., 2015).

This thesis made use of Green's Galactic SNR catalogue[6] (Green, 2004, 2014, 2019). HiGal[7] (Molinari et al., 2010a, 2013) is an Open Time Key Programme mapping the Galactic Plane with *Herschel*, which is an ESA space observatory with science instruments provided by European-led Principal Investigator consortia and with important participation from NASA.

[1] https://www.astropy.org/
[2] https://matplotlib.org/
[3] https://numpy.org/
[4] https://pandas.pydata.org/
[5] https://docs.scipy.org/
[6] http://www.mrao.cam.ac.uk/surveys/snrs
[7] https://hi-gal.ifsi-roma.inaf.it/higal/

PUBLICATIONS

'You ask 'What if I fall?' Oh but my darling, what if you fly?'

ERIN HANSON

1. **Chawner, H.**, Marsh, K., Matsuura, M., Gomez, H. L., Cigan, P., De Looze, I., Barlow, M. J., Dunne, L., Noriega-Crespo, A., Rho, J. *A catalogue of Galactic supernova remnants in the far-infrared: revealing ejecta dust in pulsar wind nebulae*, 2019, MNRAS, 483, p70-118

2. De Looze, I.; Barlow, M. J.; Bandiera, R.; Bevan, A.; Bietenholz, M. F.; **Chawner, H.**; Gomez, H. L.; Matsuura, M.; Priestley, F.; Wesson, R., *The dust content of the Crab Nebula*, 2019, MNRAS, 488, p164-182

3. **Chawner, H.**, Gomez H.L., Matsuura M, Papageorgiou, A., Rho, J., Noriega-Crespo, A., De Looze, I., Barlow, M.J., Cigan, P., Dunne, L., Marsh, K. *A Complete Galactic Plane Catalogue of Far-infrared Supernova Remnants with Herschel: an inventory of dusty supernovae in the Milky Way*, 2020, MNRAS, 493, p2706-2744

4. Priestley, F. D.; Barlow, M. J.; De Looze, I.; **Chawner, H.**, *Dust masses and grain size distributions of a sample of Galactic pulsar wind nebulae*, 2020, MNRAS, 491, p6020-6031

5. **Chawner, H.**, A. D. P. Howard, H.L. Gomez, M. Matsuura, F. Priestley, M. J. Barlow, I. De Looze, A. Papageorgiou, K. Marsh, M.W.L Smith, A. Noriega-Crespo, J. Rho and L. Dunne *A Galactic Dust Devil: far-infrared observations of the Tornado*, MNRAS, accepted

ABSTRACT

'I know nothing with any certainty but the sight of the stars makes me dream.'

VINCENT VAN GOGH

This thesis investigates the question of whether supernovae (SNe) are important contributors of dust to the interstellar medium (ISM). Using far-infrared (FIR) observations of 190 supernova remnants (SNRs) covered by the *Herschel* Infrared Galactic Plane Survey (HiGal), we augment the current sample of dusty SNRs with an additional 38 from which dust emission is newly detected. This gives a 21 per cent detection rate of dust within SNRs in the Galactic Plane, although this is expected to be a lower limit given confusion with the ISM in this region. The majority of detected SNRs are young (<5 kyr), as expected since these objects tend to be more compact and have higher surface brightness, making them more easily detected above the level of the ISM. Nevertheless, we expand the age range of SNRs containing dust to ~ 100 kyr. Of our detections, 13 are from core collapse (CC) and 2 from Type Ia SNe (24 are of unknown type). Consistent with previous observations and theoretical models, we find that dust detected within the Type Ia SNRs is not expected to be of ejecta origin, but is more likely to have been swept up from the ISM. It is likely that many of our other detections are also dominated by ISM, although there are several objects within which we expect that the FIR emission originates from freshly formed ejecta material, including G350.1$-$0.3

We make new discoveries of ejecta dust within pulsar wind nebulae (PWNe) associated with three SNRs: G11.2$-$0.3, G21.5$-$0.9, and Kes 75. Using point process mapping (PPMAP) to analyse the FIR emission indicates the presence of dust within each object with temperatures between 20 and 40 K, and a PWN dust mass

of $0.34 \pm 0.14\,M_\odot$, $0.29 \pm 0.08\,M_\odot$, $0.51 \pm 0.13\,M_\odot$ for G11, G21, and Kes 75 respectively. This suggests that SNe are important contributors of dust to the ISM, and PWNe in particular may play an important role in this. Although some of this dust may yet to be destroyed, there is evidence that the reverse shock has already reached the centre of G11, leaving behind a considerable mass of surviving dust. We use PPMAP further in an attempt to examine the dust properties, by studying the emissivity index, β. The signal-to-noise in the longer wavebands is too low to constrain β for G11 or Kes 75; however, we find some evidence of a variation in the dust properties of ejecta dust within G21 ($\beta = 1.4 \pm 0.5$), compared with that of the surrounding ISM ($\beta = 1.8 \pm 0.1$).

We study the dust within 11 of the other detected SNRs which are in regions with limited ISM variation, making background subtraction and thus dust analysis possible. By producing temperature maps, using their 24 – 70 µm flux ratios, we reveal the presence of warm dust (25 - 40 K) within all of these objects. For the objects with associated distance estimates, this analysis gives dust masses of between 0.2 and $340\,M_\odot$, some of which are extremely large compared to the typical combined mass of freshly formed and swept up material. It is most likely that, despite careful background subtraction, the largest of these masses are overestimated due to contaminating ISM, which reduces the average dust temperature. As the dust mass is highly sensitive to even small changes in the estimated temperature, ISM confusion is the largest barrier to overcome when analysing the dust content of SNRs within the Galactic Plane.

We detect a region of dust coincident with a strange radio source at the centre of G351.2−0.1. Previous studies have suggested that this could a PWN, or simply an unrelated HII region; we therefore attempt to determine its nature using FIR observations. Its spectral energy distribution (SED) suggests that the region consists of two dust components: $(3.9 \pm 0.4) \times 10^{-6}\,M_\odot$ of warm dust with a temperature of 242 ± 7 K, and $0.18\,M_\odot$ of cool dust with a temperature of 45.8 K. The temperature of the dust is higher than typical for a HII region, although not unheard of, and when considering the IR colours the emission from the core is consistent with either a HII region or SNR. We therefore cannot rule out either option based only on the IR emission, and the G351.2 core could be either an unrelated HII region, or a PWN with a considerable dust mass.

A large region of dust was detected within a very unusual object known as the Tornado, G357.7−0.1. This is an object with a very uncertain past, which, it has been suggested, could have been formed by a SN or an X-ray binary. We detect FIR emission from multiple components of the Tornado: a filamentary structure within the tail region, peaks within the head, and an unrelated HII region dubbed the 'eye'. Using PPMAP we reveal complex dust structures within the Tornado head and tail with temperatures between 15 and 61 K, and a total dust mass for the head of 16.7 $M_\odot$. Within the head there is clear variation in the IR emission: an IR peak is detected to the north-west where the head is thought to be expanding into dense molecular material, and there is IR emission along radio filaments found towards the east. Comparing the IR and IR – radio colours highlights a variation in the emission from the two regions, suggesting that the dust properties or heat processes are different. When considering the nature of the Tornado, the head can be explained by a SNR aged between 2 and 8 kyr, with a large mass of dust swept up from the dense surrounding material. However, the tail is bizarre and more difficult to explain with a SN origin. We find it unlikely that it was formed by a progenitor prior to exploding. The structures in the tail could have been formed by jets from an X-ray binary, and we propose that the Tornado is similar to the W50 – SS 433 system, in which the jets of an X-ray binary plough into the SNR shell.

This thesis has found a considerable dust mass contained within numerous Galactic SNRs, with several examples of newly detected ejecta dust. In particular, PWNe seem to be significant in the search for dusty SNRs. These findings suggest that SNe are important contributors of dust to the ISM.

CONTENTS

LIST OF TABLES

List of Figures

Chapter 1
Introduction

'Would you like an adventure now, or shall we have our tea first?'

Lewis Carroll, Alice in Wonderland

1.1 Cosmic Dust

Astronomers have long been confused by voids in the sky where there is an apparent lack of stars, but it is a relatively new idea that these 'holes' might be more than just that.

Only at the start of the 19th century was it suggested by William Herschel that space might contain more than just stars (Herschel, 1811). The first evidence of cosmic dust came soon after, when Wilhelm Struve hypothesised that starlight might be absorbed in some way, finding that the numbers of stars seems to decline with distance (Struve, 1847). It was later found that at least some of the 'star voids' contained interstellar clouds which were absorbing and scattering light (Barnard, 1907), although the theory did not gain traction and even Kapteyn, who recognised its significance (Kapteyn, 1909), did not include extinction in his other work. Finally, in 1930 Robert Trumpler proved the extinction effect by studying the luminosity and size of star clusters. By comparing the light from different spectral types, Trumpler demonstrated that interstellar extinction is a function of wavelength, and that this is caused by small, solid particles known as cosmic 'smoke' or dust (Trumpler, 1930).

Dust transforms our view of the Universe, having absorbed around half of all the stellar light emitted since the Big Bang (Puget et al., 1996; Fixsen et al., 1998; Dole et al., 2006; Driver et al., 2016). Dust obscures some of the most interesting astronomical events, from young stars in the Milky Way to the formation of new galaxies at high redshift. Hot sources radiate UV and optical light, heating enshrouding dust which re-radiates infrared light. Only by understanding dust can we learn about the objects that it hides from us.

However, dust is not just a hindrance obstructing our view of more interesting objects, it is involved in many processes which shape the Universe. Just after the Big Bang the Universe contained only very light elements: hydrogen, helium, and some traces of lithium. Heavier elements were synthesised by stars, and the majority of interstellar metals (e.g. C, Si, Mg, Fe, Al, Ti, Ca) in galaxies are now locked up in dust grains, ranging in size between $\sim$10 nm and $\sim$10 µm (e.g. Mathis et al., 1977; Kim et al., 1994; Kim & Martin, 1994; Jones et al., 1996). As such, dust gives us a window through which we can view the chemical evolution of the Universe (e.g. Popping et al., 2014; De Vis et al., 2019). These dust grains are key to the formation and survival of molecules such as molecular hydrogen, acting as a catalyst for chemical reactions (Gould & Salpeter, 1963), and shielding them from radiation fields. Dust emission can be used to trace the gas within a galaxy and to estimate the total ISM mass to higher accuracy than previous methods (e.g. Hildebrand, 1983; Boselli et al., 2002; Eales et al., 2012), thus revealing to us the evolutionary path of galaxies (e.g. Dunne et al., 2011; Beeston et al., 2018; Millard et al., 2020). Although seemingly insignificant, tiny dust grains also serve as the seeds for planetary formation, condensing into protoplanetary discs which collapse into planetesimals to form planets, such as those in our Solar System (e.g. Goldreich & Ward, 1973). Dust is involved in astronomical processes at all levels, and to explain how our Solar System came to be and how the Universe continues to evolve we must understand cosmic dust and its origins.

1.2 Supernovae and their Remnants

As will be discussed in Section 1.3, supernovae (SNe) play an important role in the formation and destruction of cosmic dust.

SNe are the very dramatic, explosive death of stars and are categorised into two main groups: the thermonuclear detonation of degenerate stars known as Type Ia SNe, or the core collapse of high mass stars ($>8\,M_{\odot}$). SNe of the most

Main Sequence Mass, $M_\odot$	Supernova Type	Remnant
$\lesssim 8$	Type Ia, thermonuclear	SNR, no compact object
$\sim 8-10$	Core collapse, electron capture	Neutron star
$\sim 10-100$	Core collapse, Fe dissociation	Neutron star
$\sim 100-130$	Pulsational pair-instability	Neutron star
$\sim 130-260$	Pair-instability	None
$\gtrsim 260$	?†	Black hole

Table 1.1: The fate of stars of various mass which die as SNe, assuming non-rotation (Woosley et al., 2007). †The most massive stars disappear quietly into black holes, but are included here for completeness.

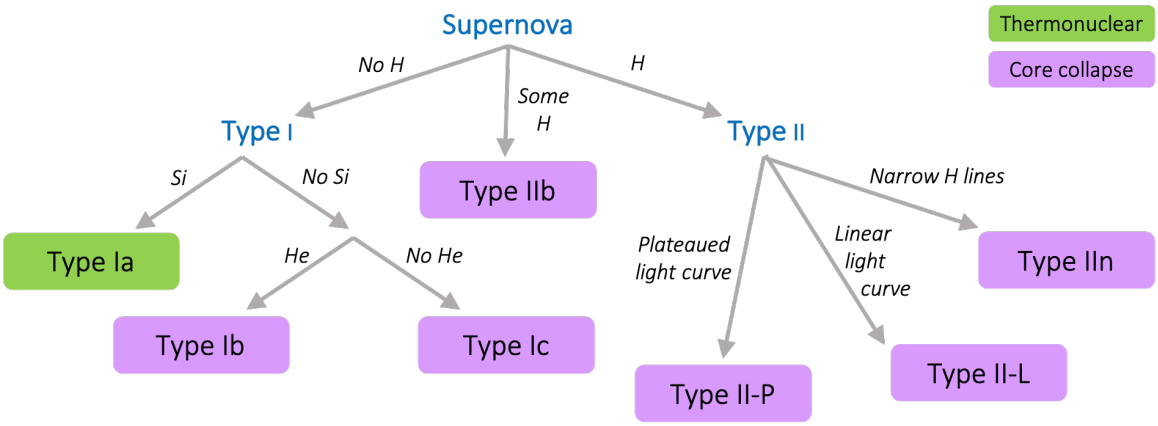

Figure 1.1: Process of classifying SNe, based on emission lines in their optical spectra, and the shape of their light curve.

massive progenitors ($>100\,M_\odot$) are the results of pair instabilities at the core. Table 1.1 gives the expected route of SN for various stellar initial mass. In most cases, a nebula of stellar material is left behind from the explosion, initially comprising material ejected during the SN. This supernova remnant (SNR) expands into the surrounding ISM, sweeping up material and shaping the local environment.

SNe are classified by the system in Figure 1.1, based on line emission in their optical spectra and the shape of their light curve (e.g. Turatto, 2003, and therein). These observations vary for different progenitors and explosion mechanisms. Type I SNe are characterised by a lack of hydrogen (Minkowski, 1941). The progenitors of these types are either very massive stars which have expelled their hydrogen shell prior to exploding (Type Ib/c), or degenerate carbon-oxygen (CO) cores (Type Ia), in which case silicon is also detected due to CO fusion (Elias et al., 1985; Wheeler & Harkness, 1990). Further classification of Type I SNe is based on the presence of helium which may also be expelled from a massive core-collapse progenitor shell. Type II SNe result from the core collapse of massive stars

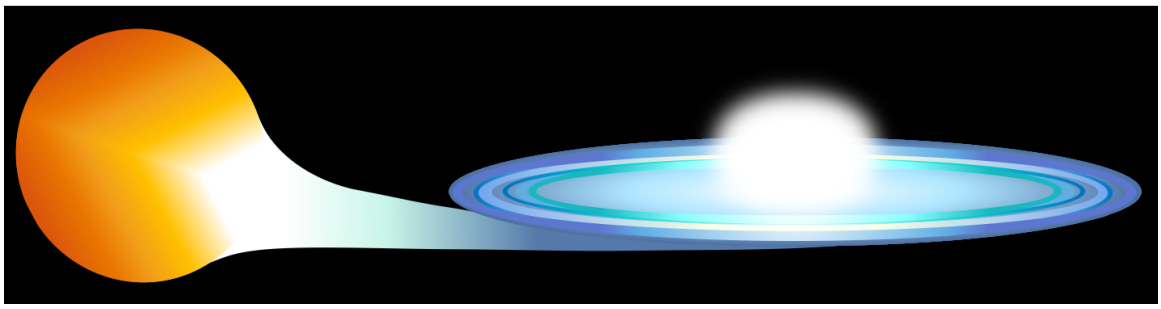

Figure 1.2: The single degenerate route for a Type Ia supernova: a binary system involving a star which has filled its Roche Lobe and feeds the accretion disc of a White Dwarf progenitor.

which have retained at least part of their hydrogen shell. Other spectral features are used to classify these SNe, including narrow hydrogen lines (Type IIn) which arise from interactions with CSM, and a plateau in the SN light curve (Type IIP) due to recombination in the hydrogen envelope.

1.2.1 Type Ia Supernovae

The most widely accepted route for a Type Ia SN involves a degenerate star which reaches the Chandrasekhar mass by accretion, at which point the centre ignites, and triggers an explosion (e.g. Whelan & Iben, 1973). The white dwarf (WD) progenitor evolves alongside a lower mass star in a binary system (e.g. Hoyle & Fowler, 1960; Nomoto et al., 1997). The companion, which can be either degenerate or non-degenerate, fills its Roche lobe and forms a hydrogen-helium accretion disc or envelope around the carbon-oxygen WD, as shown in Figure 1.2. The extra mass causes the WD to contract and heat, and material at the core-envelope interface ignites, initially forming a pure helium layer and then adding carbon and oxygen to the core. Carbon at the centre ignites when the core reaches the Chandrasekhar limit, the burning propagates outwards and causes the star to go supernova.

A WD can also go supernova with a sub-Chandrasekhar mass (Woosly & Weaver, 1994), the most popular theory for which is double-detonation (e.g. Iben & Tutukov, 1984; Webbink, 1984). Similar to the previous channel, a CO WD accretes a helium layer from a donor star; however, in this case the helium ignites before the star reaches the Chandrasekher mass and causes a powerful shock-wave inwards. This compresses the CO which ignites and sets off outwards detonations (Weaver & Woosley, 1980; Nomoto, 1980, 1982a,b; Sutherland & Wheeler, 1984).

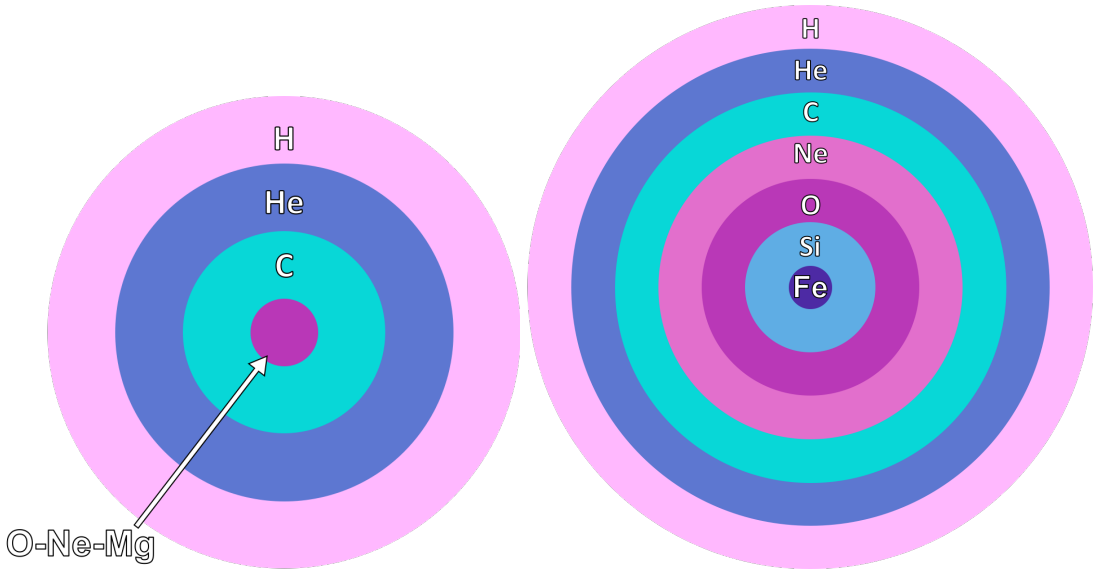

Figure 1.3: The structure of high mass stars before exploding as core collapse supernovae. *Left:* stars with a main sequence mass of $\lesssim 10\,M_\odot$ become super-AGB stars towards the end of their lives, and explode as electron-capture SNe. *Right:* more massive stars ($10 \lesssim M \lesssim 100\ M_\odot$) form an iron core and collapse by iron dissociation.

1.2.2 Core Collapse Supernovae

Stars with Main Sequence masses of more than $8\,M_\odot$ end their lives as core collapse SNe (CCSNe). After burning through the hydrogen reserves at their core these stars leave the Main Sequence and continue to form layers of progressively heavier and more stable elements, as shown in Figure 1.3. Each higher stage of nuclear burning is less efficient than the last as the energy lost to neutrino-antineutrino pairs increases, and the star's evolution accelerates considerably. When the central temperature reaches $\sim 10^9$ K the neutrino losses are greater than radiation losses and the evolution of the core separates from the surrounding shell. The core loses gravitational stability as it loses energy and continuously contracts, with the final process by which it implodes depending on the progenitor mass.

Smaller progenitors of less than $\sim 10\,M_\odot$ are triggered through electron capture (Poelarends et al., 2008). These stars form an oxygen-neon-magnesium core through carbon burning, which is supported by electron degeneracy pressure (Nomoto, 1984, 1987; Miyaji & Nomoto, 1987; Poelarends et al., 2008). The core grows in mass and density as the shell continues to burn hydrogen and helium, and the star becomes a super-asymptotic giant branch star (SAGB) (Siess, 2007; Nomoto et al., 2014). Eventually the star's core passes a critical density, when it reaches the Chandrasekhar mass (Nomoto, 1984), at which point magnesium nuclei begin to

capture electrons, reducing the degeneracy pressure; the core becomes gravitationally unstable and collapses (Miyaji et al., 1980; Miyaji & Nomoto, 1987; Hashimoto et al., 1993).

In progenitors with a larger mass ($\sim$10 – 100 $M_\odot$, e.g. Janka, 2012) nuclear fusion continues to produce heavier elements until an iron core is formed. The core becomes unstable when it reaches extremely high temperatures of $\sim 10^{10}$ K. The resulting high energy radiation causes the photo-dissociation of iron nuclei into α-particles and nucleons, causing the core to contract. As the density increases, electron capture accelerates, and implosion speeds up.

Collapse stops suddenly when the core reaches nuclear density due to the short range repulsion of the strong force. The inner core rebounds, causing a supersonic crash into in-falling matter, and a shock front forms. The compact core remains after the star has exploded.

1.2.3 Pair Instability Supernovae

The most massive stars ($\gtrsim$100 $M_\odot$) experience pair instability towards the end of their lives. Because of very high temperatures (10^9 K) at the core, high energy radiation produces electron and positron pairs, decreasing the internal radiation pressure (Fowler & Hoyle, 1964; Rakavy & Shaviv, 1967). The star's core begins to contract, increasing the temperature and causing rapid carbon, oxygen, and possibly silicon burning. For very massive stars ($\gtrsim$260 $M_\odot$) the core collapses completely to a black hole. However, for less massive stars, energy from the burning reverses the collapse and the star may explode as a pair instability SN, leaving no remnant behind (e.g. Ober et al., 1983; Bond et al., 1984; Glatzel et al., 1985; Heger & Woosley, 2002; Umeda & Nomoto, 2002; Scannapieco et al., 2005; Woosley & Heger, 2015). If there is insufficient burning for the star to explode ($95 \lesssim M_* \lesssim 130\, M_\odot$), the core expands and expels material from its outer layers, before again contracting and experiencing pair instability. The process repeats and may be observed as a pulsational pair instability supernova (e.g. Woosley et al., 2007; Chatzopoulos & Wheeler, 2012; Yoshida et al., 2016; Woosley, 2017). Once enough material has been expelled such that pair instability is avoided, the star forms an iron core and dies as a core collapse supernova.

1.2.4 Supernova Remnant Evolution

After a supernova, the remnant continues to evolve, going through four main stages of evolution as described in Figure 1.4 (Woltjer, 1972).

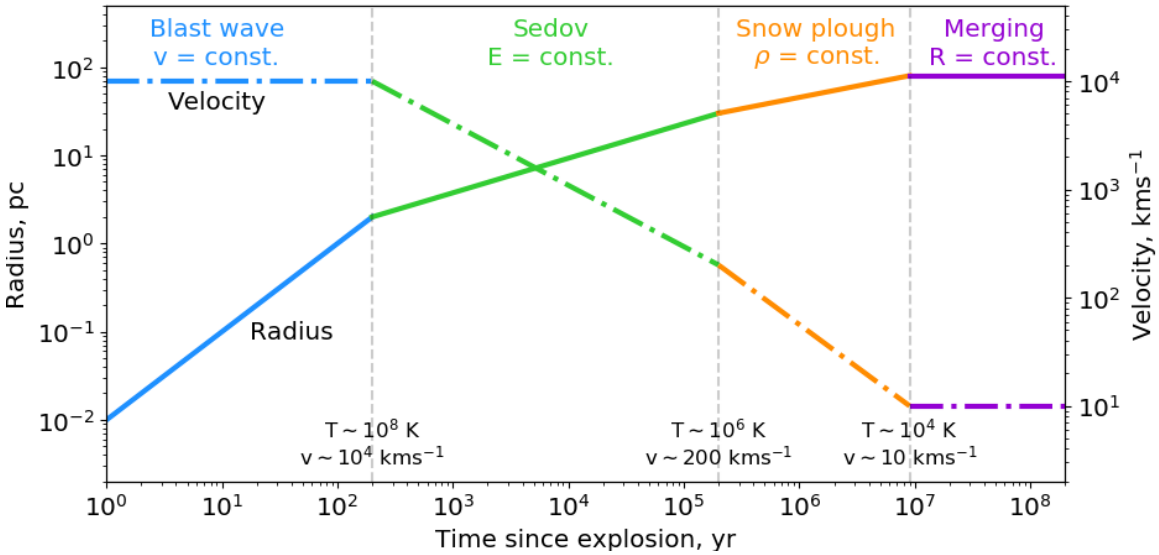

Figure 1.4: The radius and velocity of a core collapse SNR as it progresses through the stages of evolution. The time-frames vary depending on the density of the surrounding ISM and the progenitor type. *Reproduced from Micelotta et al. (2018).*

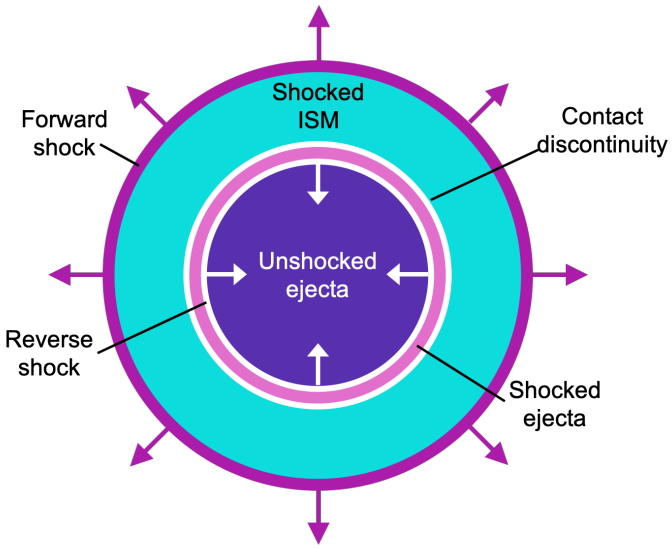

Figure 1.5: A SNR expanding into the ISM. A forward shock propagates into the ISM, sweeping up a shell of shocked material. Interaction with the ISM sends a reverse shock back towards the centre of the SNR where the unshocked ejecta material is found.

Initially the SNR shock expands freely into the ISM at supersonic speeds (e.g. Blandford & Ostriker, 1978), such that its shock radius is given by $R \approx v_e t$, where v_e is the expansion velocity and t is the time since explosion. Interstellar gas accumulates behind the shock front which is heated to very high temperatures and has a mass given by:

$$M \approx \frac{4}{3}\pi R^3 \rho_0 = \frac{4}{3}\pi (v_e t)^3 \rho_0 \tag{1.1}$$

where ρ_0 is the initial ISM density.

A contact discontinuity forms between ejecta and the swept up material, that is that the material have the same pressure and velocity but different densities. The reverse shock begins to form behind the contact discontinuity (Mckee, 1974; Cioffi et al., 1988), as shown in Figure 1.5 and then starts to move back towards the centre of the SNR, heating the ejecta material. The free expansion phase ends when the swept up mass is equal to the ejected mass.

After reverse-shock heating, the ejected material is extremely hot, its atoms are ionised and no recombination can occur. Radiation losses are very small and the SNR expands adiabatically, cooling only via its expansion (Taylor, 1950; Sedov, 1959). At this stage the radius and velocity (Truelove & McKee, 1999) are given by:

$$R \approx \left(\frac{5}{2}\right)^{2/5} \left(\frac{E}{\pi \rho_0}\right)^{1/5} t^{2/5} \tag{1.2}$$

$$v_e \approx \left(2.1 \frac{2}{3\pi} \frac{0.7E}{\rho_0}\right)^{1/2} R^{-3/2} \propto t^{-3/5} \tag{1.3}$$

where E is the SN explosion energy.

There is efficient radiative cooling when the SNR reaches temperatures of 10^6 K as ionised atoms de-excite and capture free electrons (Dubner & Giacani, 2015). This causes thermal pressure in the post-shock to decrease and the expansion slows down (Cioffi et al., 1988). During this stage the radius and velocity can be given by:

$$R \approx R_0 \left(1 + 4\frac{V_0}{R_0}(t - t_0)\right)^{1/4} \propto t^{1/4} \tag{1.4}$$

$$V = V_0 \left(1 + 4\frac{V_0}{R_0}(t - t_0)\right)^{-3/4} \propto t^{-3/4} \tag{1.5}$$

where R_0, V_0, and t_0 are initial radius, volume, and age of the SNR when it

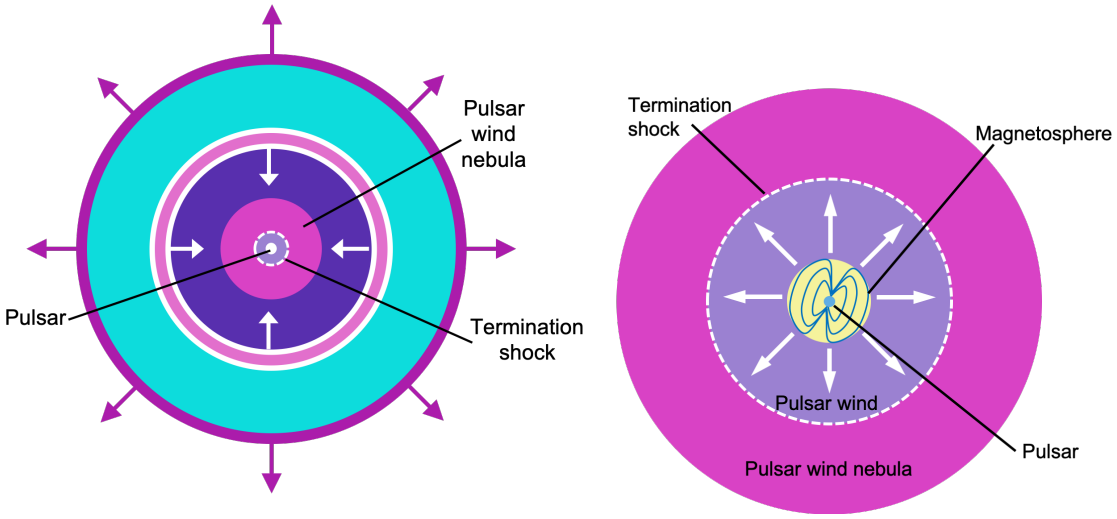

Figure 1.6: *Left:* A composite SNR comprising an expanding shell and reverse shock, as in Figure 1.5, as well as a pulsar near to the centre which powers the PWN surrounding it. *Right:* A pulsar powers a relativistic wind which interacts with the surrounding medium to form a termination shock, beyond which the PWN is found.

enters this stage of evolution.

Finally the Rayleigh-Taylor instability causes the SNR shell to break up and the material disperses into the ISM.

1.2.5 Pulsar Wind Nebulae

In 1968 a strange pulsing radio signal was detected for the first time (Hewish et al., 1968). Although initially attributed to 'Little Green Men', it was soon established that this was a pulsar, a rotating neutron star which emits radiation from its magnetic poles. Pulsars were detected soon after within the Crab and Vela nebulae (Lovelace et al., 1968; Large et al., 1968; Staelin & Reifenstein, 1968), confirming the prediction from just over 30 years earlier that some SNe could produce neutron stars (Baade & Zwicky, 1934).

We now know that high mass stars collapse into neutron stars as CCSNe, as described in Section 1.2.2. Young pulsars are surrounded by a bubble of relativistic electrons and ionised atoms, as shown in Figure 1.6, known as a pulsar wind nebula (PWN), the evolution of which is dictated by the properties of the pulsar and interactions with the surrounding SNR. PWNe are observed to have a centre-filled morphology, a flat radio spectrum, and non-thermal emission across the electromagnetic spectrum.

Figure 1.7: The Crab Nebula across the spectrum: a composite image of the radio (VLA, red), IR (*Spitzer*, yellow), optical (Hubble Space Telescope, green), UV (*XMM-Newton*, blue), and X-ray emission (*Chandra*, purple). The X-Ray emission shows a toroidal shape with perpendicular jets. At lower energies there is a large shell of material with filamentary features formed by interactions between the nebula and the surrounding SN ejecta it is expanding into. Image credit: NASA, ESA, G. Dubner (IAFE, CONICET-University of Buenos Aires) et al.; A. Loll et al.; T. Temim et al.; F. Seward et al.; VLA/NRAO/AUI/NSF; Chandra/CXC; Spitzer/JPL-Caltech; XMM-Newton/ESA; and Hubble/STScI

When a pulsar is formed in a CCSN, asymmetry of the explosion gives the pulsar a random velocity which is small compared to the initial expansion velocity of the SNR blast wave, and the pulsar is found roughly central to the SNR (Gaensler & Slane, 2006). This may be observed as a composite SNR, as in Figure 1.6, if the SNR has swept up a shell of ISM. A small amount of the pulsar's rotational energy goes into pulses of emission as detected by Hewish et al. (1968), but the majority is depleted as it powers highly relativistic, magnetised winds made up of electron-positron pairs (Rees & Gunn, 1974). The pulsar wind has a very high pressure and expands supersonically, driving a shock into the surrounding ejecta, called the termination shock (Kennel & Coronitti, 1984). At this boundary the wind is thermalised, the magnetic field is compressed, and relativistic particles from the wind are accelerated to ultra-relativistic speeds with energies of

up $\sim 10^4$ TeV (Reynolds & Chevalier, 1984; Hester, 2008). This forms the PWN: a plasma of relativistic, magnetised particles which emits synchrotron radiation. The nebula sweeps up a shell of SN ejecta as it expands supersonically into the SNR. This shell is more dense than the expanding plasma, and Rayleigh-Taylor instabilities lead to filamentary features which are photoionised by synchrotron radiation from the surrounding nebula, as seen in the Crab Nebula in Figure 1.7 (Hester et al., 1996).

After a few thousand years, when the SNR is in its Sedov Taylor phase of evolution, the reverse shock moves towards the centre of the SNR and collides with the PWN. As the PWN is compressed its pressure increases, triggering sudden expansion (Reynolds & Chevalier, 1984). Reverberations cause the PWN to oscillate over several thousands of years, during which time there is mixing of the SNR material and PWN, producing complicated filamentary structures of thermal and non-thermal material (Chevalier, 1998) and increasing the flux density of the PWN (van der Swaluw et al., 2001). As the reverberations fade, the PWN begins to expand steadily into the hot, shocked ejecta at a subsonic speed (van der Swaluw et al., 2001).

The pulsar continues to travel through the SNR, moving outside of its original PWN which is left as a relic, whilst a new, smaller nebula forms around it (van der Swaluw et al., 2004). As the SNR cools, the relative pulsar motion becomes supersonic and it forms a bow shock though the SNR (Chevalier, 1998; van der Swaluw et al., 1998). Eventually the pulsar escapes SNR shell and continues to propagate through the ISM (van der Swaluw et al., 2003).

1.2.6 Green's Catalogue of Galactic SNRs

This thesis relies on Green's Catalogue of Galactic supernova remnants (Green, 2014, 2019). Initially compiled in 1984, the catalogue is now in its 8th revision and includes a detailed online version which was first made available in 1995. The current (2019) iteration includes 294 SNRs which were identified by studies across the EM spectrum, and the detailed version includes information about objects which were previously mis-identified as SNRs. The 2019 catalogue consists of 80% shell type SNRs, 13% composite, and 3% filled-centre, where the remaining objects either do not fit with conventional types, or their type is unclear.

Green (2019) discusses the selection effects which limit the detection of Galactic SNRs, where these are mostly dominated by selection effects in the radio region. Detections are difficult where an object has low surface brightness or has a

small angular size, associated with young and distant SNRs. No SNRs have been added to the catalogue since 2009 which have a 1 GHz surface brightness above $\Sigma \approx 10^{-20}\,\mathrm{Wm^{-2}Hz^{-1}sr^{-1}}$, and only 9 SNRs in the catalogue have an angular diameter of $\leq 3'$.

1.3 Dust Formation, Destruction, and Heating

1.3.1 The mysterious origins of cosmic dust

Dust grains form from gas by a similar process to that of water droplets in the Earth's atmosphere (Salpeter, 1974), explained by classical nucleation theory (CNT, Feder et al., 1966). For a gas below the condensation temperature of a material, when the density of that material is high enough it begins to condense into clusters, as particles in the gas encounter each other. When clusters reach a critical size, growth becomes more rapid and clusters become macroscopic. Unlike condensation of water droplets, chemical reactions bind dust clusters, and the cluster materials are different to the gas particles from which they condense.

A large amount of Galactic dust is produced in over-densities within the atmospheres of low-to-intermediate-mass stars (LIMS) along the Asymptotic Giant Branch (AGB) stage of evolution (e.g. Matsuura et al., 2009; Ventura et al., 2014; Schneider et al., 2014; Dell'Agli et al., 2015, 2017). Dust grains can form between two boundaries within which the star's envelope has a temperature and density above that of the average ISM, and the shell is below the dust condensation temperature of around 1500 K, these bounds are typically around 10 and 10^4 times the star's radius (Whittet, 1992). The dust composition depends on the type of star and the ratio of carbon-to-oxygen (C/O) within the atmosphere, as the least abundant will be almost completely locked up in CO gas (Gilman, 1969). The atmospheres of oxygen-rich stars are usually dominated by silicate dust, and amorphous carbon dust dominates carbon-rich stellar atmospheres. Initially, AGB stars, within the Milky Way, have atmospheres with C/O of ~ 0.5, however, for stars above around $2\,\mathrm{M_\odot}$ at solar metallicity (this limit is lower at lower metallicity) (Karakas & Lattanzio, 2007; Höfner & Olofsson, 2018), newly formed carbon is dredged up by thermal pulses (Straniero et al., 1997). This makes the atmosphere increasingly carbon-rich and alters the dust composition as the star evolves (Marigo et al., 1996). Periodic pulsational instabilities cause variations in temperature and density throughout the atmosphere, causing cycles of grain nucleation, growth, and

ejection into the ISM. Newly formed dust grains absorb and scatter stellar photons, transferring the photon momentum to the dust grains, which in turn accelerate the surrounding gas (Bowen, 1988). This creates outflows from the star's atmosphere and forms an envelope of circumstellar material (CSM) (e.g. Höfner et al., 1998; Höfner & Andersen, 2007). AGB stars typically have mass loss rates of $10^{-8}-10^{-5}\,M_{\odot}\,year^{-1}$ (e.g. Zhukovska & Henning, 2013; Matsuura et al., 2013; Schneider et al., 2014; Dell'Agli et al., 2017), which increases as the star evolves and pulsational activity increases, and can be higher than $10^{-4}\,M_{\odot}\,year^{-1}$ in extreme objects (Höfner & Olofsson, 2018).

Although it is widely accepted that AGB stars are an important source of dust, studies of dust production and destruction rates in local (e.g. Matsuura et al., 2009; Dunne et al., 2011; Mattsson et al., 2014; De Vis et al., 2017) and high-redshift galaxies (e.g. Morgan & Edmunds, 2003; Dwek et al., 2007; Michałowski et al., 2010; Gall et al., 2011a,b,c; Rowlands et al., 2014; Michałowski, 2015) have indicated a discrepancy of up to an order of magnitude between the mass of dust observed in the ISM of galaxies, and the production rate of AGB stars. This is especially problematic at redshifts of $z \geq 5$ where the age of the Universe is comparable to the evolutionary timescale of low-mass evolved stars ($10^{8} - 10^{9}$ yr) and yet large masses of dust are observed (e.g. Morgan & Edmunds, 2003; Bertoldi et al., 2003; Dwek et al., 2007; Watson et al., 2015). Some argue that LIMS could evolve more rapidly and contribute significant masses of dust after only 150 – 500 Myr (Valiante et al., 2009) or that very high mass Population III stars could form large masses of carbon grains (Nozawa et al., 2014), yet this is highly dependent on the initial mass function and metallicity (Dwek & Cherchneff, 2011; Ventura et al., 2012, 2014; Di Criscienzo et al., 2013; Dell'Agli et al., 2017).

It has been proposed that dust formation by SNe can account for the shortfall in the dust budget, and that they must be the dominant source of dust at high redshift (e.g. Dunne et al., 2003; Bianchi & Schneider, 2007; Kozasa et al., 2009; Gall et al., 2011c; Sarangi & Cherchneff, 2015). With lifetimes of up to only tens of millions of years, massive stars evolve much more quickly than LIMS, and SNe can inject dust into the ISM with a more immediate effect than AGB stars. During the explosion, shock waves trigger explosive nucleosynthesis which lasts for a few hours, until expansion cools the gas enough to stop the reactions (Todini & Ferrara, 2001). Heavy elements are formed very quickly within the ejecta and the final composition of the dust depends on how well these elements are mixed in the He-rich layer (e.g. Nozawa et al., 2003; Cherchneff & Lilly, 2008; Cherchneff & Dwek, 2009). Silicate and carbon grains can form in the ejecta just a few hundred

days after the explosion (Kozasa et al., 1991; Todini & Ferrara, 2001; Nozawa et al., 2003) and models suggest that SNe can produce between 0.1 and 1.0 $M_\odot$ of dust in their ejecta (Todini & Ferrara, 2001).

1.3.2 Dust Destruction

Dust formation by SNe is no longer a controversial idea; however, there is still the issue of how much of this dust, if any, can survive to be injected into the ISM (e.g. Micelotta et al., 2018). Interactions between SNRs and the ISM trigger forward and reverse shocks which propagate through the surrounding ISM and the ejecta within the SNR respectively. Shocks heat gas and dust as they pass, and can cause substantial destruction of dust grains (e.g. Jones et al., 1996; Kozasa et al., 2009; Bocchio et al., 2016). Destruction occurs by two processes: sputtering and shattering. Sputtering describes the erosion of dust grains by impacts with energetic gas particles or ions which are accelerated either thermally, by high temperatures, or non thermally, e.g. by magnetic fields. Grains can also be shattered or evaporated by collisions with each other.

There is huge uncertainty in the survival rates of dust after the passage of the reverse shock, with estimates varying from near to 0 to 100 % (e.g. Jones et al., 1996; Bianchi & Schneider, 2007; Nozawa et al., 2007; Nath et al., 2008; Sankrit et al., 2010; Silvia et al., 2010, see also Micelotta et al., 2018, Table 2). Simulations of dust destruction in the ISM and SNe suggest that sputtering is responsible for a large amount of dust destruction (e.g. Jones et al., 1997; Bocchio et al., 2014; Micelotta et al., 2016) and destruction rates of up to $3.7 \times 10^{-2} M_\odot yr^{-1}$ have been estimated for SNRs in the Magellanic Clouds (Temim et al., 2015). However, the extent of dust destruction by shocks is dependent on a range of factors which affect the properties of the ejecta, such as the progenitor type, the ejecta composition, ejecta clumpiness and density and the metallicity, as well as external factors including the local density and the SN shock velocity.

The size of dust grains has a huge influence on the likelihood of their survival as small dust grains ($\leq$ 0.1 µm) are destroyed by sputtering with a higher efficiency, and are more easily trapped in the encroaching gas behind a reverse shock (Nozawa et al., 2007, 2010; Kozasa et al., 2009; Silvia et al., 2010). The grain size is determined in part by the evolution of the progenitor star prior to exploding. Where a progenitor expels all or most of its hydrogen shell (e.g. Type Ib/c or Type IIb SNe progenitors) it leaves only a thin hydrogen envelope around its SNR, which cannot significantly decelerate the expanding He core. As a result,

the ejected material has a gas density which is too low for large dust grains to form (e.g. Nozawa et al., 2008, 2010; Kozasa et al., 2009). Additionally, the reverse shock reaches the dust forming region early, with a relatively high gas density behind the shock, and efficiently destroys newly formed dust. The clumpiness of the ejecta also impacts the grain size, and therefore the survival rate (Silvia et al., 2010) as dust clusters form earlier in clumpy ejecta, giving more time for grains to grow before the reverse shock reaches them (Sarangi & Cherchneff, 2015). Dust in clumps is also protected from sputtering, especially when paired with dense ejecta (Biscaro & Cherchneff, 2016; Priestley et al., 2019; Kirchschlager et al., 2019).

1.3.3 Which SNe form dust?

As discussed in Section 1.3.2, the injection rate of dust to the ISM is highly dependent on the SN types, which are described in Section 1.2. This is mainly due to the difference in the mass of hydrogen which envelops the SN, as this affects the expansion of the He core and thus the size of grain which can be formed, and the time at which the reverse shock reaches the ejecta.

Theoretical models suggest that Type Ia SNe, such as Tycho or Kepler, contribute large amounts of heavy elements which may be involved in grain growth in molecular clouds, and between 0.1 and 1.0 $M_\odot$ of dust can be formed in the SN (Nozawa et al., 2011). However, the lack of a H-envelope and the small radii of the grains ($\leq$0.01 µm) mean that the dust is trapped by a reverse shock that arrives relatively early on (<500 yr) and the consequent sputtering is highly efficient (Nozawa et al., 2011). Consistent with observations, which have not found any ejecta dust associated with Type Ia SNRs (Gomez et al., 2012a), it is expected that there is complete destruction of any dust formed by a Type Ia SN.

In CCSNe the likelihood of dust surviving is conditional on the progenitor mass, as massive stars (>25 $M_\odot$) are stripped of their hydrogen envelope, and theory indicates that this makes dust survival unlikely (e.g. Kozasa et al., 2009; Nozawa et al., 2010). There is observational (e.g. Elmhamdi et al., 2004; Di Carlo et al., 2008; Kankare et al., 2014) and theoretical evidence (Nozawa et al., 2008) of dust formation in hydrogen deficient SNe (Type Ib/c and IIb) at early times and they are likely to form large masses of dust, as detected in the Type IIb SNR Cas A discussed above. Yet, like Type Ia SNRs, the dust grain size distribution is bottom heavy and it is efficiently destroyed by the reverse shock (e.g. Nozawa et al., 2010; Biscaro & Cherchneff, 2014, 2016). Nevertheless, there is observational evidence of shocked ejecta dust in Cas A, suggesting that some grain compositions may be less

susceptible to destruction or that fast moving material is more likely to escape (De Looze et al., 2017).

The most common sites for the detection of freshly formed SN dust are in Type IIP and IIn SNe/SNRs. Type IIP SNe suffer the least amount of stripping of their hydrogen envelope, leaving them with a He core which is typically $10^2 - 10^3$ times as dense as that of a SN IIb (e.g. Sarangi et al., 2018). Type IIP are considered the most effective SN type for the synthesis of dust (e.g. Sarangi & Cherchneff, 2015; Biscaro & Cherchneff, 2016; Matsuura, 2017) and, as the most abundant SN type in our local universe (Barbon et al., 1979), models predict that they could produce enough dust to account for the budget shortfall discussed in Section 1.3.1 (e.g. Nozawa et al., 2010). Unlike SNe IIP, dust in Type IIn is expected to form in both the ejecta and the post-shock region between the CSM and SN ejecta (e.g. Smith et al., 2012b) and dust has been detected in both regions (e.g. Smith et al., 2012a; Gall et al., 2014; Bevan et al., 2019)

1.3.4 Dust Heating

Dust is heated via two processes, where the dominance of each depends on the environment and has implications for the temperature that the dust can reach. Predominantly, cosmic dust is heated radiatively, absorbing photons from the interstellar radiation field (ISRF), which is made up of mainly stellar radiation. In the solar neighbourhood, the ISRF has a mean energy density of $\sim 7 \times 10^{-14}$ Jm^{-3} (Whittet, 1992), although it varies depending on the objects in the region. If dust is located in an X-ray plasma, such as in a SN shock, it is also heated by collisions with energetic gas particles, and the energy that it absorbs depends on the particle energy and the dust properties. The radiative and collisional heating rates are given by:

$$H_{rad} = \pi a^2 \langle Q_v \rangle cU \tag{1.6}$$

$$H_{coll} = \pi a^2 \left(\frac{32}{\pi m_e} \right)^{1/2} n_e (kT_e)^{3/2} h(a, T_e) \tag{1.7}$$

where a is the grain radius, $\langle Q_v \rangle$ is the Planck averaged absorption coefficient (Draine & Lee, 1984), U is the radiant energy density and cU is the irradiance or incident flux, n_e is the electron density, T_e is the gas temperature, and $h(a, T_e)$ is the grain heating efficiency which is equal to $\sim$1 for most temperatures and grain sizes (Dwek et al., 1987; Arendt et al., 1999).

Small grains ($a \lesssim 50$ Å) are stochastically heated such that their temperatures vary over short periods of time as the energy deposited by an incident photon or particle is much greater than the internal energy of the grains. As such, small grains peak in temperature at the time of absorbing a photon, and cool significantly as they quickly re-radiate the absorbed energy (Dwek & Arendt, 1992). Larger grains ($a \gtrsim 200$ Å) however have a more steady temperature (Draine, 2003). The grains are at an equilibrium temperature when their absorption rate is equal to their emission rate, as the heating and cooling processes act equally:

$$H_{rad} + H_{coll} = L = 4\pi a^2 \sigma T_d^4 \langle Q(a, T_d) \rangle. \tag{1.8}$$

For dust heated only by radiation, the dust temperature is given by:

$$T_d = \left(\frac{\langle Q_\nu \rangle}{(a, T_d)\rangle} \frac{cU}{4\sigma} \right)^{1/4}. \tag{1.9}$$

In SN shocks and X-ray plasmas, collisional heating dominates over radiative, and the dust temperature is given by:

$$T_d = \left(\frac{(\frac{32}{\pi m_e})^{1/2} n_e (kT_e)^{3/2} h(a, T_e)}{4\sigma (a, T_d)\rangle} \right)^{1/4}. \tag{1.10}$$

The efficiency of absorption and emission of light varies depending on grain properties. As such, $(a, T_d)\rangle$ depends on the emissivity index of the dust, β, such that $Q \propto T_d^2$ for silicates ($T_d \leq 40$ K) and $Q \propto T_d$ for carbon ($5 \leq T_d \leq 10^3$ K) (Draine, 1981).

1.4 Observing Dust Emission

FIR astronomy is a relatively young science, partly because of the many challenges of observing in these bands. Ground-based observations are challenging, if not impossible, as the majority of IR light travelling towards Earth is absorbed by O_2 and H_2O in the atmosphere. At high and dry locations such as the peak of Mauna Kea in Hawaii, or in the Atacama desert, there are a few FIR windows which can be observed, although absorption and background emission are still problematic.

A large part of the FIR - submm spectrum can only be observed from space.

Observatory	Camera	Band (μm)	FOV (arcsec)	Pixel Size (arcsec)	Beam FWHM
Spitzer	IRAC	3.6	5.2×5.2	1.221	1.66/1.95
Spitzer	IRAC	4.5	5.2×5.2	1.213	1.72/2.02
Spitzer	IRAC	5.8	5.2×5.2	1.222	1.88
Spitzer	IRAC	8.0	5.2×5.2	1.220	1.98
Spitzer	MIPS	24	5.4×5.4	2.5	6
Spitzer	MIPS	70	2.6×5.2	10	18
Spitzer	MIPS	160	5.3×2.1	16	40
Herschel	PACS	70	3.5×1.75	3.2	6 ($5.8 \times 12.1^{\dagger}$)
Herschel	PACS	100	3.5×1.75	3.2	7
Herschel	PACS	160	3.5×1.75	4.5	12 ($11.4 \times 13.4^{\dagger}$)
Herschel	SPIRE	250	8×4	6.0	18
Herschel	SPIRE	350	8×4	8.0	24
Herschel	SPIRE	500	8×4	11.5	35

Table 1.2: Beam sizes for the different FIR and submillimetre observatories and pixel sizes for the data sets used in this Thesis. † The PACS beam sizes are the nominal diffraction-limited beam sizes. Those in parenthesis are the beam sizes due to the Hi-GAL observing strategy (which observed at 70 and 160 in parallel mode).

Yet even for space-based missions, there are significant challenges to overcome. Radiation from the telescope or observatory would drown out any astronomical signal: observing in the IR has been compared to taking an optical image with a camera on fire. Therefore, instruments must be cooled cryogenically such that astronomical emission can be detected above the level of any remaining instrumental noise. The extra mass of a cryogen can make launch more difficult, and the lifetime of the mission is dictated by the supply of coolant.

Because of these hurdles, it wasn't until 1983 that the first FIR space telescope was launched. The Infrared Astronomical Satellite (IRAS) studied the entire sky at 12, 20, 60, and 100 µm over the course of ten months, detecting around 350,000 IR sources and inspiring the next generations of FIR – submm observatories. The face of FIR astronomy has changed a great deal over the course of the last 50 years thanks to space missions such as IRAS, the Infrared Space Observatory (ISO, Kessler & Habing, 1996), *Spitzer* (Werner et al., 2004), Akari (Murakami et al., 2007), and *Herschel* (Pilbratt et al., 2010).

A summary of some of the properties of the datasets used in this Thesis is provided in Table 1.2.

1.4.1 SPITZER SPACE TELESCOPE

30 years after IRAS conducted the first ever IR scan of the sky, the *Spitzer* Space Telescope (*Spitzer*) was launched in 2003 (Werner et al., 2004). This was the first IR space telescope that could operate for an extended length of time, with a cryogenic lifetime of 5.7 years, compared to only 10 months for IRAS and 28 months for ISO. *Spitzer*'s warm launch meant that this lifetime could be achieved with a smaller, lighter cryostat and a relatively small amount of cryogen. Throughout the prime mission the telescope could be cooled to ≤ 6 K. When the cryogen was depleted in 2009 the majority of the detectors were saturated and unusable. However, observations continued in the shorter IRAC bands, at 3.6 and 4.5 µm, in the warm mission.

Spitzer housed three IR instruments: the Infrared Spectrograph (IRS, Houck et al., 2004), the Multiband Imaging Photometer for *Spitzer* (MIPS, Rieke et al., 2004), and the Infrared Array Camera (IRAC, Fazio et al., 2004). Both high and low spectroscopy could be performed with IRS; MIPS and IRAC were *Spitzer*ś photometers, and MIPS could also be use for high- and low-resolution spectroscopy.

1.4.1.1 MIPS

MIPS (Rieke et al., 2004) was the FIR camera aboard *Spitzer*, observing three wavebands centred at 24, 70, and 160 µm. This was the first instrument with which it was possible to observe in the FIR with high sensitivity, a large imaging field, and high angular resolution. At 70 µm it was possible to observe with a narrower FOV of $2.7' \times 1.35'$and increased magnification.

Multiple operating modes were available dependent on the required depth and field size. The Scan Mapping mode was used for observing large regions; sources were measured ten times at 24 and 70 µm but only once at 160 µm such that multiple scans were required for high-quality 160 µm data. Small ($\leq 2'$) and point sources were best observed in the Photometry and Super Resolutions mode, with which it was possible to observe with a narrower FOV ($2.7' \times 1.35'$) and increased magnification at 70 µm, whilst very extended emission such as zodiacal light could be mapped in the Total Power mode.

1.4.1.2 IRAC

IRAC (Fazio et al., 2004) was *Spitzer*'s near - mid IR photometer and could observe four wavebands at 3.6, 4.5, 5.8, and 8.0 µm. Observations were taken of

two fields simultaneously, one at 3.6 and 5.8μm, and the other at 4.5 and 8.0μm, each with a FOV of $5.2' \times 5.2'$and angular resolution of $\sim 2''$(FWHM). IRAC had three operating modes, the main one being Full-Array mode which had multiple frame times available and could be used to scan large areas of the sky. Stellar Photometry mode could be used for observing objects, usually stars, which are much brighter at 3.6 and 4.5 μm compared with the longer wavebands. In this mode short exposures were used at the shorter wavelengths to prevent saturation, and long exposures at the longer wavelengths. Finally, Sub-Array mode could be used for very bright sources, providing images with a smaller FOV of $38'' \times 38''$. This required that each waveband be observed in turn.

1.4.2 Herschel Space Observatory

The launch of the *Herschel* Space Observatory (Pilbratt et al., 2010) on 14 May 2009 marked the start of a new era in FIR astronomy. As the largest IR space observatory to date, *Herschel* opened the window to the FIR ($\sim 50-200$ μm) and submillimetre ($\sim 200-1000$ μm) universe. To make this possible *Herschel* housed the largest single-dish mirror ever sent into space, with a diameter of 3.5 m, nearly four times larger than any previous infrared space telescope. Having such a large mirror is vital for observations in FIR and submillimetre bands which have angular resolution around 1000 times worse than optical bands. With improved resolution, objects with small angular sizes can be studied in more detail, and we can more easily disentangle objects which would otherwise be confused, allowing study of fainter sources.

Resolution is not the only obstacle at these wavelengths. As discussed earlier, IR radiation from the observatory itself would drown out any images in this regime. To reduce the instrumental noise the whole system was cooled with cryostats containing liquid helium. This cooled the majority of the system to an operating temperature of 1.7 K, and the detectors were cooled to 0.3 K. Operating at 85 K, the primary mirror was the largest source of instrumental noise. Additionally, a sunshield provided protection from solar radiation, and Earth straylight. These measures meant that *Herschel* could be used to study objects with temperatures of $\lesssim 100$ K. The mission lifetime of *Herschel* was dependent on the supply of helium, which ran out in April 2013, after nearly 4 years of observations.

Herschel held three instruments: the *Herschel*-Heterodyne Instrument for the Far-Infrared (HIFI, De Graauw et al., 2010), the Spectral and Photometric Imaging Receiver (SPIRE, Griffin et al., 2010), and the Photodetector Array Camera and

Spectrometer (PACS, Poglitsch et al., 2010). HIFI was *Herschel*'s dedicated spectrometer, whilst both SPIRE and PACS had a spectrometer and photometer. In this thesis images are used from the SPIRE and PACS photometers.

1.4.2.1 SPIRE PHOTOMETER

The SPIRE photometer (Griffin et al., 2010) was designed to observe cold interstellar dust ($\lesssim 30$ K) and observed simultaneously in three wavebands centred at 250, 350, and 500 µm. SPIRE could exploit this previously neglected region and more accurately determine dust temperatures than any previous instrument.

The photometer sampled a target area by scanning the region whilst taking continuous observations. SPIRE could scan in different modes dependent on the required observations. Small map mode was used for observing point sources or small extended sources, and could cover a 5′ patch of sky at a scanning speed of $30''s^{-1}$. For larger areas, large map mode could be used which had two options of scan speed, $30''s^{-1}$ and $60''s^{-1}$, used depending on the required depth of images. Finally, in parallel mode SPIRE could be used alongside PACS to save time where observations with both instruments were required. In this mode the scan speed could be fast, $60''s^{-1}$, or slow, $20''s^{-1}$.

In the past, missions observing shorter wavelength light have used photoconducting detectors, in which electrons are excited across a band-gap by incident photons and the material is chosen such that the band-gap has the same energy as the observed photons. FIR and submm light cannot be detected in the same way as the photons have such a low energy that there is no viable material with the required band-gap. Instead, bolometers were used for SPIRE. Bolometers contain a low temperature absorbing element which heats up slightly when light is absorbed. Small changes in the temperature induce a measurable change in the resistive properties.

1.4.2.2 PACS PHOTOMETER

The PACS photometer (Poglitsch et al., 2010) observed three wavebands centred at 70, 100, and 160 µm, sampling the peak of the SED for cold interstellar dust. PACS offers much better resolution compared with instruments which had previously targeted this spectral window, providing images which are 4 times more resolved than *Spitzer* (see Table 1.2), and 6 times more resolved than IRAS.

Like SPIRE, PACS used bolometers as its detectors. As PACS only held two detector arrays it could observe in two bands simultaneously, 160 µm and either

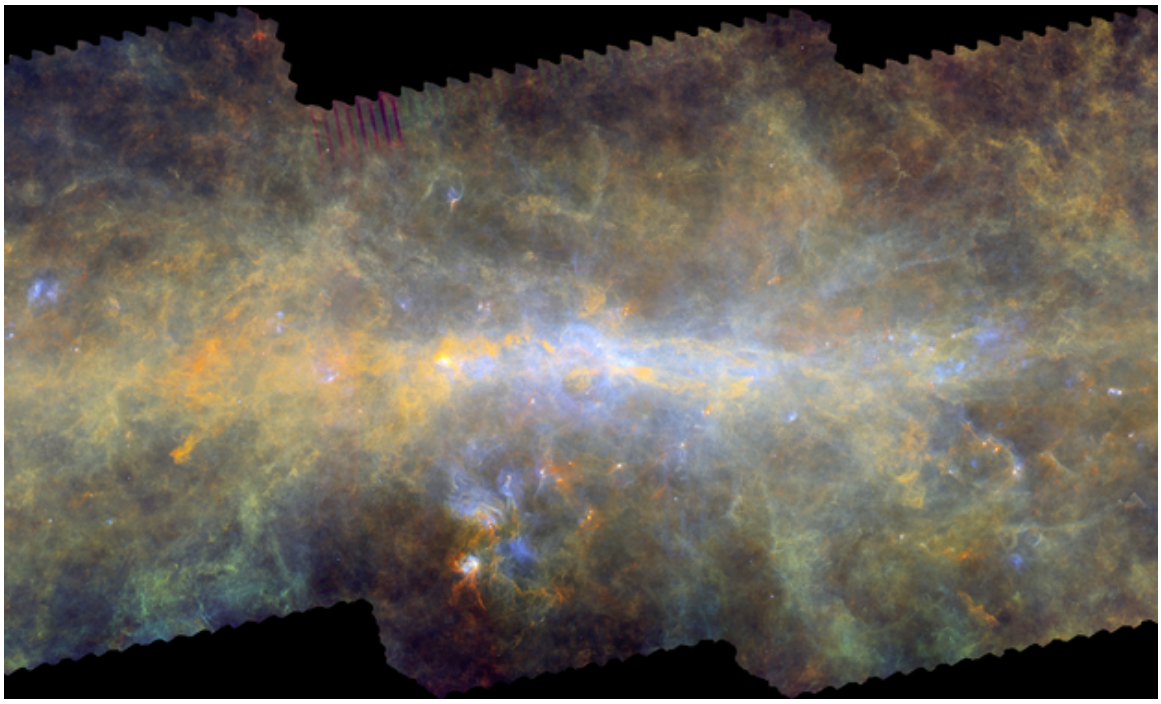

Figure 1.8: The dusty Galactic Centre, as seen by *Herschel* during the Hi-GAL survey. A composite image where blue = 70 µm, green = 160 µm, and red = 350 µm. Credit: ESA/Herschel/PACS, SPIRE/Hi-GAL Project, acknowledgement: G. Li Causi, IAPS/INAF, Italy

70 or 100 µm. Various scanning modes could be used to optimise observations. A mini-scan mapping mode which produced 3′ maps was available for small sources. Larger maps were commonly needed and these were produced by the scan mapping mode. This mode had two options available for scan speed of $20''s^{-1}$ and $60''s^{-1}$. Blurring in the faster scan speed lead to degradation of the PSF with increased ellipticity and FWHM. This effect was worsened when observing in parallel mode as the scan rate was not optimised for PACS. Sampling was completed with orthogonal scans to reduce the effects of both time-variant instrumental noise and the PSF ellipticity.

1.4.3 Hi-GAL

In this Thesis, we will use data from the *Spitzer* and *Herschel* archives and from observations taken with *Herschel* as part of the *Herschel* Infrared Galactic Plane Survey (Hi-GAL, Molinari et al., 2010b). Hi-GAL is a FIR and submm photometric survey of the a 2° strip of the Galactic Plane ($| b | \leq 1°$), initially covering the central 60°, and later the entire Galactic Plane. Surveys were completed across five *Herschel* wavebands with PACS (70 and 160 µm) and SPIRE (250, 350, and 500 µm)

in parallel mode at the maximum scan speed ($60''s^{-1}$), to maximise survey speed and wavelength coverage.

Hi-GAL was a *Herschel* Open Time Key Project aiming to detect early stages of the formation of molecular clouds and high mass stars. To do so, Hi-GAL was designed to complement previous surveys of the Galactic Plane. Together with other IR (e.g. GLIMPSE Benjamin et al., 2003 and MIPSGAL Carey et al., 2009 with *Spitzer*) and millimetre (e.g. Bolocam GPS Aguirre et al., 2011 and ATLASGAL Schuller et al., 2009) surveys, the entire thermal dust continuum could be traced within the Galactic Plane. The Hi-GAL observing and data reduction strategy was designed to recover extended emission making it appropriate for studies of Galactic supernovae remnants. The Hi-GAL images are set to a common calibrated zero level by comparison with Planck and IRIS all sky maps (Molinari et al. 2016). Calibration uncertainties are typically quoted as ∼5 and 7% for PACS and SPIRE respectively (Balog et al., 2014; Bendo et al., 2013). At all wavelengths, the map noise in Hi-GAL maps is dominated by Galactic Plane cirrus confusion (Molinari et al., 2013).

1.4.3.1 Other Ancillary Data

Where available, the FIR and submillimetre observations from *Spitzer* and *Herschel* are supplemented in this Thesis with radio observations. This includes Very Large Array 20 cm data from the Multi-Array Galactic Plane Imaging Survey (MAGPIS, Helfand et al. 2006) for sources within the range $b < 0.8°$ and $5° < l < 48.5°$; 1420 MHz images from the Canadian Galactic Plane Survey (CGPS) for sources in the range $52° < l < 192°$ (Taylor et al., 2003); and 0.843 GHz images from the MOST Supernova remnant catalogue for sources within the range $245° < l < 48.5°$ (Whiteoak & Green, 1996).

1.5 Analysing Dust Emission

1.5.1 Canonical Modified Blackbody Fitting

Dust emits in the FIR with a thermal continuum. Kirchhoff's Law states that a body in thermal equilibrium will absorb and emit energy with equal efficiency, where the efficiency of a radiator is known as its absorptivity or emissivity. This means that dust must emit radiation with the same rate at which it absorbs from

the local radiation field. Blackbody sources, with an emissivity of one, perfectly absorb incident radiation, and re-radiate all of the energy as a function of frequency, ν, in the form of a temperature dependent Planck function:

$$B_\nu(T) = \frac{2h\nu^3}{c^2} \frac{1}{e^{\frac{h\nu}{k_B T}} - 1} \tag{1.11}$$

where h is the Planck constant and k_B is the Boltzmann constant. Dust does not absorb and radiate with complete efficiency and its FIR spectral energy distribution (SED) can be described by a blackbody function modified by an efficiency term which varies with frequency:

$$Q_\nu \propto \nu^\beta \tag{1.12}$$

where β is the emissivity spectral index which depends on the grain composition, structure, and size. β has values between 1 and 2 for most types of dust, where silicates are usually described by $\beta \simeq 2$, whilst $\beta = 1$ corresponds to amorphous carbon (Tielens & Allamandola, 1987; Mennella et al., 1998). Observational evidence indicates that the majority of low redshift galaxies can be well described by a value of 2, and measured values for the Milky Way vary typically between 1.65 and 1.90. (Hildebrand, 1983; Dunne & Eales, 2001; Chapin et al., 2009; Clemens et al., 2013; Smith et al., 2013; Planck Collaboration XLVIII, 2016)

When determining the mass of dust in a cloud, it is usually assumed that grains are spherical and the total mass can be defined by the grain volume, V, the number of particles, n, and the volume density of the grain material, ρ such that the dust mass (M_d) is given by:

$$M_d = V\rho n = \frac{4}{3}\pi a^3 \rho n \tag{1.13}$$

where a is the dust grain radius. Dust grains are generally much smaller than the wavelengths of FIR and submm light by which they emit and we can assume that clouds of dust will by optically thin such that the optical depth, τ_ν, is much less than one. Consequently, for grains in radiative equilibrium the effect of radiative transfer on the spectral radiance (or surface brightness), I_ν, is given by:

$$I_\nu = (1 - e^{-\tau_\nu}) B_\nu(T) \simeq \tau_\nu B_\nu(T). \tag{1.14}$$

The optical depth is:

$$\tau_\nu = \pi a^2 N Q_\nu \approx \pi a^2 \frac{n}{A} Q_\nu \tag{1.15}$$

where πa^2 is the grain cross sectional area, N is the column density of grains, and A is the cross-sectional area of the cloud. We can combine equations 1.14 and 1.15 and multiply by A to find the spectral radiance over the whole cross-sectional area of the dust cloud:

$$AI_\nu = \pi a^2 n Q_\nu B_\nu(T). \tag{1.16}$$

The flux density measured at a distance, D, from the cloud is given by the relation:

$$S_\nu = \frac{AI_\nu}{D^2} = \frac{\pi a^2 n Q_\nu B_\nu(T)}{D^2} \tag{1.17}$$

which can be substituted into Equation 1.13 to give:

$$S_\nu = \frac{3}{4}\frac{Q^2}{\rho a}\frac{M_d B_\nu(T)}{D^2} = \frac{\kappa_\nu M_d B_\nu(T)}{D^2} \tag{1.18}$$

where κ_ν is the dust mass absorption coefficient:

$$\kappa_\nu = \frac{3Q_\nu}{4a\rho} \tag{1.19}$$

incorporating the unconstrained terms Q_ν, ρ, and a. Q_ν is highly dependent on a range of dust properties such as the composition, the shape, and the size. This generates large uncertainty in κ_ν and derived values vary across more than three orders of magnitude for various dust properties (Clark et al., 2016, 2019; Cigan et al., 2019). Values of κ_ν are extrapolated from reference, measured values using the frequency dependency:

$$\kappa_\nu = \kappa_{\nu_0}\left(\frac{\nu}{\nu_0}\right)^\beta \tag{1.20}$$

in the far-infrared.

1.5.2 The Point Process Mapping Procedure

Although SED fitting, as described in Section 1.5.1, can provide dust mass and temperature estimates, as well as the synchrotron contribution, it is limited as it must assume that the dust has a uniform temperature and a fixed emissivity index. To overcome these shortfalls we can use point process mapping (PPMAP, Marsh et al., 2015, 2017; Howard, 2020). With PPMAP we can study the dust emission from an object at an increased resolution, as shown in Figure 1.9, without assuming constant dust properties.

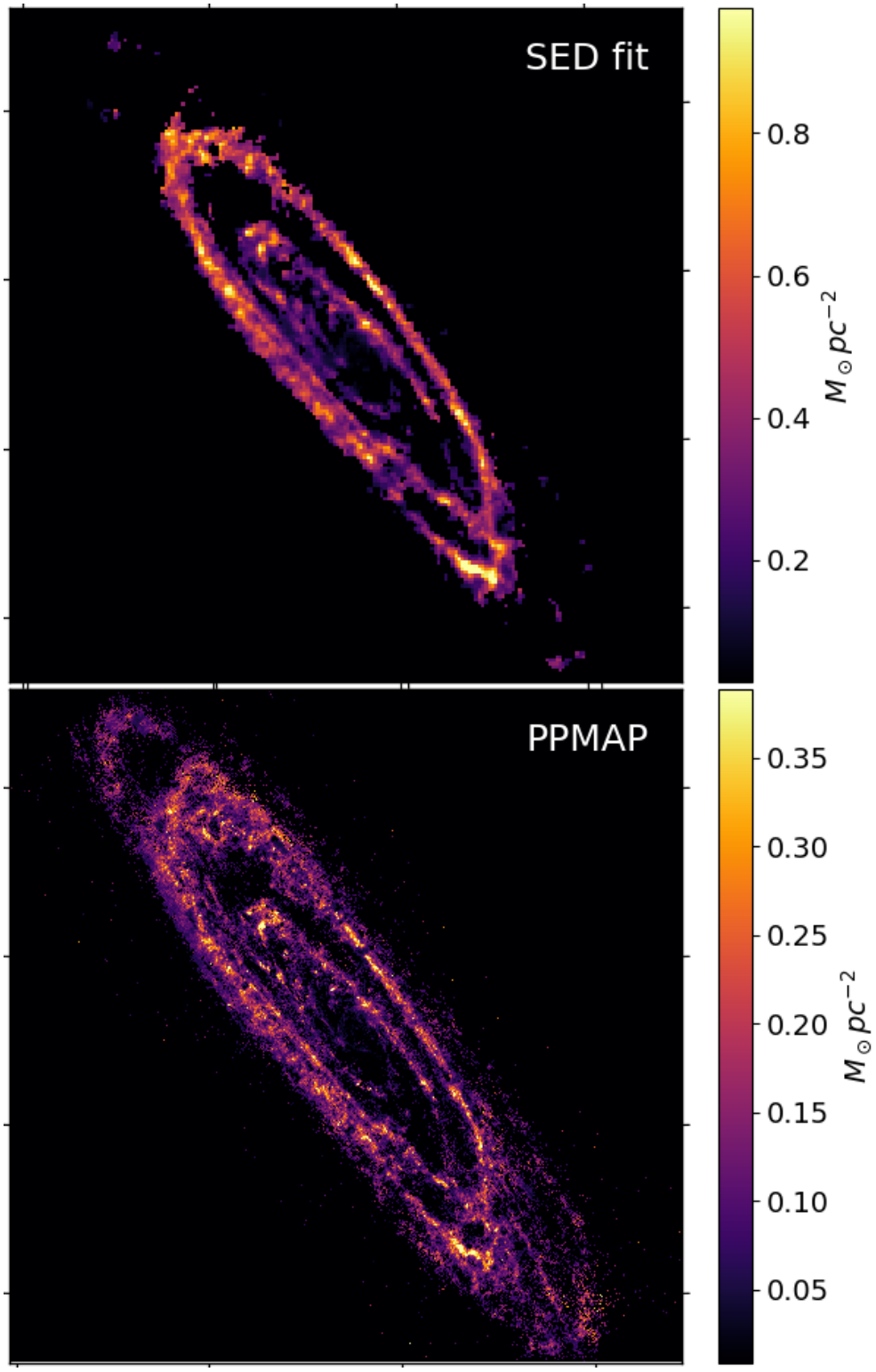

Figure 1.9: Dust mass content of the Andromeda galaxy M31, estimated by SED fitting (Smith et al., 2012a, *top)* and with PPMAP (Marsh et al., 2018, *bottom)*. With PPMAP Marsh et al. (2018) were able to study the dust at 30 pc resolution, compared with 140 pc resolution achieved by Smith et al. (2012a) using an SED fitting technique.

PPMAP performs a Bayesian analysis on images of dust emission in order to provide column density values as a function of dust temperature rather than flux as a function of wavelength. PPMAP works on the principle that astrophysical systems can be represented by a series of points in a well-defined state space (Marsh et al., 2015). Maps of differential dust column density are created for a grid of temperatures using point spread function information from each instrument to create high resolution dust temperature maps. Observations are taken in at their native resolution and are deconvolved with the appropriate instrument beam profiles such that there is no need to smooth the data to the lowest resolution image. Furthermore, PPMAP can fit multiple dust temperatures along the line of sight through each pixel, unlike the modified blackbody technique described in Section 1.5.1 which assumes a single dust temperature and dust emissivity index β. PPMAP can fit two or three dimensions: the position on the sky and dust temperature, $T_{\rm d}$, and one representing the dust emissivity index, β, if this is not set to a fixed value.

Full details of the PPMAP routine (along with tests on synthetic data) are provided in Marsh et al. (2015). PPMAP operates in different dimensions to conventional (β, T_d) pixel-to-pixel fits, instead estimating a density distribution of mass throughout the 4D state space (x, y, T_d, β). In this procedure, astrophysical systems such as SNRs are represented as a collection of primitive objects which each have unit column density. Assuming that structures are optically thin, flux maps are considered as the total instrumental response to all objects. The distribution of column density is then defined by the number of objects appearing at any point in the 4D state space (x, y, T_d, β) .

PPMAP aims to find the optimal estimate for the distribution of objects by using a procedure based on Bayes' theorem. The expectation number of objects per unit volume in the 4D state space, $\rho(x, y, T_d, \beta)$, can be equated to the differential column density and is found through a stepwise approach. Initially, the measurement noise is artificially increased to the point at which no information can be obtained from the data. At this point the optimal solution is the a priori value of ρ. In the absence of further prior information, this function is flat everywhere. The noise is then decreased over a series of time-steps until the original signal-to-noise ratio is obtained; ρ is updated at each step, using the previous optimal solution as the new prior. The data at each stage can be described by a model of the form:

$$\mathbf{d} = \mathbf{A\Gamma}(\mathbf{t}) + \nu(t) \tag{1.21}$$

where $\mathbf{d}$ is the data vector at a given time step whose m^{th} component gives the pixel value at x_m, y_m for the wavelength λ_m; the vector $\mathbf{\Gamma}(\mathbf{t})$ describes the actual distribution of objects in state space; $\nu(t)$ gives the measurement noise at each time step, t, and is assumed to be Gaussian; and $\mathbf{A}$ is the system response matrix where the m^{th} element gives the m^{th} measurement response to an object in the n^{th} cell of state space i.e. (x_n, y_n, T_n, β_n). It is given by

$$A_{mn} = H_{\lambda_m}(X_m - x_n, Y_m - y_m) K_{\lambda_m}(T_n) B_{\lambda_m}(T_n) \kappa_{\lambda_m}(\beta_n) \Delta\Omega_m \tag{1.22}$$

where $H_{\lambda_m}(x, y)$ is the convolution of the PSF at λ_n with the profile of a source object; $K_{\lambda_m}(T_n)$ is a colour correction; $B_{\lambda_m}(T_n)$ is the Planck function; $\Delta\Omega_m$ is the solid angle subtended by the m^{th} pixel. By finding an optimal solution for $\mathbf{A}$, we can obtain the most likely distribution of β and T_d at each location in (x, y). When running PPMAP we provide prior information for β.

Throughout the procedure, PPMAP acts in the direction of minimising the reduced χ^2, derived from the sums of squares of deviations between the observed and model pixel values over each local region, after dividing by the number of degrees of freedom. The model pixel values are estimated from a modified blackbody model of the form given in Equation 1.18. The variation of κ_λ at different wavelengths depends on the value of β as in Equation 1.20, where PPMAP adopts a reference value at 300 μm of $\kappa_{300} = 1.0\,\mathrm{m^2\,kg^{-1}}$ (Marsh et al., 2017). Finally, PPMAP requires an estimate of the noise levels for each band (the pixel-to-pixel variation).

PPMAP provides additional information over the standard modified blackbody technique described in Section 1.5.1 to derive dust masses because it (i) does not assume a single dust temperature along the line of sight through each pixel, (ii) uses point spread function information to create column density maps without needing to smooth data to a common resolution, and (iii) although it first makes the assumption that the dust is optically thin, it can check this retrospectively. Therefore PPMAP could be powerful tool for analysing dust emission in supernova remnants.

1.6 A Review of Previous Studies of Dust in Supernova Remnants

As discussed in Section 1.3, historically, evolved stars have been considered the main source of dust in galaxies, especially AGB stars (e.g. Dwek, 1998). However, there is some disparity between the dust injection rates of evolved stars and the mass of dust observed, which is exacerbated at high redshifts where the evolutionary timescales of such stars are close to, or longer than, the age of the Universe (Morgan & Edmunds, 2003; Dwek et al., 2007; Michałowski et al., 2010; Gall et al., 2011c; Mancini et al., 2015; Rowlands et al., 2014; Michałowski, 2015). On the other hand, models suggest that SNe can quickly produce substantial amounts of heavy elements (Todini & Ferrara, 2001; Nozawa et al., 2003). The ejecta contain an abundance of heavy elements and the temperature drops quickly with expansion, providing ideal conditions for grain formation and growth. However, there is huge uncertainty in the amount of dust which can survive the harsh environment of a SNR as this depends on a wide range of factors. Observations of dust in a range of SNRs are therefore crucial in confirming whether dust can survive destructive processes and, if so, how much dust is injected into the ISM.

Along with line and continuum emission from gas, IR dust emission is thought to be one of the key cooling processes of SNRs (Dwek et al., 1987; Draine, 1981; Ostriker & Silk, 1973). FIR emission from SNRs can be thermal or non-thermal. Thermal FIR emission will arise from warm dust such as warm ejecta material, shock-heated dust in the forward or reverse blast waves, photo-ionised material near a PWN, or swept-up ISM. Non-thermal emission in the FIR originates from synchrotron emission from shocks or PWNe, although this is not expected to be significant, except in the case of plerion objects such as the Crab where synchrotron emission contributes between 19 and 88% of the flux in the various *Herschel* wavebands (Temim et al., 2012; Gomez et al., 2012b; De Looze et al., 2019). Line emission may also be detected in the IR, mostly from atomic and molecular gas within evolved SNRs in which the gas has sufficiently cooled to allow recombination (Reach et al., 2006). IR emission therefore provides important information about the dust within a SNR and can help us to determine whether ejecta dust can survive.

With the advent of *Herschel*, massive quantities of colder (<50 K) SN ejecta dust have been detected in a handful of individual core collapse remnants (reviewed in detail by Sarangi et al., 2018). *Herschel* revealed filaments of ejecta dust

within the Crab Nebula, amounting to up to 0.1 – 0.4 $M_\odot$ at temperatures of 27 – 35 K (Gomez et al., 2012b; Owen & Barlow, 2015), a mass which is more than an order of magnitude larger than that detected by *Spitzer* (Temim et al., 2012), although the dust masses were recently revised to 0.05-0.09 $M_\odot$ (Nehmé et al., 2019; De Looze et al., 2019) due to more sophisticated measures of the background level. It is expected that the filamentary dust within the Crab is heated by non-thermal synchrotron radiation from the pulsar wind nebula (PWN) (e.g. Davidson & Fesen, 1985; Macalpine & Satterfield, 2008). A shell of SN-condensed dust was discovered in association with another PWN, G54.1+0.3. *Herschel*, *Spitzer*, and APEX observations suggest a minimum total dust mass of 0.07 – 1.10 $M_\odot$ for this object (Temim et al., 2017; Rho et al., 2018), which is heated either by the PWN or a nearby cluster of stars. Lau et al. (2015) also found evidence that 0.02 $M_\odot$ of warm (∼100 K) dust had survived the reverse shock within the 10^4 yr old Sgr A SNR (G0.0+0.0).

Dust in the O-rich SNR Cassiopeia A was initially discovered using IRAS and ISO, which found a warm dust mass of only $10^{-4} - 10^{-2}$ $M_\odot$ (e.g. Braun et al., 1987; Dwek et al., 1987; Arendt et al., 1999; Douvion et al., 2001). With submm observations from SCUBA, Dunne et al. (2003, 2009) detected orders of magnitude more cold dust. This was later resolved into two regions with *Herschel* and *Spitzer*: a warm dust component in the outer, reverse shock region, and a central region of cold (<25 K), unshocked ejecta dust (Barlow et al., 2010). The total dust mass is as high as 0.3 − 1.0 $M_\odot$ (Dunne et al., 2003; Rho et al., 2008; Barlow et al., 2010; De Looze et al., 2017)[1]. However, a *Herschel* and *Spitzer* study of the more evolved O-rich remnant, G292.0+1.8, found that the IR emission is dominated by pre-existing dust in the circumstellar medium (CSM) (Ghavamian & Williams, 2016), fuelling debate as to whether the reverse shock destroys all newly formed ejecta dust (e.g. Lau et al., 2015; Micelotta et al., 2016; Biscaro & Cherchneff, 2016).

Outside of the Milky Way, ∼ 0.5 $M_\odot$ of cold (<25 K) ejecta dust was detected in SN 1987A, in the Large Magellanic Cloud (LMC), by *Herschel* and Atacama Large Millimetre Array (ALMA) observations (Matsuura et al., 2011, 2015; Indebetouw et al., 2014; Dwek & Arendt, 2015). Later this was revised to 0.2 − 0.4 $M_\odot$ for amorphous carbon, with a maximum of 0.7 $M_\odot$ for amorphous silicate, using the predicted nucleosynthesis yields as an upper limit (Cigan et al., 2019). This is compared to only 10^{-4} $M_\odot$ of dust estimated at 775 days from data between 1.7 and

[1] Krause et al. (2004) instead posited that there was no cold dust in Cas A, claiming that Dunne et al. (2003) was in fact observing unrelated interstellar material along the line of sight. Later work by Dunne et al. (2009) and De Looze et al. (2017) showed that a significant dust mass does exist within the SNR, and found that a high fraction of the submm emission is emitted by highly polarised grains aligned with the magnetic field of the SNR.

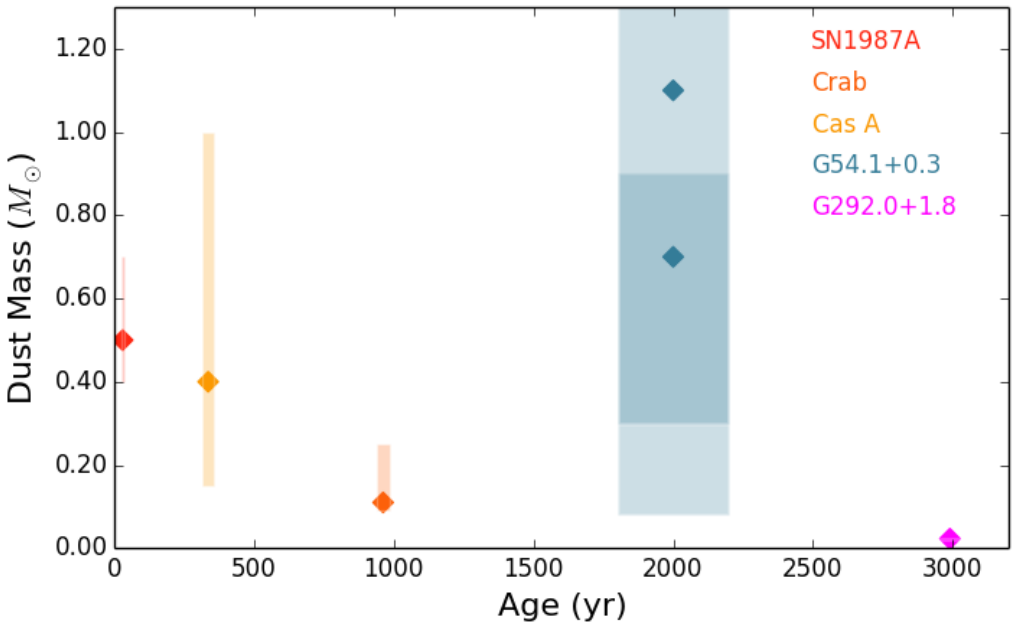

Figure 1.10: Dust mass versus age for historical remnants of core-collapse supernovae observed with *Herschel*. Scatter points are the 'best-fit' masses from the literature with shaded regions indicating the estimated error in age and dust mass (if available). These include the Crab Nebula (Temim et al., 2012; Gomez et al., 2012b; De Looze et al., 2019), Cas A (Dunne et al., 2003, 2009; Barlow et al., 2010; De Looze et al., 2019), G292.0+1.8 (Ghavamian & Williams, 2016), G54.1+0.3 (Temim et al., 2017; Rho et al., 2018) and the LMC SNR, SN 1987A (Matsuura et al., 2011; Indebetouw et al., 2014; Matsuura et al., 2015; Cigan et al., 2019). (G0.0+0.0 is not included as it is older than the range of ages shown here, at ∼4000 yrs old, Lau et al., 2015.)

12.6 µm (Wooden et al., 1993; Ercolano et al., 2007). At early times the dust may have been locked into IR optically thick clumps, such that the dust mass could have been underestimated as proposed by Dwek & Arendt (2015). However Wesson et al. (2014) suggest that the majority of the dust mass formed at a later stage, well after the SNR was first detected at MIR wavelengths.

Although there is evidence that CCSNe may contribute large masses of dust to the ISM, only a small sample of sources have been studied in detail. A summary of the dust mass versus age of the 'historical' core-collapse *remnants* discussed above is shown in Figure 1.10. The majority of the objects which contain ejecta dust are relatively young core-collapse SNRs which are still to undergo further interactions with the ISM and reverse shocks. As such, it may be that these are not representative of the entire SNR population.

In contrast to CCSNe, *Herschel* observations of the historical Type Ia remnants Tycho and Kepler by Gomez et al. (2012a) showed that although dust structures associated with the SNR material (as traced by X-ray and radio emission) were clearly detected, these dust structures originated from the swept up circumstellar and interstellar medium respectively (see also Ishihara et al., 2010) with no evidence of emission from freshly-formed ejecta dust.

1.6.1 Previous infrared surveys of supernova remnants

The discussion in the previous sections suggests that CCSNe can produce significant quantities of dust that would help to explain high-redshift dust masses. However, this is based on SN dust formation and dust mass estimates only being investigated in a limited number of Galactic sources (Cas A, G54.1+0.3, Crab, SN 1987A, G0.0+0.0, G292.0+1.8 and G350.1-0.3). We can now move on from small numbers of individual studies thanks to the availability of large surveys of the Galactic Plane with IR and FIR observatories. Prior to the *Spitzer* and *Herschel* era, FIR surveys of Galactic SNRs with the Infrared Astronomical Satellite (IRAS) (Arendt, 1989; Saken et al., 1992) detected emission from dust in 11 and 17 SNRs respectively within the Galactic Plane ($b \leq |\ 1^{\circ}\ |$), based on the Green (2014) catalogue. These FIR surveys used observations centred at 12, 25, 60, and 100 µm at respective resolutions of $0.5'$ at 12 µm and $2'$ at 100 µm. Unfortunately, confusion within our Galaxy is the major limitation when studying dust in Galactic SNRs. Confusion with the ISM makes SNRs extremely difficult to detect or distinguish from surrounding (or even line of sight) dust structures, and proved to be a significant issue for the initial surveys with IRAS (Saken et al., 1992; Arendt, 1989). Follow up IR surveys of SNRs in the Milky Way were completed by Reach et al. (2006) and Pinheiro Goncalves et al. (2011) using data from *Spitzer* IRAC and MIPS respectively. A more recent whole sky survey with *AKARI* at wavelengths of 2.4 – 160 µm and angular resolution of $0.5'$ in the 65 µm band, studied 20 Galactic SNRs (Koo et al., 2016). However, surveys at these shorter wavebands may miss cool dust components within SNRs, such that the amount of dust formed after the SN explosion may be underestimated (e.g. Barlow et al., 2010).

With the advent of *Spitzer* and *Herschel* Galactic plane surveys, there are now hundreds of images of SNRs with observations from the near-IR to submillimetre (NIR – submm, 3.6 – 500 µm). Previous studies have used the shorter wavelength *Spitzer* data for dust signatures associated with SNR, including Reach et al. (2006) and Pinheiro Goncalves et al. (2011). They reported the detection of dust

emission associated with SNRs in 18 and 39 SNRs respectively, over a region of the Galactic Plane covering ∼100 square degrees, suggesting that SN-related dust emission is rather common. Confusion persists even in a large fraction of the sources for which there are clear MIR dust signatures coincident with SNR X-ray and radio emission (e.g. Pinheiro Goncalves et al., 2011). A statistical survey of SNRs in the Galaxy is sorely needed, one that takes all of the available IR – submm information to probe the range of dust temperatures that exist in the supernova environment, and to provide a *total* measure of the dust mass.

1.7 Unresolved Questions

1. Although there is evidence that CCSNe may contribute large masses of dust to the ISM, only a small sample of sources have been studied in detail, and these tend to be biased towards very young remnants. A larger statistical sample is urgently needed to verify the importance (or not) of SNe as dominant dust producers in galaxies and to determine which SNe form dust in their ejecta material.

2. With only a limited sample of dusty SNRs analysed to date, the extent to which their location affects the amount of newly formed dust which can survive is unclear. It is expected that CCSNe dominate SNe dust formation and these are mostly concentrated in star-forming regions at low latitudes within the Galactic Plane, where we may expect to find the majority of dusty SNRs. However, the survival of freshly formed dust is inversely correlated with the local ISM density, which is increased towards the centre of the Galactic Plane where destruction may be more problematic.

3. As discussed in section 1.3.3, theoretical models indicate that only some types of CCSNe can form dust which enriches the ISM. However, there are only a limited number of detections of dust in SNRs, making any conclusions uncertain about the types of SNRs in which freshly formed dust can survive.

4. One remaining critical question is whether or not Type Ia SNe could also produce dust in their ejecta. Is it possible that the properties of the expanding ejecta in the aftermath of a Type Ia explosion are not conducive to forming dust grains efficiently?

A more complete survey is required to establish the importance of SN as dust producers, and to investigate how the dust content varies across SNR types,

evolutionary stages, and environment. In this Thesis we present a survey of (FIR) counterparts of known SNRs in the Galactic plane (360° in longitude and $b = \pm 1$) at 70–500 μmm with *Herschel*. Covering longer wavelengths than *Spitzer*, *Herschel* is sensitive to cold dust which could have been missed in previous surveys. Moreover, *Herschel*'s angular resolution is 5 times better than *Spitzer* at 70 - 160 µm. The 190 SNRs we explore in this Thesis at FIR wavelengths with *Herschel* should allow us to more easily disentangle dust associated with supernovae and unrelated interstellar dust emission, and to confirm or update the dust-detections of SNRs from previous studies with IRAS and *Spitzer*. A breakdown of the rest of the Thesis, where we attempt to investigate some of these remaining questions, is listed below.

- In Chapter 2, we investigate the importance of SNe as contributors to the dust budget within galaxies by searching for IR and sub-mm emission from ejecta dust in SNRs across the Galactic Plane. To complement the *Spitzer* catalogues of Reach et al. (2006) and Pinheiro Goncalves et al. (2011) we search for SNRs within Hi-GAL I. This survey extends from Galactic longitudes of $10° <\mid l \mid< 60°$ and latitudes of $\mid b \mid \pm 1°$. We classify SNRs by assigning levels 1 – 4 where a level 1 detection denotes FIR emission within the SNR which is clearly correlated with radio, MIR, or X-ray structures and can be distinguished from the ISM, and where level 4 is not detected in the FIR.

- In Chapter 3, we take a closer look at the dust properties of a few SNRs discovered in Chapter 2, in particular focusing on dusty pulsar wind nebulae.

- In Chapter 4 we complement the earlier chapters by searching for FIR counterparts of known SNRs in the *entire* Galactic plane, as surveyed by *Herschel* (covering 360° in longitude and 2° in latitude) at 70 – 500 µm. Without the limitation of the availability of *Spitzer* data, this increases the area of sky surveyed by a factor of 2.

- In Chapter 5, we again take a closer look at the dust properties of a few SNRs discovered in the full Galactic Plane survey, in particular focusing on dust masses and temperatures for the detection level 1 SNRs detected in this work.

- In Chapter 6 we explore the complicated dust structures we observed in Chapter 4 within multiple regions of the candidate supernova remnant the 'Tornado' (G357.7−0.1). We use Point Process Mapping, PPMAP, to investigate the distribution of dust in the Tornado at a resolution of 8″. We combine

the FIR-submillimetre analysis with X-ray and radio emission to investigate the origin of this engimatic source.

- In Chapter 7 we summarise our findings in the preceding Chapters and provide some details of future work.

CHAPTER 2
A FIRST LOOK GALACTIC CATALOGUE OF DUSTY SUPERNOVAE

'We have calcium in our bones, iron in our veins, carbon in our souls, and nitrogen in our brains. 93 percent stardust, with souls made of flames, we are all just stars that have people names'

NIKITA GILL

The importance of supernovae as a contributor to the dust budget of galaxies at all cosmic epochs remains an unresolved question (Morgan & Edmunds, 2003; Dwek et al., 2007; Matsuura et al., 2009; Gall et al., 2011c; Rowlands et al., 2014; Mancini et al., 2015). One way to resolve this is to search for infrared (IR) and submillimetre (submm) emission from ejecta dust in nearby supernovae (SNe) and supernova remnants (SNR), where the sources are close enough to resolve dust structures in the far-infrared (FIR). In this Chapter, we search for FIR (70 – 500 µm) counterparts of known supernova remnants (SNRs) in the Galactic plane over the same region as the well-known MIR SNR catalogue of Reach et al. (2006). We use the *Herschel* Infrared Galactic Plane Survey I (Hi-GAL) which extends from Galactic longitudes of $10^\circ <\mid l \mid< 60^\circ$ and latitudes of $\mid b \mid \pm 1^\circ$. This work has been published in Chawner et al. (2019).

2.1 Survey for Far Infrared Supernova Remnant Emission

To make a catalogue of FIR SNRs we use data obtained by the Photodetector Array Camera and Spectrometer (PACS, Poglitsch et al., 2010) and the Spectral and Photometric Imaging Receiver (SPIRE, Griffin et al., 2010) on board the *Herschel Space Observatory* (hereafter *Herschel*) (Pilbratt et al., 2010) during the *Herschel* Infrared Galactic Plane Survey (Hi-GAL Molinari et al., 2010b). Hi-GAL mapped a 2° latitude strip of the Galactic Plane using two PACS and three SPIRE wavebands centred on 70, 160, 250, 350 and 500 µm. In order to provide a comparison with Reach et al. (2006), we study 71 remnants within the region where $10^\circ < \mid l \mid < 60^\circ$ and $\mid b \mid \leq 1$, which is covered by Hi-GAL I. There are a total of 127 SNRs in this area based on the radio catalogue from Green 2014. *Herschel* has a diffraction limited angular resolution of $5.0-35.9''$, 30 times better than the IRAS resolution of $\sim 6-8'$ (Saken et al., 1992). Also, the PACS 70 µm maps have an angular resolution of $6.4''$, an improvement over that of the MIPS 70 µm maps of $18''$ (Carey et al., 2009). Higher angular resolution is important to resolve SNR dust features from the foreground/background or surrounding ISM. At all wavelengths, the map noise is dominated by Galactic Plane cirrus confusion (Molinari et al., 2013).

Table 2.1 lists the 71 Galactic SNRs from HiGal studied in this survey; hereafter this will be referred to as the first look survey. Each remnant was first inspected as a false colour image combining the 70, 160, and 250 µm *Herschel* waveband maps (images are provided in Appendix A, Figure A.1), which are re-gridded and convolved to the resolution of the 250 µm band. A circle was overlaid to show the SNR radio size (from the Green, 2014 catalogue) and X-ray location (the radio location from Green's catalogue is used where X-ray is not available). Various colour scales were applied in order to reveal any FIR structures potentially related to the SNR. We also assessed *Herschel* images in individual bands if any potential SNR dust emission was detected in the initial inspection. The level of FIR detection was then determined by comparing the structure in the *Herschel* images with that at MIR wavelengths using *Spitzer* (Reach et al., 2006; Pinheiro Goncalves et al., 2011), X-ray and/or radio wavelengths where possible. See Appendix A, Figure A.2 for a compilation of IRAC, MIPS and radio images of our sample. Where available, VLA 20 cm images from the Multi-Array Galactic Plane Imaging Survey (MAGPIS) (Helfand et al., 2006) [1] were used (Figure A.2) for sources within the range

[1] the MAGPIS database is available at https://third.ucllnl.org/gps/

$| b | < 0.8°$, $5° < l < 48.5°$; 1420 MHz images from the Canadian Galactic Plane Survey (CGPS) were used for sources in the range $52° < l < 192°$ (Taylor et al., 2003); and 0.843 GHz images from the MOST Supernova remnant catalogue for sources within the range $245° < l < 48.5°$ (Whiteoak & Green, 1996).

Detection levels were assigned based on the classification scheme adopted by Reach et al. (2006). That is:

- 1 = detection (FIR emission which is clearly correlated with radio, MIR, or X-ray structures and can be distinguished from ISM),
- 2 = possible detection (FIR emission in the region of the SNR, potentially related to radio, MIR, or X-ray structures but confused with ISM),
- 3 = unlikely detection (detection of FIR emission but probably unrelated to the SNR),
- 4 = not detected in the FIR.

In Section 2.1.1 we summarise our findings based on Figures A.1 and A.2 and in Section 2.1.2 we provide individual notes on each of the level 1 and level 2 detections.

Table 2.1: Supernova remnants in the Hi-GAL I Survey ($10^\circ \mid l \mid < 60^\circ$)

SNR	Name	Size [a] (arcmin)	PWN [b] (FIR)	Age (kyr)	SN Type	Ref [c]	GLIMPSE [d]	MIPSGAL [e]	Hi-GAL [f]	Dust features [g]	Comparison [h]
G10.5−0.0		6					-	1	2		R
G11.1−1.0		18x12					-	-	1	Shell	OR
G11.1−0.7		11x7					-	3	3		R
G11.1+0.1		12x10					-	1	1	Western shell	R
G11.2−0.3		4	Y (Y)	1.4−2.4	Type cIIb or Ibc	1	1	1	1	Shell Central region (PWN)	RX
G11.4−0.1		8					3	3	3		R
G11.8−0.2		4					-	2	3		
G12.0−0.1		7	Y (N)	0.3−3.0	Core collapse	2	3	3	3		
G12.5+0.2		6x5					-	1	3		
G14.1−0.1		6x5					-	1	1		
G14.3+0.1		5x4					-	1	1	Partial shell	R
G15.9+0.2		7x5		$\leqslant 2.4$	Core collapse	3; 4	3	1	1	Partial shell	RX
G16.4−0.5		13					-	1	1	Central region	R
G16.7+0.1		4	Y (N)	2.1	Core collapse	5	3	2	3		R
G17.0−0.0		5					-	2	3		
G17.4−0.1		6					-	3	2		R
G18.1−0.1		8		5		6	-	4	3		R
G18.6−0.2		6	? (N)	13	Core collapse	7	-	1	1	Outer filaments	R
G18.8+0.3	Kes 67	17x11		16		8	3	3	3		R
G19.1+0.2		27					-	3	3		
G20.0−0.2		10	Y (N)		Core collapse	9; 10	3	3	3		R
G20.4+0.1		8					-	1	1	Shell	R
G21.0−0.4		9x7					-	3	3		R
G21.5−0.9		5	Y (Y)	0.87	Type IIP or Ib/Ic	10; 11	-	1	1	Central region (PWN)	X
G21.5−0.1		5					-	1	1	Central region	R
G21.6−0.8		13					-	-	3		
G21.8−0.6	Kes 69	20		5		12	1	1	3		R
G22.7−0.2		26	? (N)				1	2	3		R
G23.6+0.3		10?					3	1	2		R
G27.4+0.0	4C-04.7 Kes 73	4		$0.75 - 2.1$	SN IIL/b	13; 14	3	1	2		R
G27.8+0.6		50x30	? (N)	$35 - 55$	Core collapse	15; 16	3	3	4		
G28.6−0.1		13x9					3	1	3		R

Table 2.1: Supernova remnants in the Hi-GAL I Survey ($10^\circ \mid l \mid < 60^\circ$)

SNR	Name	Size [a] (arcmin)	PWN [b] (FIR)	Age (kyr)	SN Type	Ref [c]	GLIMPSE [d]	MIPSGAL [e]	Hi-GAL [f]	Dust features [g]	Comparison [h]
G29.6+0.1		5		<8		17; 18	4	3	2		R
G29.7−0.3	Kes 75	3	Y (Y)	<0.84	Type Ib/c	18; 19	3	1	1	Central region (PWN)	RX
										Partial shell	
G31.9+0.0	3C391	7x5		4		20	1	1	1	Partial shell	R
										Northwestern radio bar	
G32.4+0.1		6					-	2	3		
G32.8−0.1	Kes 78	17		6		21; 22	3	3	3		
G33.2−0.6		18					3	2	1	Western shell	R
G33.6+0.1	Kes 79	10		4.4 − 6.7	Type II	22; 23	2	1	2		R
G34.7−0.4	W44	35x27	Y (N)	2	Core collapse	24; 25	1	1	1	North and western shell	R
										Central filaments	
G35.6−0.4		15x11		2.3		25; 26	-	1	2		R
G39.2−0.3	3C396	8x6	Y (N)	7		26; 27	1	1	1	Western shell	R
G41.1−0.3	3C397	4.5x2.5		1.35 − 1.75	Type Ia	27; 28	1	1	3		R
G43.3−0.2	W49B	4x3		1 − 4	Bipolar Ib/Ic	29; 30	1	1	1	Fe/radio loop	R
										H_2 filament	
G54.1+0.3		12?	Y (Y)	2	Core collapse	31	3	3	1	PWN southern rim	
G54.4−0.3	(HC40)	40		95		32	1	1	1	Outer filaments	
G55.0+0.3		20x15?		≤1900		33	2	2	2		
G296.8−0.3	1156-62	20x14		2 − 10		34	3	1	3		
G304.6+0.1	Kes 17	8		28 − 64	Core collapse	35	1	1	1	Western shell	
G310.6−0.3	Kes 20B	8					2	3	3		
G310.8−0.4	Kes 20A	12					1	1	1		
G311.5−0.3		5		23		36	1	1	1	Shell	
G332.0+0.2		12					4	3	3		
G332.4−0.4	RCW 103	10		2	Type IIP	37; 38	1	1	1	Southern arc	X
G332.4+0.1	MSH 16-51	15		3		39	2	2	3		
	Kes 32										
G336.7+0.5		14x10					4	1	3		R
G337.2−0.7		6		0.75 − 3.5	Type Ia	40; 41	4	1	2		X
G340.4+0.4		10x7		3.1		42	4	3	3		
G340.6+0.3		6		2.6		42	2	1	1	Shell	R
G341.2+0.9		22x16	Y (N)	32.6	Core collapse	43	4	3	3		
G341.9−0.3		7		5		42	4	3	3		
G342.0−0.2		12x9		11.7		42	3	3	3		

Table 2.1: Supernova remnants in the Hi-GAL I Survey ($10^\circ \mid l \mid < 60^\circ$)

SNR	Name	Size [a] (arcmin)	PWN [b] (FIR)	Age (kyr)	SN Type	Ref [c]	GLIMPSE [d]	MIPSGAL [e]	Hi-GAL [f]	Dust features [g]	Comparison [h]
G344.7−0.1		8		3	Type Ia	44; 45	1	1		R	
G345.7−0.2		6					4	1			
G346.6−0.2		8		47	Type Ib/Ic/II	36	1	2			
G347.3−0.5	RX J1713.7-3946	65x55		1.59 − 2.1	Type Ib/c	46	3	3			
G348.5−0.0		10?					1	1		R	
G348.5+0.1	CTB37A	15?		32 − 42		36	1	1		R	
G348.7+0.3	CTB 37B	17?		5	Core collapse	47	3	1		R	
G349.2−0.1		9x6					3	3			
G349.7+0.2		2.5x2		1.8		48	1	1		R	

[a] Radio size from Green's catalogue. [b] 'Y' indicates that a source contains an associated PWN, '?' indicates an unconfirmed PWN candidate. FIR detection of the PWN is indicated in brackets.

Level of detection for each SNR is listed for the following surveys: [d] *Spitzer*GLIMPSE (IRAC, Reach et al., 2006), [e] *Spitzer*MIPSGAL (MIPS, Pinheiro Goncalves et al., 2011), [f] *Herschel* Hi-GAL (PACS & SPIRE, this work). [g] Location of FIR detected dust features. [h] Waveband of previous detection to which FIR structure is compared: O = optical, R = radio, X = X-ray.

Detection level of remnants: 1 = likely detection, 2 = possible detection, 3 = unlikely detection but confused, 4 = not detected, - = unstudied.

[b] References for SNR age and SN type: [1]Borkowski et al., 2016, [2]Yamauchi et al., 2014a, [3]Reynolds, 2006, [4]Klochkov et al., 2016, [5]Helfand et al., 2003a, [6]Leahy et al., 2014, [7]Voisin et al., 2016, [8]Dubner et al., 1999, [9]Petriella et al., 2013, [10]Bietenholz & Bartel, 2008, [11]Bocchino et al., 2005, [12]Tian & Leahy, 2008, [13]Kumar et al., 2014, [14]Chevalier, 2005, [15]Reich & Furst, 1984, [16]Misanovic et al., 2010 [17]Gaensler et al., 1999, [18]Leahy & Tian, 2008a, [19]Morton et al., 2007, [20]Chen et al., 2004, [21]Zhou & Chen, 2011, [22]Zhou et al., 2016, [23]Sato et al., 2016, [24]Wolszczan et al., 1991, [25]Zhu et al., 2013, [26]Harrus & Slane, 1999, [27]Leahy & Ranasinghe, 2016, [28]Yamaguchi et al., 2015, [29]Pye et al., 1984; Smith et al., 1985; Hwang et al., 2000, [30]Lopez et al., 2013, [31]Bocchino et al., 2010, [32]Park et al., 2013, [33]Matthews et al., 1998, [34]Gaensler et al., 1998, [35]Combi et al., 2010b, [36]Pannuti et al., 2014b, [37]Nugent et al., 1984; Carter et al., 1997, [38]Frank et al., 2015, [39]Vink, 2004, [40]Rakowski et al., 2006, [41]Takata et al., 2016, [42]Caswell et al., 1983a, [43]Frail et al., 1994, [44]Giacani et al., 2011, [45]Yamaguchi et al., 2012, [46]Tsuji & Uchiyama, 2016, [47]HESS Collaboration, 2008a, [48]Tian & Leahy, 2014.

Detection Type		Number Detected
SNR Region ♮	Shell / outer shock region	23
	Inner ejecta region	8
	Confirmed PWN †	4
Age (kyr)	≤ 1	2
	1 <Age $\leq$ 10	12
	10 <Age $\leq$ 20	1
	>20	4
	Unknown	9
SN Type	Type Ia	1
	Core collapse	12
	Unknown	16

Table 2.2: Summary of the level 1 detected sample in this work. ♮The total number for this classification is larger than the number of level 1 detected sources as dust in some SNRs in detected in both outer and inner regions. †SNRs for which there is evidence that the detected central region is associated with the confirmed PWN.

Of the 29 SNRs detected in this survey, 13 are in common with Reach et al. (2006) and 21 with Pinheiro Goncalves et al. (2011). Reach et al. (2006) detected 18 of 95 SNRs from GLIMPSE and Pinheiro Goncalves et al. (2011) detected 39 of 121 SNRs from the MIPSGAL Survey; their classifications of our sample are listed in Table 2.1. We detect one additional SNR, G11.1−1.0, which was not in the Pinheiro Goncalves et al. (2011) or Reach et al. (2006) samples.

2.1.1 Summary of the Sample

Table 2.2 and Figure 2.1 give a summary of the types of SNRs detected in this study. Of our new FIR detections, we observe dust emission from the shell / outer shock region of 23 SNRs, and within the inner ejecta region (interior to the reverse shock) of 8 sources. We detect 1 SNR from a Type Ia explosion (G344.7−0.1) and 12 from core collapse SNe; the emission from the Type Ia SNR is thought to arise from a shocked cloud in front of the SNR rather than the ejecta (see Section 2.1.2 for more details). Of the SNRs in our survey with SN type classification, 87% are core collapse with only three Type Ia SNe. This adds 27 new sources to the current sample of three Galactic objects (4 including Large Magellanic Cloud) with confirmed cool dust (<50 K).

Figure 2.1 demonstrates that we are biased towards detecting young SNRs

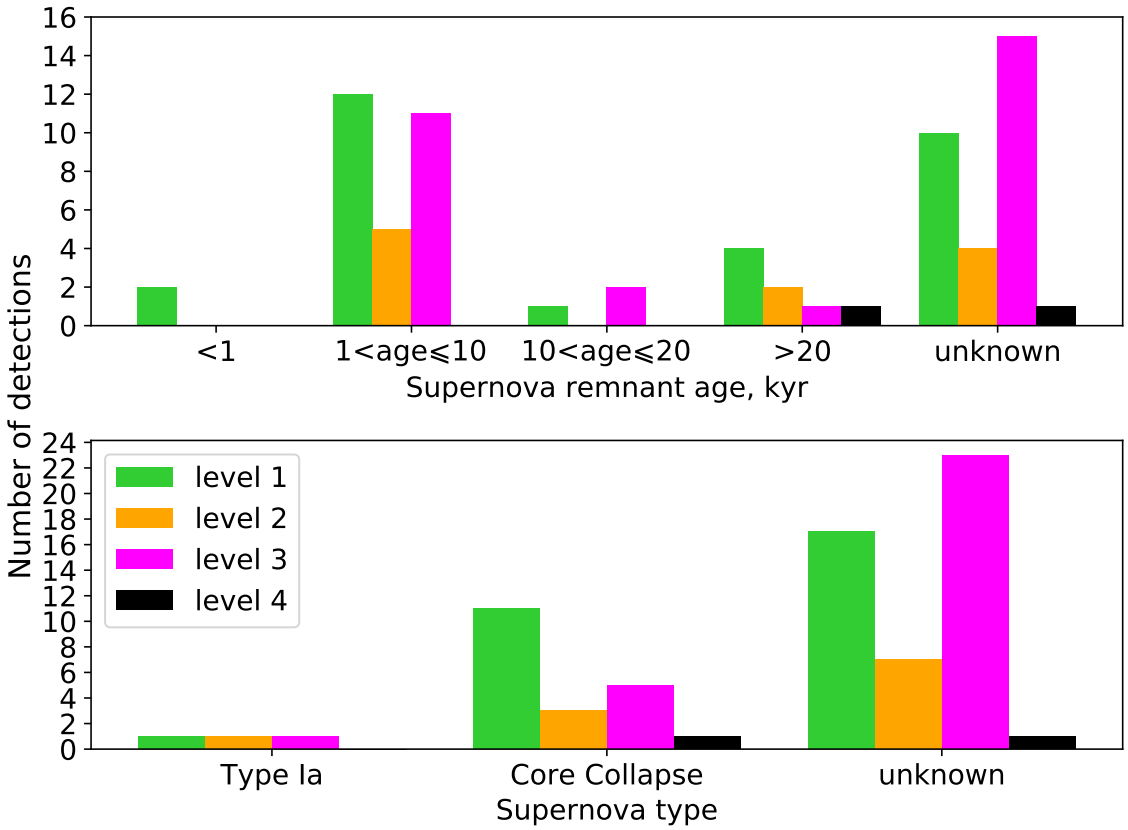

Figure 2.1: Source types detected in the sample. *Top*: Number of detections of sources of different ages. *Bottom*: Number of detections of different SN types.

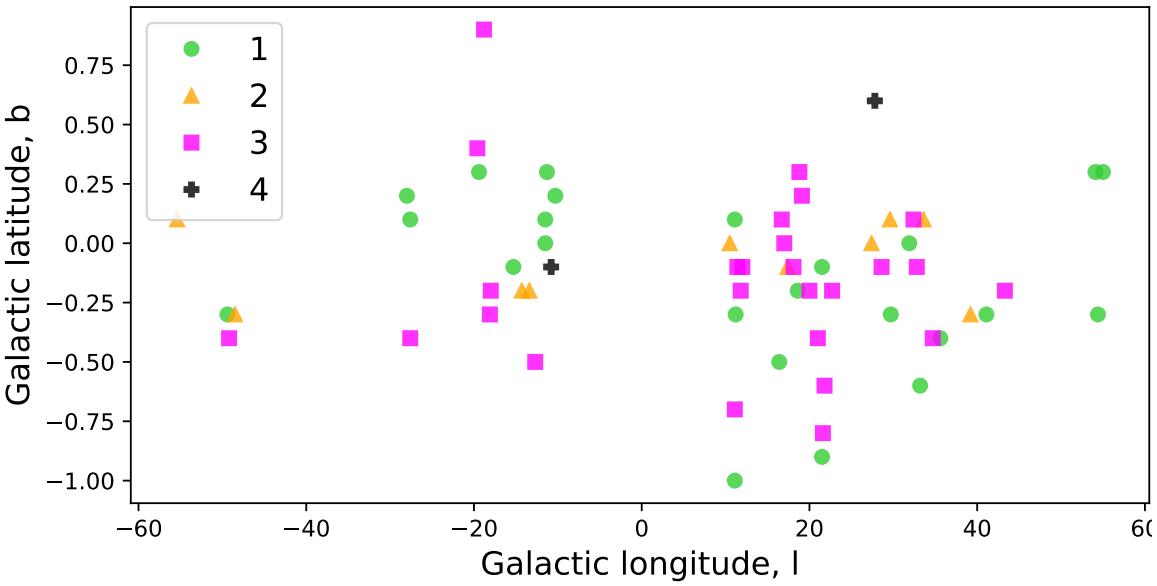

Figure 2.2: Location of sources from our sample within the Galactic Plane. We do not see any bias in the location of detected sources.

as those aged $\leqslant$5 kyr make up 61% of the sources in our survey which have estimated ages. We are least likely to detect sources which do not have an estimated age. These sources make up a large proportion of the fainter sources in our sample, making up 53 per cent of sources with a 1 GHz flux below 5 Jy. Furthermore, the majority of these sources are not very well studied and there are few images available to compare morphology.

Figure 2.2 compares the location of the sources on the sky with their assigned detection level in this work to check if there is any bias due to location (e.g. due to higher levels of confusion expected towards the Galactic centre). We see little evidence for any such bias.

We find that five Pinheiro Goncalves et al. (2011) detections are only a level 2 with *Herschel* and a further four are level 3 in this study. Some of these differences are due to limitations of observing at FIR wavelengths. In many cases the FIR emission is too confused to distinguish between the ISM and any SNR related emission which may be at a similar temperature. Furthermore, the *Spitzer* data ($\leq$ 24μm) has higher angular resolution ($<$ 26″ at 3.6 – 8.0 µm and 6″ at 24 µm) than that of *Herschel* and so may be better at resolving dust structures which emit at both MIR and FIR wavelengths. An example of this issue is G27.4+0.0 (Figure 2.3) from which Pinheiro Goncalves et al. (2011) detected clear structure at 24 µm similar to the X-ray structure (Figure 22 in Pinheiro Goncalves et al. (2011)). We detect some emission at 70 µm which may be associated with the SNR. However, extensive interstellar dust emission to the west of the SNR makes any related dust emission difficult to distinguish from the local ISM in *Herschel* wavebands. We note that synchrotron radiation may also contribute at the long wavelengths but since the majority of our detected sources are brightest at the shortest *Herschel* wavelengths, the synchrotron contamination is minimal. We also do not expect the *Herschel* flux to be dominated by line emission; studies of line intensity in two SNRs found a negligible contribution in the *Herschel* wavebands (Gomez et al., 2012b; De Looze et al., 2017).

We detect FIR emission from four out of the nine confirmed PWN sources in our sample: G11.2−0.3, G21.5−0.9, G29.7−0.3 and G54.1+0.3 (see Section 2.1.2). The discovery of cold dust in G54.1−0.3 has previously been reported based on FIR and MIR observations (Temim et al., 2017; Rho et al., 2018). We do not detect dust features related to the four 'unconfirmed' PWN candidates in our sample (G12.0−0.1, G18.6−0.2, G22.7−0.2, and G27.8+0.6). The four detected PWNe all have ages less than 2.5 kyr which could indicate a lack of dust in older PWNe due

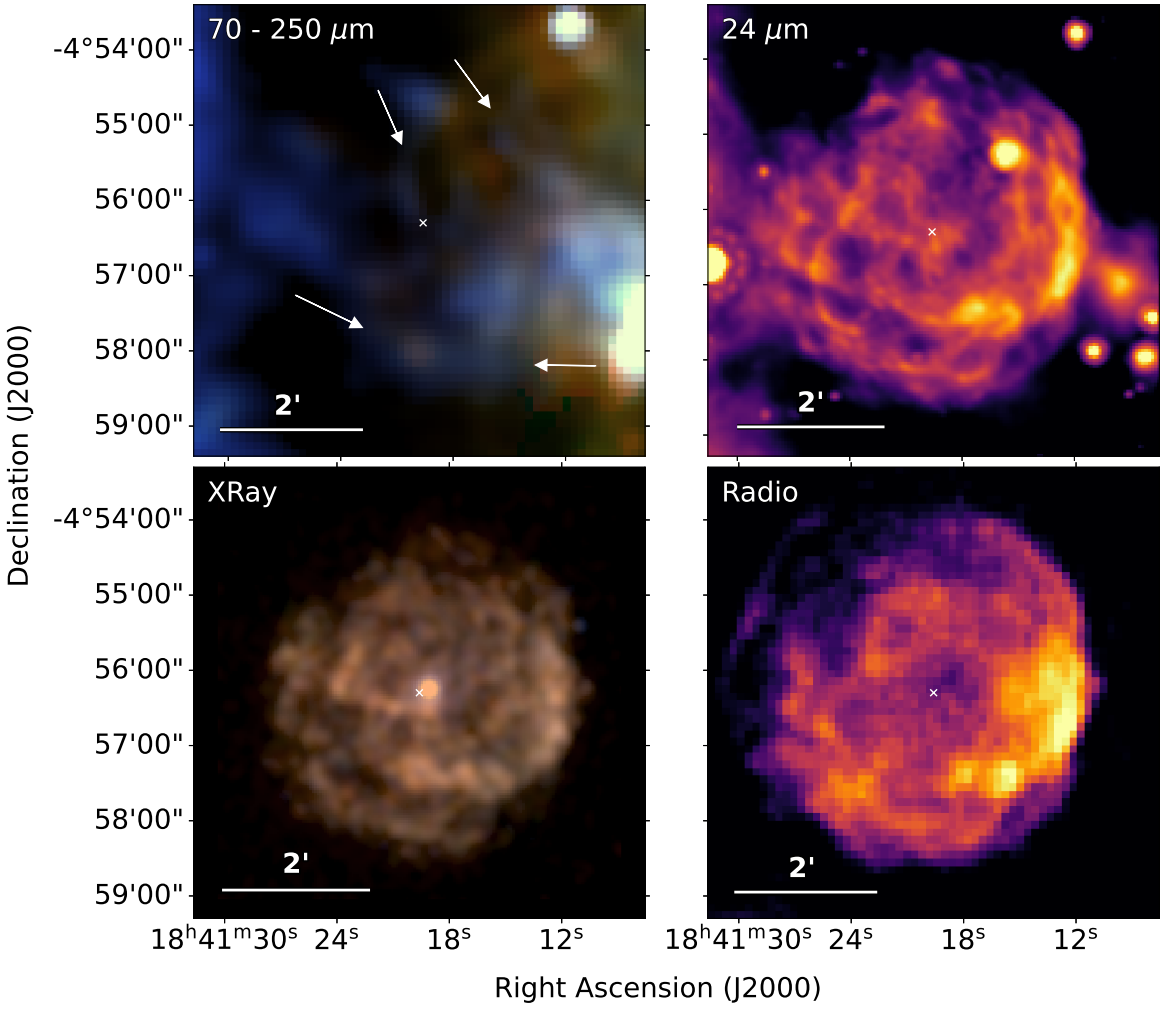

Figure 2.3: G27.4+0.0 - *Top-left*: *Herschel* colour image with X-ray contours overlaid, colours are red = 250 µm, green = 160 µm, and blue = 70 µm. The same *Herschel* colour combinations are used in Figures 2.4 - 2.31. The white arrows indicate emission at 70 µm which may be associated with SNR filaments detected at other wavelengths. However, extensive dust emission to the west makes the region very confused and FIR emission cannot be conclusively distinguished from the local ISM. There is no dust emission detected at other *Herschel* wavelengths which corresponds to the X-ray contours. *Top-right*: *Spitzer* MIPS 24 µm image. *Bottom-left*: *Chandra* three colour image, colours are red = 0.8 − 1.7 keV, green = 1.7 − 2.6 keV, and blue = 2.6 − 7.0 keV. The pulsar PSR J1841-0456 can be seen at the centre of the SNR. *Bottom-right*: VLA 20 cm radio image. The white cross shows the X-ray coordinates of the SNR centre.

to destruction by the reverse shock at later times. However, this is a limited sample making it difficult to come to general conclusions, especially since the reverse shock in G11.2−0.3 has already passed the ejecta material (Borkowski et al., 2016). Both G29.7−0.3 and G54.1+0.3 were classified as level 3 detections by Reach et al. (2006) using *Spitzer* but have been classified here as level 1 detections. The *Herschel* dust emission is clear in the images of these sources due to the dust temperature being above the typical ISM dust, potentially due to heating by the central PWN. There is no IRAC detection of the PWNe associated with G11−0.2 or G21.5−0.9. It may be that this source of heating does not increase the dust temperature by an adequate amount for strong emission in the shorter wavelength IRAC bands.

Clearly there are limitations to detecting SNRs in the FIR and we have quite complex selection effects. We easily detect dust in SNRs where the dust is at a different temperature to the local ISM or where there is little contaminating foreground/background dust. This biases us towards younger SNRs, or those with a source of heating, such as a PWN or shock heating. A further selection effect arises from the availability of radio and X-ray data as these images are used to visually compare FIR structures and determine if any FIR structures correlate with the X-ray and radio structures associated with the SNR. If radio and X-ray data are unavailable it can be difficult to clearly distinguish SN and ISM material.

2.1.2 Results for Individual Remnants

Here we provide notes on individual sources for which we detect dust within the SNR (shell or inner ejecta) in the *Herschel* three colour images. Detected remnants (level 1 in Table 2.1) are highlighted in bold and possible detections (level 2 in Table 2.1) are highlighted in italics. *Herschel* FIR, *Spitzer* NIR/MIR and radio images (where available) for the entire sample are shown in Figures A.1 and A.2.

G10.5-0.0: Brogan et al. (2006) detected a partial radio shell at a wavelength of 90 cm from this remnant which has a potential X-ray counterpart (Sugizaki et al., 2001). Pinheiro Goncalves et al. (2011) classified this source as a level 1 MIR detection as there is 24 µm emission which roughly coincides with radio structures in places. There is FIR emission to the north of the 24 µm structure, close to a radio peak at $\alpha = 18^{h}09^{m}02.4^{s}, \delta = -19°48'06.2''$ although we do not see a convincing likeness to the radio structure (Figure A.2). There are also FIR peaks at $\alpha = 18^{h}09^{m}07.4^{s}, \delta = -19°46'18''$ and $\alpha = 18^{h}09^{m}06.8^{s}, \delta = -19°47'09.8''$ which do not correlate with any radio emission.

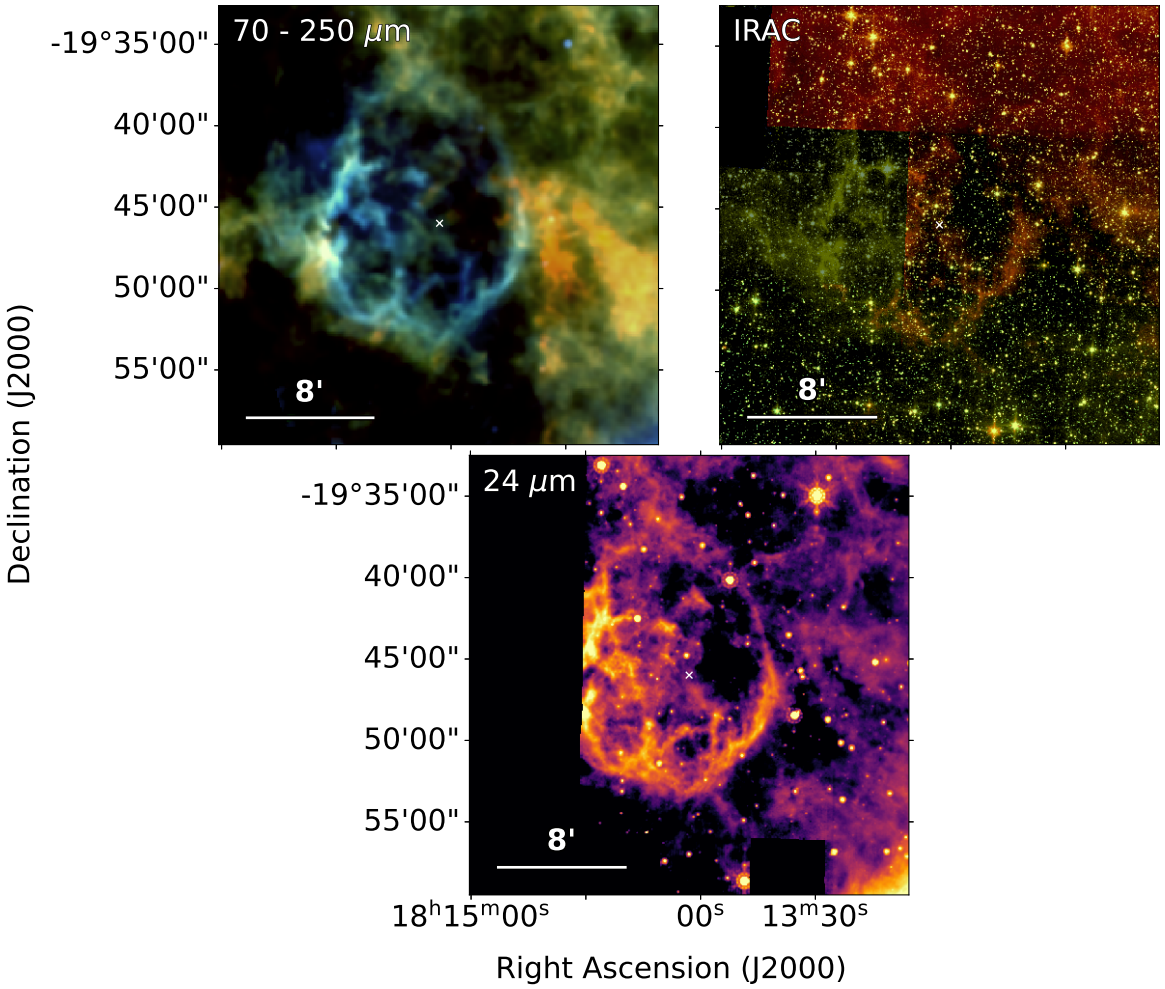

Figure 2.4: G11.1−1.0 - *Top left*: *Herschel* colour image. *Top right*: *Spitzer* IRAC four colour image, colours are red = 8.0 µm, yellow = 4.5 µm, green = 5.8 µm, and blue = 8.0 µm. *Bottom*: *Spitzer* MIPS 24 µm image. In both images, filaments of dust are seen at the outer edges of the shocks. The white cross shows the radio coordinates of the SNR centre from Green (2014).

G11.1−1.0 (Figure 2.4): Unstudied by both Reach et al. (2006) and Pinheiro Goncalves et al. (2011), we detect a shell of FIR dust emission in Figure 2.4. This is brightest in the south-eastern region which is detected across all of the *Herschel* bands. The structure is very similar to that in the 90 cm radio (Brogan et al., 2006) and Hα (Stupar & Parker, 2011), especially in the filaments near to $\alpha = 18^{h}14^{m}29^{s}, \delta = -19°43'53''$, $\alpha = 18^{h}14^{m}30^{s}, \delta = -19°49'00''$, and $\alpha = 18^{h}13^{m}56^{s}, \delta = -19°49'38''$. There is also bright 24 µm and IRAC (5.8 and 8.0 µm) emission from the shell coinciding with the *Herschel* emission, although the entire structure is not covered by the 4.5 and 8.0 µm GLIMPSE bands or the 24 µm band.

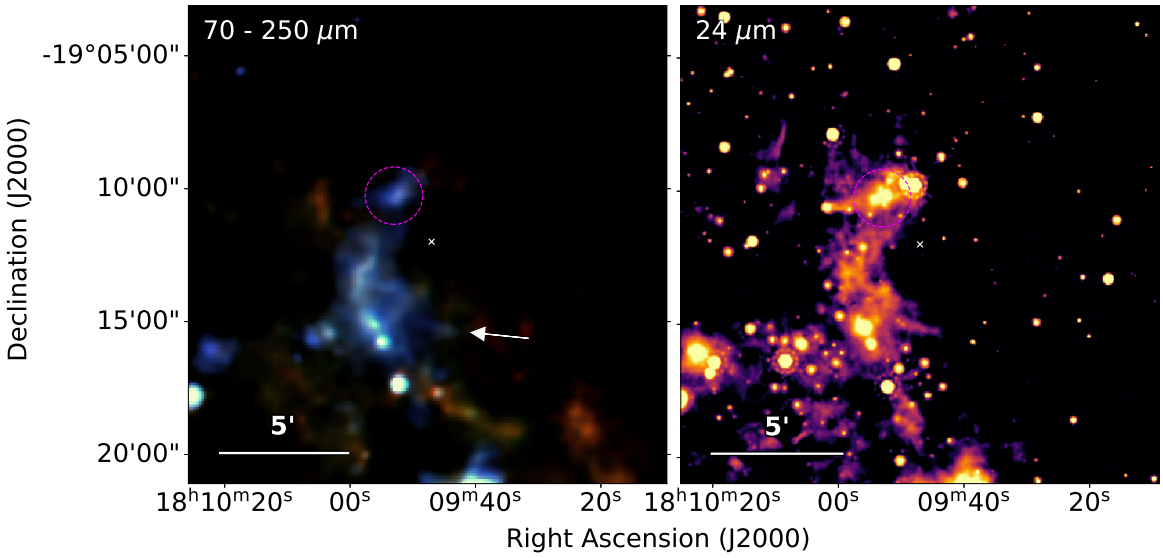

Figure 2.5: G11.1+0.1 - *Left: Herschel* three colour image. *Right: Spitzer* MIPS 24 µm image. Dust is seen in an arc, with small clumps to the east of the remnant at the outer shock (blue in the *Herschel* image). The white cross shows the radio coordinates of the SNR centre from Green (2014).

G11.1+0.1 (Figure 2.5): This region is very confused; however, there is FIR dust emission in a partial shell structure detected to the east of this remnant which correlates with 90 cm radio emission detected by Brogan et al. (2004). Emission is detected across all *Herschel* bands from a clump centred at $\alpha = 18^{h}09^{m}53^{s}, \delta = -19°10'21''$ and a much fainter extended filament near to $\alpha = 18^{h}09^{m}46^{s}, \delta = -19°15'12''$. Unstudied by Reach et al. (2006), this remnant was also a level 1 detection by Pinheiro Goncalves et al. (2011) who detected 24 µm emission at the locations of bright radio knots.

G11.2−0.3 (Figure 2.6): This core-collapse remnant has a composite radio morphology which is very similar to the X-ray shell (Vasisht et al., 1996; Chevalier, 2005). Also associated with the SNR is a central pulsar (AX J1811.5-1926) at $\alpha = 18^{h}11^{m}29.22^{s}, \delta = -19°25'27.6''$ (Kaspi et al., 2001) which has almost the same energy as expected at birth. X-ray morphology indicates that the surrounding PWN has been compressed and all ejecta reheated by the passage of the reverse shock (Torii et al., 1997; Borkowski et al., 2016). Detection of 1.644 µm [FeII] emission from the shell and knots surrounding the PWN indicates the presence of shocked CSM and ejecta material (Koo et al., 2007; Moon et al., 2009).

Expansion rates suggest that this is a young SNR with an estimated age of around 1400 – 2400 yrs (Tam & Roberts, 2003; Borkowski et al., 2016). Reach et al. (2006) suggested that, because of this young age, IRAC emission from shocked

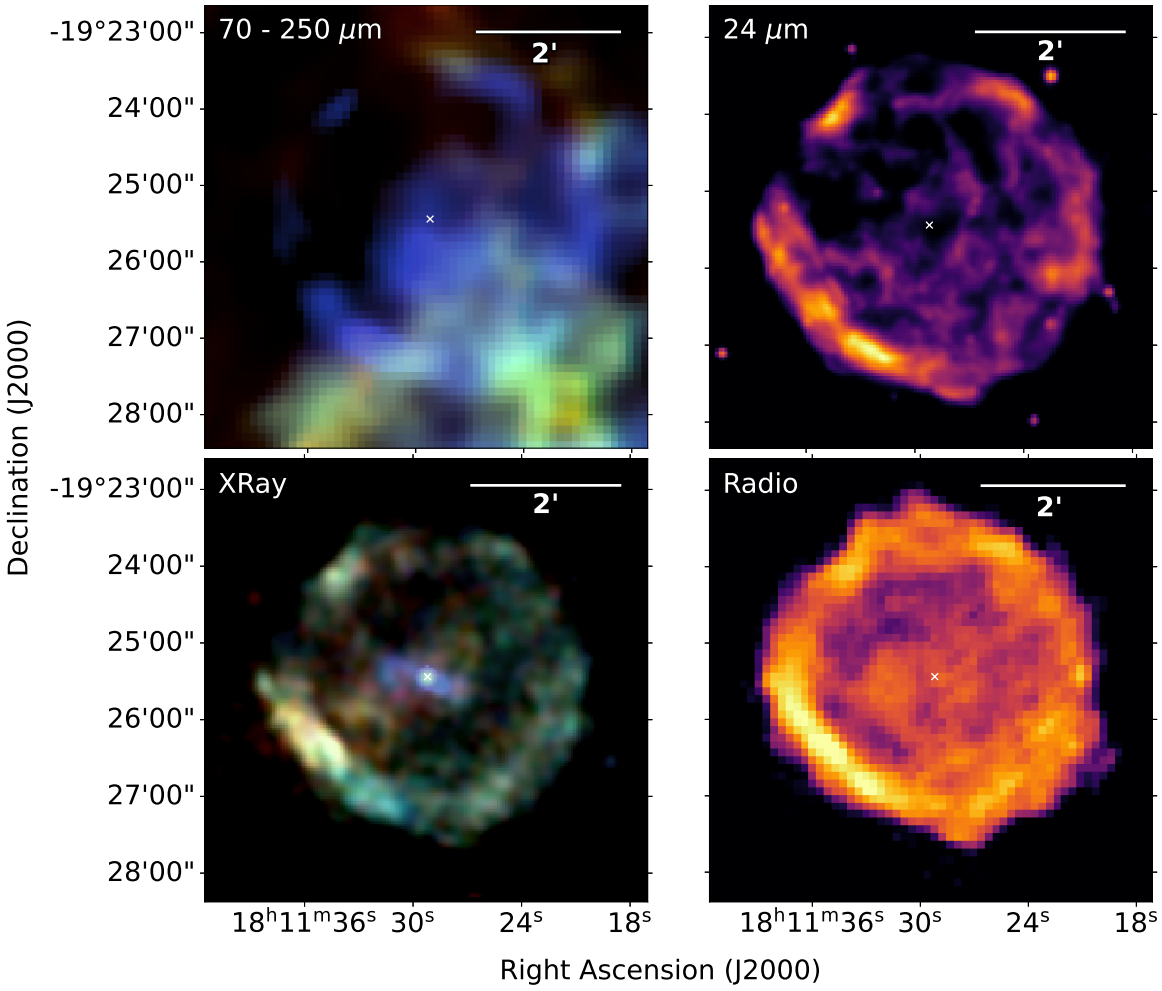

Figure 2.6: G11.2−0.3 - *Top-left*: *Herschel* three colour image with X-ray contours overlaid showing the location of the PWN and outer shocks, due to interaction with surrounding ISM / CSM. Dust is clearly seen in a bright ring and south of the pulsar and its nebula. *Top-right*: *Spitzer* MIPS 24 µm image. *Bottom-left*: *Chandra* three colour image, colours are red = 0.8 − 1.2 keV, green = 1.2 − 2.0 keV, and blue = 2.0 − 10.0 keV. *Bottom-right*: VLA 20 cm radio image. The white crosses show the X-ray coordinates of the SNR centre, which is at the location of the central pulsar.

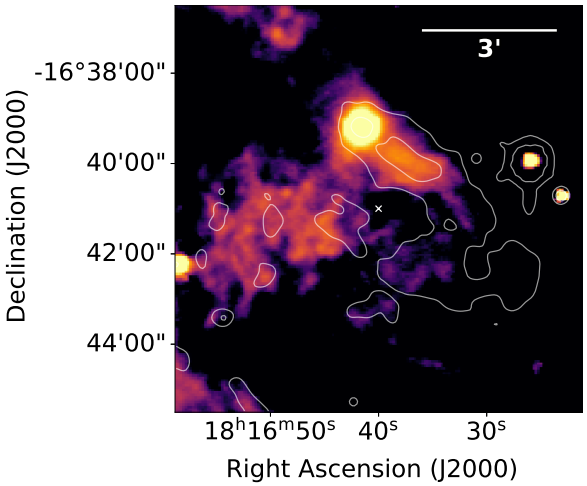

Figure 2.7: G14.1−0.1 - *Herschel* 70 µm image with 24 µm contours overlaid. The magenta cross shows the radio coordinates of the SNR centre from Green (2014).

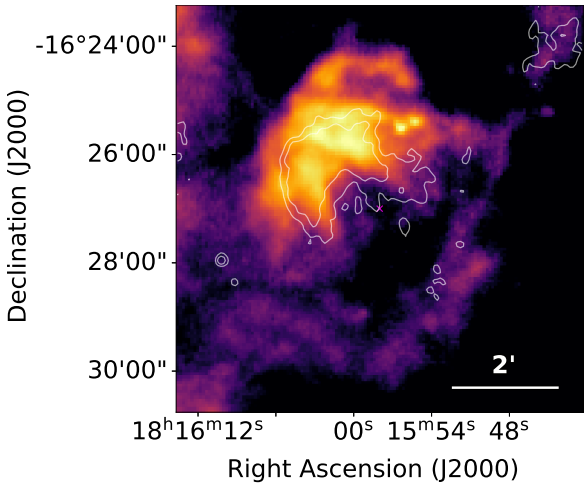

Figure 2.8: G14.3+0.1 - *Herschel* 70 µm image with 24 µm contours overlaid. The magenta cross shows the radio coordinates of the SNR centre from Green (2014).

gas in filaments near $\alpha = 18^h11^m35^s, \delta = -19°26'23''$ may originate from ejecta. Pinheiro Goncalves et al. (2011) detected the same filaments as diffuse, unresolved MIPS emission, and a shell which correlates with X-ray structures. Almost identical to the X-ray and 24 µm structure, we detect a ring of dust emission which is especially bright at 70 µm in Figure 2.6. The southern rim of the SNR is the brightest region at 70 µm, as well as in the X-ray and MIR (MIPS and IRAC). The emission in this region is much more confused at the longer *Herschel* bands. There is also bright dust emission in the central region centred at $\alpha = 18^h11^m29^s, \delta = -19°25'54''$ which coincides with X-ray emission from the central pulsar and its nebula. We suggest that this could be ejecta dust heated by the PWN. We checked ^{12}CO (J = 3→2) data from the CO High Resolution Survey (COHRS, Dempsey et al. (2013)) and found no detection from the SNR or surrounding ISM clouds.

G14.1−0.1 (Figure 2.7): Pinheiro Goncalves et al. (2011) detected a horseshoe shape of 24 µm emission roughly matching the radio shell structure (Brogan et al., 2004). There is diffuse 70 µm emission to the north-east of the shell and a FIR peak coinciding with a radio peak at roughly $\alpha = 18^h16^m41.6^s, \delta = -16°39'11''$.

G14.3+0.1 (Figure 2.8): We clearly observe 70 µm emission coincident with the radio partial shell structure detected by Brogan et al. (2006). There is emission in the longer *Herschel* wavebands, however the structure is different and association with the SNR is unclear.

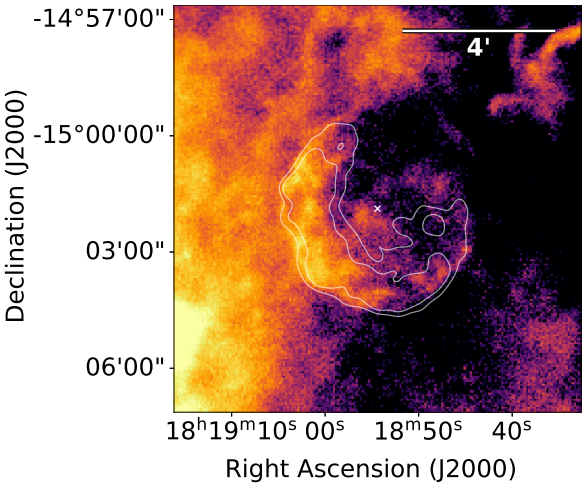

Figure 2.9: G15.9+0.2 - *Herschel* 70 µm image with X-ray contours overlaid. Dust is detected at 70 µm in a partial shell which is brightest to the east. The white cross shows the radio coordinates of the SNR centre from Green (2014).

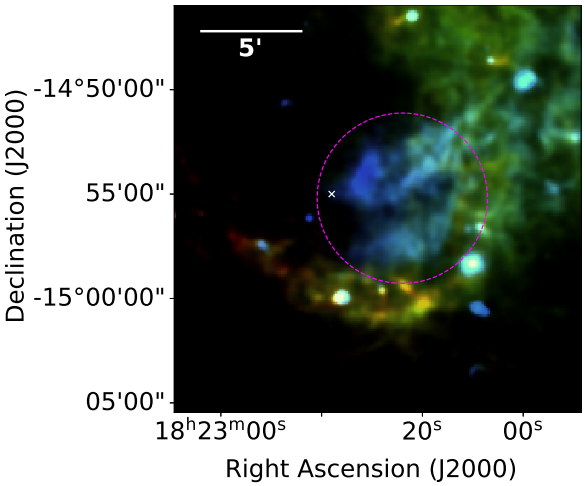

Figure 2.10: G16.4−0.5 - *Herschel* three colour image. Diffuse dust emission is detected in the central region in blue as indicated by the magenta circle. A ridge of dust is detected at wavebands of 250 µm and greater along the southern edge of the remnant which probably is not associated. The white cross shows the radio coordinates of the SNR centre from Green (2014).

G15.9+0.2 (Figure 2.9): This relatively young source ($\leqslant$2400 yr) is the remnant of a CCSN and contains the neutron star CXOU J1818 (Reynolds, 2006; Klochkov et al., 2016). Strong lines in the X-ray indicate the presence of ejecta. This source is undetected by IRAC; however, the 24 µm structure closely correlates with the X-ray and radio. A partial shell of dust is detected around the eastern and south-eastern edge of this remnant at the location of the X-ray and radio emission.

G16.4−0.5 (Figure 2.10): Unstudied by Reach et al. (2006), Pinheiro Goncalves et al. (2011) classified this SNR as a level 1 MIPS detection. This SNR has a partial radio shell morphology (Brogan et al., 2006). A region of diffuse dust emission at 70 µm is detected towards the centre of the remnant, identified by a magenta circle in Figure A.2, which corresponds to emission at 24 µm. A 4′ long filament centred on $\alpha = 18^{\rm h}22^{\rm m}17^{\rm s}, \delta = -14^{\circ}52'51''$ is detected across all five *Herschel* wavebands and coincides with MIPS (Pinheiro Goncalves et al., 2011) and IRAC emission.

There is bright emission in all *Herschel* bands along the southern ridge (red structure in Figure 2.10). This emission seems to be of a similar temperature to, or cooler than, the surrounding ISM and association with the SNR is unlikely.

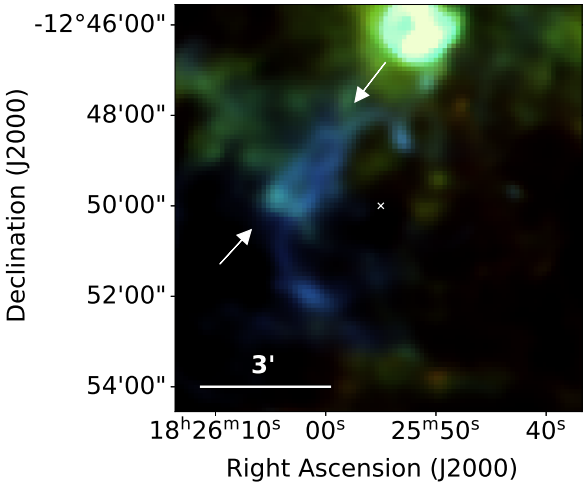

Figure 2.11: G18.6−0.2 - *Herschel* three colour image. A partial shell of dust is detected at the eastern edge of this remnant, at the same location as radio structures. Two parallel filaments of dust are detected in the north-eastern shell, between the two arrows. The white cross shows the radio coordinates of the SNR centre from Green (2014).

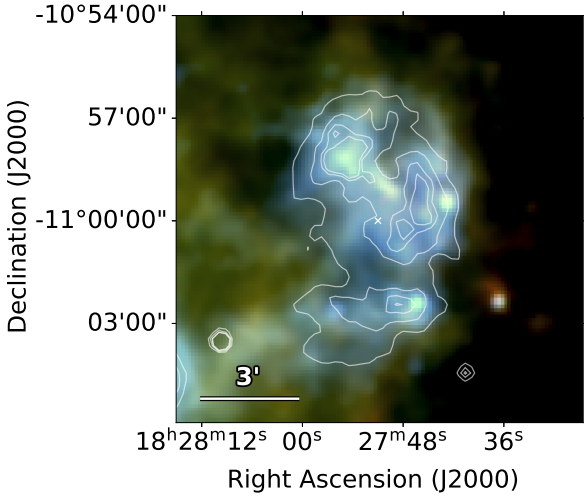

Figure 2.12: G20.4+0.1 - *Herschel* three colour image with 20 cm VLA contours overlaid. FIR emission is detected within the contours at all *Herschel* wavelengths. The white cross shows the radio coordinates of the SNR centre from Green (2014).

G17.4−0.1: This SNR has a partial shell radio structure. The region is confused in the FIR and it is difficult to distinguish any SNR emission from that of the ISM. There is a bright FIR region to the west of the SNR which coincides with 24 µm emission and a radio peak detected by Brogan et al. (2006), although the morphology is different and association is unclear.

G18.6−0.2 (Figure 2.11): Voisin et al. (2016) suggested that the pulsar PSR J1826−1256 may be associated with this remnant as their estimated distances are similar. Although there is dust emission in the region of the pulsar in Figure 2.11 at $\alpha = 18^{h}26^{m}08.2^{s}, \delta = -12^{\circ}56'46''$, it is indistinguishable from the local ISM and unclear as to whether any of this is associated to the PSR J1826−1256. Dust emission is detected at 70 µm from the eastern region of this shell-type SNR which is brightest from two parallel filaments detected near to $\alpha = 18^{h}26^{m}00^{s}, \delta = -12^{\circ}49'26''$ and $\alpha = 18^{h}26^{m}02^{s}, \delta = -12^{\circ}49'08''$. The morphology seems to correlate with 90 cm radio emission from Brogan et al. (2006) and the partial shell detected by Pinheiro Goncalves et al. (2011). At 160 µm the region is too confused to determine if any emission is associated with the SNR, and in the longer *Herschel* wavebands there is no evidence of SNR emission.

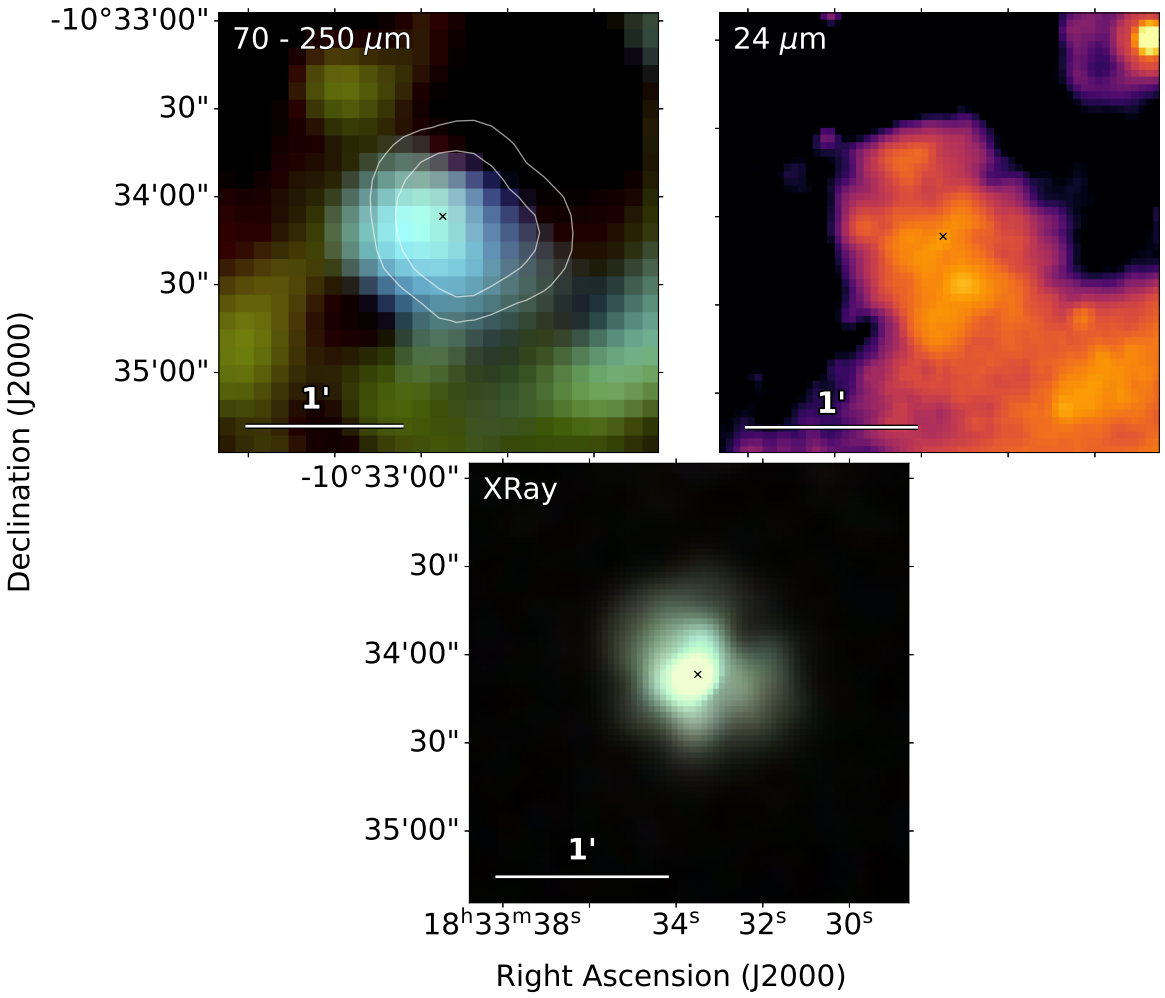

Figure 2.13: G21.5−0.9 - *Left*: *Herschel* three colour image with X-ray contours overlaid to show the location of the pulsar and PWN. Dust is observed in a clump in the central area, at the location of the PWN. *Right*: *Spitzer* MIPS 24 μm image. *Bottom*: *Chandra* colour image (red = 1.0 - 2.1 keV, green = 2.1 - 4.0 keV, and blue = 4.0 - 10.0 keV). The black crosses shows the X-ray coordinates of the SNR centre.

G20.4+0.1 (Figure 2.12): Pinheiro Goncalves et al. (2011) detected emission correlating with the radio shell of this SNR. We detect FIR emission at all *Herschel* wavelengths which lies within the radio contours, as shown in Figure 2.12.

G21.5−0.9 (Figure 2.13): This Crab-like remnant has a pulsar (PSR J1833-1034) at its centre with a non-thermal X-ray halo (Camilo et al., 2006). Properties of the PWN, the pulsar, and the shell suggest that the remnant is $\lesssim$ 1000 years old (Camilo et al., 2006) and HI and CO observations tell us that this SNR is at a distance of 4.8 kpc (Tian & Leahy, 2008). Emission at all *Herschel* bands is detected at $\alpha = 18^{h}33^{m}33.8^{s}, \delta = -10°34'14''$, slightly offset from the location of the central pulsar and its wind nebula as shown by X-ray contours in Figure 2.13.

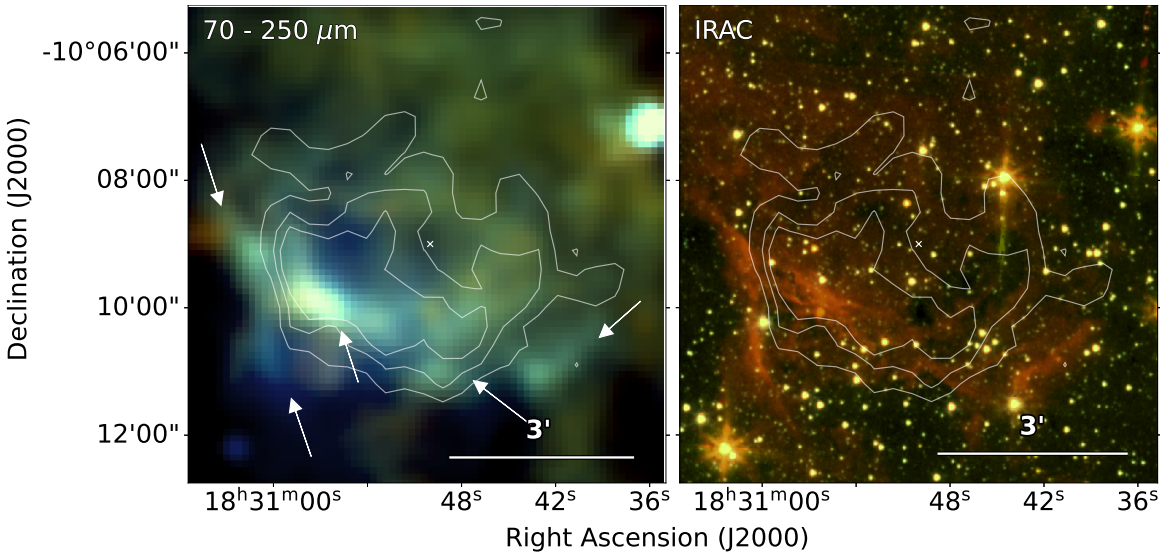

Figure 2.14: G21.5−0.1 - *Left*: *Herschel* three colour image. Dust is observed in the central region in a filled shell. The arrows indicate filaments of dust which correlate with the IRAC detection by Reach et al. (2006). *Right*: *Spitzer* IRAC four colour image, colours are red = 8.0 µm, yellow = 5.8 µm, green = 4.5 µm, and blue = 3.6 µm. The white cross shows the radio coordinates of the SNR centre from Green (2014).

This is more confused with the local environment at longer wavebands. Pinheiro Goncalves et al. (2011) also made a level 1 detection of the central region. We suggest that dust in this region is heated by the PWN. We checked ^{13}CO (J = 1→0) data from the Galactic Ring Survey (GRS, Jackson et al. (2006)) and found no CO detection towards the SNR.

G21.5−0.1 (Figure 2.14): Dust is observed in a filled shell from this remnant at all *Herschel* wavelengths, which correlates with the 24 µm emission (Pinheiro Goncalves et al., 2011) and the 90 cm radio structure detected by Brogan et al. (2006). Filaments of dust are indicated in Figure 2.14. This includes a $\sim 2.5'$ bright filament detected to the east, centred near $\alpha = 18^{\rm h}31^{\rm m}01^{\rm s}, \delta = -10°09'54''$ which is also detected in the MIR. Another FIR detected filament is centred near $\alpha = 18^{\rm h}30^{\rm m}41.5^{\rm s}, \delta = -10°10'47''$ and is roughly $1.6'$ long. Although unstudied by Reach et al. (2006), Pinheiro Goncalves et al. (2011) detected MIPS and IRAC emission along the southern ridge.

Nevertheless, the origin of this emission requires further study. Anderson et al. (2017) suggests that this is a H II region which has been incorrectly classified as a SN structure. This is because the entire structure coincides with the WISE H II region G21.560−0.108 and Pinheiro Goncalves et al. (2011) derived a high MIR to

radio flux ratio indicative of H II regions

G23.6+0.3: Pinheiro Goncalves et al. (2011) detected an elongated region of 24 µm emission at the location of the SNR radio structure. However, they argue that the SNR morphology more closely resembles that of a HII region than a SNR, and the nature of this object should therefore be reconsidered. There is FIR emission in the region of the radio structure, however this is offset (A.2).

G27.4+0.0: This shell-type SNR is thought to have been produced by a very massive progenitor ($\gtrsim 20 M_{\odot}$) between 750 and 2100 years ago (Kumar et al., 2014). Although there is a very good detection at 24 µm, the region is confused at *Herschel* wavelengths (Figure 2.3). We find some evidence of dust emission at 70 µm in the region which may be associated with X-ray and 24 µm SNR filaments. However, we cannot definitively conclude this as there is extensive interstellar dust emission to the west confusing the region at FIR wavelengths.

G29.6+0.1: This is a young remnant (< 8000 yrs, Gaensler et al., 1999) with a non-thermal radio shell and an associated compact source (AX J1845−0258) which is likely a pulsar (Gaensler et al., 1999; Vasisht et al., 2000). Broad molecular lines have been detected towards the remnant, suggesting that it is interacting with a molecular cloud (Kilpatrick et al., 2016). Numerous young stellar objects are detected in this field, including FIR bright sources at $\alpha = 18^{\mathrm{h}}44^{\mathrm{m}}51^{\mathrm{s}}, \delta = -02^{\circ}55'18''$, $\alpha = 18^{\mathrm{h}}44^{\mathrm{m}}53.3^{\mathrm{s}}, \delta = -02^{\circ}56'03''$, and $\alpha = 18^{\mathrm{h}}44^{\mathrm{m}}49.2^{\mathrm{s}}, \delta = -02^{\circ}58'15''$ (Veneziani et al., 2013). There is also FIR emission across all *Herschel* and *Spitzer* bands coincident with the radio source at $\alpha = 18^{\mathrm{h}}44^{\mathrm{m}}55.1^{\mathrm{s}}, \delta = -02^{\circ}55'36.9''$ (Gaensler et al., 1999). The radio shell is not detected by IRAC or MIPS, although at *Herschel* wavelengths there is emission which may be associated (Figure A.2). However, contamination from local ISM to the south-west makes it difficult to distinguish SNR emission.

G29.7−0.3 (Figure 2.15): It is possible that this SNR resulted from a Wolf-Rayet star which exploded as a type Ib/c SN after clearing a $\sim$ 10 pc bubble (Morton et al., 2007). CO observations of an associated molecular cloud puts the remnant at a kinematic distance of $\sim$ 10.6 kpc, at the far side of the Sagittarius arm (Su et al., 2009). Although there is bright MIPS emission from this remnant in both a partial shell and central region (level 1 by Pinheiro Goncalves et al. (2011)), there is no clear emission at IRAC wavelengths from the SNR (level 3 by Reach et al. (2006)). It was suggested that the lack of IRAC emission from the shell is due to shock destruction of small dust grains (Morton et al., 2007).

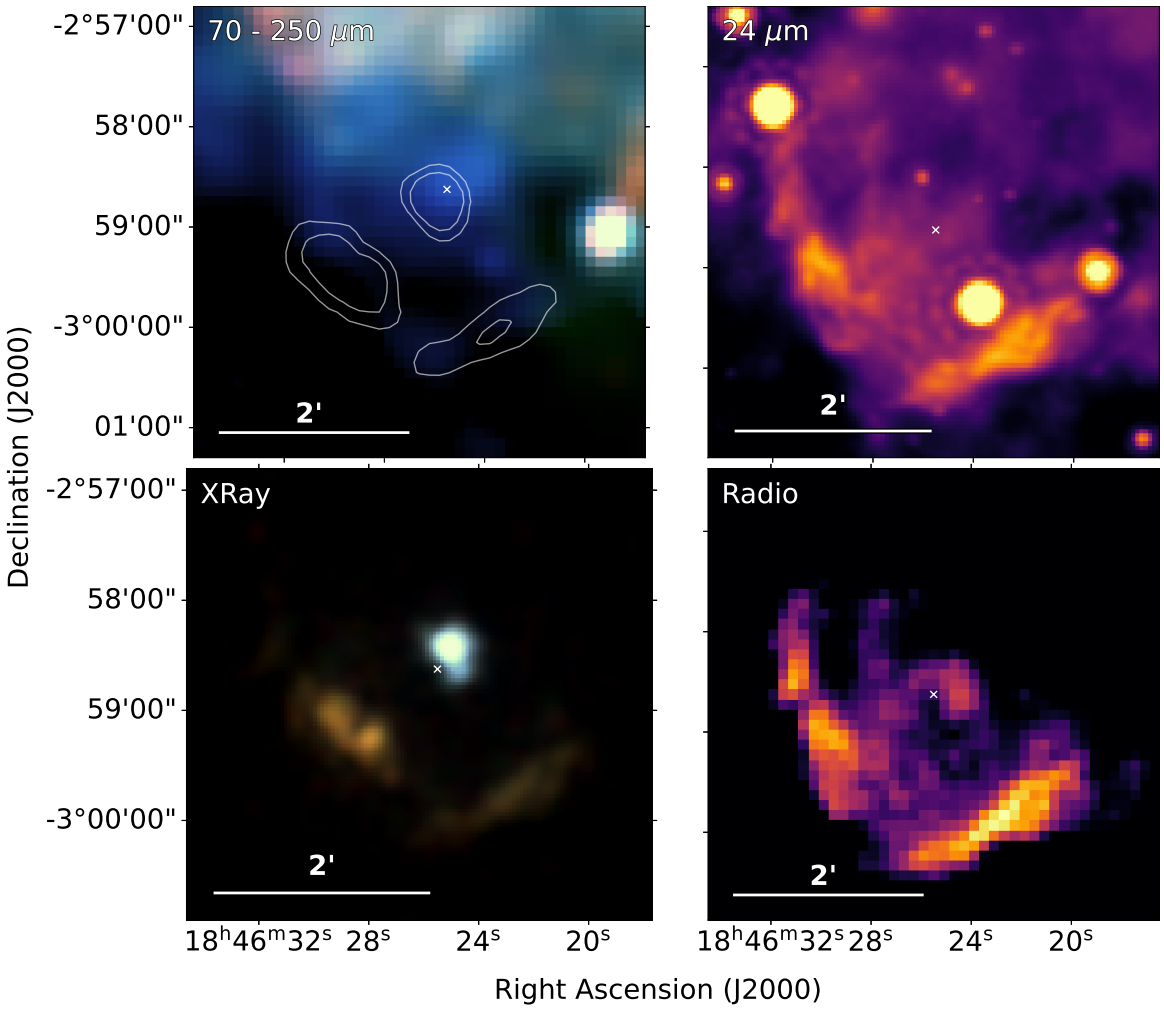

Figure 2.15: G29.7−0.3 (Kes 75) -*Top-left*: *Herschel* three colour image with X-ray contours from *Chandra* overlaid. Dust is detected in a central clump at the same location as the pulsar and PWN. *Top-right*: *Spitzer* MIPS 24 µm image. *Bottom-left*: *Chandra* colour image (red = 1.0 - 1.7 keV, green = 1.7 - 2.6 keV, and blue = 2.6 - 8.0 keV). *Bottom-right*: VLA 20 cm radio image. The white crosses shows the X-ray coordinates of the SNR centre.

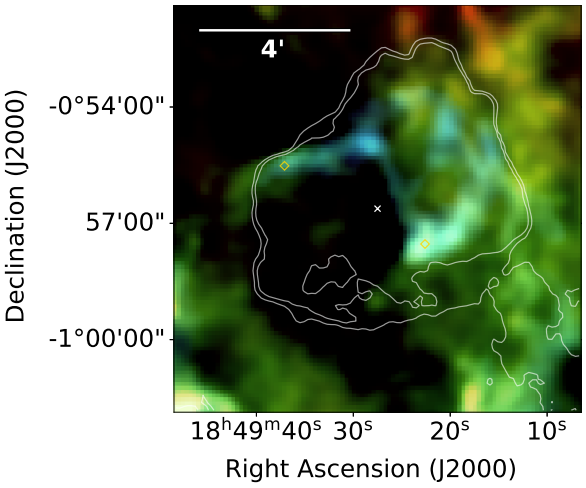

Figure 2.16: SNR 3C391 (G31.9+0.0) - *Herschel* three colour image with X-ray contours overlaid. The two diamonds indicate the locations of the two OH masers (Frail et al., 1996). Dust is detected at the outer edges of the shock in a semi-circular shell. The white cross shows the X-ray coordinates of the SNR centre.

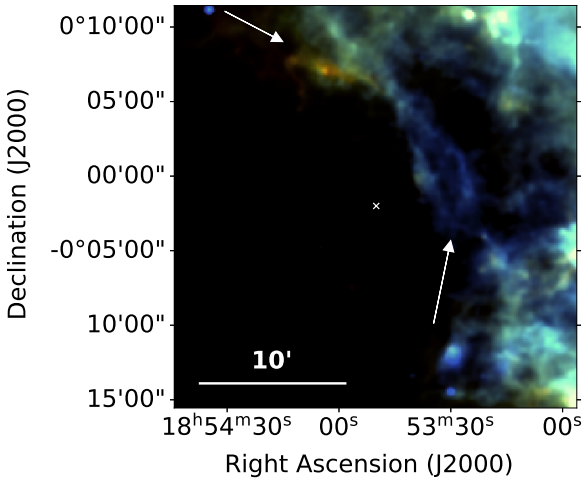

Figure 2.17: G33.2−0.6 - *Herschel* three colour image. Dust is detected in filaments in an arc towards the western shell of the SNR, indicated by the lower arrow. Two filaments seem to extend to from this arc as indicated by the upper arrows; a filament extending to the north is detected in all *Herschel* wavebands, and a cooler filament extending to the north-east is detected in all but 70 µm. The white cross shows the radio coordinates of the SNR centre.

At 70 µm in Figure 2.15 we detect a region of diffuse dust emission centred at $\alpha = 18^{h}46^{m}24.9^{s}, \delta = -02°58'30''$, at the same location as X-ray emission from the PWN and the central pulsar (Helfand et al., 2003b). At the longer *Herschel* wavelengths there is too much confusion to distinguish if there is any cold dust in the SNR. There is FIR emission from the shell region coinciding with a bright 24 µm structure, however this is much less bright and difficult to detect in some regions. The object detected at $\alpha = 18^{h}46^{m}19^{s}, \delta = -02°59'03''$ is a young stellar object (Veneziani et al., 2013).

3C 391, G31.9+0.0 (Figure 2.16): This is a young mixed-morphology SNR with an incomplete radio shell structure (Goss et al., 1979). Both Reach et al. (2006) and Pinheiro Goncalves et al. (2011) classified this SNR as a level 1 detection. Reach et al. (2006) found MIR emission originating from shocked molecular gas at $\alpha = 18^{h}49^{m}23^{s}, \delta = -00°57'38''$ and $\alpha = 18^{h}49^{m}29^{s}, \delta = -00°55'00''$, at the ends of the SNR's bright semicircular radio shell. The southern patch is coincident with one of two 1720 MHz OH masers detected in the SNR where the remnant seems to

be breaking into the edge of a molecular cloud (Frail et al., 1996). The MIR patches are well detected by *Herschel* in Figure 2.16; the southern patch is detected at all *Herschel* bands, however the northern patch is detected only at 70 and 160 µm. Beyond these points, FIR emission extends into an arc around the northwestern shell in all *Herschel* bands, although there is confusion at bands other than 70 µm.

Reach et al. (2006) discussed a bar of shocked, ionised gas from which both Reach et al. (2006) and Pinheiro Goncalves et al. (2011) concluded there was a contribution of [Fe II] 5.34 µm line emission. This bar coincides with the brightest part of the radio shell and is also detected in the FIR at 70 and 160 µm near to $\alpha = 18^{h}49^{m}16^{s}, \delta = -00°55'03''$. The FIR emission is likely associated with dust rather than line emission considering the high luminosity of dust at 70 – 160 µm as in the cases of the Crab, Cas A (Gomez et al., 2012b; De Looze et al., 2017), and three SNRs studied ourselves in Section 3.1.

G33.2−0.6 (Figure 2.17): A partial shell is detected to the western edge of this remnant which has a higher temperature than the surrounding medium as seen in Figure 2.17. This arc corresponds to the 1465 MHz radio structure detected by Dubner et al. (1996). Most noticeable are two filaments; the inner one is $\sim 5'$ with a midpoint near $\alpha = 18^{h}53^{m}35^{s}, \delta = -00°00'36''$, and the outer filament is $\sim 15.5'$ near to $\alpha = 18^{h}53^{m}43^{s}, \delta = +00°04'22''$. These filaments are detected at *Spitzer* wavelengths, although neither Reach et al. (2006) nor Pinheiro Goncalves et al. (2011) classified this source as a clear detection. FIR emission is also detected at the location of the compact IRAS source (IRAS 18509−0015) to the south-west of the SNR at $\alpha = 18^{h}53^{m}29^{s}, \delta = -00°12'03''$. To the north of the remnant there are two filaments detected, one cooler which is visible in red in Figure 2.17, and another warmer filament extending to the north which is visible in blue and is detected in all *Herschel* wavebands. Both of these filaments are outside of the region of radio emission, and we therefore cannot confidently determine whether these are associated with the remnant.

Kes 79, G33.6+0.1: This mixed-morphology SNR is most likely in the Sedov-Taylor phase of evolution, with an age of 4.4 – 6.7 kyr (Zhou et al., 2016). CO observations suggest that the remnant is interacting with molecular clouds to the east (e.g. Green & Dewdney, 1992; Zhou et al., 2016). Pinheiro Goncalves et al. (2011) detected 24 µm emission corresponding to the X-ray filaments to the east and the brightest X-ray contours.

Although there are FIR features which may correspond to the SNR (Figure A.2) this isn't clear; the region is confused and there is extensive FIR emission

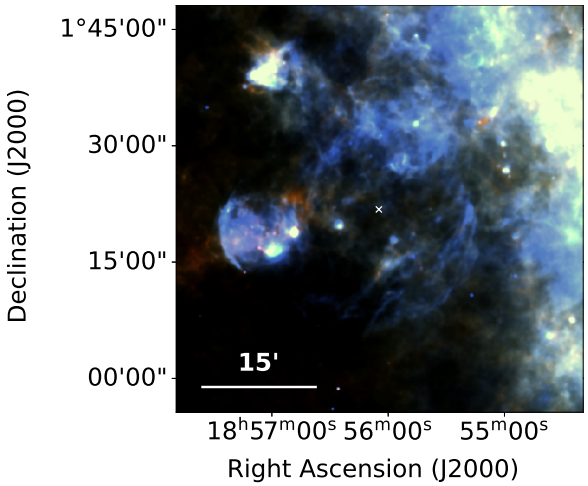

Figure 2.18: SNR W44 (G34.7−0.4) - *Herschel* three colour image. Dust is seen in filaments at the outer edges of the shock and is brightest to the west. The bright patch of emission to the east is likely an H II region (Rho et al., 1994). The white cross shows the X-ray coordinates of the SNR centre.

from the local ISM. A circle of FIR emission of radius $\sim 0.66'$ at $\alpha = 18^h52^m39^s, \delta = +00°41'59''$ coincides with an IR bubble (Simpson et al., 2012) and an X-ray dark region. There are also FIR point sources corresponding to MIR sources which may be protostars (Reach et al., 2006) in an infrared dark cloud along the eastern edge. There is no dust emission in the region of the X-ray point source.

W44, G34.7−0.4 (Figure 2.18): This large core-collapse SNR has a well defined radio shell which is centrally filled by thermal X-ray emission (Jones et al., 1993; Rho et al., 1994) and was a level 1 detection by both Reach et al. (2006) and Pinheiro Goncalves et al. (2011). Similar to the MIR structure, the FIR dust emission traces the radio elliptical shell, although the FIR is fainter towards the south. At MIR wavelengths shocked H_2 is detected along the eastern border (Reach et al., 2005b) where the SNR is interacting with a molecular cloud (Giacani et al., 1997; Yusef-Zadeh et al., 2003; Reach et al., 2006). We detect 70 and 160 µm emission at this edge which is possibly from shock-heated dust. We also detect bright FIR filaments at the western edge, closely following the radio structure. There is some potential detection of emission at the longer *Herschel* wavebands, however the emission is much more confused. The patch of bright emission to the east, centred at $\alpha = 18^h57^m05^s, \delta = +01°18'40''$ is probably an HII region (Rho et al., 1994). We do not detect emission in the region of the pulsar, PSR B1853+01, which is located at $\alpha = 18^h56^m10.65^s, \delta = +01°13'21.3''$.

G35.6−0.4: Recently re-classified as a SNR rather than a HII region, this

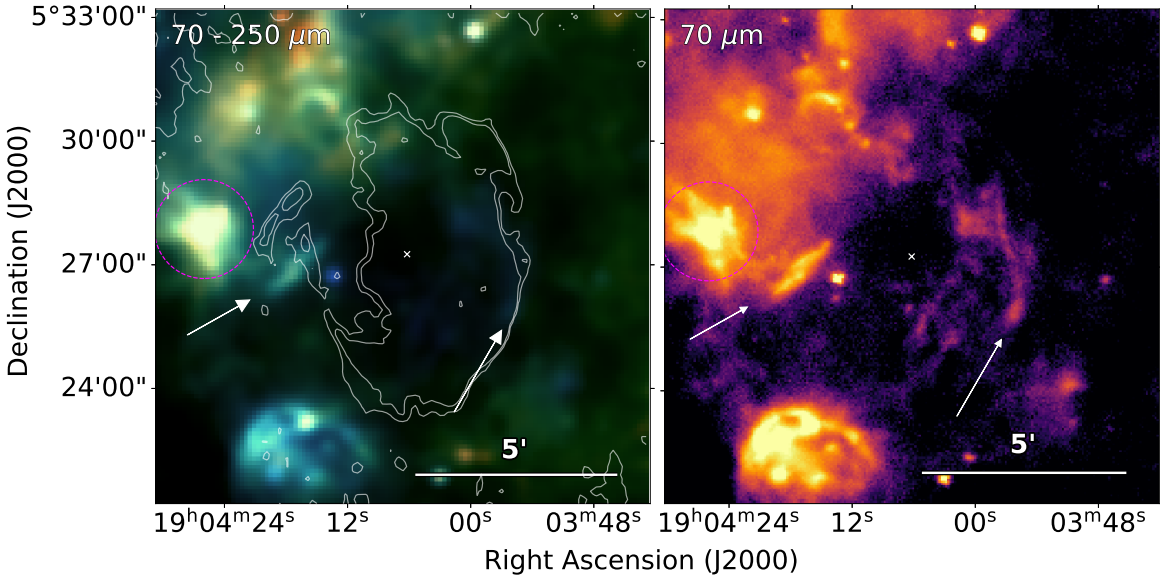

Figure 2.19: SNR 3C 396 (G39.2−0.3) - *Left: Herschel* three colour image with radio (20 cm) contours overlaid. *Right: Herschel* 70 µm image. Within the magenta circle, FIR emission is detected at the location of a blowout tail detected at 1465 MHz (Patnaik et al., 1990). Filamentary dust is detected at the western outer edges of the shocks and in regions of very high radio polarisation, as indicated by the arrows. The white cross shows the X-ray coordinates of the SNR centre.

shell-type remnant is likely around 30,000 yrs old and at a distance of 3.6 ± 0.4 kpc (Green, 2009; Zhu et al., 2013). Pinheiro Goncalves et al. (2011) classed this as a level 1 detection although there is not a convincing likeness between IR and radio emission. There is a FIR structure to the south-east of the SNR which does not have a similar morphology to radio emission (Zhu et al., 2013). A 3.5′ rim of dust at $\alpha = 18^{\rm h}58^{\rm m}12^{\rm s}, \delta = +02°08'47''$ may be associated with the radio structure, although this is unclear.

FIR emission is detected from the planetary nebula PN G35.5−0.4 at $\alpha = 18^{\rm h}57^{\rm m}59.5^{\rm s}, \delta = +02°07'07''$ whose distance has been estimated as 3.8 ± 0.4 kpc (Zhu et al., 2013). There is also dust emission coinciding with a molecular clump towards the centre of the gamma ray source HESS J1858+020 at $\alpha = 18^{\rm h}58^{\rm m}21^{\rm s}, \delta = +02°05'12''$ (HESS Collaboration, 2008c). A YSO embedded in this clump probably belongs to a larger molecular cloud which is interacting with G35.6−0.4 and a nearby H II region (Paron et al., 2011).

3C 396, G39.2−0.3 (Figure 2.19): There was a level 1 detection of this SNR by both Reach et al. (2006) and Pinheiro Goncalves et al. (2011). Similar to the MIR detection described by Reach et al. (2006), FIR emission from this SNR is mainly detected from three regions:

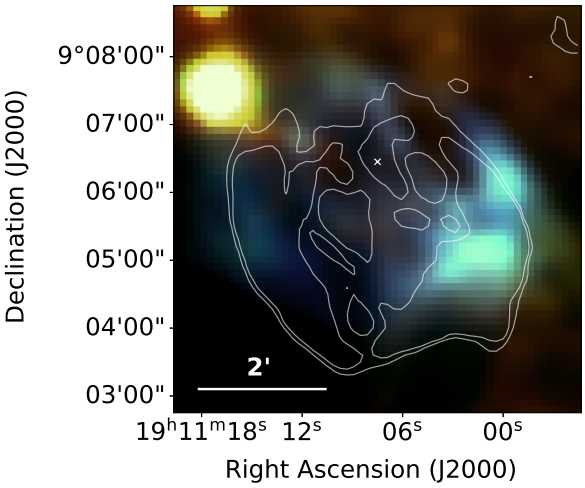

Figure 2.20: W49B (G43.3−0.2) - *Herschel* three colour image overlaid with radio 20 cm contours. Shock heated dust is seen in filaments in a barrel-hoop structure. The white cross shows the X-ray coordinates of the SNR centre.

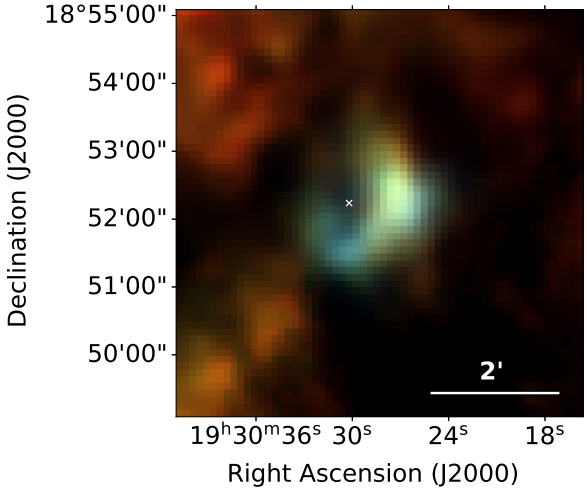

Figure 2.21: G54.1+0.3 - *Herschel* three colour image with X-ray contours from *Chandra* overlaid. Dust is observed in a central region at the location of the PWN. The white cross shows the X-ray coordinates of the SNR centre. For details on the discovery of dust in this source see Temim et al. (2017) and Rho et al. (2018).

A bright region of emission in Figure 2.19 at $\alpha = 19^h04^m26^s, \delta = +05°27'55''$ (within the magenta circle) coincides with the radio blowout tail (see Patnaik et al., 1990 Figures 1 and 2) which extends out of the east shell and over the top of the SNR. FIR emission from the tail is detected in the five *Herschel* bands. High radio polarisation and bright emission in the longer *Herschel* channels is consistent with synchrotron dominated FIR emission in the region. Cruciani et al. (2016) found a significant correlation between the FIR and radio, 1.5 GHz, emission in this region, although they could not rule out that this is due to diffuse interstellar emission.

Filamentary emission is detected on the western side of this remnant, near to $\alpha = 19^h03^m56^s, \delta = +05°25'46$, across all of the *Herschel* bands, although at bands longer than 70 µm this is very confused with ISM emission. It is suggested that MIR emission at the same location originates from shocked, ionised gas (Reach et al., 2006) suggesting that the FIR emission in this region could originate from warm, shocked dust.

FIR emission is detected at all *Herschel* wavelengths to the east of the SNR in a region of very high radio polarisation. At 70 and 160 µm this is resolved into two filaments at $\alpha = 19^h04^m17^s, \delta = +05°27'07''$ and $\alpha = 19^h04^m19^s, \delta = +05°26'33''$ (right panel of Figure 2.19).

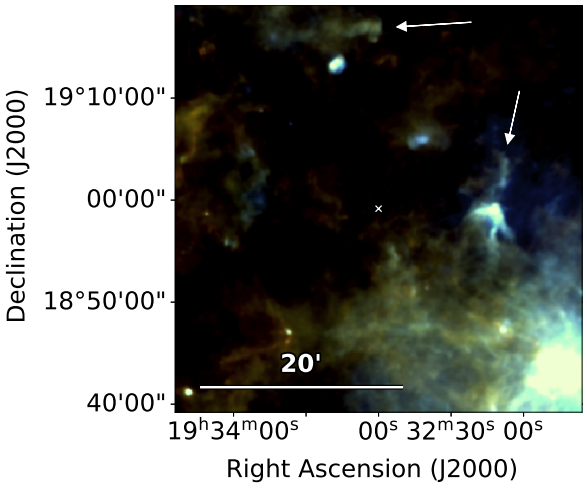

Figure 2.22: G54.4−0.3: *Herschel* three colour image. Filaments of dust are observed at the outer edges of the shocks, as indicated by the white arrows. The white cross shows the X-ray coordinates of the SNR centre.

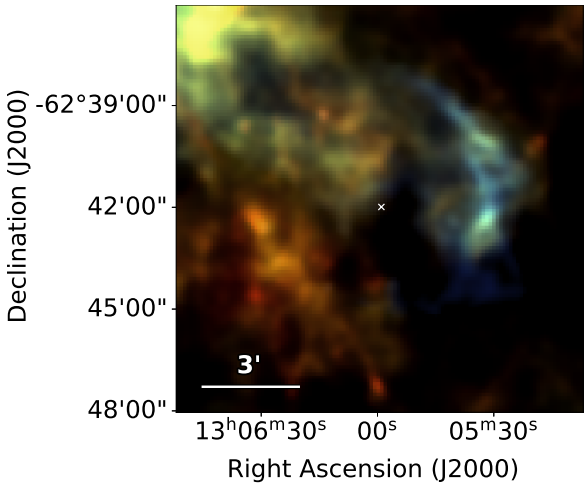

Figure 2.23: Kes 17 (G304.6+0.1) - *Herschel* three colour image. An arc of dust is seen on filaments to the western edge of the outer shocks. The white cross shows the radio coordinates of the SNR centre from Green (2014).

W49B, G43.3−0.2 (Figure 2.20): W49B is the first bipolar Type Ib/Ic SNR discovered in the Milky Way, which contributes to its rather unique radio barrel-hoop structure (Moffett & Reynolds, 1994; Lopez et al., 2013). X-ray emission is dominated by ejecta emission which suggests that the SNR is young (Hwang et al., 2000). The radio/IR morphologies seem anti-correlated with the X-ray emission.

Both Reach et al. (2006) and Pinheiro Goncalves et al. (2011) detected this SNR to level 1. The FIR emission at 70, 160 and 250μm in Figure 2.20 follows the MIR and radio morphology. The emission is especially bright to the southwest where there is a detection in all *Herschel* wavebands although in the longer wavebands it is very confused. At 70 – 250 µm we detect a $\sim 1'$ filament of emission centred at $\alpha = 19^{h}11^{m}07^{s}, \delta = +09°07'01''$. Reach et al. (2006) detected MIR emission due to ionic shocks from this filament, as we detect FIR continuum emission, it is likely that this is from shock-heated dust. Reach et al. (2006) also established that MIR emission in the outer shell to the east and southwest is from shocked molecular gas where the SNR is interacting with a molecular cloud which encapsulates the wind-blown bubble surrounding the SNR (Keohane et al., 2007).

G54.1+0.3 (Figure 2.21): Described as a 'close cousin' of the Crab Nebula, this remnant has a central PWN and an IR shell $\sim$1.5$'$ from the pulsar (Koo et al., 2008). Timing measurements of the central pulsar suggest a characteristic age of 2900 yr (Camilo et al., 2002) and CO and HI observations suggest a distance of

6.2 kpc (Leahy et al., 2008).

Both Reach et al. (2006) and Pinheiro Goncalves et al. (2011) classified this SNR as a level 3 detection, although there is bright 24 µm emission at the location of the PWN. Temim et al. (2017) detected an infrared shell to the south and west of the PWN. They completed a detailed analysis of MIR and FIR emission from the shell in the region of the PWN and found that their models require a minimum dust mass of $1.1 \pm 0.8\,M_{\odot}$. Rho et al. (2018) fit the FIR-mm SED to derive a total dust mass of 0.08 - $0.9 M_{\odot}$ depending on the grain composition. It is thought that the reverse shock has not yet reached this shell which might originate from dust in the SN ejecta potentially heated by early-type stars (Temim et al., 2010). However, the origin of the emission requires further investigation as Anderson et al. (2017) suggest that the structure is a mistakenly classified H II region, although faint, diffuse radio emission in the centre area may be associated with the SNR.

G54.4−0.3 (Figure 2.22): This SNR is located in an extended cluster of young population I objects from which molecular material was blown in to a shell by stellar winds before the supernova exploded (Junkes et al., 1992). Reach et al. (2006) detected two MIR filaments likely corresponding to the location of shocks propagating into the bubble and/or molecular cloud, although their MIR colours are consistent with photo-dissociation regions (Reach et al., 2006). The same filaments are detected by Pinheiro Goncalves et al. (2011) and across the five *Herschel* wavebands as shown in Figure 2.22 at $\alpha = 19^{\mathrm{h}}32^{\mathrm{m}}08^{\mathrm{s}}, \delta = +19°02'56''$ and $\alpha = 19^{\mathrm{h}}33^{\mathrm{m}}13^{\mathrm{s}}, \delta = +19°16'20''$.

G55.0+0.3: This shell-type remnant is at an estimated distance of 14 kpc and is highly evolved, aged around 1.9×10^6 yrs (Matthews et al., 1998). Like Reach et al. (2006) and Pinheiro Goncalves et al. (2011) at MIR wavelengths, we detect an arc of FIR emission near to $\alpha = 19^{\mathrm{h}}32^{\mathrm{m}}05^{\mathrm{s}}, \delta = +19°46'41''$ which could be associated with the eastern shell (Figure A.2). However, it is difficult to disentangle SNR and ISM emission, making an association unclear.

Kes 17, G304.6+0.1 (Figure 2.23): This middle-aged SNR (28 – 64 kyr, Combi et al., 2010b) is interacting with several massive molecular clouds causing bright filaments to the west by shock compression (Combi et al., 2010b). Reach et al. (2006) attributed MIR emission in the shell to molecular shocks. As shown in Figure 2.23, there is bright FIR emission in this region across all of the *Herschel* bands which is likely due to dust heated by shocked gas. There is also some diffuse 70 µm emission along the southern ridge and longer wavelength emission towards the

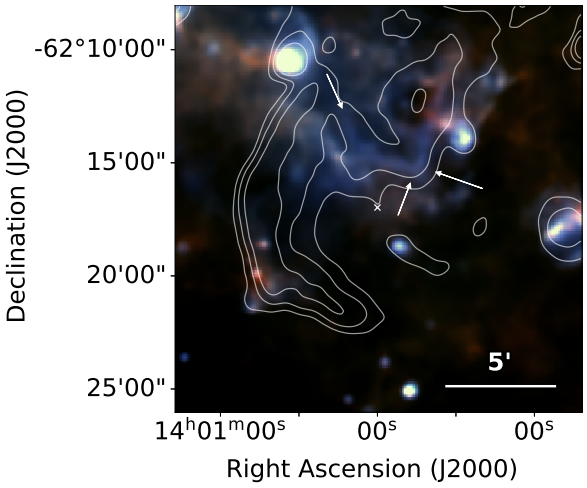

Figure 2.24: G310.8−0.4 - *Herschel* three colour image with radio contours from MOST overlaid. The arrows indicate FIR emission which correlates with radio structure.

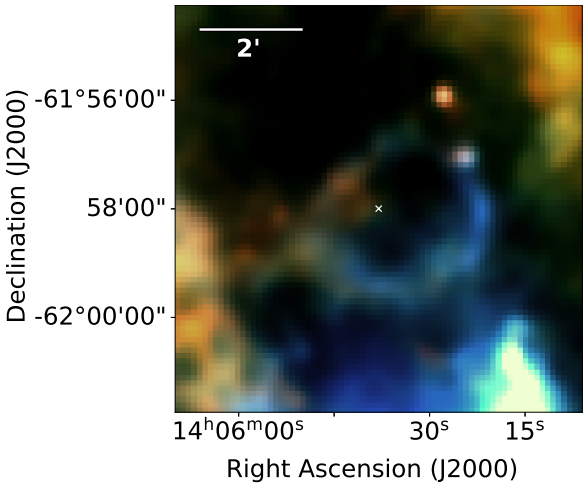

Figure 2.25: G311.5−0.3 - *Herschel* three colour image. A ring of dust emission is detected at the outer edges of the shocks. The white cross shows the X-ray coordinates of the SNR centre.

south east, although it is unclear whether this is associated with the SNR.

G310.8-0.4 (Figure 2.24) This SNR has a bright eastern radio shell at 0.843 GHz which is less defined to the west (Whiteoak & Green, 1996). Reach et al. (2006) and Pinheiro Goncalves et al. (2011) detected emission coinciding with radio contours to the south-east and part of the structure in the north-west. A 4.4′ rim of diffuse FIR emission is detected near $\alpha = 14^{h}00^{m}44^{s}, \delta = -62°19'03''$ which may be associated with the SNR (Figure A.2). However this is unclear as the region is very confused in FIR and potentially related emission cannot be distinguished from the local ISM. Filaments of FIR emission to the north of the SNR seems to correlate with radio emission, as indicated by the arrows.

G311.5−0.3 (Figure 2.25): This shell-type SNR is clearly detected by *Herschel* in Figure 2.25 as a shell of dust emission similar to that detected by Reach et al. (2006) and Pinheiro Goncalves et al. (2011). Detection of H_2 emission suggests that this SNR is interacting with molecular clouds (Andersen et al., 2011) and Reach et al. (2006) suggested that MIR emission is from shocked gas. At 70 µm the FIR shell is brightest along the south west ridge, especially near $\alpha = 14^{h}05^{m}22^{s}, \delta = -61°58'06''$. However in the longer wavelength *Herschel* images the brightest emission is towards the eastern and south-eastern edge of the shell. Like Reach et al. (2006) we detect bright sources near $\alpha = 14^{h}05^{m}24.3^{s}, \delta =$

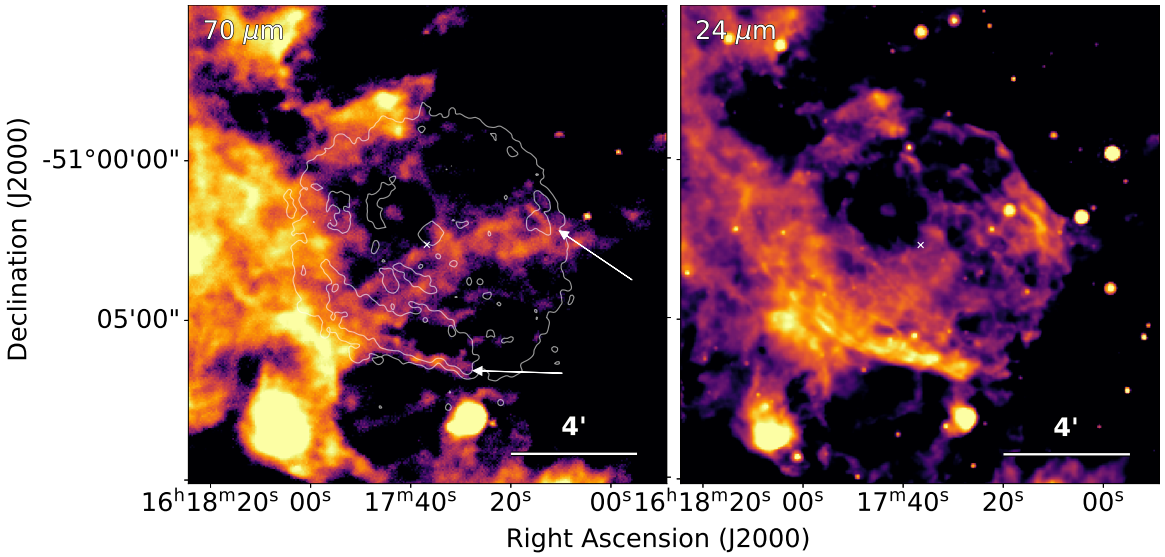

Figure 2.26: RCW 103, G332.4−0.4 - *Left*: *Herschel* 70 µm image with X-ray contours overlaid. An arc of dust in the south coincides with X-ray structure and filaments to the north-west correspond with dust emission at 24 µm, as indicated by the arrows. *Right*: *Spitzer* MIPS 24 µm image. The white cross shows the X-ray coordinates of the SNR centre.

$-61°57'07''$ and $\alpha = 14^h05^m23.5^s, \delta = -61°56'58''$, although at the *Herschel* resolution these two sources are unresolved.

RCW 103, G332.4−0.4 (Figure 2.26): This shell-type remnant is at a distance of ∼3.1 kpc and the expansion velocity suggests an age of around 2000 yrs (Carter et al., 1997). The associated compact central object, 1E 161348-5055, which does not have a detected PWN (e.g. Tuohy & Garmire, 1980; Reynoso et al., 2004) is most likely a magnetar with an extremely long period of 6.67 hrs (Rea et al., 2016). X-ray emission across the SNR is dominated by shocked CSM with weaker emission from metal-rich ejecta and has been suggested to have had a $\sim 18-20 M_\odot$ progenitor with high mass-loss rate (Frank et al., 2015). The SNR is interacting with a molecular cloud on its southern side (Oliva et al., 1990, 1999).

There is a $\sim 1.7'$ rim of 70 µm emission along the southern edge of the SNR in Figure 2.26, near $\alpha = 16^h17^m36^s, \delta = -51°06'13''$, which is undetected in the other *Herschel* bands. This coincides with X-ray and MIR structure detected by Reach et al. (2006) and Pinheiro Goncalves et al. (2011) and is at a higher temperature than FIR structures to the east. The more resolved IRAC image suggests that this region consists of two emitting areas dominated by ionic and molecular shocks.

G337.2−0.7: Pinheiro Goncalves et al. (2011) detected 24 µm emission from

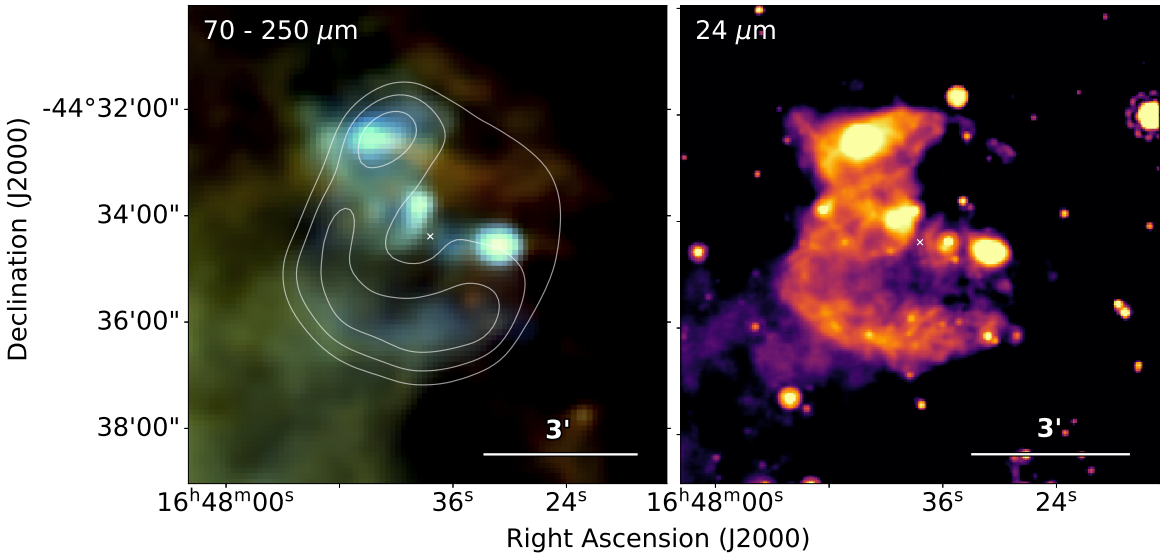

Figure 2.27: G340.6+0.3 - *Left*: *Herschel* three colour image. A shell of dust correlates is seen which is brightest along the southern edge. *Right*: *Spitzer* MIPS 24 µm image. Overlaid contours are radio MOST (white) and *Chandra* (cyan). The white cross shows the X-ray coordinates of the SNR centre.

filaments in this SNR which form two shell type features, corresponding to X-ray structure. Although there is some emission at 70 µm (Figure A.2) it is unclear whether this is associated with the SNR. There is a FIR region to the north-east coinciding with 24 µm emission, however this does not correspond to the X-ray structure and it is unlikely to be associated with the SNR.

G340.6+0.3 (Figure 2.27): This shell-type SNR is at a distance of 15 kpc, on the other side of the Galaxy (Kothes & Dougherty, 2007). Like Pinheiro Goncalves et al. (2011), we detect a shell of dust, as seen in Figure 2.27, which correlates with the 1.4 GHz radio shell (Caswell et al., 1983a). This emission is not seen in the IRAC wavebands (Figure A.2); some MIR emission is detected in the region but is not clearly associated with the SNR.

G344.7−0.1 (Figure 2.28): This relatively young SNR (∼3000 yrs) has an estimated distance of 14 kpc (Yamaguchi et al., 2012) and is classified as a mixed-morphology remnant, having thermal X-ray emission which completely fills the radio shell (Yamauchi et al., 2005; Combi et al., 2010a; Giacani et al., 2011). The radio emission is brightest towards the north-western side where the remnant is expected to be interacting with a molecular cloud (Combi et al., 2010a). Strong Fe K-shell ejecta emission and the abundance pattern of α-elements suggests that this is a Type Ia SNR (Yamaguchi et al., 2012). The SNR contains a large mass of

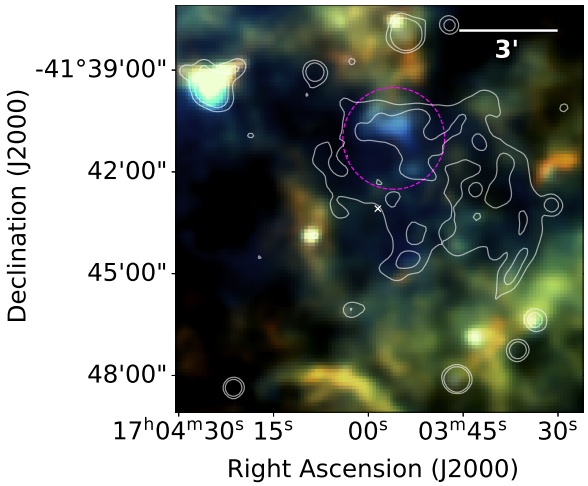

Figure 2.28: G344.7−0.1 - *Herschel* three colour image. A region of dust emission is detected to the north of the remnant (within the magenta circle), centred at $\alpha = 17^{h}03^{m}55^{s}, \delta = -41°40'43''$. MIPS 24 µm contours are overlaid. The white cross shows the X-ray coordinates of the SNR centre.

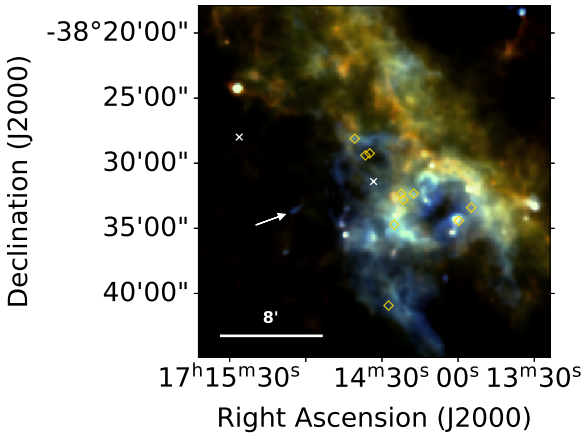

Figure 2.29: G348.5−0.0 and CTB 37A, G348.5+0.1 - *Herschel* three colour image. The diamonds indicate the locations of OH 1720 MHz masers (Frail et al., 1996). Dust emission from G348.5−0.0 is detected as indicated by the arrow, and emission from CTB 37A is detected along the north-western edges of the remnant. The white crosses show the radio and X-ray coordinates of the centres of G348.5−0.0 (north-east) and G348.5+0.1 (south-west) respectively.

hydrogen ($\gtrsim$150 $M_{\odot}$) which implies that the SNR is dominated by swept up ISM.

Reach et al. (2006) detected an irregular MIR structure to the north of the SNR originating from shocked ionised gas, which coincides with a central radio peak (Giacani et al., 2011). We also detect FIR emission from this structure in Figure 2.28, centred at $\alpha = 17^{h}03^{m}55^{s}, \delta = -41°40'43''$, although the *Herschel* detection is less resolved. It is likely that this emission arises from the interaction between the SN shock and a molecular cloud in front of the SNR (Giacani et al., 2011).

G345.7−0.2: This SNR has a faint disk radio morphology and a peak close to the pulsar PSR J1707-4053, which is probably unrelated (Taylor et al., 1993; Whiteoak & Green, 1996). We detect a diffuse region of 70 µm emission (Figure A.2) centred at $\alpha = 17^{h}07^{m}39^{s}, \delta = -40°54'31''$, extending roughly 2′ which correlates with MIPS 24 µm and 0.843 GHz radio emission (Whiteoak & Green, 1996). We find no other evidence of SNR-related emission in the region. We suggest that the SNR centre is offset from that of Green (2014) and the bar detected could be part of a

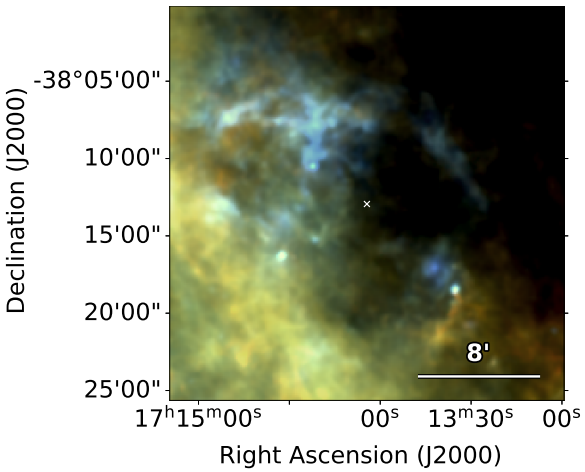

Figure 2.30: CTB 37B, G348.7+0.3 - *Herschel* three colour image. Dust emission is detected in a partial shell structure around the northern edge of the remnant. The white cross indicates the X-ray coordinates of the SNR centre.

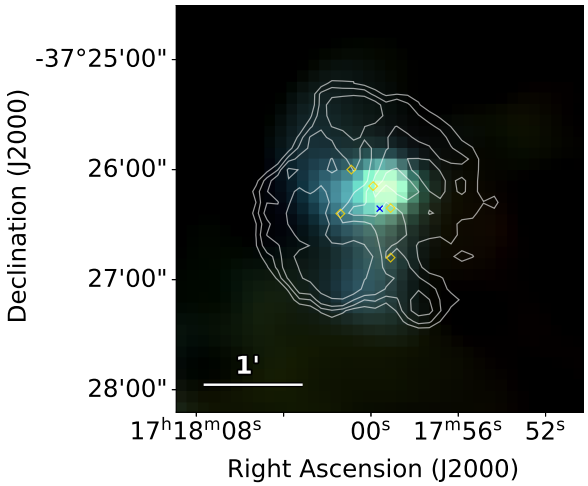

Figure 2.31: G349.7+0.2 - *Herschel* three colour image with X-ray contours overlaid. The five OH masers are indicated by diamonds (Frail et al., 1996). Dust emission is observed at the western edge, where the remnant is interacting with a dense cloud. The blue cross shows the X-ray coordinates of the SNR centre.

structure extending to the east.

G346.6−0.2: Reach et al. (2006) detected a narrow rim of emission connecting three OH 1720 MHz masers along the southern shell. There is FIR emission which potentially corresponds to this structure (Figure A.2), however the region is very confused as there is extensive dust emission to the north and west of the SNR.

G348.5−0.0 (Figure 2.29): Originally thought to be a jet associated with CTB 37A, this was classified by Kassim et al. (1991) as a separate partial shell remnant. HI 21-cm absorption measurements suggest that this remnant is at a distance of $\leq$6.3 kpc (Tian & Leahy, 2012). In Figure 2.29 we detect a $\sim$1.7′ arc of dust emission centred at $\alpha = 17^{\rm h}15^{\rm m}03.5^{\rm s}, \delta = -38°33'30''$. This is detected across all *Herschel* wavebands, although is very confused for $\lambda > 160\,\mu$m. Reach et al. (2006) suggested that this MIR emission is dominated by emission lines from shocked gas.

The OH 1720 MHz masers at $\alpha = 17^{\rm h}14^{\rm m}34.8^{\rm s}, \delta = -38°29'16''$ and $\alpha = 17^{\rm h}14^{\rm m}36.5^{\rm s}, \delta = -38°29'25''$ have a significantly different velocity to the other eight in the region which are associated with CTB 37A (Frail et al., 1996). It is suggested that these two are related to a nearby molecular cloud (Reynoso & Mangum,

2000) lying to the west of G348.5−0.0 with which the remnant is likely to be interacting. We do not detect FIR emission at the location of these masers.

CTB 37A, G348.5+0.1 (Figure 2.29): Recently classified as a mixed morphology remnant (Sezer et al., 2011; Yamauchi et al., 2014b), this SNR has a radio shell-like structure in the north and a "breakout" to the south-west, and has thermally dominated central X-ray emission. At a distance in the range of 6.3 – 9.5 kpc, its proximity to both G348.5−0.0 and CTB 37B is coincidental (Tian & Leahy, 2012). There are eight OH 1720 MHz masers associated with the SNR which have a similar velocity to incident CO (1–0) clouds detected by Reynoso & Mangum (2000) which are to the north-west and centre of the SNR.

The *Herschel* emission in Figure 2.29 is very confused. Similar to Reach et al. (2006), we detect dust emission along the northern edge in a $\sim 4.3'$ arc centred at $\alpha = 17^{h}14^{m}35^{s}, \delta = -38°28'22''$ and filaments along the western edge near to $\alpha = 17^{h}14^{m}46^{s}, \delta = -38°32'33''$. Emission in the northern region coincides with an OH 1720 MHz maser and is suggested by Reach et al. (2006) to originate from shocked molecular gas where the SNR has encountered very dense gas. We also detect dust emission in the region of the "breakout" structure to the south of the SNR.

CTB 37B, G348.7+0.3 (Figure 2.30): This relatively young (∼4900 yrs, HESS Collaboration, 2008a) SNR has a non-thermal radio shell (Whiteoak & Green, 1996) and a magnetar which is slightly off-centre (Halpern & Gotthelf, 2010). 21 cm HI absorption indicates a distance of ∼13.2 kpc (Tian & Leahy, 2012).

The region around the SNR is confused due to bright emission from IR bubbles at $\alpha = 17^{h}14^{m}38.2^{s}, \delta = -38°10'18''$ and $\alpha = 17^{h}13^{m}40.3^{s}, \delta = -38°17'33''$. We detect dust emission in Figure 2.30 around the northern edge of the SNR which coincides with the radio structure and is at a higher temperature than the surrounding medium.

G349.7+0.2 (Figure 2.31): The radial velocities of OH 1720 MHz masers suggest that this shell-type SNR is at a large distance of $\sim$ 22 kpc (Frail et al., 1996), making it one the most X-ray luminous Galactic remnants (Slane et al., 2002). X-ray temperature fits give an age of ∼2800 yrs. The presence of OH 1720 MHz masers and shocked molecular gas imply that the SNR is interacting with a molecular cloud. The MIR SNR shell is much brighter to the eastern side where a shock is propagating into the edge of a roughly cylindrical cloud (Reach et al., 2006). Like the MIR, the FIR emission in Figure 2.31 peaks in the region of the OH 1720 MHz

masers, near $\alpha = 17^{h}18^{m}00^{s}, \delta = -37^{\circ}26'09''$.

2.2 CONCLUSIONS

We follow Reach et al. (2006) and Pinheiro Goncalves et al. (2011) who previously studied dust in Galactic SNRs using MIR emission, and search for FIR structures and potentially cooler dust emission using *Herschel* images. We classify SNRs as levels 1 – 4 where level 1 is a detection (FIR emission which is clearly correlated with radio, MIR, or X-ray structures and can be distinguished from ISM) and level 4 is not detected in the FIR. From our sample of 71 sources, we add 27 new SNRs to the current sample of four (Cas A, Crab, Kepler, and Tycho) in our Galaxy that contain cool dust (<50 K) associated with the SNR. This is a lower limit to the number of dusty SNRs in our sample as we suffer from a number of biases, such as confusion with cool ISM and reliance on previous detections in other wavebands, which make more evolved, cooler, and/or fainter SNRs more difficult to detect.

We show that dust is detected from the central region of 8 sources, one of which was recently discussed elsewhere (Temim et al., 2017; Rho et al., 2018) and three of which (G11.2−0.3, G21.5−0.9, and G29.7−0.3) are *new detections of FIR emission coinciding with the locations of pulsar wind nebulae.*

CHAPTER 3
DUSTY PULSAR WIND NEBULAE

'The most exciting phrase to hear in science, the one that heralds the most discoveries, is not 'Eureka!' but 'That's funny'...'

ISAAC ASIMOV

In Chapter 2 we discovered dust emission in the central regions of three pulsar wind nebulae (PWNe), G11.2−0.3, G21.5−0.9, and G29.7−0.3. In this Chapter, we derive dust masses and temperatures for these three PWNe using traditional modified blackbody fits to the FIR and submm spectral energy distributions and also by using a more advanced technique (PPMAP) to derive dust masses and investigate dust properties. This work has been published in Chawner et al. (2019).

3.1 THE MASS OF DUST IN G11.2−0.3, G21.5−0.9, AND G29.7−0.3

3.1.1 FLUXES OF G11.2−0.3, G21.5−0.9, AND G29.7−0.3

To estimate the mass of dust within G11.2−0.3, G21.5−0.9, and G29.7−0.3, we must first measure the flux. The flux density for the central region (PWN) of each SNR was estimated using aperture photometry on MIR – FIR images from *Spitzer* MIPS (24 μm) and *Herschel*. The IRAC images are not used as we do not see emission from the SNRs in the region of the PWN in these wavebands and the measured emission is dominated by unrelated point sources. Apertures of

Wavelength, μm	Flux Density, Jy		
	G11.2−0.3	G21.5−0.9	G29.7−0.3
24	5.6 ± 0.3	0.19 ± 0.02	0.20 ± 0.03
70	47.7 ± 6.7	4.1 ± 0.3	5.6 ± 1.0
160	71.9 ± 15.7	6.6 ± 0.7	3.2 ± 4.0
250	26.6 ± 5.5	3.0 ± 0.9	0.55 ± 2.10
350	10.1 ± 3.0	1.5 ± 0.8	0.19 ± 1.15
500	2.3 ± 0.9	1.2 ± 0.4	0.02 ± 0.20

Table 3.1: Background subtracted flux measured for each SNR at FIR wavelengths.

1.9′, 1.7′, and 1.2′ in diameter were centred at $\alpha = 18^{h}11^{m}29^{s}, \delta = -19°25'54''$, $\alpha = 18^{h}33^{m}34.2^{s}, \delta = -10°34'18.5''$, and $\alpha = 18^{h}46^{m}25^{s}, \delta = -02°58'30''$ for G11.2−0.3, G21.5−0.9, and G29.7−0.3 respectively.

The background ISM level for G21.5−0.9 was estimated using an annulus around the source as the local environment seems reasonably uncluttered. For G11.2−0.3 and G29.7−0.3, eight apertures were placed around the SNRs so as to avoid the shell and the bright cloud to the south of G11.2−0.3, and to avoid the young stellar object to the west of G29.7−0.3. Areas were selected to cover a range of flux levels to account for fluctuations in the ISM within the image cut-out. The background-subtracted flux densities are given in Table 3.1. Due to large variations in the ISM level, the background subtraction is the largest source of uncertainty in our estimation of dust mass.

Flux calibration uncertainties are assumed as a percentage of the measured flux in each band; that is 4% for MIPS (Engelbracht et al., 2007), 7% for PACS (Balog et al., 2014), and 5.5% for SPIRE data (Bendo et al., 2013). Uncertainty in the ISM level is estimated as the standard deviation of the background ISM values; both of these uncertainties are added in quadrature.

3.1.2 Accounting for Synchrotron Emission

A power-law synchrotron radiation spectrum, from charged particles accelerated in a magnetic field, can be detected across the electromagnetic spectrum. The contribution varies across SNR type. PWNe and Crab-like remnants tend to have a very flat radio spectrum and a steeper X-ray spectrum due to synchrotron losses, whereas shell-type SNRs have a much steeper radio spectrum.

In order to estimate the dust mass, first non-thermal synchrotron emission must be removed from the IR fluxes. The synchrotron flux density at a frequency, ν, can be fitted by equation 3.1,

$$S_\nu = S_{\nu_0} \left(\frac{\nu}{\nu_0} \right)^{\alpha} \tag{3.1}$$

where S_{ν_0} is the synchrotron flux density at frequency ν_0, and α is the spectral index which describes the flux density dependence on frequency. We use a least squares fitting routine to estimate α. Like the Crab Nebula, the power law slope may break in the FIR region (e.g. Arendt et al., 2011; Gomez et al., 2012b), in which case we would be overestimating the synchrotron contribution to the MIR and FIR fluxes.

The uncertainty in α is estimated using a Monte Carlo technique by producing 1000 sets of normally distributed radio flux values, using the measured flux at each frequency as mean and flux uncertainty as standard distribution. Fitting a power law to each set gives 1000 values of α and the standard deviation is used as the uncertainty in the estimated value.

The integrated synchrotron flux values for the SNR PWN regions and spectral index from the fit are given in Table 3.2. A least squares fit to G11.2−0.3 radio data (Kothes & Reich, 2001) of the central compact object gives a spectral index of $\alpha = -0.10 \pm 0.08$. A single power law cannot fit the spectra for G21.5−0.9 (Salter et al., 1989b) as the slope breaks at 40 GHz due to synchrotron losses. Fitting to radio data between 70 and 143 GHz (Salter et al., 1989b; Salter et al., 1989a; Planck Collaboration XXIX, 2016), *Spitzer* MIPS (24 μm) and *Herschel* (500 μm) data, gives a spectral index of $\alpha = -0.53 \pm 0.01$. Whereas at lower frequencies (Morsi & Reich, 1987; Bietenholz & Bartel, 2008), the fitting routine gives a flat spectral index of $\alpha = -0.032 \pm 0.034$. A least squares fit to radio data of the Crab-like component of G29.7−0.3 (Salter et al., 1989b) gives a spectral index of $\alpha = -0.43$. It has been suggested that there may be a spectral break at around 55 GHz (Bock & Gaensler, 2005), in which case our synchrotron flux in FIR wavebands will be overestimated.

The synchrotron contribution to the SNR SEDs is only significant for G21.5−0.9, for which it contributes between 9.5 and 96.7 per cent (160 and 500 μm respectively) of the background subtracted flux at each wavelength. For G29.7−0.3, the contribution at 500 μm is $\sim$ 59 per cent, however for the other wavebands it is less than 9 per cent, and for G11.2−0.3 the contribution in all wavebands is less than 3.5 per cent.

SNR	Frequency (GHz)	Flux (Jy)	Ref	Spectral Index [a]	Wavelength (μm)	Estimated Synchrotron Flux (Jy)[b]
G11.2−0.3	1.4	0.11 ± 0.02	1	-0.10 ± 0.08	24	$(43 \pm 40) \times 10^{-3}$
	32	0.08 ± 0.02	1		70	$(46 \pm 44) \times 10^{-3}$
					160	$(48 \pm 44) \times 10^{-3}$
					250	$(50 \pm 44) \times 10^{-3}$
					350	$(51 \pm 44) \times 10^{-3}$
					500	$(52 \pm 43) \times 10^{-3}$
G21.5−0.9	327×10^{-3}	7.3 ± 0.7	2	-0.032 ± 0.038	24	0.23 ± 0.05
	1.43	7.0 ± 0.4	2		70	0.40 ± 0.08
	5	6.7 ± 0.3	3		160	0.63 ± 0.13
	32	5.6 ± 0.3	4	-0.56 ± 0.02	250	0.80 ± 0.16
	70	4.3 ± 0.6	5		350	0.95 ± 0.18
	84.2	3.9 ± 0.7	6		500	1.16 ± 0.22
	90.7	3.8 ± 0.4	7			
	100	2.7 ± 0.5	5			
	141.9	2.5 ± 1.2	7			
	143	3.0 ± 0.4	5			
G29.7−0.3	1.4	0.35	6	-0.43	24	9.64×10^{-3}
	4.9	0.25	6		70	15.2×10^{-3}
	5.0	0.28	8		160	21.7×10^{-3}
	15	0.17	6		250	26.3×10^{-3}
	89	0.08	9		350	30.4×10^{-3}
					500	35.4×10^{-3}

Table 3.2: [a] Estimated by fitting a power law to the radio fluxes on the same line and below. [b] Synchrotron flux estimated by extrapolating the fitted power law to FIR wavelengths. Radio fluxes for the core are taken from: [1] Kothes & Reich (2001); [2] Bietenholz et al. (2011); [3] Bietenholz & Bartel (2008); [4] Morsi & Reich (1987); [5] Planck Collaboration XXXI et al. (2016); [6] Salter et al. (1989b); [7] Salter et al. (1989a); [8] Becker & Helfand (1984); [9] Bock & Gaensler (2005).

3.1.3 Dust Emission

After removing the synchrotron contribution from the SNR SEDs, we assume that the remaining thermal MIR-FIR flux takes the form of a modified blackbody (see Chapter 1, Section 1.4). We fit the spectral energy distribution from 24 – 500 µm using Equations 1.18 and 1.20 with a least-squares fit, assuming that the dust absorption coefficient κ_ν follows a power law with emissivity index of $\beta = 1.9$ (indicative of normal interstellar dust grains; Planck Collaboration XIV, 2014) where $\kappa_{\lambda_0} = 0.07 \pm 0.02\,\mathrm{m^2 kg^{-1}}$ for $\lambda_0 = 850\,\mu$m (Dunne et al., 2000; James et al., 2002; Clark et al., 2016). We attempt both a single and double temperature modified blackbody fit. In order to derive physical estimates, the temperature and mass are constrained: a cold dust component must have a temperature of $15 < T_c < 50$K, a warm component must have a temperature of $50 < T_w < 150$K. We assume distances of 4.4 kpc (Green, 2004), 4.7 kpc (Camilo et al., 2006), and 10.6 kpc (Su et al., 2009) for G11.2−0.3, G21.5−0.9, and G29.7−0.3 respectively. [1] The best fit SEDs for all three PWNe are shown in Figures 3.1 to 3.2.

The 1-σ uncertainties in the derived mass and temperature are estimated in a similar way to the uncertainty in α in section 3.1.2. A modified blackbody is fit to 1000 sets of flux values to give distributions of dust mass and temperature estimates. The uncertainties in the fit parameters are taken as the 16th and 84th percentiles. The largest source of uncertainty is the background subtraction; there is a large variation in the ISM level across the regions surrounding the SNRs making an estimate of the ISM contribution very uncertain. The best fit and median values derived for dust temperature and mass are shown in Table 3.3.

G11.2−0.3: We find that the thermal FIR emission between 24 and 350 μm for this SNR is best described by the sum of two modified blackbodies with best-fit parameters for the cold temperature $T_c = 27.3$ K, and warm temperature $T_w = 180$ K. The cold component requires a best-fit mass of $M_d = 0.9\,M_\odot$ and the warm component requires a mass of $M_d = 7.9 \times 10^{-6}\,M_\odot$, as seen in Figure 3.1.

There is large uncertainty in the mass and temperature of the warmer dust component as this peak mostly depends on the 24 μm flux. This makes the position of the SED peak extremely uncertain, giving a wide range of possible temperatures and masses. The Monte Carlo method gives a skewed distribution of possible

[1] There are various approaches that can be take to determine the distance of an SNR, which can give varying results. Estimates of dust mass are in turn sensitive to the assumed distance, such that increasing the assumed distance by a factor of two will provide a dust mass estimate which is four times as large.

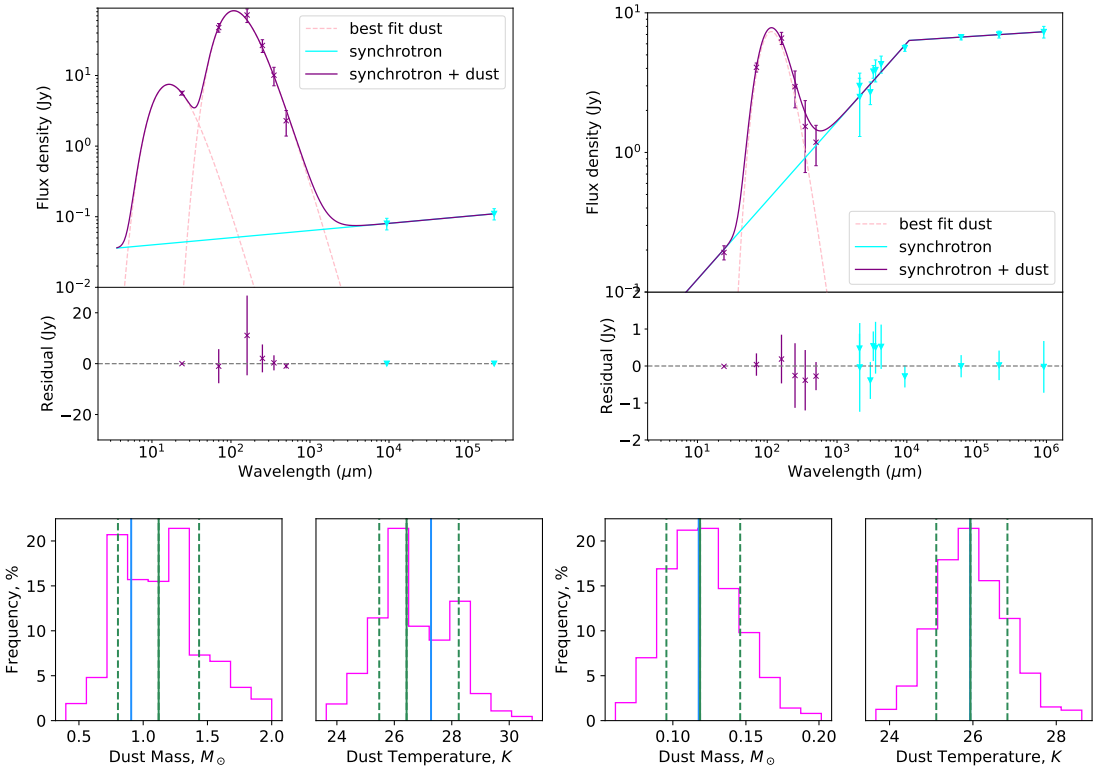

Figure 3.1: *Top*: FIR SED of *Left:* G11.2−0.3 and *Right:* G21.5−0.9. The dashed pink lines are single temperature components fit to the FIR fluxes. The solid cyan line is the synchrotron component fit to the radio flux of the compact object (cyan points). The solid purple line is the total SED of all components. *Bottom*: The distribution of source masses obtained by the Monte Carlo routine, fitting SEDs to 1000 normally distributed samples of flux values for *Left:* G11.2−0.3 and *Right:* G21.5−0.9. The dashed green lines indicate 1 σ uncertainties, the solid green line is the median value, and the solid blue line is the best fit value. The best fit and median values derived for dust temperature and mass are shown in Table 3.3.

values for the cold dust mass and temperature. There is a tail of high dust masses, skewing the median to values > 1 $M_\odot$.

G21.5−0.9: We find that the global thermal emission in this SNR is well described by a single temperature dust component with a best-fit temperature of T = 25.9 K and best-fit mass of $M_d = 0.12\,M_\odot$ as seen in Figure 3.1. The Monte Carlo method gives roughly Gaussian-shaped distributions of dust masses and temperatures and the result from this analysis is in agreement with the best fit result.

G29.7−0.3: The thermal emission in this SNR can be fitted by a single temperature dust component with a best-fit temperature of T = 45.7 K and dust mass of $M_d = 0.03\,M_\odot$ as seen in the top panel of Figure 3.2. There is a large difference in

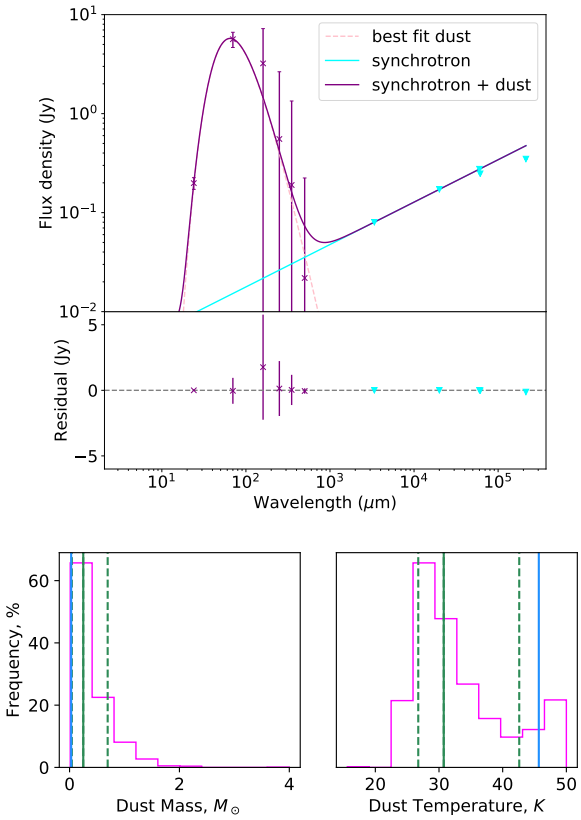

Figure 3.2: *Top*: FIR SED of G29.7−0.3. *Bottom*: The distribution of source masses obtained by the Monte Carlo routine, fitting SEDs to 1000 normally distributed samples of flux values. The colour schemes are the same as for Figure 3.1. The best fit and median values derived for dust temperature and mass are shown in Table 3.3.

the ISM flux level between the north and south of this remnant making it difficult to obtain an accurate value for the ISM level, as indicated by the large error bars in the SNR fluxes. At wavelengths longer than 70 μm the error bars indicate that a dust mass cannot be determined as the source flux is at a similar level to that of the ISM. The median dust temperature from the Monte Carlo analysis is low compared to that of the best fit, resulting in a larger estimate for the dust mass. This discrepancy is caused by large uncertainty in the flux at long wavelengths, as indicated by the error bars in Figure 3.2. A large fraction of the simulated fluxes at long wavelengths are much greater than the measured value, forcing the SED to peak at a longer wavelength. Therefore the Monte Carlo analysis is unable to give a constrained dust mass in these cases, although we clearly detect SN dust at a warmer temperature than the local ISM. This will be revisited in Section 3.1.4 where the dust temperature and mass will be analysed with a more rigorous routine.

		Best Fit[a]				Monte Carlo Median[b]				PPMAP[c]
	Distance	Cold dust		Warm dust		Cold dust		Warm dust		Cold Dust
SNR	(kpc)	T_d	M_d	T_d	M_d	T_d	M_d	T_d	M_d	M_d
G11.2−0.3	4.4 [1]	27.3	0.9	180	7.9×10^{-6}	$26.7^{+1.7}_{-1.3}$	$1.1^{+0.4}_{-0.3}$	$92.4^{+87.6}_{-12.7}$	$(2.2^{+3.5}_{-2.1}) \times 10^{-4}$	0.34 ± 0.14
G21.5−0.9	4.7 [2]	25.9	0.12	–	–	26.0 ± 0.7	0.12 ± 0.02	–	–	0.29 ± 0.08
G29.7−0.3	10.6 [3]	45.7	0.03	–	–	$30.7^{+11.7}_{-4.0}$	$0.3^{+0.4}_{-0.2}$	–	–	0.51 ± 0.13

Table 3.3: Source distances are from: [1]the near distance from HI absorption(Green, 2004); [2]HI and CO observations (Camilo et al., 2006); [3]the kinematic distance of an associated molecular cloud (Su et al., 2009). Dust temperature (K) and mass ($M_\odot$) values are derived from: [a] a least squares SED fit to the data; [b] median results from a Monte Carlo routine as described in Section 3.1; [c] the PPMAP analysis as described in Section 3.1.4, where we do not assume a single dust temperature.

.

3.1.4 Analysing the dust properties with point process mapping (PPMAP)

In Section 3.1 we estimated approximate dust masses and temperatures for our three PWNe. However, this was assuming a uniform dust temperature and fixed emissivity index of 1.9, and required us to convolve all of the images to a common resolution set by the longest *Herschel* waveband. Next we employ PPMAP, as described in Section 1.5.2, to analyse a wider range of dust properties, including β, dust temperatures and mass at a high resolution. We apply PPMAP to study G11.2−0.3, G21.5−0.9, and G29.7−0.3 using the 24 – 500 μm maps, and compare with the surrounding ISM for which we use only the *Herschel* maps due to potential issues with optical thickness, discussed in more detail later.

The PPMAP procedure is applied to estimate the column density over a grid of 12 temperature bins, centred at temperatures equally spaced in $\log(T_D)$, and up to 7 values of β between 0 and 3 (Marsh et al., 2015). As the PWN dust has best-fit modified blackbody temperatures of > 25 K, we initially use a temperature grid ranging from 25 to 75 K. If there is emission from components outside of this temperature range, PPMAP will return higher column density at the bounding temperatures. We therefore repeat the analysis extending our temperature range (20 – 90 K) to search for cooler and warmer components. For this study a Gaussian prior is assumed for distribution of material across β, with a mean of 1.9 (Planck Collaboration XXXI et al., 2016) and standard deviation of 0.25.

We estimate the cool dust mass of each SNR by summing the column density within the apertures described in Section 3.1 across the entire temperature and β grids. By averaging the temperature maps, PPMAP allows the amount of dust column density for each β value to be determined. After summing the differential column density over temperature, we obtain the density-weighted mean β along each line of sight.

3.1.5 Revised dust masses for our three PWNe

The column density map of dust emission at each of the temperature grid points from PPMAP are shown in Figures 3.3-3.5 for the three SNRs, G11.2−0.3, G21.5−0.9, and G29.7−0.3. Prior to running the PPMAP analysis, an average ISM level is subtracted from the SNRs. This is estimated from annuli around the SNRs, as shown in Figure 3.6, which are sigma-clipped to remove especially bright objects. The dust mass within each PWN is estimated by aperture photometry on the

column density maps. This involves a second background subtraction, again using an average level from the annuli in Figure 3.6, to ensure that there is minimal ISM contributing to our estimate. Figure 3.7 shows the total SED for each remnant and the contribution from each temperature component, as estimated by PPMAP.

G11.2−0.3: In Figure 3.3 we can see that the SNR is indistinguishable from the surrounding ISM at 25 K highlighting the difficulty in removing ISM emission where the temperatures are similar to dust in the ISM. Dust in the central region is brightest between 34 and 41 K and is not detected above 46 K.

By contrast, there is evidence of two temperature components in the shell as we find that there is dust at 28 – 41 K and at 75 K. The tightly bound inner shell could indicate that the warmer shell dust may be reverse-shock heated, as seen in Cassiopeia A (Rho et al., 2008). However, it is thought that the reverse shock has already reached the centre of this remnant and expansion into an anisotropic CSM has caused the sharpness of the shell's inner edge (Borkowski et al., 2016) so it is unclear what is heating the shell dust. The dust structures are clearly seen when combining three of the temperature maps from Figure 3.3 (31, 41, and 75 K) to produce a 'super-resolved' colour image in Figure 3.6 (top panel). The dust emission from the PWN towards the centre is very clear in this image compared to the three-colour image derived using the native *Herschel* maps (Figure 2.6) as the PPMAP results match the best available *Herschel* angular resolution i.e. 6.4″ from the 70μm images (Traficante et al., 2011).

The PPMAP generated SED for G11.2−0.3 in Figure 3.7 shows how some of the temperature components revealed using PPMAP contribute to the total SED (here we show the full range investigated using PPMAP i.e. 20-90 K). We can see that the 20-23 K component contributes a significant amount of the total FIR flux measured in the apertures even after background subtracting the ISM. Since we have previously discussed that the PPMAP dust structures seen at temperatures of 20-25 K for this source are likely unrelated to the supernova, we therefore subtract these colder dust components from the final PPMAP derived dust mass. The dust mass is therefore derived by summing the column densities at the range of temperatures where SNR-related emission is seen, providing an estimated dust mass for the central ejecta region of G11.2−0.3 of $M_d = 0.34 \pm 0.14\,M_\odot$ (Table 3.3).[2]

This dust mass estimate is considerably smaller than the the traditional

[2] If we were to include the PPMAP dust components at temperatures below 25 K, the dust mass for G11.2−0.3 would be $M_d = 0.50 \pm 0.22\,M_\odot$.

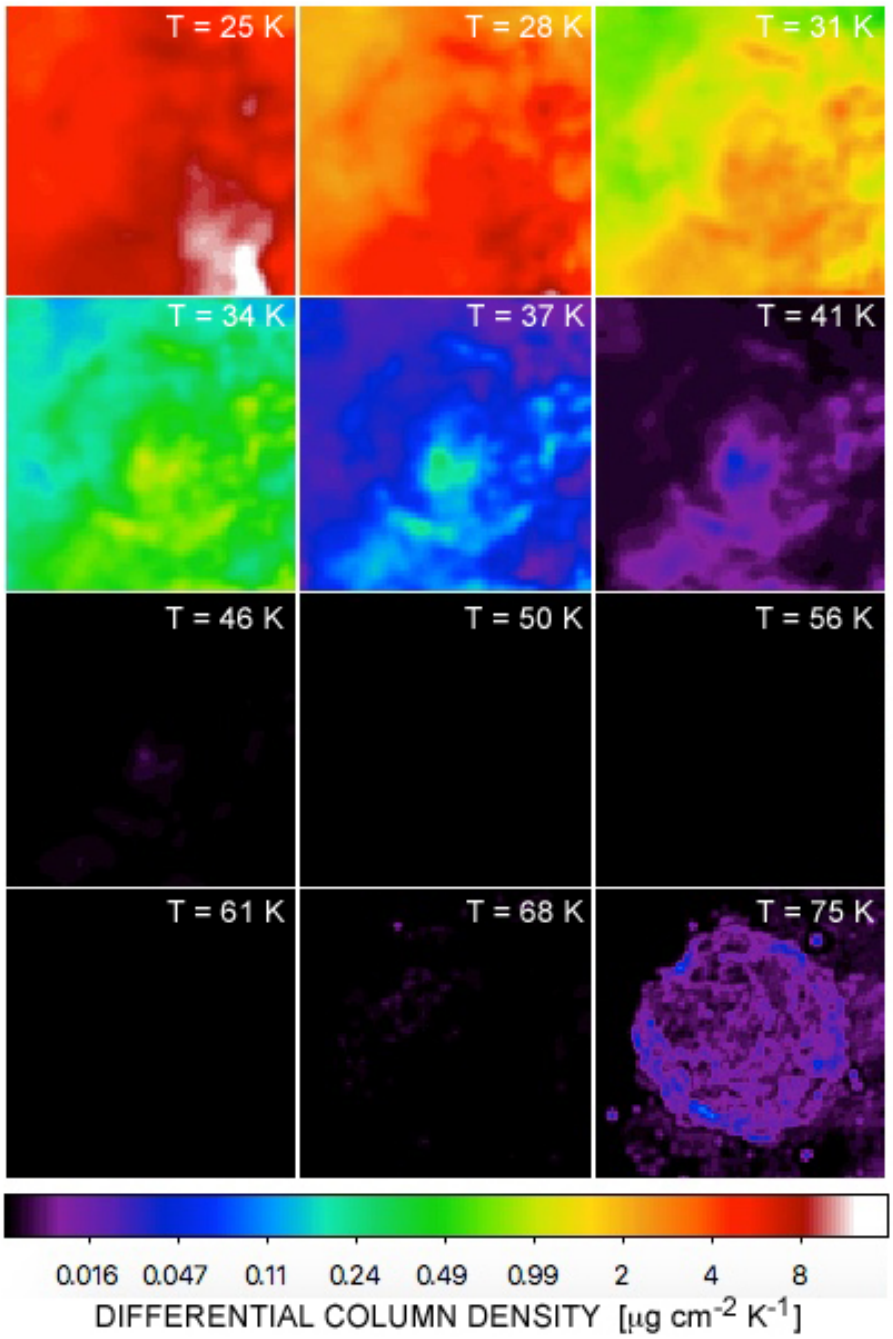

Figure 3.3: PPMAP generated maps of differential dust column density split in different temperature ranges for G11.2−0.3. The corresponding dust temperature is indicated in the top-right of each panel. At temperatures less than 25 K in G11.2−0.3, the column density map begins to be dominated by unrelated interstellar dust along the line of sight and thus temperatures below 25 K for these sources are not used in the analysis.

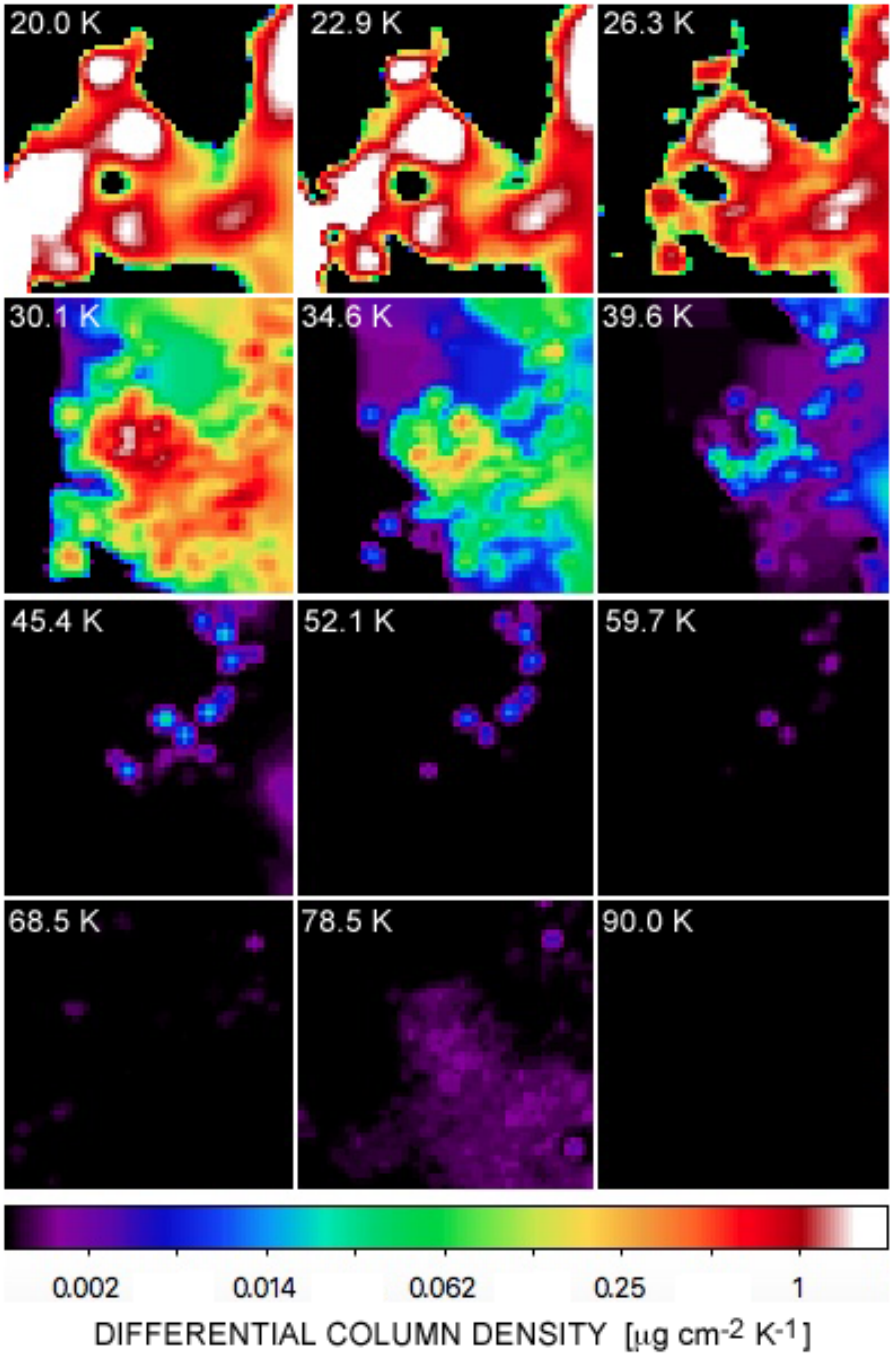

Figure 3.4: PPMAP generated maps of differential dust column density split in different temperature ranges for G21.5−0.9. The corresponding dust temperature is indicated in the top-right of each panel.

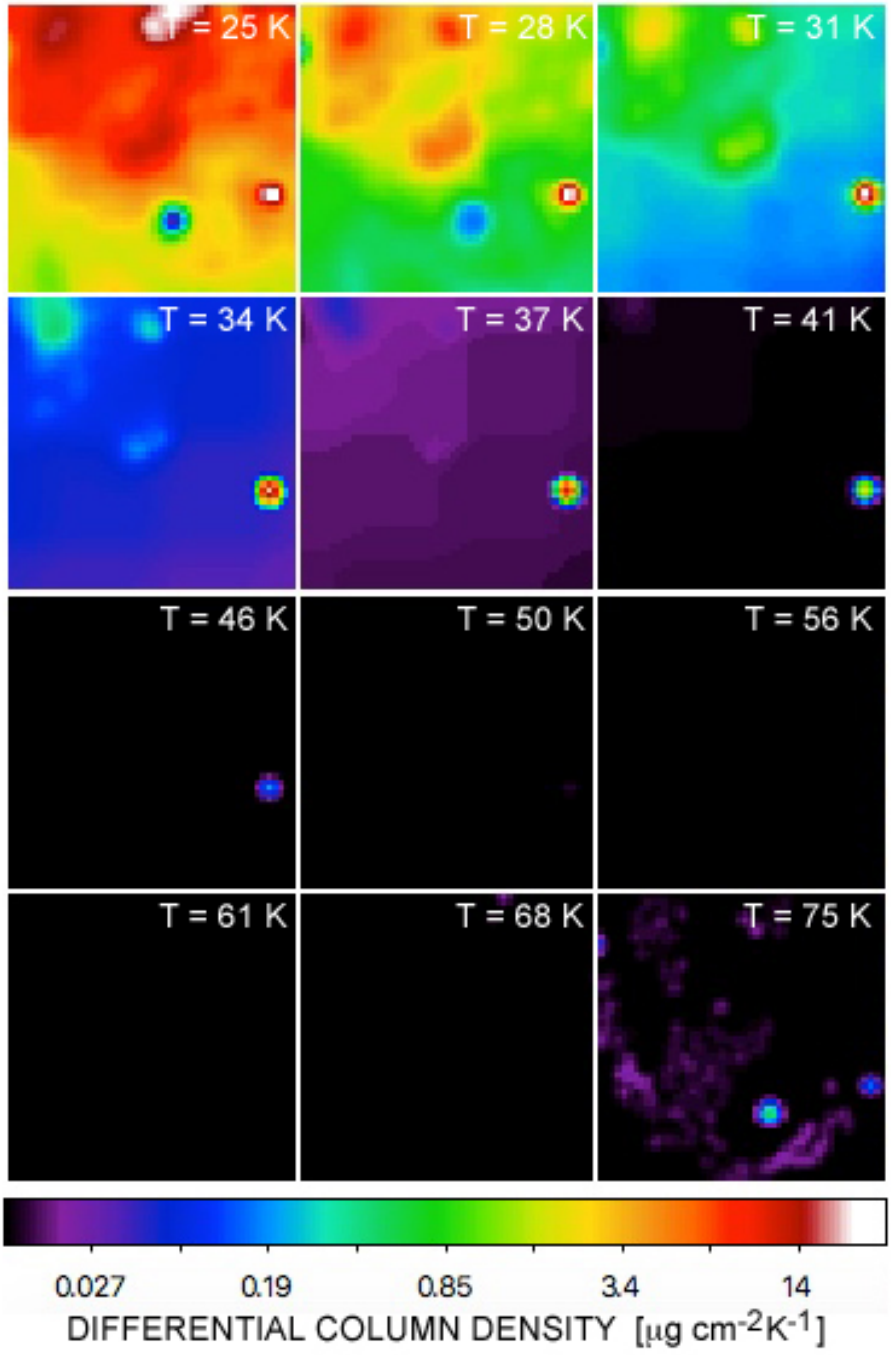

Figure 3.5: PPMAP generated maps of differential dust column density split in different temperature ranges for G29.7−0.3. The corresponding dust temperature is indicated in the top-right of each panel. At temperatures less than 25 K in G29.7-0.3, the column density map begins to be dominated by unrelated interstellar dust along the line of sight and thus temperatures below 25 K for these sources are not used in the analysis.

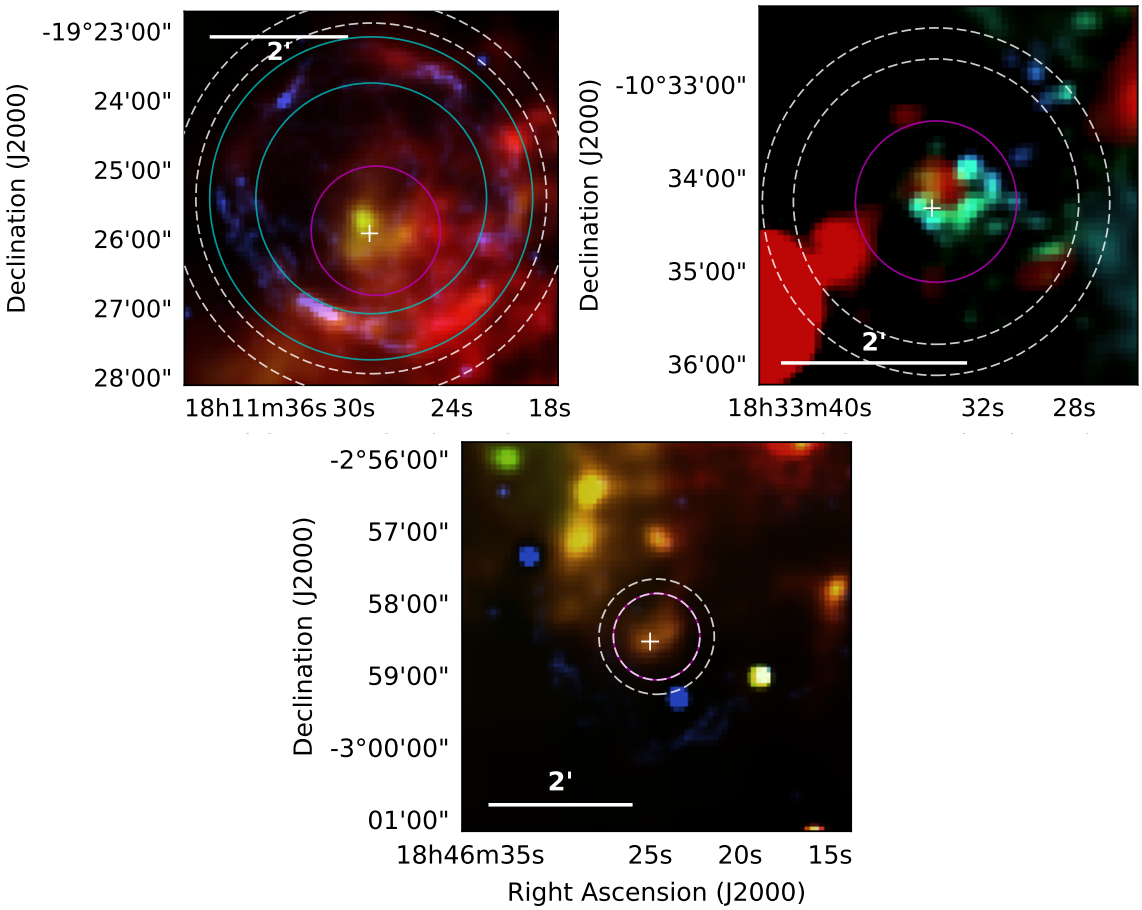

Figure 3.6: PPMAP-generated three colour maps of differential dust column density created using dust temperature slices from Figures 3.3-3.5. Colours show dust in G11.2−0.3 (*top-left*): 31 K (red), 41 K (green), and 75 K (blue). In G21.5−0.9 (*top-right*): 20 K (red), 34.6 K (green), and 39.6 K (blue). In G29.7−0.3 (*bottom*): 28 K (red), 31 K (green), and 75 K (blue). The white crosses indicates the X-ray centres, magenta circles show the apertures used for PWN dust, the cyan and white circles indicate the shell and/or ISM emission respectively.

modified blackbody fits in Section 3.1. This is a combination of differences between the two methods in the background subtraction, and therefore the final FIR fluxes attributed to the SNR (this discrepancy is larger between 160 and 350 μm), and the fact that by inspecting the temperature components visually with PPMAP, we were able to conclude that dust at temperatures below 25 K were likely not SN-related, hence resulting in an additional subtraction from the final PPMAP dust mass. Indeed Section 3.1, suggests that the cool dust in G11.2 is at 26.7 K whereas PPMAP finds that part of this dust is at warmer temperatures, thus giving a smaller estimate for the total dust mass.

G21.5−0.9: As shown in Figure 3.4, for this source we need to extend the temperature grid down to 20 K to show all the dust features, as there is a clear

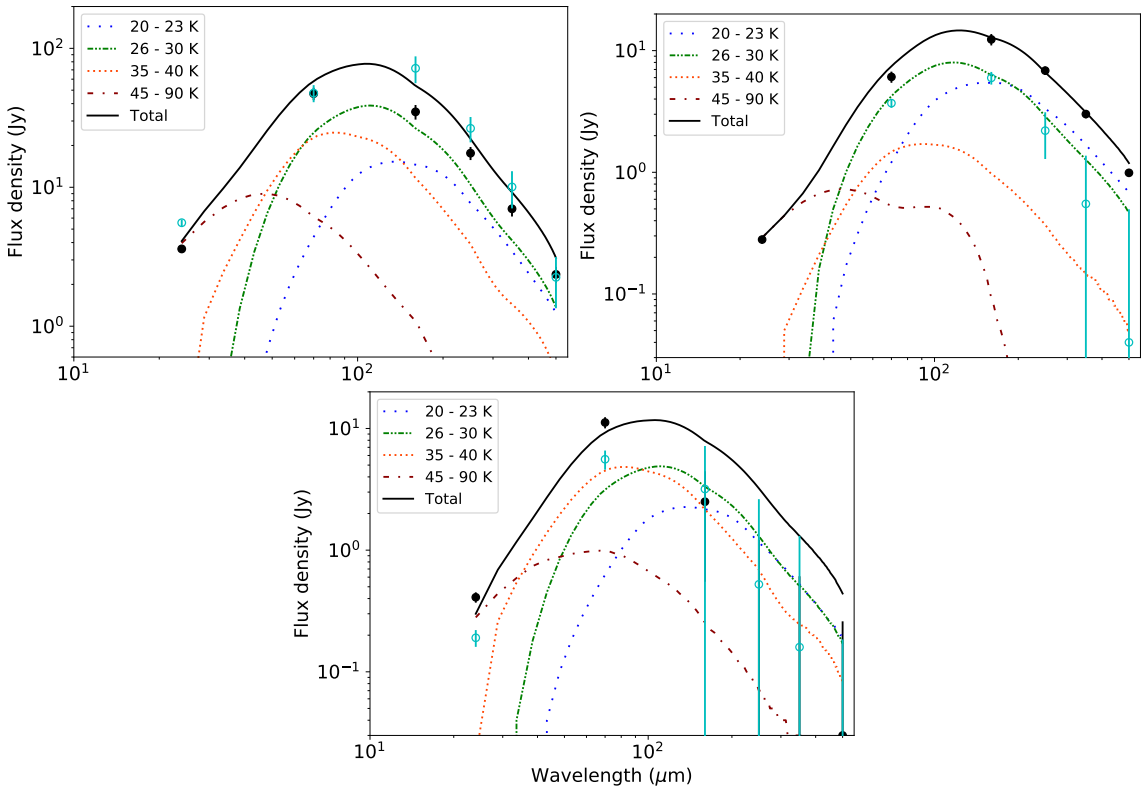

Figure 3.7: FIR SED as measured with PPMAP, analysing dust at temperatures between 20 and 90 K, for the PWN in G11.2−0.3 (*top-left*), G21.5−0.9 (*top-right*), and G29.7−0.3 (*bottom*). The open markers indicate the thermal flux estimated by aperture photometry in Section 3.1 and the filled markers indicate the estimated PPMAP flux in Section 3.1.4, where the difference is due to a variation in the estimate of the ISM level. Both sets of fluxes are background and synchrotron subtracted. There is a considerable contribution to the SEDs of both G11.2−0.3 and G29.7−0.3 from a cold dust (20 – 23 K) component. By visually inspecting the columns density maps for these sources we find that dust at temperatures below 25 K are not related to the SNR. These cool dust components are therefore excluded when estimating the dust masses to avoid contamination from the ISM.

detection of PWN dust at temperatures of 20 – 25 K. The cold dust component is visible in the grid at temperatures from 20 – 27 K across the entire PWN region. Warmer dust between 30 and 37 K forms a shell-like structure close around the south-west of the central region in which the pulsar is located. The distribution of dust in this source is similar to seen in G54.1−0.3, a bright peak of dust is evident to the north-west of the PWN shell which is significant and is robust to changes in mapping parameters. The PPMAP three-temperature map for G21.5−0.9 is shown in Figure 3.6 (middle panel) where these features are clearly visible (with the coldest dust emission highlighted in red).

Using PPMAP, we retrieve a dust mass for G21.5−0.9 of $M_d = 0.29 \pm 0.08\,M_\odot$ (including all the emission from 20-90 K). This is $\sim$ 2.5 times larger than both the

best-fit and median dust masses quoted in Section 3.1. Figure 3.7 indicates that the fluxes used for the PPMAP analysis are greater than those used in Section 3.1. This is due to a combination of differences in the level of the background emission derived between PPMAP and Section 3.1 (this leads to a factor of 1.5 – 2 difference in the FIR fluxes attributed to the SNR) and PPMAP allowing for a wider range of temperatures in each pixel instead of putting all of the dust at a single temperature in the modified blackbody fits.

Thus G21.5−0.9 joins Cas A and G54.1 in the small list of Galactic SNRs for which dust at temperatures < 25 K has been detected. PPMAP, with its better resolution and ability to map dust at different temperatures, has revealed significantly more dust in this source than from traditional modified blackbody fits.

G29.7−0.3: In Figure 3.5, the PWN structure clearly contains dust at 28 – 31 K, although the surrounding medium is also at a similar temperature making the detection more confused than the other sources. There is warm (75 K) dust in the shell around the south-east of the SNR at the location of 24 and 70 μm emission observed in Figure 2.15. This emission likely arises from shocked dust. Similar to G11.2−0.3, there is some evidence for warm dust in filaments within the shell, however this is much fainter and more confused in this case.

Similarly to G11.2−0.3, when inspecting the temperature grid of G29.7−0.3 between 20 and 90 K we do not see evidence for any material related to the SNR structure at temperatures below 25 K. The PPMAP-derived SED shown in Figure 3.7 shows that dust below these temperatures contributes significantly to the total FIR emission of this source, yet we have no evidence that this is associated with the SNR. Therefore we only use the temperature components revealed by PPMAP at 25 K and above when determining the dust mass for this source. For the central ejecta region in G29.7−0.3, PPMAP therefore estimates a dust mass of $M_d = 0.51 \pm 0.13\,M_\odot$[3]. In this case we expect that the estimate suffers from contamination by unrelated ISM and is artificially large. Again this is significantly larger than the best-fit values derived in Section 3.1, although within the uncertainties it is consistent with the median from the Monte Carlo fits. This is not surprising since the single temperature best-fit SEDs can be biased towards allocating a warmer dust temperature ($\sim$46 K), whereas the Monte Carlo estimate allows for random selection of lower temperature components ($\sim$30 K) and therefore higher dust masses than the best-fit SED. The temperature grid from PPMAP in Figure 3.3 shows emission from

[3] If we were to include the PPMAP dust components at temperatures below 25 K, the dust mass for G29.7−0.3 would be $M_d = 0.64 \pm 0.18\,M_\odot$.

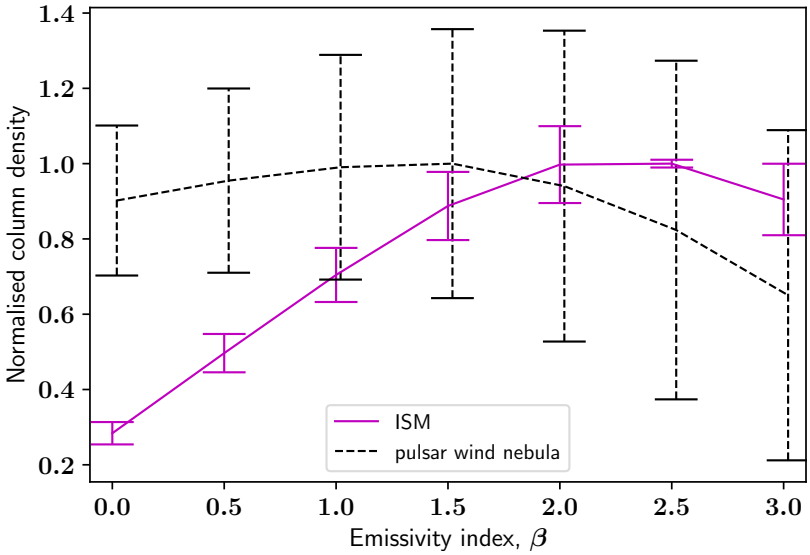

Figure 3.8: Estimated column density within each region at a given β for G21.5−0.9, measured from temperature averaged PPMAP images. The column density in each region is normalised by dividing by the peak column density of that region for easier comparison of the two curves. This is the resulting dust column density β profile assuming a flat β prior. (Figure 3.9 shows the same profile from PPMAP assuming a Gaussian prior instead). The broad PWN profile reflects our inability to discriminate different values of β with low S/N.

SN-related dust at lower temperatures than the best fit and therefore is more in agreement with the Monte Carlo estimate from Section 3.1.

3.2 Is the dust emissivity index different in SNe ejecta?

PPMAP also allows us to evaluate β of the SNR and ISM dust as shown in Figure 3.8. We estimated the density-weighted mean value of β within an aperture around the PWN and within annuli encapsulating the surrounding medium and, for G11.2−0.3, the SNR shell (Figure 3.6). We can therefore compare the emissivity index of material within the SNR components to that of the surrounding ISM using a β profile (Figure 3.8). As the SNR β parameter is sensitive to the estimate of the ISM level, a lack of careful analysis can result in spurious variations in β. We therefore subtract the ISM from the source flux prior to analysis of the column density using the annuli shown in Figure 3.6; this process is only applied to the SNRs, not to the ISM. This provides more robust results than subtracting the background of the resulting column density maps.

Additionally, the PPMAP analysis assumes that all media are optically thin, however, we find that the optical depth of the surrounding ISM in the 24 μm image is not negligible. We therefore disregard this band when evaluating β for the dust emission originating in the ISM, although this does not have a significant impact on any results for the cool dust components. The SNR material is likely optically thin and therefore the PPMAP analysis can be applied to this region using the 24 μm image.

We compare the dust column density in the PWN and surrounding (unrelated) interstellar dust found in each β 'bin' using the standard PPMAP assumption of a Gaussian prior with peak 1.9 and $\sigma = 0.25$. However we find inconclusive results for β variations between the PWN and ISM in all three of our sources. These profiles are shown in Figure 3.9 for completeness. Although the dust column density profiles with β appear to have a 'peak' column density for β of 1.8 – 2.0, we believe this is simply returning the prior distribution of β for the dust in the shell, ISM emission and the PWN. To confirm this we vary the prior to a lower mean, in which case PPMAP returns a correspondingly lower peak value of β. Thus, there is a systematic difference in the β of the ISM, shell, and PWN. However, the "peak" value of β returned depends on the prior.

Next we test how robust the PPMAP β analysis is given changes to the prior assumptions. Assuming a flat β prior instead of the Gaussian assumed earlier, we see no differences in the results for G11.2−0.3 and G29.7−0.3, but the column density-β profile for G21.5−0.9 does change (Figure 3.8). The dust column density in the ISM now appears to peak at $\beta_{\rm ISM} \sim 2.5$ whereas the PWN peaks at lower values of $\beta_{\rm PWN} = 1.4 \pm 0.3$, though the error bars are large. The wide dispersion in β of the PWN is a result of the large uncertainties, reflecting our inability to discriminate different values of β at the low signal-to-noise ratio. As we do not apply a β prior in this case we are more susceptible to β-temperature anti-correlation, which is included in this uncertainty. Although there is a range of possible solutions, as indicated by the large uncertainty, there is some indication of a variation.

The density-weighted mean value of β along the line of sight for the ISM aperture is $\beta_{\rm ISM} = 1.8 \pm 0.1$ (this takes into account which values of β represents more of the mass), whereas for the PWN, this value is still consistent with the peak profile of $\beta = 1.4$.

Finally we re-ran PPMAP using a Gaussian prior with mean of 1.4 (instead of 1.9). Again we found no differences in the results for SNRs G11.2−0.3 and G29.7−0.3. However, for G21.5−0.9, the new β profile is very similar to Figure 3.8, but with a reduced χ-squared by ∼10 per cent, supporting the (marginal) result

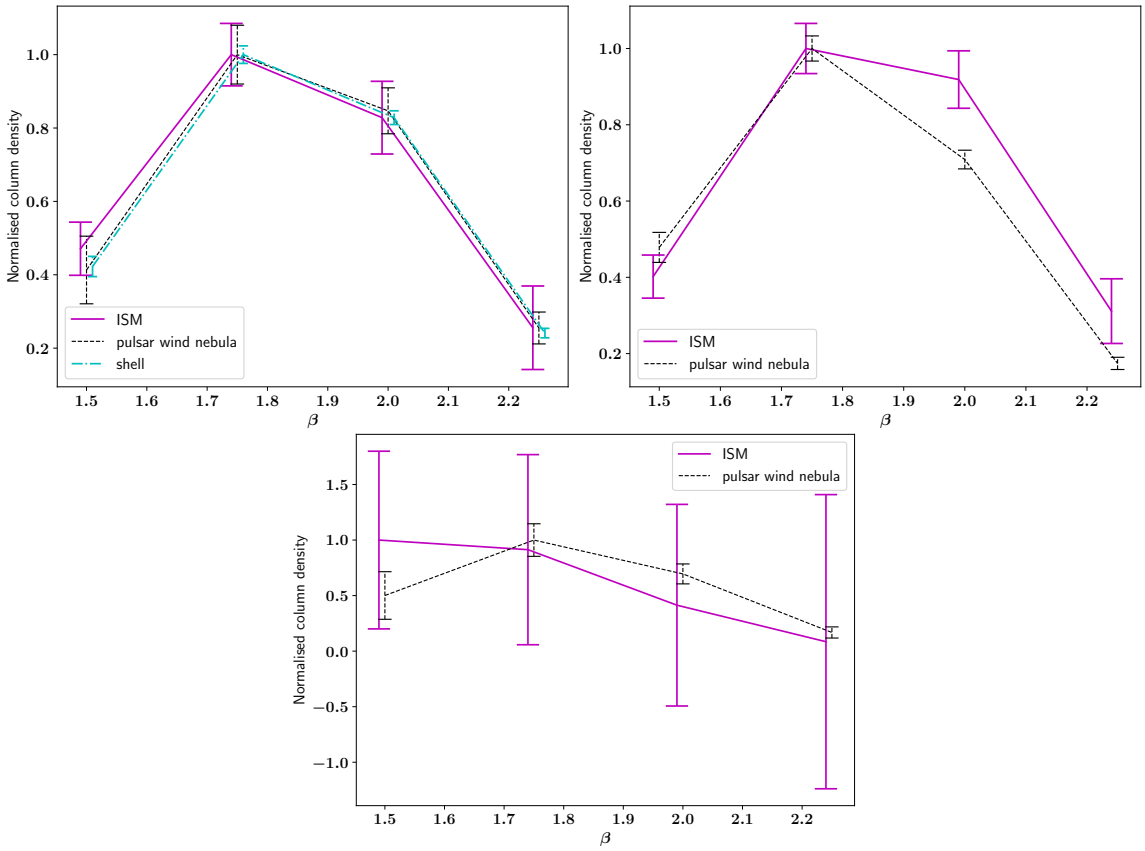

Figure 3.9: Estimated column density with β using a Gaussian β prior with mean 1.9 and $\sigma = 0.25$. *T*op-left: G11.2−0.3: for the PWN, the shell and the ISM dust. *T*op-right: G21.5−0.9: PWN and ISM and *B*ottom: G29.7−0.3. The column density in each region is normalised by dividing by the peak column density for comparison purposes. As we have low signal to noise for these SNRs, we cannot constrain β. PPMAP is effectively returning the Gaussian posterior for these three PWNe.

that the dust emissivity index in this PWN is smaller than the canonical ISM value.

3.3 TESTING THE RELIABILITY OF OUR PPMAP RESULTS

In order to check whether the results from PPMAP have been affected due to any assumptions, we test for potential biases due to overestimating the flux from hot dust, our chosen grids of dust temperatures and on the prior assumptions for β.

- The warmer dust components detected in the shells of G11.2−0.3 and G29.7−0.3 may artificially arise from contributions due to line emission at 24 μm. We therefore tested the PPMAP process for our SNRs after subtracting 30 per cent

of the flux in the 24 μm band. This level was chosen as it is similar to the fraction of the Crab Nebula 24 μm flux expected to originate from line emission (Temim et al., 2012). We find this does not affect any of the dust mass or β results.

- We next check if PPMAP is, in fact, able to extract values of β or is simply returning its prior value. We test this by simulating several 26 K Gaussian sources with a 1′ FWHM, varying β between 1.5 and 2.4 (simulations were carried out by K. Marsh, priv. communications). The images are convolved to the *Herschel* beam sizes and we add Gaussian noise for a signal-to-noise ratio between 3 and 10,000, which is constant across the spectrum. Assuming a flat β prior between 0 and 3, we then use PPMAP to estimate β for each simulated source in order to verify if PPMAP can return the correct value from the simulations. We find that the ability of PPMAP to pull out precise values of β is critically dependent on the signal-to-noise of the FIR data. At high signal-to-noises ($\sim$100) we find that the returned β matches the original value with an error less than 0.15. Figure 3.10 shows how the uncertainty in the PPMAP estimated values of β varies with the signal-to-noise of the input simulations.

  The lowest signal-to-noise ratio in this test ($\sim$ 3) is typical of our most resolved PWN source, G21.5−0.9. The other two SNRs have larger FIR uncertainties (due to the high background levels) and therefore this confirms that we would not be able to derive the value of β in G11.2−0.3 and G29.7−0.3 with any precision. For G21.5−0.9, this suite of simulations therefore suggests our uncertainty in the β value derived in Section 3.2 is slightly larger, i.e. $\beta_{\rm PWN} = 1.4 \pm 0.5$.

In our images the signal-to-noise ratio is not constant across the spectrum as we have much more confusion at longer wavelengths. In order to constrain β, our tests show that higher signal-to-noise at the Rayleigh-Jeans end of the spectrum is required. This is difficult given the current large uncertainties and variation in the ISM flux for most Galactic SNRs observed with *Herschel*. With higher resolution or longer wavelength data we could constrain β to within a smaller uncertainty range and potentially draw out any differences in the dust properties between different SNR regions. It may be easier to constrain β for SNRs in the regions of the Galactic plane at $\mid l \mid > 60^{\circ}$ which, on average, suffer from lower levels of background interstellar dust emission.

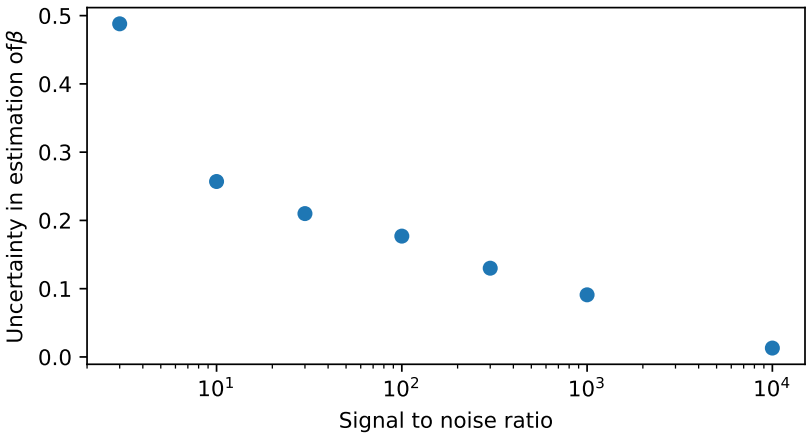

Figure 3.10: The root mean square uncertainty of the β value derived by PPMAP based on simulations for a 26 K source with Gaussian noise applied.

3.4 Conclusions

The main conclusions of this Chapter are:

- A modified blackbody SED fit to the NIR-radio data of the three PWNe, G11.2−0.3, G21.5−0.9, and G29.7−0.3, gives cold dust temperatures of 27.3 K, 25.9 K, and 45.7 K and dust masses of 0.9 $M_\odot$, 0.12 $M_\odot$, and 0.03 $M_\odot$ respectively.

- A Monte Carlo analysis for G11.2−0.3, G21.5−0.9, and G29.7−0.3 gives median dust temperatures of $26.7^{+1.7}_{-1.3}$ K, 26.0 ± 0.7 K, and $30.7^{+11.7}_{-4.0}$ K, and dust masses of $1.1^{+0.4}_{-0.3}$ $M_\odot$, 0.12 ± 0.02 $M_\odot$, and $0.3^{+0.4}_{-0.2}$ $M_\odot$. Large uncertainties in our fluxes at the longest FIR wavelengths for G29.7−0.3 pull the median estimate to a lower dust temperature and larger dust mass than that of the best fit.

- We use PPMAP to more rigorously analyse the material within the three SNRs. This confirms the presence of cold dust (20 – 40 K) within the PWN regions, which is clearly distinguishable from the surrounding ISM, and warm dust in the shells of G11.2−0.3 and G29.7−0.3. Through this analysis we estimate significant cold dust masses within the PWNe of 0.34 ± 0.14 $M_\odot$, 0.29 ± 0.08 $M_\odot$, 0.51 ± 0.13 $M_\odot$, for G11.2−0.3, G21.5−0.9, and G29.7−0.3 respectively. For both G11.2−0.3 and G29.7−0.3 these estimates are much more constrained than those of the traditional SED-fitting routine. PPMAP allows for a range of dust temperatures across the SNRs making these results more reliable.

- Using PPMAP we analyse the variation in the dust emissivity index, β, across the SNRs and compare with the values derived for the SN shell and ISM regions. We are unable to constrain β within G11.2$-$0.3 and G29.7$-$0.3 due to the low signal-to-noise at long wavelengths. For G21.5$-$0.9, we estimate $\beta_{\rm PWN} = 1.4 \pm 0.5$ in the PWN (with uncertainty in β derived from simulated data sets), and find $\beta_{\rm ISM} = 1.8 \pm 0.1$ in the ISM dust based on using a flat β prior. We show that with higher signal-to-noise in the FIR (or indeed longer wavelength data), our simulations suggest that in future, we could further constrain β within the PWNe and potentially draw out any differences in the dust properties with respect to dust in the interstellar medium. This may be easier for Galactic plane SNRs at $\mid l \mid > 60^{\circ}$ where there are lower levels of background interstellar dust emission on average.

CHAPTER 4
THE FULL GALACTIC PLANE CATALOGUE WITH *Herschel*

'Twinkle twinkle little star, how I wonder what you are!'

JANE TAYLOR

In Chapters 2 and 3 we investigated whether or not supernovae are an important contributor to the dust budget of galaxies at all cosmic epochs by searching for infrared (IR) and submillimetre (submm) emission from ejecta dust in nearby supernovae (SNe) and supernova remnants (Chawner et al., 2019) over a small area of the Milk Way. This survey (our first look catalogue) covered the same area as previously studied in the near and mid-infrared with *Spitzer* by Reach et al. (2006) and later by Pinheiro Goncalves et al. (2011). Those works reported the detection of dust emission associated with SNR structures in 29, 18 and 39 SNRs respectively over a region of the Galactic Plane covering ∼100 square degrees, suggesting SN-related dust emission is rather common. Chapter 3 also demonstrated clear evidence for dust formation in the ejecta of the pulsar wind nebulae (PWNe) G11.2−0.3, G21.5−0.9 and G29.7−0.3 alongside the previously discovered G54.1+0.3 (Temim et al., 2017; Rho et al., 2018), suggesting a detection rate of ∼45 % for this class of remnant within the area studied. Such a high detection rate implies that many PWNe may contain dust, some of which can be freshly formed ejecta dust (see also Omand et al., 2019). In order to verify the importance (or not) of SNe as dominant dust producers in galaxies and to determine which SNe form dust in their ejecta material, a larger statistical sample is needed. In this Chapter,

we complement the earlier work by searching for far-infrared (FIR) counterparts of known supernova remnants (SNRs) in the *entire* Galactic plane, as surveyed by *Herschel* covering 360° in longitude and 2° in latitude) at 70 – 500 μm. The work in this Chapter has been published in Chawner et al. (2020).

4.1 A Complete Galactic Survey for Far Infrared Supernova Remnant Emission

As first discussed in Chapter 2, using *Herschel* in the FIR to search for dust signatures is not always superior to using MIR observations from, for example, *Spitzer* (particularly at 24 μm where searching for dust signatures can be easier since the hotter dust emission can be more clearly disentangled from interstellar material). However, the increased sensitivity and resolution with *Herschel* at wavelengths $\geq$ 70 µm compared to lower resolution FIR observatories can be important for disentangling interstellar and SN-related structures in confused regions compared to e.g. *Spitzer* at the same wavelengths, IRAS, and AKARI (Murakami et al., 2007). The longer *Herschel* wavebands have the added advantage of being able to reveal the presence of any existing colder dust potentially missed by shorter wavelength observations (e.g. Barlow et al., 2010; Matsuura et al., 2011; Gomez et al., 2012b; Temim et al., 2017; Rho et al., 2018, see also Chapter 3).

Unfortunately, confusion with the ISM is the major limitation when studying dust in SNRs (e.g. in Cas A). Indeed in the *Herschel* Galactic SNRs studied in Chapter 2 (Chawner et al., 2019), confusion meant that SN dust structures could not be separated from unrelated ISM in more than 60 % of the sample, and even for those sources with clear FIR dust signatures coincident with known X-ray and radio emission originating from the SNRs, confusion still persists in a large fraction (also noted by Pinheiro Goncalves et al. 2011).

It has been proposed that SNe and SNRs have two key roles in dust evolution, first as a source of dust, forming large amounts in their ejecta which is injected into the ISM, and second by destroying dust as SN shock waves propagate into the ISM. A larger statistical sample is needed to determine the roles that SNe play in dust evolution in galaxies. Here we widen our search for SNRs to an area twice as large as that surveyed in Chapter 2.

Table 4.1: Level 1 dust detected supernova remnants in the Complete Hi-GAL Survey.

SNR	Name	PWN [a] (FIR)	Age (kyr)	SN Type	Dust features [b]	Comparison [c]	References
G6.4−0.1	W28		10		Filaments	R	1; 2
G8.3−0.0					Shell	R	
G11.1−1.0					Shell	OR	
G11.1+0.1					Western shell	R	
G11.2−0.3		Y (Y)	1.4 − 2.4	Type cIIb or Ibc	Shell	RX	3
					Central region (PWN)		
G13.5+0.2					Filaments	R	4
G14.1−0.1							
G14.3+0.1					Partial shell	R	
G15.9+0.2			$\leqslant$ 2.4	Core collapse	Partial shell	RX	5; 6
G16.4−0.5					Central region	R	
G18.6−0.2		? (N)	13	Core collapse	Outer filaments	R	7
G20.4+0.1			3.6		Shell	R	
G21.5−0.9		Y (Y)	0.87	Type IIP or Ib/Ic	Central region (PWN)	X	8; 9
G21.5−0.1					Central region	R	
G29.7−0.3	Kes 75	Y (Y)	$<$ 0.84	Type Ib/c	Central region (PWN)	RX	10; 11
G31.9+0.0	3C391		4		Partial shell		12
G33.2−0.6					Western shell	R	4
G34.7−0.4	W44	Y (N)	2	Core collapse	North and western shell	R	13; 14
					Central filaments		
G39.2−0.3	3C396	Y (N)	7		Western shell	R	15; 16

Table 4.1: Level 1 dust detected supernova remnants in the Complete Hi-GAL Survey.

SNR	Name	PWN [a] (FIR)	Age (kyr)	SN Type	Dust features [b]	Comparison [c]	References
G43.3−0.2	W49B		1 − 4	Bipolar Ib/Ic	Fe/radio loop	R	17;18;19;20
					H_2 filament		
G54.1+0.3		Y (Y)	2	Core collapse	PWN southern rim		21
G54.4−0.3	(HC40)		95		Outer filaments		22
G65.8−0.5					Eastern structure	OR	23
G67.8+0.5						OR	
G298.6−0.0					Outer filaments	XR	24
G304.6+0.1	Kes 17		28 − 64	Core collapse	Western shell	R	25
G306.3−0.9			2.3	Type Ia	Inner region	XR	26;27
G310.8−0.4	Kes 20A					R	28
G311.5−0.3			25 − 42		Shell		29
G332.4−0.4	RCW 103		2	Type IIP	Southern arc	X	30; 31
G340.6+0.3			2.6		Shell	R	32
G344.7−0.1			3	Type Ia	North-central region	XR	33; 34
G348.5−0.0					Arc	R	35
G348.5+0.1	CTB37A	? (N)	32 − 42		Northern arc	R	1; 35; 36
					Breakout region		
G348.7+0.3	CTB 37B		5	Core collapse	North-eastern shell	R	37

Table 4.1: Level 1 dust detected supernova remnants in the Complete Hi-GAL Survey.

SNR	Name	PWN [a] (FIR)	Age (kyr)	SN Type	Dust features [b]	Comparison [c]	References
G349.7+0.2			1.8	Core collapse	Eastern shell	R	1; 38; 39
G350.1−0.3			0.6 − 1.2	Core collapse	Ejecta region	R	39; 40; 41
G351.2+0.1					Northern bar Central region	R	42
G357.7−0.1	MSH 17-39 The Tornado				Head and tail regions	R	1

A summary of the supernova remnants in the Hi-GAL Survey with detection level = 1: FIR emission which is clearly correlated with radio, MIR, or X-ray structure and can be distinguished from the ISM. [a] 'Y' indicates that a source contains an associated PWN, '?' indicates an unconfirmed PWN candidate. The FIR detection of the PWN is indicated in the brackets. [b] Location of FIR detected dust features. [c] Waveband of previous detection to which FIR structure is compared: O = optical, R = radio, X = X-ray. References for age and SN type for this table are: [1]Pihlström et al., 2014, [2]Rho & Borkowski, 2002, [3]Borkowski et al., 2016, [4]Case & Bhattacharya, 1998, [5]Reynolds, 2006, [6]Klochkov et al., 2016, [7]Voisin et al., 2016, [8]Bietenholz & Bartel, 2008, [9]Bocchino et al., 2005, [10]Leahy et al., 2008, [11]Morton et al., 2007, [12]Chen et al., 2004, [13]Wolszczan et al., 1991, [14]Zhu et al., 2013, [15]Harrus & Slane, 1999, [16]Leahy & Ranasinghe, 2016, [17]Pye et al., 1984, [18]Smith et al., 1985, [19]Hwang et al., 2000, [20]Lopez et al., 2013, [21]Bocchino et al., 2010, [22]Park et al., 2013, [23]Shan et al., 2018, [24]Bamba et al., 2016, [25]Combi et al., 2010b, [26]Reynolds et al., 2013, [27]Combi et al., 2016, [28]Andersen et al., 2011, [29]Pannuti et al., 2014b, [30]Nugent et al., 1984, [31]Frank et al., 2015, [32]Caswell et al., 1983a, [33]Giacani et al., 2011, [34]Yamaguchi et al., 2012, [35]Pannuti et al., 2014b, [36]Tian & Leahy, 2012, [37]HESS Collaboration, 2008a, [38]Tian & Leahy, 2014, [39]Yasumi et al., 2014, [40]Gaensler et al., 2008, [41]Lovchinsky et al., 2011, [42]Dubner et al., 1993.

4.1.1 Detection Levels in the far-infrared

We study the remaining SNRs in the Galactic Plane (Green, 2004) using Hi-Gal (Molinari et al., 2010b, 2016) covering 360° in longitude and $\mid b \mid \leq 1$. There are a total of 200 SNRs in this area, although *Herschel* images for 10 are unavailable. This work therefore includes an additional 119 sources compared to our first look catalogue, and an additional 92 and 66 sources compared to the previous dusty catalogues of Galactic SNRs studied using *Spitzer* in Reach et al. (2006, MIR, $\lambda \leq 24\,\mu$m) and Pinheiro Goncalves et al. (2011, $\lambda \leq 70\,\mu$m) respectively (an additional 163 and 137 SNRs when this work is combined with the first look catalogue in Chapter 2).

In brief, each remnant was first inspected as a false colour image combining the 70, 160, and 250 μm *Herschel* wavebands, regridded and convolved to the resolution of the 250 μm band (see Appendix B for a gallery of three colour *Herschel* images of SNRs, Figure B.1). FIR emission from SNRs can be thermal or non-thermal. Thermal FIR will arise from warm dust such as warm ejecta material, shock-heated dust in the forward or reverse blast waves, photo-ionised material near a PWN, or swept-up ISM. Non-thermal emission originates from synchrotron emission from shocks or PWNe, although this is not expected to be significant except in the case of plerion objects such as the Crab where synchrotron emission contributes between 19 and 88 % of the flux in the various *Herschel* wavebands (De Looze et al., 2019). We compare with multi-waveband images to identify dust emission associated with each SNR which, in principle, should allow us to identify the emission mechanism. For the most part we compare with radio and, where available, X-ray images, both of which trace shock-heated material, see individual notes in Section 4.1.2 for details. Where radio and X-ray structures originate from a PWN, incident FIR emission may indicate dust in a photo-ionised region. We can also use X-ray and optical images to identify ejecta material or swept-up/shocked ISM and in some cases, any correlation observed between FIR and MIR or NIR emission can help to identify a variety of FIR sources such as shock-heated dust or swept up ISM.

The method for determining if dust signatures related to SNe material are present in the *Herschel* images is described in full in Chapter 2 (Chawner et al. 2019) and is the same classification criteria as used in the *Spitzer* SNR catalogues of Reach et al. (2006) and Pinheiro Goncalves et al. (2011). Following the definition of detection levels from the MIR *Spitzer* SNR catalogue in Reach et al. (2006), we define detections as: 1 = detection (FIR emission which is clearly correlated with

radio, MIR, or X-ray structure and can be distinguished from the ISM), 2 = possible detection (FIR emission in the region of the SNR, potentially related to radio, MIR, or X-ray structure but confused with ISM), 3 = unlikely detection (detection of FIR emission which is probably unrelated to the SNR), and 4 = no detection of FIR emission. We also introduce a new category in this chapter 'i', to account for the fact that in some cases, the only dust signatures associated with the SNR (via radio and/or X-ray emission) are found in regions where the shell is known to be interacting with a molecular cloud. Table B.1 (Appendix B) lists the full 119 Galactic SNRs from Hi-GAL studied in this survey along with the 71 sources studied in the first look catalogue, with all of the SNRs classified as level 1 summarised in Table 4.1. Individual details provided for each SNR assigned a detection rate of 1 or 2 in this work (10 level 1 and 11 level 2) are listed in the following Section. We note that the availability and quality of ancillary data and the depth of those observations is not the same for all SNRs, which makes it impossible to automate the classification of the detection levels, and thus requires manual intervention and interpretation. This could introduce a bias towards bright, well studied sources that we classify as detections here, similarly this could also be a factor in the previously quoted rates for SNRs detected in near-MIR catalogues with Spitzer (Reach et al., 2006; Pinheiro Goncalves et al., 2011).

The full list of 119 sources from this Chapter are provided in Appendix B (Table B.1) along with the 71 sources studied in Chapter 2 (Table 2.1). Details provided for each SNR assigned a detection rate of 1 or some of the detection 2 cases are listed in the following Section. Images of SNRs that are not shown in the following Section are provided in the full catalogue in Appendix B, Figure B.1.

4.1.2 Notes for Individual Remnants

Notes on individual sources classed as **detection level 1** (FIR emission which is clearly correlated with radio, MIR, or X-ray SNR structure and can be distinguished from the ISM) and *detection level 2* (FIR emission in the region of the SNR, potentially related to radio, MIR, or X-ray structure but confused with ISM) are provided in this section.

G0.0+0.0 (Sgr A East): This CCSN remnant (Figure 4.1) has an elliptical radio shell with a plume of radio and X-ray emission at the northern edge. There is an associated runaway neutron star, the Cannonball, and a PWN in front of this plume (e.g. Nynka et al., 2013; Zhao et al., 2013). There are numerous unrelated HII regions in this complex; the largest, Sgr A West, is observed within the SNR shell

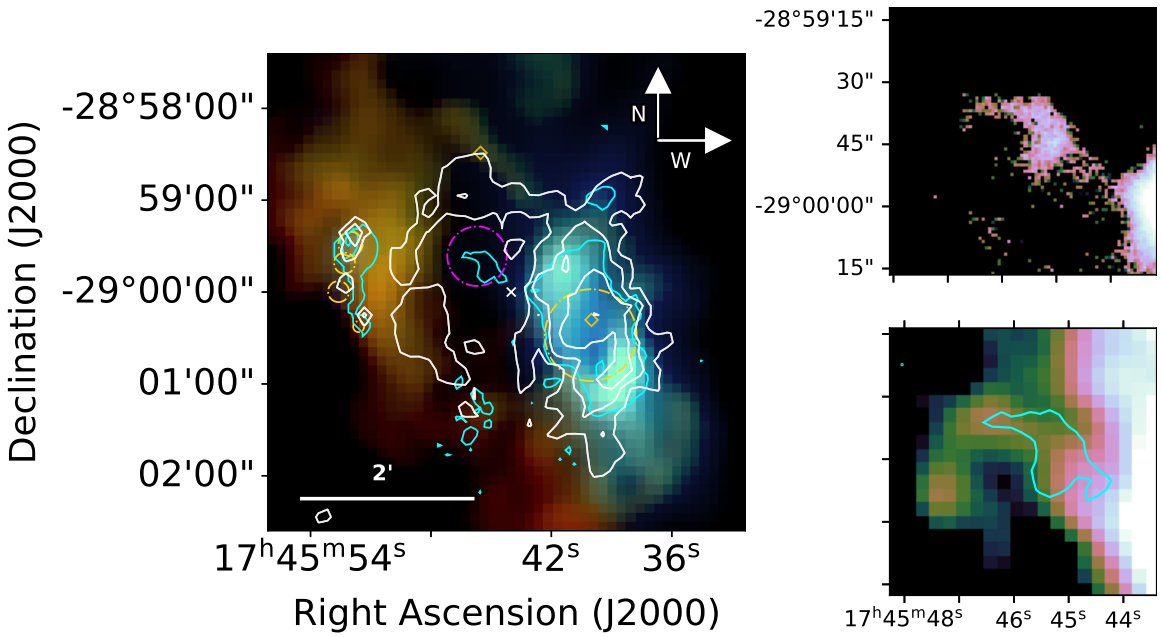

Figure 4.1: *G0.0+0.0, Sgr A East - left*: *Herschel* three colour image with JVLA 5.5 GHz contours overlaid in white and SOFIA 37.1 µm contours overlaid in cyan, colours are red = 250 μm, green = 160 μm, and blue = 70 μm. *Right:* A zoom in on the dust factory detected within the magenta circle (left) by Lau et al. (2015). *Top:* the SOFIA 37.1 µm detection from their work, and *bottom:* the *Herschel* 70 µm image with SOFIA 37.1 µm contours overlaid. Here the *Herschel* and SOFIA data have been scaled considerably to show this faint feature. (For the bottom panels we use the cube helix colour scheme (Green, 2011).) The gold circles to the east indicate the locations of HII regions (Goss et al., 1985) and the gold circle to the west indicates the location of Sgr A West. The diamond to the north indicates the location of the associated neutron star, 'The Cannonball', and the diamond to the west indicates the location of Sgr A*. The white cross shows the radio coordinates of the SNR centre from Green (2014). The same *Herschel* colour combinations and orientation are used in Figures 4.2 – 4.18.

on the western side and has a spiral structure. Four smaller regions are found to the east, just outside of the SNR radio shell. Observations of 327 MHz absorption place Sgr A West in front of the SNR (Yusef-Zadeh & Morris, 1987), although their relative distances are uncertain. There is some evidence that the two sources are at a similar distance and there has been some interaction between the expanding shell and Sgr A West (Yusef-Zadeh & Goss, 1999; Yusef-Zadeh et al., 2000; Maeda et al., 2002), although this is controversial.

The SNR age and X-ray observations of hot ejecta at its centre both suggest that the reverse shock has already reached the centre of this source (Maeda et al., 2002). Lau et al. (2015) completed a detailed analysis of the central region using data in the range 5.8–70 µm from *Spitzer* IRAC, the Faint Object Infrared Camera for the SOFIA Telescope (FORCAST), and *Herschel* PACS (70 µm). These observations indicate the presence of dust within the SNR central region, north-east of Sgr A West (indicated by the magenta circle in the top panel of Figure 4.1). They studied the 5.8–37.1 µm emission from several regions in and around the location of the SNR dust, using the 70 µm flux as an upper limit. They assumed it is composed of amorphous carbon grains with two grain sizes (large grains of ~ 0.04 µm and very small grains of $\sim 0.001\,\mu$m) and that is is heated by a nearby cluster of massive young stars. This gave a total ejecta mass of $\sim\ 0.02\,M_{\odot}$ of warm (~ 100 K) dust which has survived the passage of the reverse shock.

We compare *Herschel* maps with the JVLA 5.5 GHz image (Zhao et al., 2013). We reduced the VLA data, using the Common Astronomy Software Applications (CASA) of the National Radio Astronomy Observatory (NRAO). The C-band (4.5–6.4 GHz) continuum image of Sgr A* was produced by combining multiple VLA observations taken between March and July 2012. The data were processed in the AIPS software package (Greisen, 2003), following standard calibration and wide-band imaging procedures.

Using the five bands of *Herschel* data from Hi-GAL we search for dust features associated with the SNR and with the Lau et al. (2015) dust discovery (see the bottom panel of Figure 4.1). We find that the entire region inside the SNR shell is extremely confused in the *Herschel* bands (as originally noted by Lau et al. 2015). The flux at 70 µm due to background emission (determined by placing multiple apertures across the map outside of the bright dust features) is of order 1000 Jy. Integrating the emission within the Lau et al. (2015) dust region (cyan contours in Figure 4.1) and subtracting the background we estimate that ~ 95 % of the flux in that area originates from unrelated background flux i.e. there is no significant detection above the background noise in the *Herschel* 70 – 500 µm bands. The $3\,\sigma$

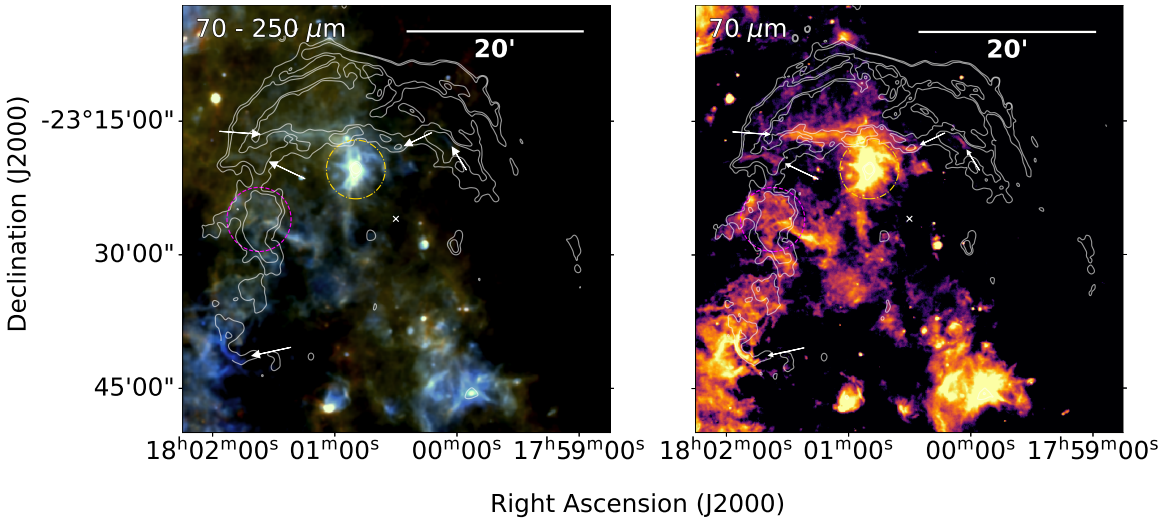

Figure 4.2: **G6.4−0.1, W28** - *Left: Herschel* three colour image and *right: Herschel* 70 µm image, both with radio (90 cm) contours overlaid. The arrows and magenta circle indicate filaments of 70 µm emission which are coincident with radio structure. There is FIR emission at the location of other radio emission, although the structure is different and association is unclear. The gold circle indicates the location of an unrelated HII region. The white cross shows the radio coordinates of the SNR centre from Green (2014).

upper limit we derive for the dust region from the 70 µm map is ∼12 Jy which is consistent with the Lau et al. (2015) estimate. This region is too heavily confused to constrain if there is cooler dust at this location using the *Herschel* images and therefore we assign this a detection level 2.

There is bright emission to the west in the 70 – 250 µm bands at the location of the HII region Sgr A West which appears bluer compared to the surrounding dust emission (Figure 4.1), and which is coincident with the brightest region in the radio. There is also an IR structure to the east of the source in all *Herschel* wavebands (orange structure in the top panel Figure 4.1). It is thought that the SNR is interacting with a molecular cloud on this side (e.g. Sjouwerman et al., 2010; Tsuboi et al., 2015). This continuum emission may originate from shock-heated dust, however, it does not correspond to the radio morphology and it is more likely that it is unrelated.

G6.4−0.1 (W28): W28 is a well-studied mixed morphology remnant with evidence of a molecular cloud-SN blast wave interaction (e.g. Wootten, 1981; Reach et al., 2005a). We see many filaments of 70 µm emission which follow the radio contours in Figure 4.2. Although the proximity of HII regions makes this region confused, we propose that the structure in the *Herschel* data (arrows and magenta

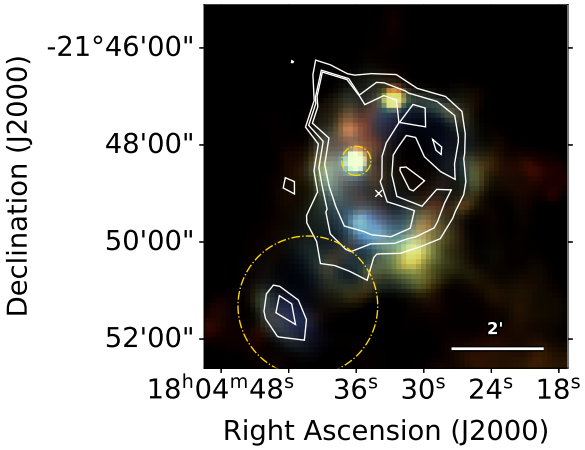

Figure 4.3: **G8.3−0.0** - *Herschel* three colour image with VLA 20 cm contours overlaid. A shell structure is detected across all *Herschel* wavebands. There is some variation in the FIR structure compared with the radio, however there is coincidence between the two. The large gold circle indicates the location of an IR bubble. The white crosses shows the X-ray coordinates of the SNR centre and the small gold circle indicates the location of a maser.

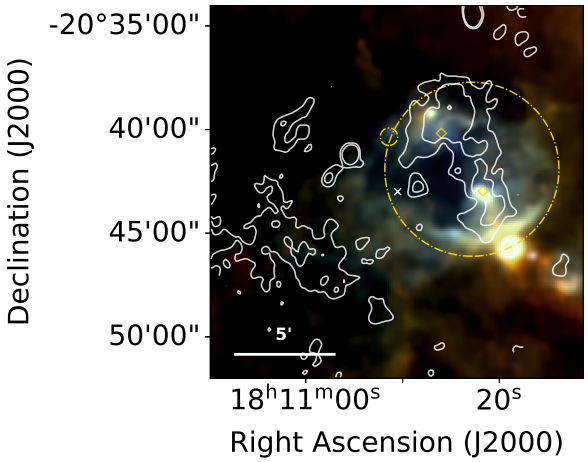

Figure 4.4: *G9.9−0.8* - *Herschel* three colour image with VLA 90 cm contours overlaid. There is FIR emission in a shell structure at the western/north-western edge of the radio shell. However, the morphology of the structures are different and there are multiple HII regions (gold diamonds) and FIR bubbles (gold circles) (Simpson et al., 2012), as such, we can not confirm if this is associated with the SN. The white crosses shows the radio coordinates of the SNR centre.

circle in Figure 4.2) on the eastern side of the remnant, and to the north is associated with the SNR due to its close correlation with radio emission. The 70 μm emission on the eastern side is also coincident with shocked H_2 emission (Reach et al., 2005a) from the interaction border between the SNR and molecular clouds. Furthermore, the dusty region in the magenta circle and the northernmost part of the dust feature indicated by the arrows overlap with shocked molecular gas (^{12}CO(3-2), Figure 1b in Zhou et al., 2014, see also Arikawa et al., 1999). Although the region is confused in the *Herschel* images, given the strong association of the 70 µm filaments with the radio structures, we classify this as a level 1 detection.

G8.3−0.0: Brogan et al. (2006) detected a radio shell at 90 cm with a very bright region at $\alpha = 18^h04^m38^s$, $\delta = -21°47'17''$. There is a shell of emission detected across all *Herschel* wavebands which correlates with the radio structure as shown in Figure 4.3. As such, this satisfies our criteria for a level 1 detection. There is a marked colour variation within this shell. At wavelengths longer than 70 μm there is a bright patch to the south-west, and emission is detected at all wavelengths from the location of a maser at $\alpha = 18^h04^m36.02^s, \delta = -21°48'19.6''$

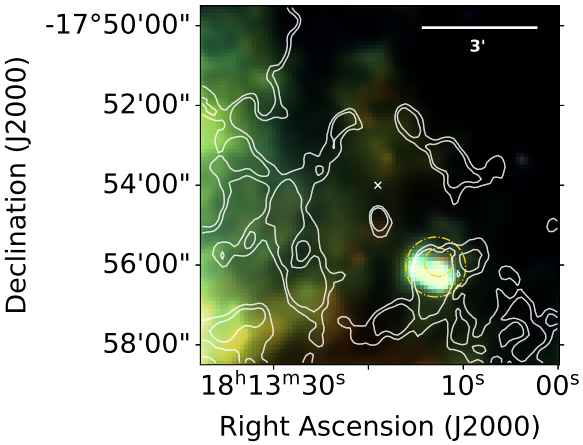

Figure 4.5: *G12.7−0.0* - *Herschel* three colour image with VLA 20 cm contours overlaid. The region is very confused to the east, there is FIR emission in the south-western region of the SNR shell. There are also FIR bubbles at this location (Simpson et al., 2012), as indicated by the gold circles. The white crosses shows the radio coordinates of the SNR centre.

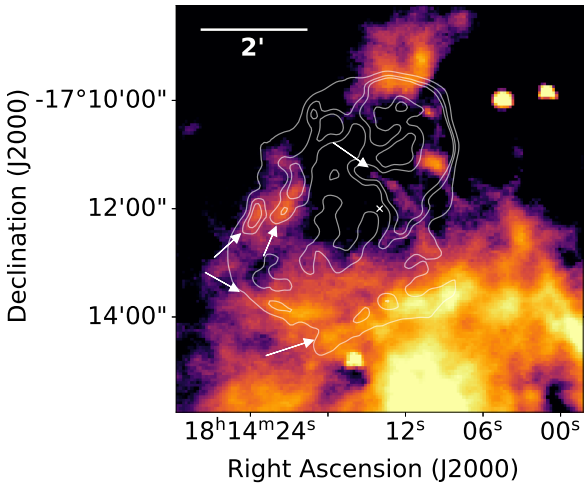

Figure 4.6: **G13.5+0.2** - *Herschel* 70 µm image with VLA 20 cm contours overlaid. Filaments are detected at 70 μm which are coincident with radio emission, and are indicated by the arrows. These are more confused at 160 µm, and cannot be distinguished from surrounding ISM in the longer *Herschel* wavebands. The white cross shows the radio coordinates of the SNR centre from Green (2014).

(Green et al., 2010; Hewitt & Yusef-Zadeh, 2009a). There is also FIR emission across all *Herschel* wavebands to the south-east of the SNR, near $\alpha = 18^{\rm h}04^{\rm m}43.5^{\rm s}, \delta = -21^{\circ}51'29.5''$, although this region is at the edge of a FIR bubble (Simpson et al., 2012, Figure 4.3) making its association with the SNR unclear.

G9.9−0.8: This SNR has a shell structure detected in radio (90 cm, Brogan et al., 2006) and optical (Hα, Stupar & Parker, 2011) wavebands. As seen in Figure 4.4, there is FIR emission detected at the location of the western edge of the radio shell. However, there are multiple HII regions and FIR bubbles (Simpson et al., 2012) at this location, and the FIR structure is distributed differently to that of the radio. Although molecular hydrogen from an interaction between the SNR and molecular clouds was discovered in Hewitt & Yusef-Zadeh (2009a), there is no accompanying image to compare with the dust features. We therefore argue that the FIR features are potentially related to the SNR, as such this satisfies our criteria for a level 2 detection.

G12.7−0.0: Brogan et al. (2006) detected a radio shell from this SNR. There

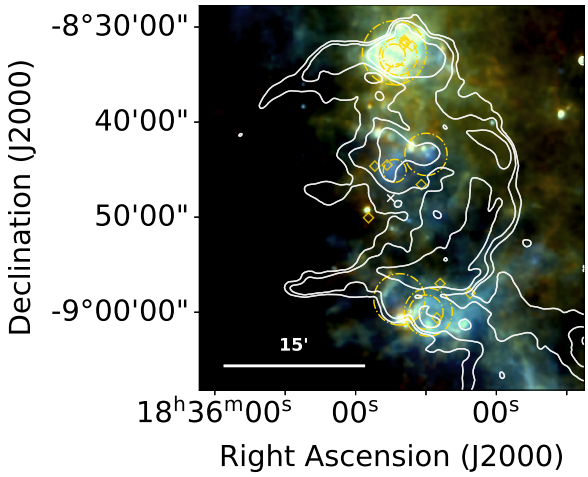

Figure 4.7: *G23.3−0.3 (W41) - Herschel* three colour image with VGPS 21 cm contours overlaid. The gold circles indicate the locations of some of the unrelated sources in this region, such as molecular clouds and bubbles. The gold diamonds at $\alpha = 18^{h}34^{m}51.8^{s}, \delta = -08°44'38.2''$ and $\alpha = 18^{h}34^{m}46.6^{s}, \delta = -08°44'31.4''$ indicate the locations of a gamma-ray source (HESS J1834–087) and OH (1720 MHz) maser lines. The other gold diamonds indicate the locations of masers.

is FIR emission in Figure 4.5 coincident with the south-western region of the radio shell, although there is a FIR bubble (Simpson et al., 2012) at this location and therefore we cannot be sure of the origin of this emission. We therefore classify this as a level 2 detection.

G13.5+0.2: We detect filaments of emission at 70 and 160 μm which correlate with VLA 20 cm radio structure (Helfand et al., 1989) as indicated by the arrows in Figure 4.6. There is 70 µm emission along the south-western edge, within the VLA contours. It is thought that this may be a ridge of shock-heated dust resulting from the interaction between the SNR and surrounding molecular clouds, which is in agreement with the detection of H_2 from this source (Froebrich et al., 2015). There is more confusion in the longer wavebands and there does not seem to be any associated structure in those bands. Based on the coincidence with the 70 µm filaments and radio features, we therefore classify this as detection level 1.

G23.3−0.3 (W41): This SNR is in a very crowded region of the Galactic Plane, where there are multiple dense cores, YSOs, HII regions, and bubbles. The presence of a gamma-ray source (HESS J1834–087) and OH (1720 MHz) maser lines near the centre of the source (indicated in Figure 4.7) suggest that the SNR may be interacting with a molecular cloud (HESS Collaboration, 2015). Several molecular clouds are labelled in Figure 4.7 with gold circles. There is bright FIR emission

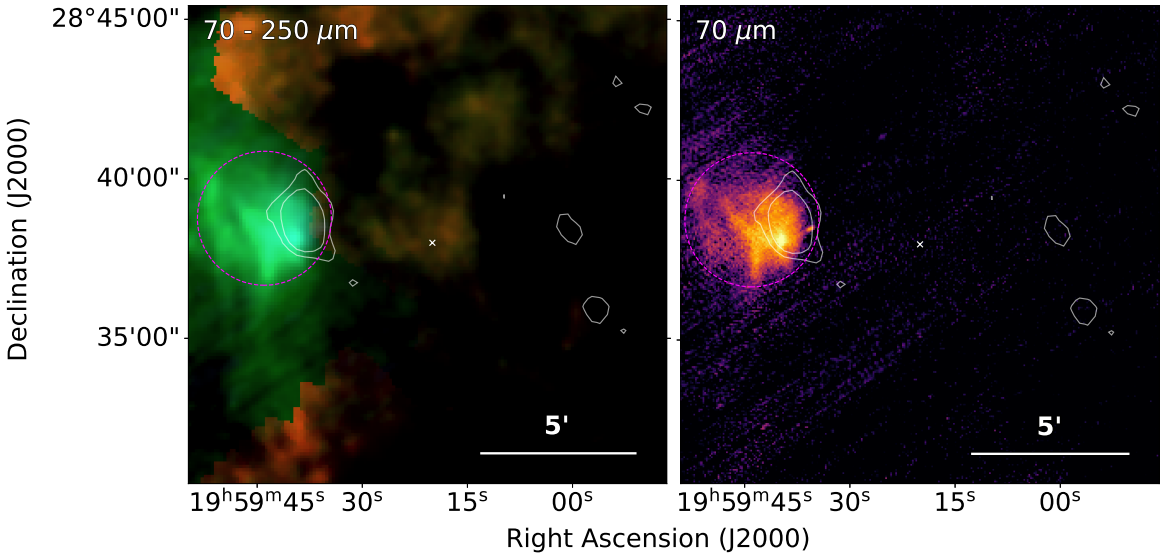

Figure 4.8: **G65.8−0.5** - *Left: Herschel* three colour image and *right: Herschel* 70 µm image, both with radio NVSS 1.4 GHz contours overlaid. FIR structure is detected at the eastern edge of the SNR, at the location of radio and Hα structure (Sabin et al., 2013). An unidentified region of FIR emission is detected at the centre of the source at 160 – 500 µm. The white cross shows the radio coordinates of the SNR centre from Green (2014).

at the location of the radio structure, however the clearest FIR is also coincident with molecular clouds. Although there may be SNR-related dust in this region, we cannot determine its association because of confusion, this therefore satisfies our criteria for a level 2 detection.

G65.8−0.5: This object was only recently classified as a SNR by Sabin et al. (2013) who used Hα to identify its nature. We compare Hα and NVSS images with *Herschel* finding bright 70 and 160 µm emission at the east of the source at the location of the Sabin et al. (2013) Hα structure. We propose that this 70 and 160 µm feature is associated with the SNR, although the structure is offset to, and more extended than the radio emission seen in the NVSS 1.4 GHz image (Figure 4.8). Unfortunately the *Herschel* SPIRE maps at 250 – 500 µm do not cover the area where the Hα and radio structure is seen. Additionally, at 160 – 500 µm there is a region of emission detected at the radio centre of the SNR, although this does not correlate with radio emission and we cannot determine if this is associated. Given the close spatial coincidence between the *Herschel* emission, Hα and radio structures to the east of the SNR, we classify this as a level 1 detection, though we note that here we do not have the full colour information in the *Herschel* bands.

G67.8+0.5: Like G65.8−0.5, this source was only recently identified as a

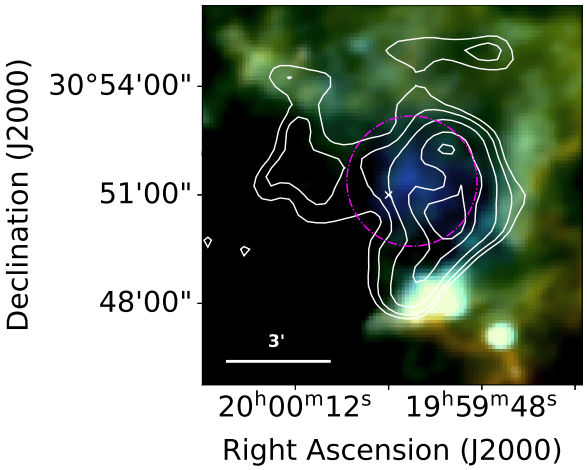

Figure 4.9: **G67.8+0.5** - *Herschel* three colour image with NVSS 1.4 GHz contours overlaid. Dust emission is detected at 70 µm from a faint radio source, and at all *Herschel* wavelengths from a partial shell along the western and south-western edges of the SNR. The white cross shows the radio coordinates of the SNR centre from Green (2014).

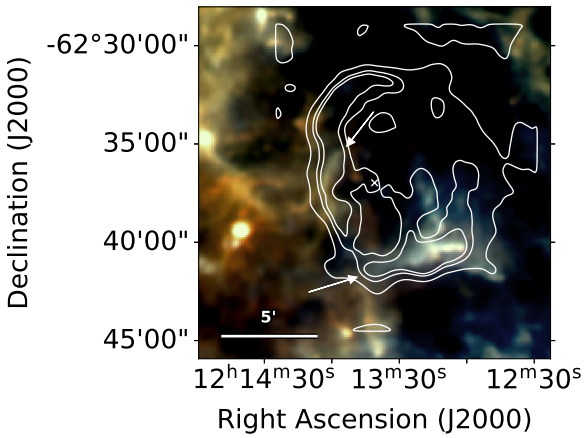

Figure 4.10: **G298.6−0.0** - *Herschel* three colour image with 843 MHz (Molonglo Observatory Synthesis Telescope, MOST) contours overlaid. Dust is detected in filaments at the east of the source, and in a ridge along the southern edge as indicated by the arrows. The white cross shows the radio coordinates of the SNR centre from Green (2014).

SNR by Sabin et al. (2013). There is bright 70 µm emission at $\alpha = 19^{h}59^{m}57.5^{s}, \delta = 30°51'26''$, coinciding with the location of an unidentified IRAS source (IRAS 19579+3043) and with emission in the WISE 22 μm archive image (though at lower resolution than *Herschel* 70 μm). Here, the FIR is anti-correlated with the radio as the *Herschel* FIR peak is located in a gap in the radio structure. There is also brighter 70 µm emission than the surroundings (bluer FIR than the surrounding emission) indicating the presence of warmer dust emission. Although this does not align with the detection criteria defined in Section 4.1, we expect that this emission is associated with the SNR due to the FIR colours and the coincidence with the radio centre. There is also a bright shell across all *Herschel* wavebands to the west and south-western edge of the SNR. We propose that the central source and outer shell are associated with the SNR and therefore classify this SNR as a level 1 detection. It is possible that the central emission, which lacks radio emission, could be cold SN ejecta dust (as seen in Cas A, Barlow et al., 2010), while the shell emission is from the ISM. Further follow up observations in other wavelengths would be needed to investigate this.

G298.6−0.0: This is a mixed-morphology SNR, with an X-ray filled centre

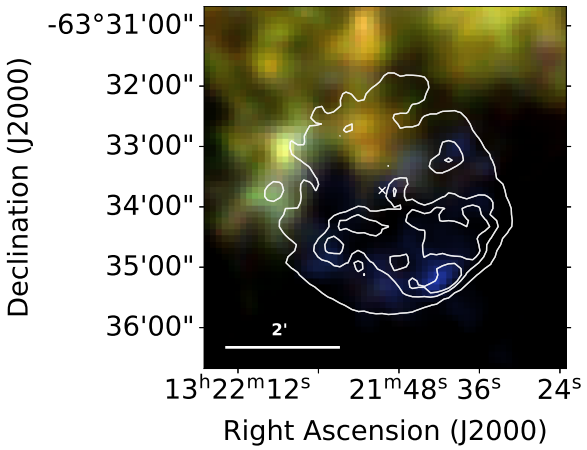

Figure 4.11: G306.3−0.9 - *Herschel* three colour image with *Chandra* contours overlaid. Dust emission is detected at 70 μm inside the X-ray contours, especially towards the south-west where there is the brightest X-ray emission. The white cross shows the X-ray coordinates of the SNR centre.

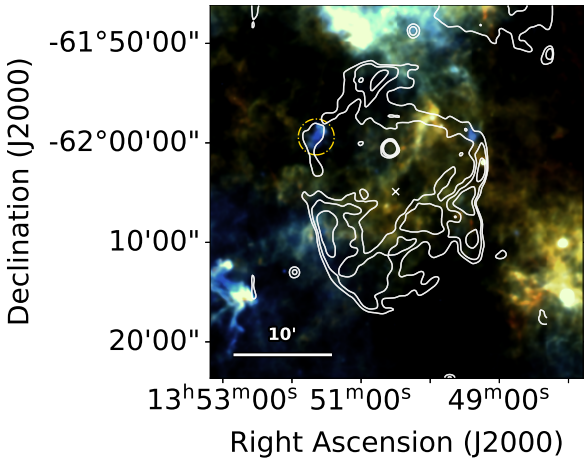

Figure 4.12: *G309.8+0.0* - *Herschel* three colour image with *Chandra* contours overlaid. The gold circle indicates a bright knot of 70 µm emission which may be associated with the SNR, although its location within the radio contours may be coincidental. The white cross shows the X-ray coordinates of the SNR centre.

and radio shell (Rho & Petre, 1998; Bamba et al., 2016). A filament of dust is detected in all *Herschel* wavebands at the eastern edge of this source at the location of a bright radio filament detected by MOST (Molonglo Observatory Synthesis Telescope) at 843 MHz (Whiteoak & Green, 1996). There is also dust detected along the south of the radio structure. At 70 µm this extends along the length of the radio contours and is brightest at the western edge, where emission at the other *Herschel* wavebands is found. We therefore classify this as a level 1 detection. Comparing the Suzaku X-ray image from Bamba et al. (2016), these features are not correlated with the centrally filled X-ray emission, and therefore are likely to originate from swept up interstellar material given the coincidence with the edge of the radio shell.

G306.3−0.9: This source is a recently discovered remnant of a Type Ia SN (Reynolds et al., 2013) in which the reverse shock has heated the central ejecta region (Combi et al., 2016). The overall morphology in the X-ray (Reynolds et al., 2013; Combi et al., 2016) is a semi-circular shape with strong radio and X-ray emission in the southwest, suggestive of an interaction with an interstellar cloud or an asymmetric SN explosion. Both X-rays and radio emission are fainter in the north. Combi et al. (2016) showed that the SNR is brighter in softer X-rays towards the centre and found distinct shock-heated ejecta regions in the northeast, central and

southwestern areas (see their Figure 7) with enhanced abundances and temperatures. Similarly, they saw distinct X-ray regions in the northwest and south of the SNR that they attributed to shockfronts interacting with the interstellar medium.

Comparisons with the X-ray, radio, and hot dust emitting at 24 μm using *Spitzer* observations were presented in Reynolds et al. (2013) and Combi et al. (2016). In the latter study, they noted that the 24 μm morphology from shocked dust grains is shell-like, matching the distribution observed in hard X-rays. The former study noted that an additional ridge feature to the south seen in radio and X-ray images is also correlated with the 24 μm emission, commenting that this could originate from swept up dust or ejecta dust. Reynolds et al. (2013) also mention that *Herschel* 160 – 500 μm images show an over density of dust in the north where the X-ray emission is the faintest. The three colour *Herschel* image is displayed in Figure 4.11. In the *Herschel* image, the dust emission is concentrated in the south, with very little dust at 70 μm in the north-east. The *Herschel* dust features that are bright at 70 μm (blue clumps in Figure 4.11) overlap with the known 24 μm features, therefore this is a clear level 1 detection.

We note that in Chapter 2, we also found dust associated with another candidate Type Ia SNe G344.7−0.1 (see also Combi et al., 2010a; Giacani et al., 2011; Yamaguchi et al., 2012), where the dust features are also consistent with a non-supernova origin. We will return to these two SNRs in Section 4.2.2.

G309.8+0.0: There is lots of FIR emission across the region, although the majority seems to be unrelated extended emission from interstellar clouds. We detect a bright knot of 70 μm emission to the east which has a similar morphology to the radio structure (indicated by the circle in Figure 4.12). However, the FIR extends slightly beyond the radio contour, and the location of this emission may be coincidental. Reach et al. (2006) listed this as a level 3 detection based on NIR *Spitzer* observations (3.6 – 8.0 μm). The SNR is listed in the table of OH detections from Green et al. (1997) but whether this originates from a maser has not been confirmed. A bright radio source, thought to be extragalactic in origin (Whiteoak & Green, 1996), is observed to the north of the SN centre at $\alpha = 13^{\rm h}50^{\rm m}35.2^{\rm s}, \delta = -62^{\circ}00'42''$; no related FIR emission is observed at this location. Given the uncertainty as to whether the dust feature within the gold circle is associated with the ejecta due to the multiple sources seen in the field with similar *Herschel* colours, we classify this SNR as a level 2 detection.

G350.1−0.3: This source is thought to be a very young core-collapse SNR (≤ 1 kyr) with an associated neutron star (Gaensler et al., 2008; Lovchinsky et al.,

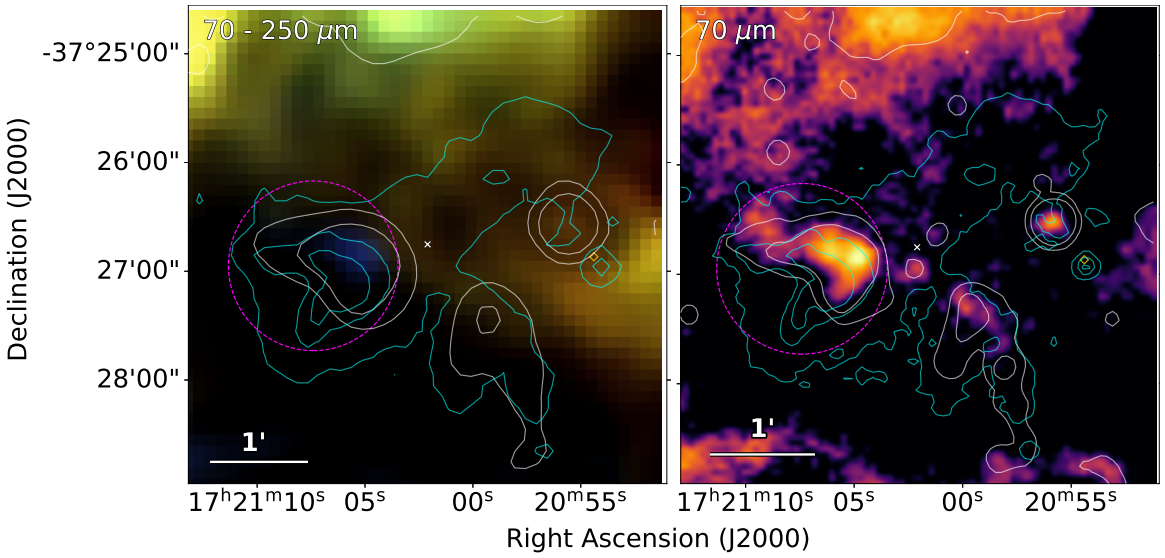

Figure 4.13: **G350.1−0.3** - *Left: Herschel* three colour image (smoothed to the 250 µm resolution). *Right: Herschel* 70 µm image. The white contours are 24 µm *Spitzer* MIPS (Lovchinsky et al., 2011) and the cyan contours are X-Ray *Chandra*. Dust emission is detected to the eastern side of this remnant, within the magenta circle. This region correlates with SNR emission in the X-ray, radio, and MIR (Gaensler et al., 2008; Lovchinsky et al., 2011). The gold diamond indicates the location of the associated neutron star, XMMU J172054.5−372652 (Gaensler et al., 2008). The white cross shows the X-ray coordinates of the SNR centre.

2011). It has a distorted clumpy structure with X-ray emission from four regions. *Spitzer* MIPS observations revealed 24 µm emission arising from two of these X-ray regions, which was suggested as likely originating from ejecta dust heated by the reverse shock (Lovchinsky et al., 2011). Although *Spitzer* MIPS did not reveal 70 µm emission associated with the SNR structures (Lovchinsky et al., 2011), with the higher resolution and more sensitive *Herschel* PACS, we have detected dust emission at 70 µm in one of the 24 µm-emitting regions to the east, as indicated by the magenta circle in Figure 4.13. We do not see any evidence of associated emission in the longer *Herschel* wavebands. Since the *Herschel* 70 µm feature overlaps with the 24 µm dust attributed to the SNR and with X-rays, we classify this source as a level 1 detection. We do not detect FIR emission at the location of the proposed compact object (CCO) (Gaensler et al., 2008) (indicated by the gold diamond). The strong 70 µm emission from the dust region is similar to the properties of the ejecta dust discovered in SNRs G11.2−0.3, G21.5−0.9, G29.7−0.3 (Chapter 2), and G54.1+0.3 (Temim et al., 2017; Rho et al., 2018). Therefore G350.1−0.3 can be added to the growing list of SNRs that contain dust within their ejecta.

G351.2+0.1: This SNR has a well defined radio shell (Caswell et al., 1983b),

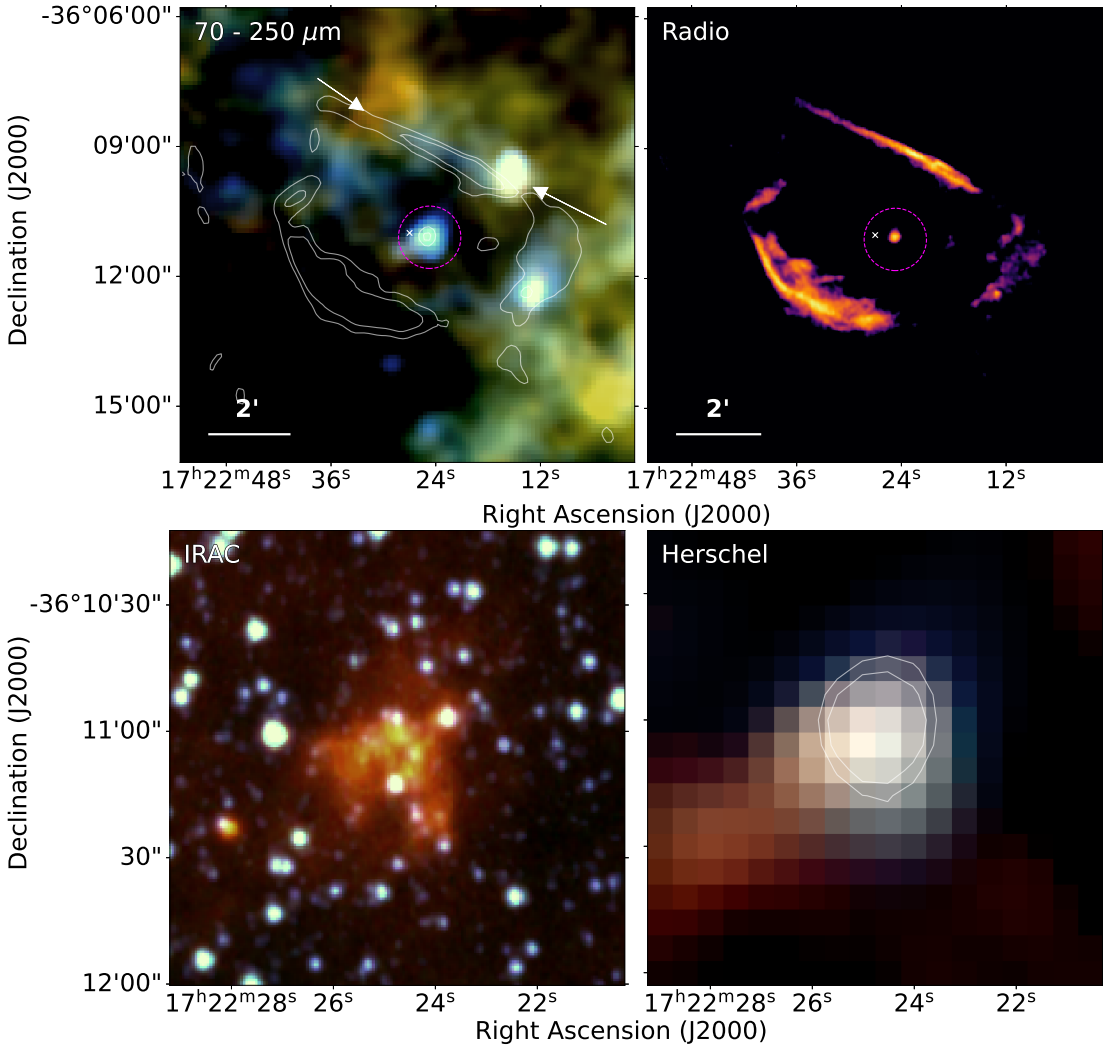

Figure 4.14: **G351.2+0.1** - *Top left: Herschel* three colour image with VLA C-band (4.5 – 6.4 GHz) contours overlaid and *Top right:* VLA C-band (4.5 – 6.4 GHz) image. FIR emission is detected in a northern bar, between the two arrows, and more faintly from the south-western shell at 70 μm. Emission from the central region within the magenta circle is detected across all *Herschel* wavebands. The white cross shows the radio coordinates of the SNR centre from Green (2014). *Bottom left:* Three colour IRAC image using bands 1 (3.6 μm - blue), 3 (5.8 μm - green) and 4 (8 μm - red). This image was made using archive data from the *Spitzer* Enhanced Imaging Products Super Mosaic Pipeline. *Bottom right: Herschel* three colour image with VLA radio contours (see top panel), note we have changed the colour scaling compared to the top right panel in order to highlight the central features more clearly.

which appears flattened in the north (Dubner et al., 1993) indicating that the shock-front is interacting with dense ISM and that the SNR is relatively young. The SNR has a compact (15″ diameter) central core in the radio (within the magenta circle in Figure 4.14) and this is attributed to synchrotron emission powered by a pulsar (Becker & Helfand, 1988). Figure 4.14 compares the radio emission at 4.8 GHz (top left panel) with the *Herschel* three colour image (top right panel). (Dr A. Papageorgiou (*priv. comm.*) processed the radio data presented in Becker & Helfand (1988) in AIPS, following standard calibration and imaging procedures.)

In the *Herschel* images, we detect emission from the northern shell of the SNR coincident with the thin radio shell seen in the VLA image, as indicated by the arrows in Figure 4.14. There is also a bright 70 μm clump on the south-western side of the SNR that coincides with a radio peak. We see very little 70 μm emission at the location of the south-east shell where the radio is bright. The brightest 70 μm emission observed in the SNR is from the central radio core (within the magenta circle, this is also visible in archival *Spitzer* MIPS 24 μm data and the *Spitzer* IRAC image in Figure 4.14). A further bright 70 μm source can be seen just north of the flattened northern shell, and a fainter point source that lies to the immediate east of the central core are also detected; these are detected in the longer *Herschel* wavebands and are likely not associated with the SNR. We classify this source as a level 1 detection due to the spatial coincidence of the central FIR core and northern FIR shell with corresponding radio features.

The potential FIR detection of a compact object, or PWN is interesting to explore, although the central core is atypical of its class. It is very faint (10 mJy at 6 cm) (Becker & Helfand, 1988) with spectral slope $\alpha = +0.27$, where flux varies with frequency as $S_\nu \propto \nu^{-\alpha}$ suggestive of a very weak source (or possibly old source), compared to Crab-like remnants where typically α ranges from ~ -0.25 to -0.3. The oddness of this source led Becker & Helfand (1988) to discuss whether it could be a HII region or stellar wind, where the spectral slope would be predicted to be -0.1 ($+2.0$) for optically thin (optically thick) emission or $+0.6$ respectively. The source was not detected by the MOST radio survey (Whiteoak & Green, 1996), though it lies below their sensitivity level. Notably, the central core is not detected in *Chandra* archive observations[1]. We note that a hard spectrum X-ray source attributed to a pulsar was observed within a 2×4 deg region with GINGA (Tawara et al., 1988) overlapping the location of G351.2+0.1 and with a previously detected X-ray source (GPS1722-363). The pulsation rate of this source is 414 s, oscillating

[1] *Chandra* maps (obsid 3844; 4591) covering the SNR footprint are presented in the massive star forming region omnibus of Townsley et al. (2018).

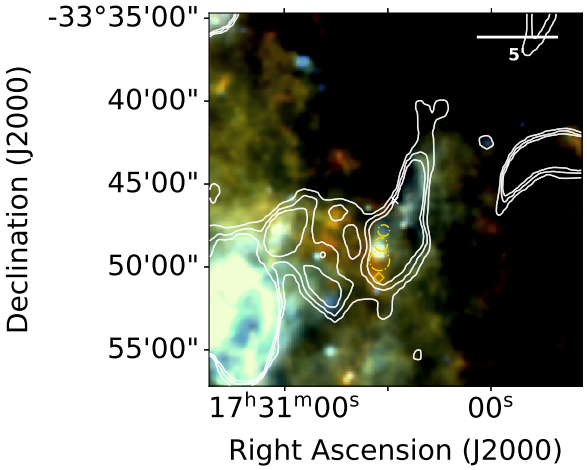

Figure 4.15: *G354.1+0.1 - Herschel* three colour image with MOST 843 MHz radio contours overlaid. FIR emission is detected from within the radio contours although association with the SNR is unclear. The gold circles indicate the locations of bubbles (Simpson et al., 2012) and a dense core (Purcell et al., 2012). The white cross shows the radio coordinates of the SNR centre from Green (2014).

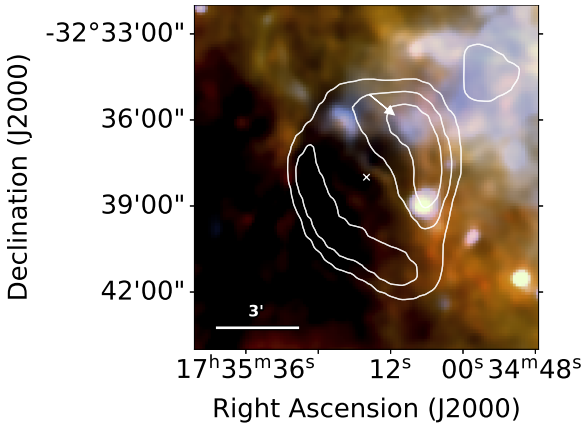

Figure 4.16: *G355.6−0.0 - Herschel* three colour image with MOST 843 MHz radio contours overlaid. There is FIR emission, with strong 70 µm flux indicated by the arrow, which may be related with SNR radio structure, although the region is extremely confused and any SNR emission is difficult to disentangle. The white cross shows the radio coordinates of the SNR centre from Green (2014).

between 1 – 4 milliCrab (where 1 Crab is equivalent to 15 keV cm^{-2} s^{-1} in the X-ray range 2 – 10 keV).

The compact core region is clearly detected in NIR archive images of the region. Figure 4.14 (bottom panel) shows a close up view of the NIR and FIR emission in the central core, with NIR *Spitzer* IRAC three colour image on left (3.6, 5.8 and 8 μm), and the FIR *Herschel* three colour image on the right. The central radio core is an extended feature in the NIR bands, and is very similar to the IRAC images of the PWN G54.1+0.3 and compact PWN in G21.5−0.9 (Zajczyk et al., 2012). In G54.1+0.3, *Spitzer* IRS spectra revealed that the IRAC feature was from argon line emission from the ejecta and a broad silicate dust feature peaking at 9 μm (Temim et al., 2017; Rho et al., 2018). The similarity of the NIR emission features could therefore suggest that G351.2+0.1 adds to the growing list of sources of SN ejecta dust detected from a PWN. We return to this source in the next Chapter.

G354.1+0.1: There are multiple radio features in this region and there are FIR filaments of emission observed in the same regions as radio structures. Assuming that the radio emission from the SNR is the region encompassing the pulsar (see Figure 4.15), the FIR may be associated with the SNR, although we cannot

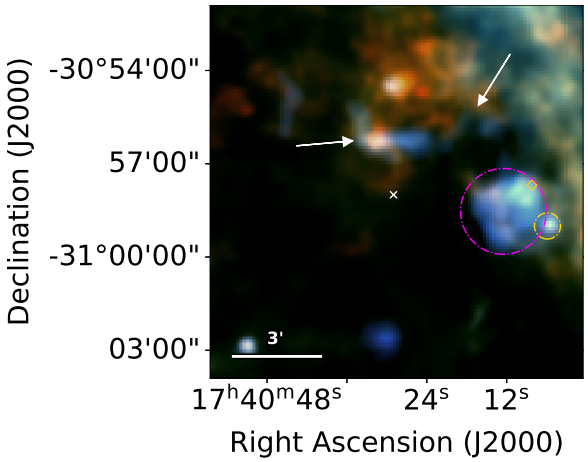

Figure 4.17: **G357.7−0.1, The Tornado** - *Herschel* three colour image. We detect dust emission across all *Herschel* wavebands for the 'head' of The Tornado, within the magenta circle. We also detect FIR emission from the 'tail' of The Tornado, and from a fainter filament extending around the head, as indicated by the arrows. The HII region known as the 'eye' of The Tornado is detected to the west of the 'head', within the gold circle. The gold diamond indicates the location of an OH (1720 MHz) maser. The white cross shows the radio coordinates of the SNR centre from Green (2014).

definitively determine an association due to the numerous unrelated FIR sources in this region (gold circles in Figure 4.15). Thus we classify this as a level 2 detection. We do not detect emission at the location of the associated pulsar, PSR 1727−33, indicated by the gold diamond in Figure 4.15 (Frail et al., 1994).

G355.6−0.0: This SNR is another mixed morphology source (Rho & Petre, 1998). As seen in Figure 4.16, radio observations show a clear shell in the MOST 843 MHz radio image (Gray 1994a, their Figure 2) with enhanced emission to the west. There are multiple FIR filaments in the region of this SNR, although the majority do not seem to correlate with the radio. There is a filament of emission near $\alpha = 17^{h}35^{m}08^{s}, \delta = -32°36'14''$ which may be associated with the radio peak at the western edge of the SNR, although the region is confused and we cannot confidently determine whether this is related. This satisfies our criteria for a level 2 detection in that there is potential FIR emission related to SN features.

G357.7−0.1 (MSH 17-39): Known as 'the Tornado', this unusual SNR candidate comprises a 'head', which appears as a shell- or ring-like feature in the radio (Shaver et al., 1985) and an unresolved extended clump in X-rays (Gaensler et al., 2003), a larger extended radio shell/filamentary structure, and an elongated 'tail'. These features are marked with a magenta circle, contours and arrows respectively

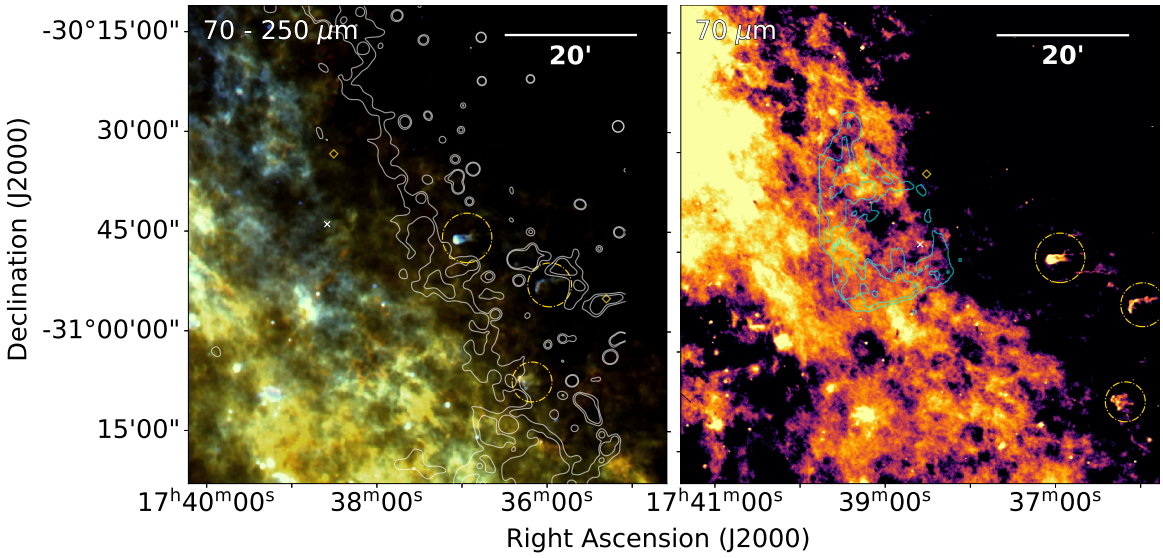

Figure 4.18: *G357.7+0.3 - Left*: *Herschel* three colour image with MIPS 24 µm contours overlaid. *Right*: *Herschel* 70 µm image with MOST 843 MHz contours overlaid (radio image is shown in Figure 2 from Gray (1994b) and Figure 1 from Rho et al. (2017)). FIR emission is observed within the gold circles from 'comet' like structures to the west detected by Phillips et al. (2009), we do not expect that these structures are associated with the SNR. The white cross shows the radio coordinates of the SNR centre from Green (2014). The gold diamond to the west indicates the location of the Mira star V1139 Sco and the diamond in the north indicates the location of an OH (1720 MHz) maser.

in Figure 6.2. The compact, bright radio source seen to the west of the head at $\alpha = 17^{\rm h}40^{\rm m}05.9^{\rm s}, \delta = -30^{\circ}59'00''$ is the so-called 'eye' of the Tornado. However, this has been shown to be unrelated to the SNR structure and is proposed to be an isolated core embedded in a foreground HII region (Brogan & Goss, 2003; Burton et al., 2004).

Although this region is confused in the FIR (Figure 6.2), the *Herschel* images show clear emission from dust, with bluer colours than the surrounding interstellar material, in the *Herschel* images at the location of the head and the tail. The coincidence of FIR emission with the radio-bright head makes this a level 1 detected source. Further analysis of this source can be found in Chapter 6.

G357.7+0.3: This source has a distinctive square morphology giving rising to the name 'the Square Nebula'. There is extended OH (1720 MHz) emission along the western edge of the SNR (Yusef-Zadeh & Goss, 1999) and the recent discovery of shocked molecules, broad CO in millimetre, shocked H_2 lines with *Spitzer*, and 158 µm [CII] with SOFIA in Rho et al. (2017) provides unambiguous evidence that this SNR is interacting with a molecular cloud. Although there is lots of extended

FIR structure making associated emission difficult to distinguish, there are filaments at the western edge, near to the OH (1720 MHz) emission, which may be related. We therefore classify this as a level 2 detection.

Phillips et al. (2009) observed comet-like structures to the west of this source which they suggest result from interactions between the SNR and nearby molecular clouds. We detect FIR emission across all *Herschel* wavebands from these structures near to $\alpha = 17^{h}36^{m}57^{s}, \delta = -30^{\circ}46'02''$, $\alpha = 17^{h}35^{m}59^{s}, \delta = -30^{\circ}53'03''$, and $\alpha = 17^{h}36^{m}11^{s}, \delta = -31^{\circ}07'40''$, indicated by the gold circles in Figure 4.18. We also see a plume of dust emission near the Mira star V1139 Sco, originally seen at 24 µm in Phillips et al. (2009). The origin of this emission is unclear; Phillips et al. (2009) propose that the wind is being swept behind the star by an interaction with the SNR, although the Mira star may be unrelated and its location coincidental. We do not expect that any of these structures are associated with the SNR. If the structures were the result of interactions with the expanding SNR we would expect them to point away from it and the brightest emission would be at the furthest point from the remnant centre. The morphology of these objects is more similar to evaporating gaseous globules (EGGs) or protoplanetary discs, it is therefore more likely that the knots are associated with star formation, which may have been triggered by the SN. In order to check whether the comet-like structures could be a result of the SNR interaction, we roughly estimate the distance to these regions and compare with the distance travelled by the SNR shock. We note that little is known about the progenitor for this source. We focus on the structures labelled A to D in Figure 2 of Phillips et al. (2009) and the closest source to the SNR, structure G357.46+0.60. To be consistent with Phillips et al. (2009) we assume that the SNR is at 4 kpc, and then assume that the comet-like structures are at the same distance. Thus the closest edge of the structures are at distances between 22 and 51 pc from the radio centre of the SNR (from Green, 2014). The distance reached by the shock front is estimated initially by assuming the most optimistic case, whereby the SNR is freely expanding since the explosion (i.e. it is not yet in the Sedov-Taylor phase). Assuming an ejecta mass between $5-15\,M_{\odot}$ and an age of <6400 years (Phillips et al., 2009), the shock wave would have reached a maximum distance of $\sim$29.3 pc in this time. We find that only the closest globule (G357.46+0.60) is within range of the shockwave, and only if the ejected mass is smaller than $8.5\,M_{\odot}$. If we assume the SNR is in the Sedov-Taylor expansion phase, the SF globules are well outside of the estimated shock wave radius (5.0 pc) for a typical ISM n(H) of $1\,cm^{-3}$. Higher interstellar densities would further reduce the reach of the SNR. Thus we do not expect that any of these structures are associated with the SNR.

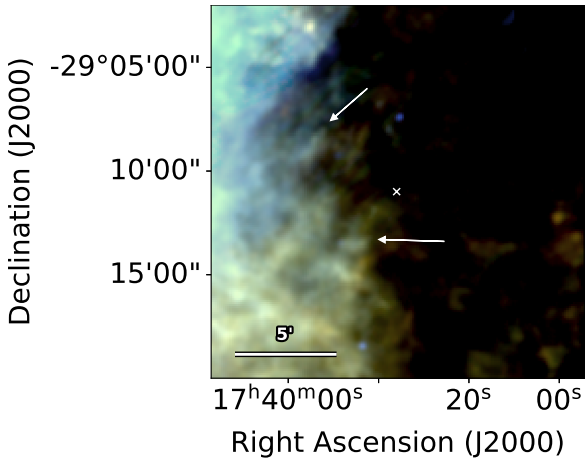

Figure 4.19: *G359.1+0.9 - Herschel* three colour image. There are FIR filaments towards the western edge of the SNR which may be associated although the region is very confused. The white cross shows the radio coordinates of the SNR centre from Green (2014).

Phillips et al. (2009) used MIPS 24 µm combined with low (arcmin) resolution IRAS data to propose that the northern-most of these structures contains dust at $\sim$30 K. Fitting a modified blackbody to background subtracted *Herschel* fluxes (see Chapter 3 for details) confirms that it contains dust at $\sim$33 K.

G359.1+0.9: This SNR has a shell-like structure in the radio (Gray, 1994a, their Figure 10). Comparing the *Herschel* emission by eye with their figure[2], we see bright extended emission to the east of this source and multiple FIR filaments at the location of the SNR. Some of these filaments may be associated with the SNR, although Figure 4.19 shows that this region is very confused and we cannot definitively distinguish SNR and unrelated emission making this a level 2 detection.

4.2 Discussion

4.2.1 Types of sources detected

Here we discuss the detection rates found in our *Herschel* survey of SNRs. The work in this Chapter reveals signatures of dust in 10 (8 %) SNRs in the Galactic Plane (detection level of 1) compared to the 29 detected in Chapter 2 (41 % detection rate). In total, we estimate a FIR detection rate of 21 % of Galactic SNRs with $\mid b \mid \leq 1^{\circ}$ and classed as a level 1 detection. Table 4.3 and Figure 4.20 give a summary of the types of SNRs detected in this study. Of our new FIR detections, we

[2] unfortunately, the radio fits data for this source or region was not available for download online.

Survey	Common Detections	Upgraded Detections	Downgraded Detections
Arendt (1989)	9	15	2
Saken et al. (1992)	7	16	8

Table 4.2: The number of sources detected in common with, upgraded to Level 1 detection, and downgraded from Level 1 in comparison with previous FIR SNR surveys.

observe dust emission from the shell/outer shock region of 8 SNRs, and from the inner ejecta region (interior to the reverse shock) of 4 sources. We detect 1 Type Ia and 1 core collapse SNe. Combining with our earlier survey, this gives *Herschel*-detected SN dust structures in 13 core-collapse SNe, including 4 *confirmed* PWNe, and 2 Type Ia's in the Hi-GAL survey. Including the other *Herschel* discovered dusty remnants in the Milky Way that were not covered by the Hi-GAL survey, that is Cas A, the Crab Nebula, Tycho, Kepler and G292.0+1.8 (hereafter, we name this group the historical dusty SNRs), the final statistics for dust features related to SN structures in the Galaxy are therefore **16 core collapse SNe, including 6 PWNe, and 4 Type Ias** (see Table 4.3). Based on these 20 sources where the SN explosion type is known, our dust-detected sample is made up of 80 % core-collapse SNRs, and 20 % Ia SNRs, closely mirroring the observed rates of core-collapse and Type Ia SN explosions (van den Bergh, 1993; The et al., 2006) with the former occurring at rates of $\sim 2 - 3$ SNe per century (van den Bergh, 1991; Dragicevich et al., 1999; Diehl et al., 2006; Li et al., 2011).

Compared with previous FIR surveys of Galactic SNRs by Arendt (1989) and Saken et al. (1992) our higher resolution at longer wavelengths helps us to better distinguish SNRs from the surrounding ISM, giving us higher detections rates within the Galactic Plane. As shown in Table 4.2, in comparison with previous FIR surveys by Saken et al. (1992) and Arendt (1989) we increase the detection rate of dust in Galactic SNRs, that is from 17 to 24 %, and 13 to 26 % respectively (excluding sources which were not included in the Green (2014) catalogue).

An interesting question is whether there exists a trend with how dusty a SNR is and its age (e.g. Otsuka et al., 2010; Gall et al., 2014). (Ages are listed in Table 2.1 where known, see references therein.) Not including those without estimated ages, Figure 4.20 shows that the highest proportion of our detected sources are young, $\leq$ 5 kyrs, which may be because the SNR is still compact so that surface brightness is higher and therefore more easily 'seen' in the comparison of the multicolour *Herschel* images. The historical dusty SNRs also lie within this age

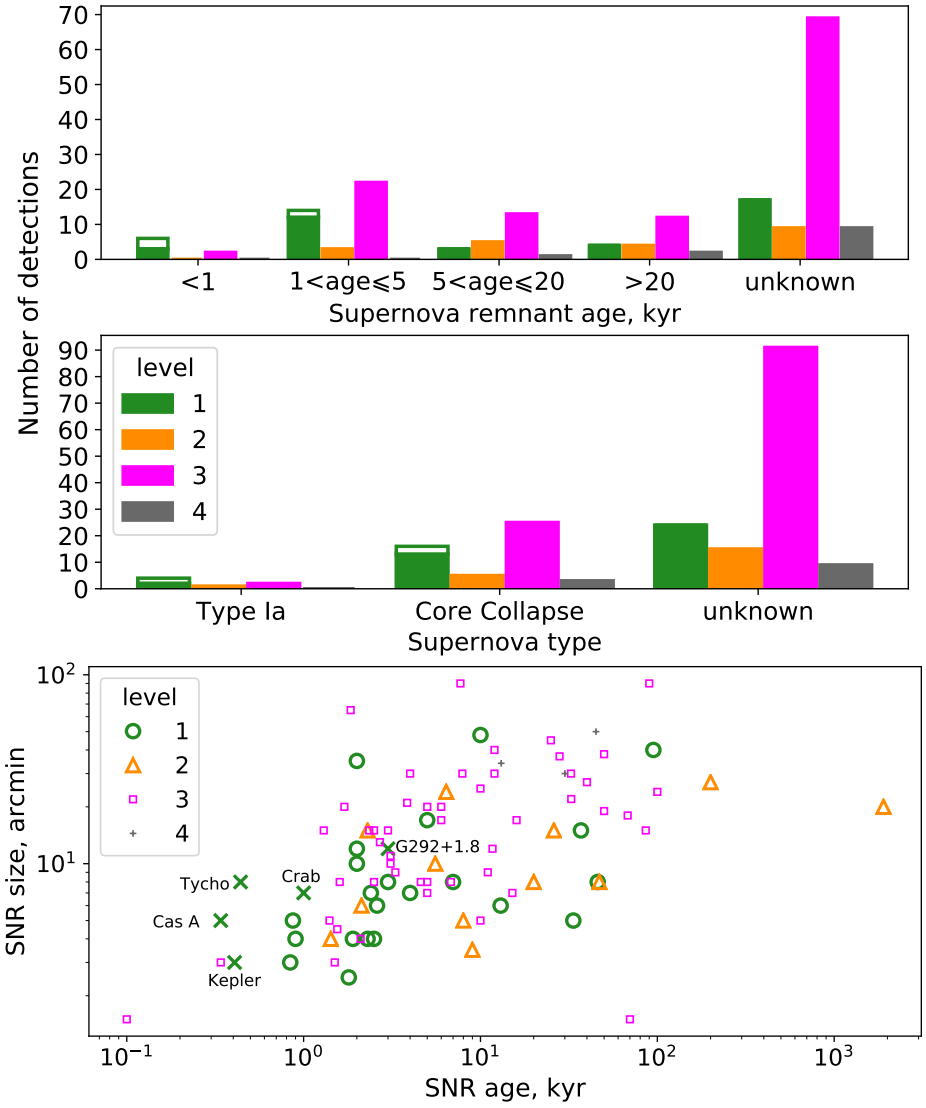

Figure 4.20: As in Chapter 2, we show a summary of the source types detected in the sample, including those in our earlier first look study. *Top*: Filled histograms compare the number of sources with different ages for a given detection classification in Hi-GAL. The unfilled bar includes the previous *Herschel* detections of Galactic SNRs not covered by the Hi-GAL survey: Cas A, the Crab Nebula, Tycho, Kepler and G292.0+1.8. *Middle*: As top panel, but showing the number of sources with different SN types for a given detection classification. *Bottom*: The detection level compared with the size and age of SNR; the crosses indicate the properties of the previous historical SNRs. The age is unknown for 104 SNRs from our sample.

Detection Type		Number Detected		
		C19	This Work	Historical
SNR Region ♮	Shell / outer shock region	23	8	3
	Inner ejecta region *	8	4	3
	Confirmed PWN †	4	0	1
	Interacting molecular cloud	0	1	
Age (kyr)	≤ 1	2	1	3
	$1 < \text{Age} \leq 10$	12	2	2
	$10 < \text{Age} \leq 20$	1	0	
	>20	4	0	
	Unknown	9	7	
SN Type	Type Ia	1	1	2
	Core collapse	12	1	3
	Unknown	16	8	

Table 4.3: Summary of the level 1 detected sample in this work and combining with our earlier survey in Chapter 2. We also include the previously detected *Herschel* Galactic SNRs as 'historical remnants': Tycho, Kepler, Cas A, the Crab Nebula and G292.0+1.8. * Sources from which we detect FIR emission from the inner region are: G11.2−0.3, G16.4−0.5, G21.5−0.9, G21.5−0.1, G29.7−0.3, G34.7−0.4, G54.1+0.3, and G344.7−0.1 (this work), and G306.3−0.9, G350.1−0.3, G351.2+0.1, and G357.7−0.1 (this work). †SNRs for which there is evidence that the detected central region is associated with the confirmed PWN. We note that G351.2+0.1 could be associated with a PWN (see Section 5.2).

range (Figure 4.20), indeed these are mostly clustered towards younger ages than the majority of the det=1 SNRs in our Hi-GAL survey (where the youngest det=1 SNR is the core-collapse SNR G29.7−0.3, Kes 75). This suggests that the previous historical dusty SNRs were biased to the youngest (and potentially dustiest) objects, whereas the sample in this work has detected dust signatures associated with SNRs at a wider range of ages up to 10^2 kyr.

However, for all SN ages and types we are more likely to find level 3 detections, where there is only unrelated FIR emission in the region. Although this may imply that there is no dust within these SNRs, we are also greatly affected by confusion in cases where sources may have a similar dust temperature to ISM dust or is already starting to mix with the ISM (i.e. larger/older), wherein it becomes more difficult to separate ejecta and unrelated material. We therefore expect that the detection levels quoted here are a lower limit on the number of SNRs within the Galactic Plane which contain dust.

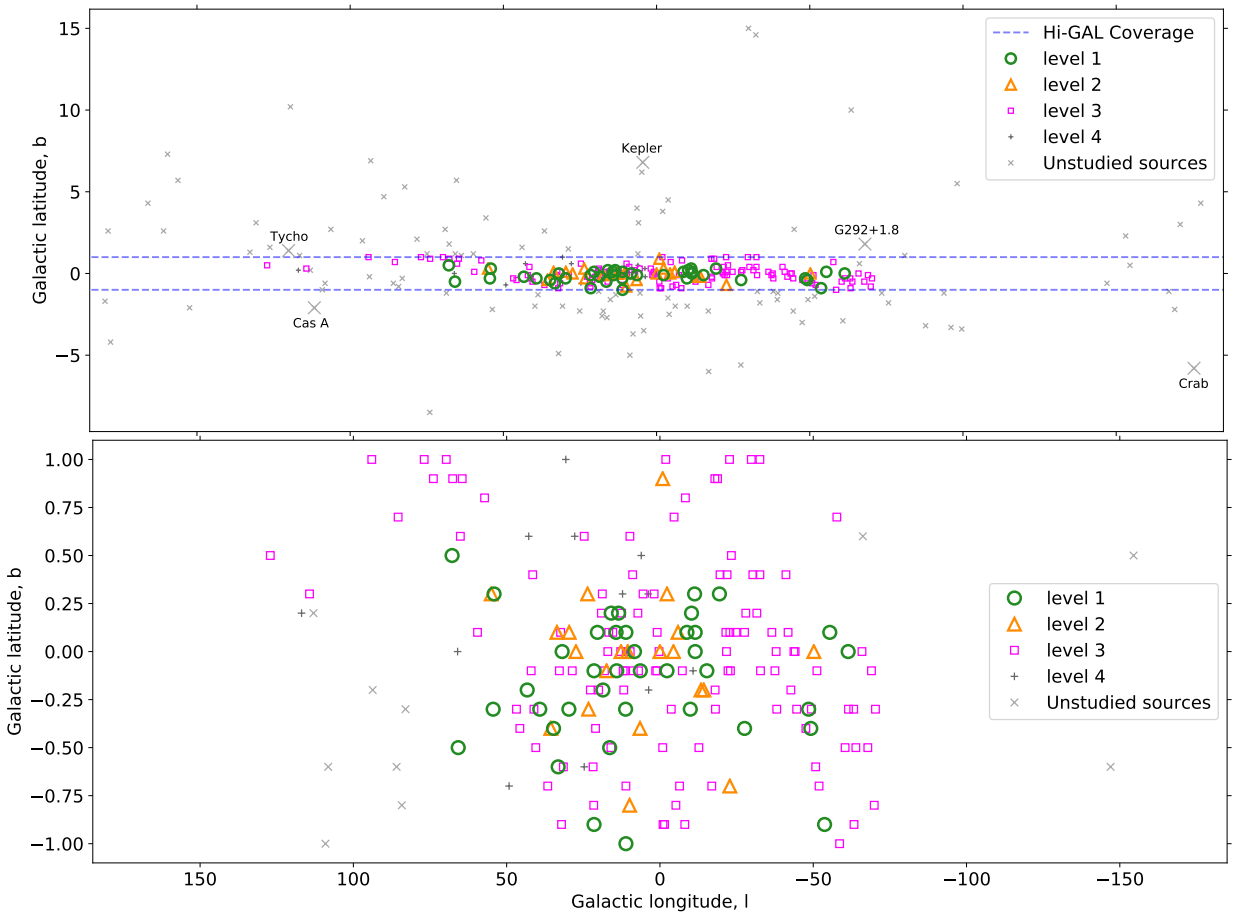

Figure 4.21: Location of Galactic SNRs from Green's catalogue as a function of their assigned detection number, 1–4 (green circles, orange triangles, magenta squares, and grey plus signs respectively) and those not covered in the Hi-GAL survey (i.e. not studied here) shown by the grey crosses. The dashed blue lines indicate the extent of the area surveyed by Hi-GAL. *Top*: All SNRs from Green's catalogue. *Bottom*: Sources within the Galactic Plane with $\mid b \mid \leq 1$ (including Chawner et al., 2019). Hi-GAL data are unavailable for 10 sources within the Galactic Plane.

4.2.2 A Closer Look at the Type Ias Detected in the Surveys

Previous studies of FIR emission associated with Type Ias remnants have attributed it to swept up ISM, rather than ejecta dust produced by the SNR. This leaves uncertainty as to whether dust can be formed by Type Ia SNe. The detection of SN-related dust features in the *Herschel* images of the Type Ias G306.3−0.9 (Section 4.1.2) and (in Chapter 2) G344.7−0.1 (Section 2.1.2) could provide further insight into dust formation in Ia SNRs. These are unusual cases since, at first glance, the IR emission appears to originate from reserve shock-heated material and therefore provides an opportunity to search for the presence of dust cooler

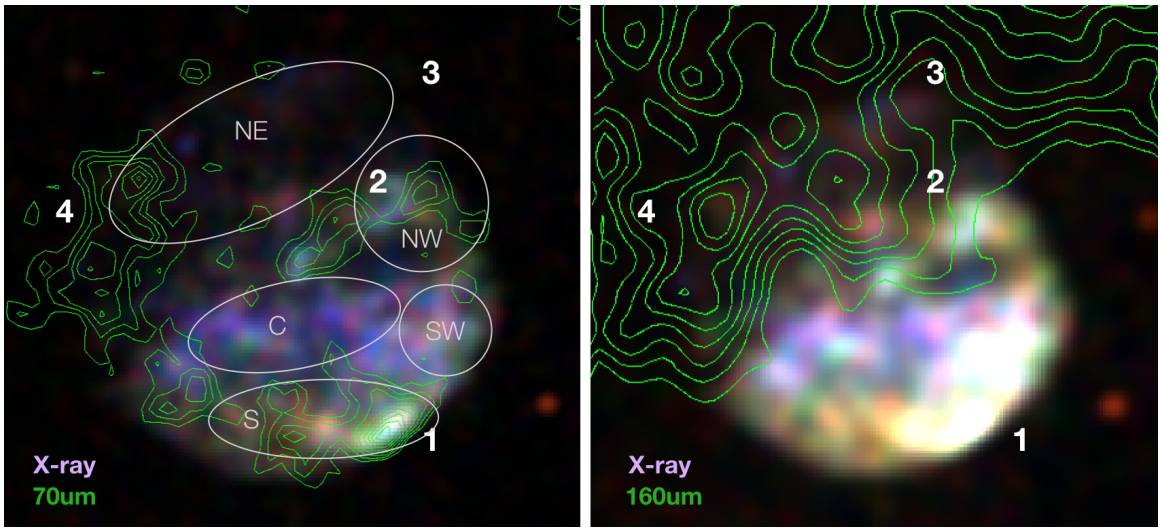

Figure 4.22: G306.3−0.9 *Left:* three colour X-ray image using *Chandra* archive images at 0.73-1.47 keV (red), 1.47-2.2 keV (green) and 2.2-3.3 keV (blue) with *Herschel* 70 μm contours overlaid. See Reynolds et al. (2013); Combi et al. (2016) for further details of the X-ray features. X-ray 'distinct' regions from Combi et al. (2016) are labeled, where regions NE, C and SW are attributed to ejecta material, and regions NW and S are consistent with foreground shock material. Dust features are labeled 1–4. *Right:* X-ray image with enhanced scale contrast and *Herschel* 160 μm contours added revealing the (potentially foreground) interstellar cloud to the north of the SNR.

than 60-100 K. However, we will show here that for both these SNRs, the dust observed in the remnants is in fact related to material swept up by the blast wave or unrelated interstellar clouds, and not due to emission from dust in the ejecta.

4.2.2.1 THE SNR G306.3−0.9

Figure 4.22 compares the *Herschel* emission at 70 μm with the X-ray distinct regions from Combi et al. (2016). NE, C, and SW show the location of the reverse shock heated ejecta regions and NW and S show regions where the X-ray originates from forward shock material. We see that the dust emission is concentrated in the south, with very little dust at 70 μm in the north-east. First we see the southern ridge from Reynolds et al. (2013) along the edge of the SNR (labeled '1' in Figure 4.22) coincident with the bright X-ray rim (and X-ray peak) in region S. This is also coincident with a limb brightened outer radio shell. The central ridge across the front of the remnant is bright at both 24 and 70 μm (labeled '2' in Figure 4.22) and overlaps with the NW X-ray region from Combi et al. (2016). There is also larger scale emission overlapping at the northern most edge of the SNR and

extending beyond the remnant (as traced by the radio shell), this peaks at wavelengths greater than 160 μm (labeled '3').

Here we also identify another dust feature in the *Herschel* maps (labeled '4' in Figure 4.22). This is a bright elongated structure to the east of the SNR which has two peaks, and lies slightly ahead of the radio shell. It appears to overlap with the eastern-most part of the NE X-ray region from Combi et al. (2016) but has very little associated X-ray and 24 μm emission. This dust feature has a very different colour to features 1 and 2, and is similar to feature 3, suggesting the dust temperature is cooler. Given the lack of X-ray and radio emission associated with features 3 and 4 and their different colour, we suggest they are unrelated to the SNR even though feature 4, at first glance, appears to be a continuation of the southern dust shell along the eastern side. Instead we propose these are part of a dust cloud that lies in front of the remnant in the north (as seen clearly in the 160 μm emission). The remaining SN-related dust features (1 and 2) originally seen in the 24 μm *Spitzer* data are spatially coincident with the forward shock material regions NW and S in Combi et al. (2016). Thus these are entirely consistent with swept up dust grains.

4.2.2.2 The SNR G344.7−0.1

SNR G344.7−0.1 has an asymmetric shell structure in the radio (Whiteoak & Green, 1996) with a bright region to the northwest. X-ray emission towards the centre correlates with the radio but the radio peaks are further away from the centre compared to the X-ray peaks (Giacani et al., 2011). This source is classified as a mixed-morphology Type Ia SNR by Yamaguchi et al. (2012) due to the elemental abundances and discovery of Fe-rich ejecta, though previous authors have argued it may be a core-collapse remnant (Combi et al., 2010a). The mixed-morphology classification for a Ia is rare, and is argued to be the result of an interaction with the ISM, with a density gradient to the west visible in both radio and X-rays to a lesser extent (e.g. Giacani et al. 2011; Andersen et al. 2011). The radio emission is brighter on the western side, with a bright radio peak observed just north to the centre of the SNR (hereafter the northern knot) where there is little X-ray emission. A pulsar wind nebula origin for this knot was ruled out by Giacani et al. (2011), instead they concluded that this bright radio feature is probably the result of strong shocks interacting with dense material.

This SNR was listed as a level 1 detection for SN-associated dust in the 3.6-8.0 μm NIR *Spitzer* catalogue of Reach et al. (2006) and the *Herschel* catalogue in this work (Chapter 2, Chawner et al., 2019). MIR dust features, including one that

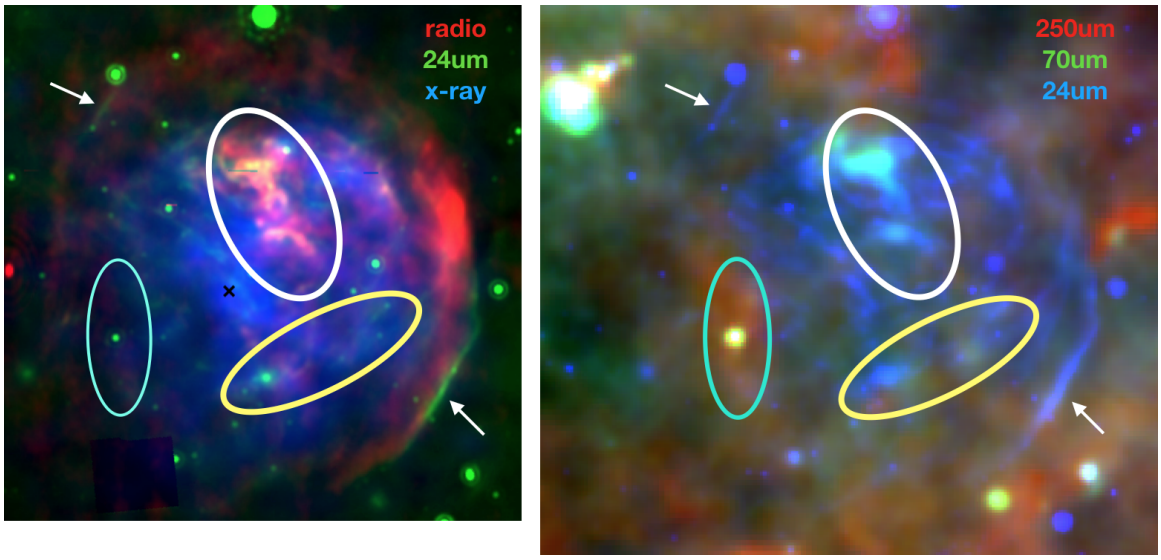

Figure 4.23: G344.7−0.1 - *Left:* Three colour image showing the X-ray (*Chandra* wide band 2.1-10 keV available from the *Chandra* SNR catalogue), radio (MOST) and hot dust emission at 24 μm (*Spitzer*) adapted from Giacani et al. (2011) (similar images have been shown in Combi et al. 2010a and Yamaguchi et al. 2012). The ellipses mark out interesting dust features (discussed in the main text). *Right:* Three colour dust image of the SNR combining 24 μm from *Spitzer* (blue) with the *Herschel* 70μm (green) and 250 μm (red); this image covers a slightly larger region than the left image. The emission seen in 'red' in the three colour dust image are likely from unrelated material, with the northern, western and eastern structures spatially coincident with atomic hydrogen in the vicinity of the SNR (Giacani et al., 2011).

overlaps with the bright radio knot towards the north, filaments and arcs were discovered in the *Spitzer* 24 μm image (Combi et al., 2010a), and were attributed to dust orginating from a swept up shell, with the emission lying ahead of the X-rays from the SN blast wave or coincident with radio features attributed to interaction with the ISM (Reach et al., 2006; Giacani et al., 2011; Yamaguchi et al., 2012). Andersen et al. (2011) derived a total dust mass of 0.58 $M_\odot$ with temperature 66 K and attributed it to shock-heated swept-up dust. Figure 4.23 (left) is adapted from Giacani et al. (2011) and compares the 24 μm, radio and X-ray emission[3]. Dust features detected in earlier works are labeled, including: MIR 'arcs' that lie ahead of the radio blast wave (arrows) and the location of the bright dust knot in the north coincident with a radio peak (which is also coincident with a gap in the X-ray emission - white ellipse). Beyond these known dust features, we label two other potentially interesting regions in the SNR: a region that includes a bright

[3] data are available from http://hea-www.cfa.harvard.edu/ChandraSNR/index.html

24 μm point source (cyan ellipse) and a region that includes both filamentary and point source emission at 24 μm (yellow ellipse). A three colour image comparing *Herschel* emission at 70 and 250 μm with the 24 μm emission is shown in the right panel of Figure 4.23. The 24 μm dust arcs from swept up material (indicated by the arrows) are not visible in the *Herschel* data, and most of the SNR dust seems to be brightest at 24 μm except for the bright northern structure which peaks at 70 μm (white ellipse).

The cyan ellipse in Figure 4.23 (left) includes a bright point source at 24um to the south-east of the SNR centre. This appears to be embedded in a more extended dust structure at wavelengths longer than 70 μm, and becomes brighter and more extended at 250 μm. This structure extends 'vertically' across the image (see the red emission in Figure 4.23, right). At 250–500 μm we also see large-scale dust structures with similar 'colours' outside the remnant to the north and to the west overlapping with a known HI cloud (Giacani et al., 2011), where the SNR is thought to be expanding into the ISM. We therefore propose that the 'red' dust features in Figure 4.23 (including the region in the cyan ellipse) are unrelated to the SNR and are interstellar in origin. These dust structures are consistent with faint neutral hydrogen seen around G344.7−0.1 near $v_{\rm LSR} \sim -115\,{\rm km\,s^{-1}}$ (see Figure 5 from Giacani et al., 2011).

The yellow ellipse in Figure 4.23 (left) indicates the location of 24 μm filaments and point sources which overlap with clumps of dust in the 70 μm image, just south of the centre of the remnant. To check if these dust clumps are related to the SNR or correlate with known ejecta material, we compared their location with X-ray emission from the Si-K and Fe-K emitting gas observed in the centre of the remnant using deep *Chandra* images (Yamaguchi, H *priv.comm*, see also the similar emission features seen in Suzaku data - Yamaguchi et al., 2012). We find no evidence that any of the dust clumps in the *Herschel* images are spatially coincident with the interior X-ray emitting knots and/or structures. Instead it is likely these clumps are part of the unrelated cloud complex that extends across the south (south of the radio shell).

This leaves only the previously detected northern dust knot (seen in both *Herschel* and *Spitzer* observations), and the 24 μm arcs/filaments as features we can associate with the SNR. Given the previous association of the coincident radio feature to the north with shocks interacting with dense material (Giacani et al., 2011), we argue there that the dust features are entirely consistent with emission from swept-up dust grains at the edge of a shell, where the SN is sweeping

up/interacting with clouds.

Is the lack of ejecta dust in these Ia's surprising? The theoretical model of dust formation in the ejecta of Type Ias from Nozawa et al. (2011) suggests approximately 0.1 $M_{\odot}$ of dust should form and survive the environment of a Ia SNR for at least 400 years. However, the lack of a hydrogen shell in Type Ias gives rise to faster expansion of its ejecta and a lower gas density. Any dust which can condense in these conditions is expected to be dominated by very small grains which are efficiently sputtered by hot gas in the reverse shock. Observations of the historical Type Ia SNRs Tycho and Kepler found a smaller dust mass than that predicted by the Nozawa et al. (2011) model (Gomez et al., 2012a), suggesting either that there is more efficient destruction or dust production is inhibited. The lack of cold dust grains in the ejecta of these four Galactic Type Ia SNe therefore suggests that if Type Ia remnants contain any ejecta dust, it is significantly less than that formed in core-collapse explosions.

4.2.3 The distribution of dusty SNRs in the Galactic Plane

Figure 4.21 shows the location of all of the SNRs studied within the Galactic Plane with *Herschel* as part of the Hi-GAL survey. We find that the majority of the SNRs with clear dust signatures (detection level = 1) are located towards the central regions of the Galactic Plane in both longitude and latitude. This distribution follows the number density of SNRs in general, which are concentrated towards low latitudes and in the inner regions of the Galaxy (Figure 4.21, top panel).

The distribution of the 'dust-detected' sources in this work can be explained due to our sample being dominated by the remnants of core-collapse SNe, which make up the majority of SNRs in the Galaxy. Core-collapse remnants are observed to be found at lower latitudes, closely linked to star forming regions concentrated in the thin disc of the Galaxy (Hakobyan et al., 2016). Instead, Type Ia's, which constitute only a small fraction of our det=1 sample with known SN types, are observed to lie at a wider range of latitudes, with Galactic scale heights of ~ 2 times that of core-collapse remnants (Hakobyan et al., 2017) due to their association with the older stellar population. We may therefore be biased against finding dust in Type Ia SNRs in this work.

In order to interpret the distribution of dusty SNRs in the Galaxy, we need to first note our selection effects. Although we start from a blind *Herschel* survey of the sky with Hi-GAL, and as such the dust information is 'complete' within $b \pm 1^{\circ}$, due to the high levels of confusion in the FIR we have to rely on the known

locations of SNRs, where we have used the Green (2004) catalogue. Since this is the fundamental selection effect for this work, here we briefly mention its completeness. Green (2015) comments that the Galactic SNR catalogue is likely missing intrinsically faint radio SNRs, SNRs where the physical size is small (diameters $< 1.5'$), and more distant SNRs with smaller angular sizes, as well as many sources having uncertain distances due to the use of the $\Sigma - D$ relation[4]. Therefore our sample will also suffer from the same selection effects. We note that our det=1 sampled follows the same l, b distribution as their radio-bright SNR subsample with a surface brightness cut (see Figure 4.24) which they argue suffers from fewer selection effects than the whole Galactic radio SNR catalogue. However, the overlap between our detections and the bright SNR sample can be attributed to the fact that we rely on the radio images (where available) to identify SN-related dust features.

We include the historical dusty SNRs for reference in Figure 4.21. These lie outside the inner Galactic Plane, and yet still have associated dust features (and indeed a significant amount of ejecta dust). Again this implies that the detection levels quoted here are likely lower limits, since there are $\sim$100 more SNRs in the catalogue of Green (2014) not included in the region surveyed by Hi-GAL (Figure 4.21, top panel).

Our previous study covered $10 \leq \mid l \mid \leq 60^{\circ}$. Although this study covers the entire Galactic longitude range, the majority of additional sources are within $\mid l \mid \leq 10^{\circ}$. This region is heavily contaminated with ISM dust, resulting in a lower detection rate in this study compared with our first look sample in Chapter 2. An additional factor causing a lower detection rate in this Chapter compared to that seen in Chapter 2 could be the lack of *Spitzer* data in some regions; in particular *Spitzer* MIPS 24 μm has better spatial resolution than *Herschel* which helps to identify warm SN dust structures more confidently. In our study, the majority of the SNRs are classified as 'heavily confused' in these regions. We remind the reader that the requirement of ancillary X-ray, radio or optical data in order to identify SN features against the surrounding ISM/CSM, and the non-uniformity of the availability and quality of this data may have further resulted in a bias in our Hi-GAL Galactic Plane SNR sample.

In summary, we are more likely to detect dust in remnants where we have

[4] The distance to Galactic SNRs can be estimated using the relation between its radio surface brightness and its diameter, $\Sigma \propto D^{\beta}$, as larger SNRs tend to have a lower surface density. Distances estimated in this way are very uncertain as many environmental factors affect both the surface density and the size of SNRs.

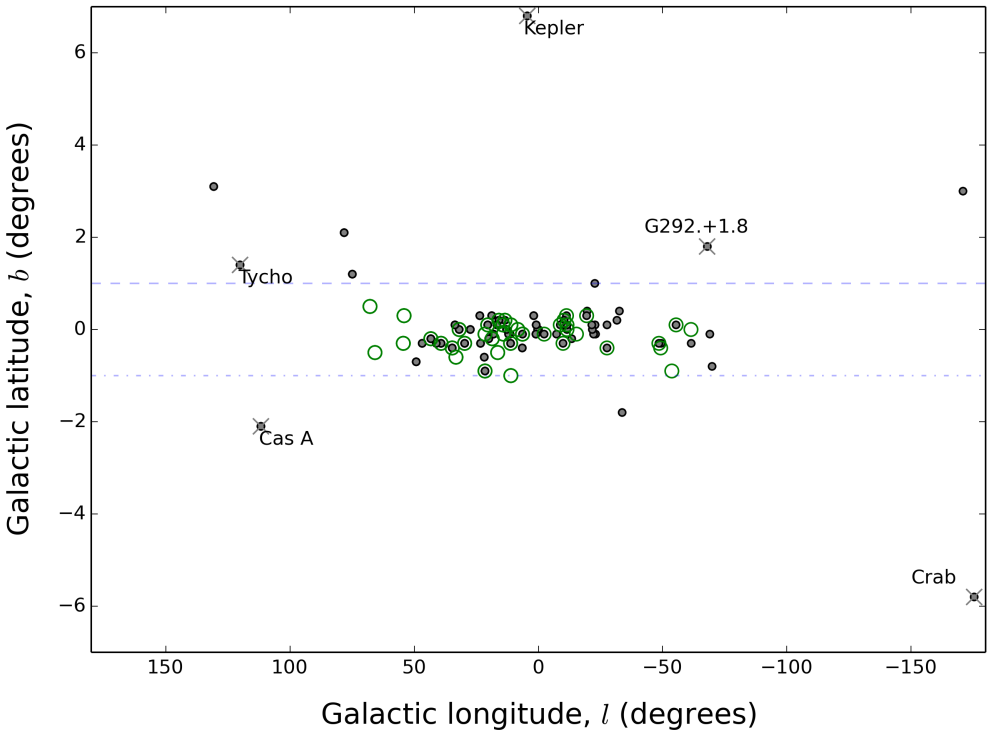

Figure 4.24: A comparison of the location of the detected level 1 SNRs from this work (green open circles) and the radio bright Milky Way SNR sample from Green (2015), with radio brightness cut of $(1\,\mathrm{GHz}) > 10^{-20}\,\mathrm{W\,m^{-2}\,Hz}$ (grey). Some historical SNRs are also shown.

good quality ancillary radio, X-ray, optical or *Spitzer* 24 μm images, that are located at low galactic latitudes due to both the higher concentration of core-collapse SNRs and bright radio SNRs in these regions, with PWNe due to the additional heating source that raises the SN dust temperatures above the ambient ISM level (similarly for shock heated dusty shells).

4.3 Conclusions

We searched for far-infrared (FIR) counterparts of known supernova remnants (SNRs) in the entire Galactic Plane, as surveyed by *Herschel* at $70-500\,\mu$m, to supplement the first-look catalogue of 71 SNRs studied in Chapter 2 (Chawner et al., 2019). Of 119 sources studied here, we find that 10 (8 %) have a clear FIR detection of dust associated with the SNR. When combined with our earlier work, this gives a total of 39 FIR detected sources out of 190 known remnants with $|\ b\ | \leq 1^\circ$ across the entire Galactic Plane (a detection rate of 21 %): with dust

signatures detected in the remnants of 13 core-collapse supernovae (SNe), including 4 Pulsar Wind Nebulae (PWNe), and 2 Type Ia SNe. A further 24 are detected in sources with unknown types.

Additionally we have shown that:

- We tend to detect dust in younger SNRs although we widen the age range of dusty remnants, detecting SNRs up to 10^2 kyr.
- We confirm the detection of ejecta dust within the core-collapse SNR G350.1−0.3, as seen in *Spitzer* 24 μm and now *Herschel* 70μm images. This adds to a sample of only ∼10 SNRs from which ejecta dust has been observed and indicates that SNe can form dust grains from elements synthesised by the SN explosion. We see no evidence of cooler dust in the ejecta nor dust located at the location of the compact central object.
- We suggest that the dust features previously proposed to be related to the G357.7+0.3 SNR (seen previously with *Spitzer*) are dust bubbles associated with young star forming regions, and not with the SNR itself.
- We reveal dust emission from the centre of the SNR G351.2+0.1 and from G357.7−0.1 (The Tornado). We will return to these sources in later Chapters.
- We observe dust structures in the *Herschel* images associated with the SNR from two Type Ia SNe, doubling the previous sample size of SN-related dust structures known in Type Ia SNRs. However, we find no evidence that there is cool dust emission within these remnants associated with the ejecta. Instead the *Herschel* features are consistent with MIR dust discovered at 24 μm and can be attributed to swept-up dust in the ISM or, are from unrelated material along the line of sight.

CHAPTER 5
PROPERTIES OF DUSTY SUPERNOVA REMNANTS

'In physics, you don't have to go around making trouble for yourself - nature does it for you.'

FRANK WILCZEK

In Chapter 4 we assigned detection levels based on the FIR emission of Galactic plane supernova remnants in the Hi-GAL survey. Here we look at some of the properties of the dust emission detected in the level 1 SNRs, in particular, focusing on the dust masses and dust temperatures. Dust heated by the PWN, a reverse shock, or a forward shock in a supernova remnant should lead to differences in dust temperatures compared to that in the surrounding interstellar medium since shocks lead to high temperature electrons which can collisionally heat dust grains (Dwek & Arendt, 1992). We will also investigate collisional heating as a source of the dust temperatures in the Level 1 dusty supernova remnants. The work in this Chapter has been published in Chawner et al. (2020).

5.1 DUST PROPERTIES OF LEVEL 1 DETECTED GALACTIC SUPERNOVA REMNANTS

We search for detection level 1 SNRs that are not in overly complex/crowded regions of the Galactic Plane, and sources that have not previously been studied in detail (this excludes G11.2−0.3, G21.5−0.9, G29.7−0.3 (see Chapter 3), G54.1+0.3 (Temim et al., 2017; Rho et al., 2018), and G357.7−0.1 (see Chapter 6). This leaves

us with a total of 11 sources out of the 39 level 1 detected SNRs. We create temperature maps of the dust in these SNRs (simulations of the temperature maps are discussed in full in Section 5.1.3) after estimating the background flux using the Nebuliser routine[1], which subtracts medium to large scale variations in the background of astronomical images.

5.1.1 Accounting for Contamination from Unrelated Interstellar Dust in the Level 1 SNRs

A large number of our level 1 detected sample are in complicated regions of the ISM where there are large variations in the fore- and background intensity. We minimise this issue by subtracting contamination from the ISM using the Nebuliser routine. Nebuliser estimates medium to large scale variations in the background which can be subtracted from our SNR regions to give a more accurate background-subtracted map. In brief, the Nebuliser algorithm takes a square of N by N pixels around a pixel and estimates the median of the intensities centred on that pixel to estimate the background at that position. The background map is smoothed using a box-car mean filter with box size chosen to be $N/2 \times N/2$ (Irwin, 2010). The value of N used varies between 75 and 350, depending on fluctuations in the background and size of the SNR, and in some cases we mask bright sources to avoid overestimating the background. We will demonstrate later in Section 5.1.3 that this approach can be used to accurately determine the properties of SNR source-related structures.

5.1.2 Far-infrared Fluxes for Level 1 Detected Remnants

[1] http://casu.ast.cam.ac.uk/surveys-projects/software-release/background-filtering

SNR	Flux (Jy)				
	70 µm	160 µm	250 µm	350 µm	500 µm
G8.3−0.0	1060 ± 76	1900 ± 135	884 ± 49	370 ± 21	
G11.1+0.1	1250 ± 675	2940 ± 2550	2102 ± 1800	1010 ± 766	425 ± 298
G16.4−0.5*	2770 ± 1211	8910 ± 4054	6582 ± 1770	2960 ± 1140	1210 ± 321
G20.4+0.1*	980 ± 241	1510 ± 918	897 ± 607	378 ± 250	148 ± 95
G21.5−0.1*	491 ± 62	1050 ± 241	697 ± 164	303 ± 69	120 ± 27
G43.3−0.2	745 ± 61	284 ± 135	74 ± 114	21 ± 54	5 ± 23
G65.8−0.5*	76 ± 6	97 ± 20	22 ± 19	8 ± 10	2 ± 4
G67.8+0.5	107 ± 8	204 ± 21	101 ± 10	47 ± 5	18 ± 2
G310.8−0.4	1730 ± 594	2150 ± 1510	935 ± 1019	364 ± 449	162 ± 184
G340.6+0.3	221 ± 30	755 ± 118	507 ± 85	208 ± 37	80 ± 14
G349.7+0.2	588 ± 42	457 ± 33	159 ± 9	60 ± 4	20 ± 1

Table 5.1: The SNR flux is measured within the dashed white circle in Figure 5.5 from background subtracted maps convolved to the resolution of the 500 µm *Herschel* map. In some cases point sources within the aperture are masked before measuring the flux. Uncertainties are estimated from the standard deviation of the background map within the aperture and the *Herschel* calibration uncertainty. *Sources which may be confused with a HII region (Anderson et al., 2017; Gao et al., 2019).

After subtracting the medium-large scale background with Nebuliser (see Figure 5.1) we estimate the FIR flux from each SNR in five *Herschel* wavebands. For several of our sample there is some contamination remaining in the background-subtracted maps as there is structure of a similar scale to the SNR which is difficult to remove. In these cases we apply a secondary subtraction estimated from the average level using an annulus. The fluxes for our 11 SNRs are shown in Table 5.1.

The uncertainty associated with the flux is estimated using a combination of the *Herschel* calibration uncertainty, variation of the Nebuliser background map within the aperture, and, where applicable, variation within the annulus used for a secondary background subtraction. In these sources the contaminating ISM flux may affect our estimates of the dust temperature, nevertheless, this effect will be much reduced compared with temperatures estimated without any background subtraction.

5.1.3 Can we use Nebuliser background subtracted maps to estimate robust temperatures?

Due to the location of the Galactic Plane SNRs, there is significant contamination from foreground/background interstellar emission for most of our sample and many of the sources (even the level 1 detections) are faint in comparison to the surrounding or foreground/background ISM. As such, any dust temperatures and dust masses derived could be significantly affected by this issue, more so than in studies of SNRs in the Large Magellanic Cloud which is a face-on galaxy. This is the biggest limitation when attempting to measure dust masses and temperatures in a statistical sample of Galactic SNe.

We test the effect of this by simulating a dusty SNR for a bright and faint case. Both simulated SNRs with varying temperatures have the same 70/160 colours, but the former is chosen to be high signal-to-noise, well above the brightness of the ISM (the simulated SNR has surface brightness levels of up to $\sim$9,000 MJy/sr and $\sim$3200 MJy/sr at 70 and 160 μm respectively compared with an average ISM value of $\sim$390 and $\sim$1370 MJy/sr), and the latter is at a similar level to the brightness of IS clouds seen at off-SNR points in our Hi-GAL maps (with 70 μm fluxes in the SNR $\sim$10 times fainter than the bright case). Our simulation consists of a SNR with an outer shell of dust with temperature 65 K (to simulate dust heated in forward shock regions e.g. Cas A (Rho et al., 2008)) and two cooler components of ejecta dust (at 25 K and 37 K) to simulate cooler ejecta dust similar to the observed PWNe remnants (Chawner et al., 2019) and a Cassiopeia A-like SNR (Barlow et al., 2010;

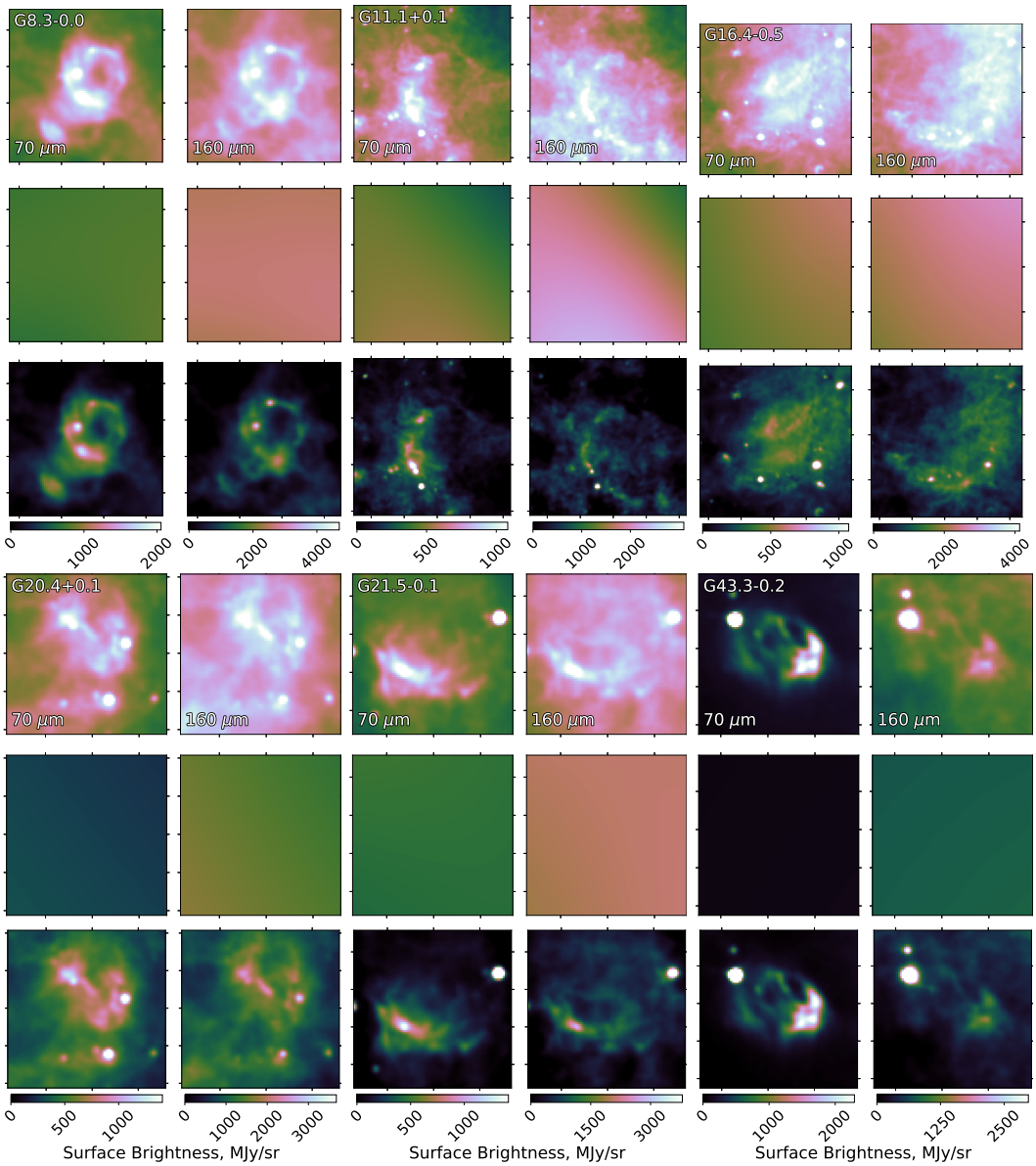

Figure 5.1: Postage stamps illustrating the background subtraction using Nebuliser for 70 µm (left) and 160 µm (right). In rows of three: *top:* original image without the background subtracted, *middle:* background estimated by Nebuliser, and *bottom:* background subtracted image. The SNR name is given in the top-left of the 70 µm non-background subtracted image.

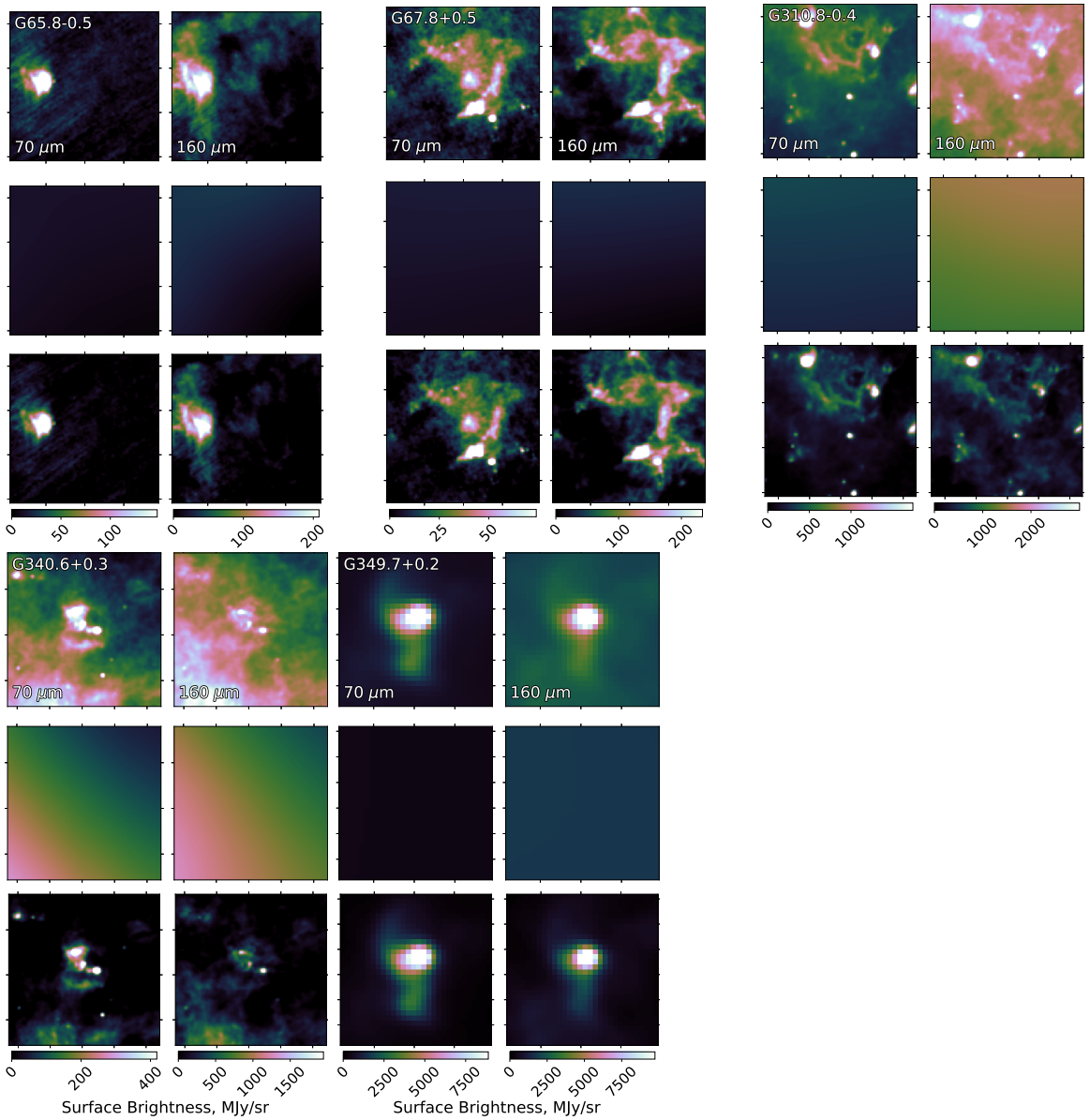

Figure 5.1: - *continued.*

De Looze et al., 2017).

We recover the input temperatures from the simulated SNR perfectly using the equation:

$$\frac{F_{70}}{F_{160}} = \left(\frac{\lambda_{160}}{\lambda_{70}}\right)^{\beta+3} \frac{\exp\left(\frac{hc}{\lambda_{160}kT}\right) - 1}{\exp\left(\frac{hc}{\lambda_{70}kT}\right) - 1}, \tag{5.1}$$

where F_{70} and F_{160} are the flux densities at 70 and 160 µm, λ is the wavelength, h is the Planck constant, c if the speed of light, k is the Boltzmann constant, and T is the dust temperature.

The simulated source is then placed onto a region of the Hi-GAL survey at $\alpha = 18^{h}07^{m}58^{s}, \delta = -19°27'16''$ (l = 10.7537, b = 0.364) as shown in the top panels of Figure 5.2, this region is chosen as there is a large variation in the background level, as is the case for several of our level 1 detected SNRs. Equation 5.1 is then used to create the dust temperature map. We see that the output dust temperatures are significantly biased towards lower temperatures than the input simulation. Across the map, the dust temperatures are lower by $5 - 15$ K compared to the simulated source, simply as a result of placing the simulated SNR onto a region with background interstellar emission. This situation is further compounded if we take the fainter simulated SNR (which is much more comparable to our real detection level 1 sources). Here the output temperatures range from 20 – 30 K compared to the input 20 – 65 K, with an offset of 30 K in the shell. For the faint source simulation, we also see more variation in the output shell temperatures compared to the bright source. It is clear that for fainter dusty SNRs, the ISM contamination affects the output dust temperatures by significant amounts (and ultimately could lead to orders of magnitude errors in any estimate of the dust mass, depending on the dust size and composition).

To address this we test the effects of attempting to remove the background level and re-derive the temperatures using Equation 5.1 on the background subtracted 70 – 160 μm simulated images. The background level for the simulated SNR is estimated, and then subtracted, using the Nebuliser routine[2] from the CASUTools suite. Nebuliser takes a region around the SNR to model large scale variations in the ISM level and then subtracts this to return a map with a zero average. We use Nebuliser as it allows us to model variations in the ISM level, rather than assuming a constant level which does not accurately represent the entire region.

[2] http://casu.ast.cam.ac.uk/surveys-projects/software-release/background-filtering

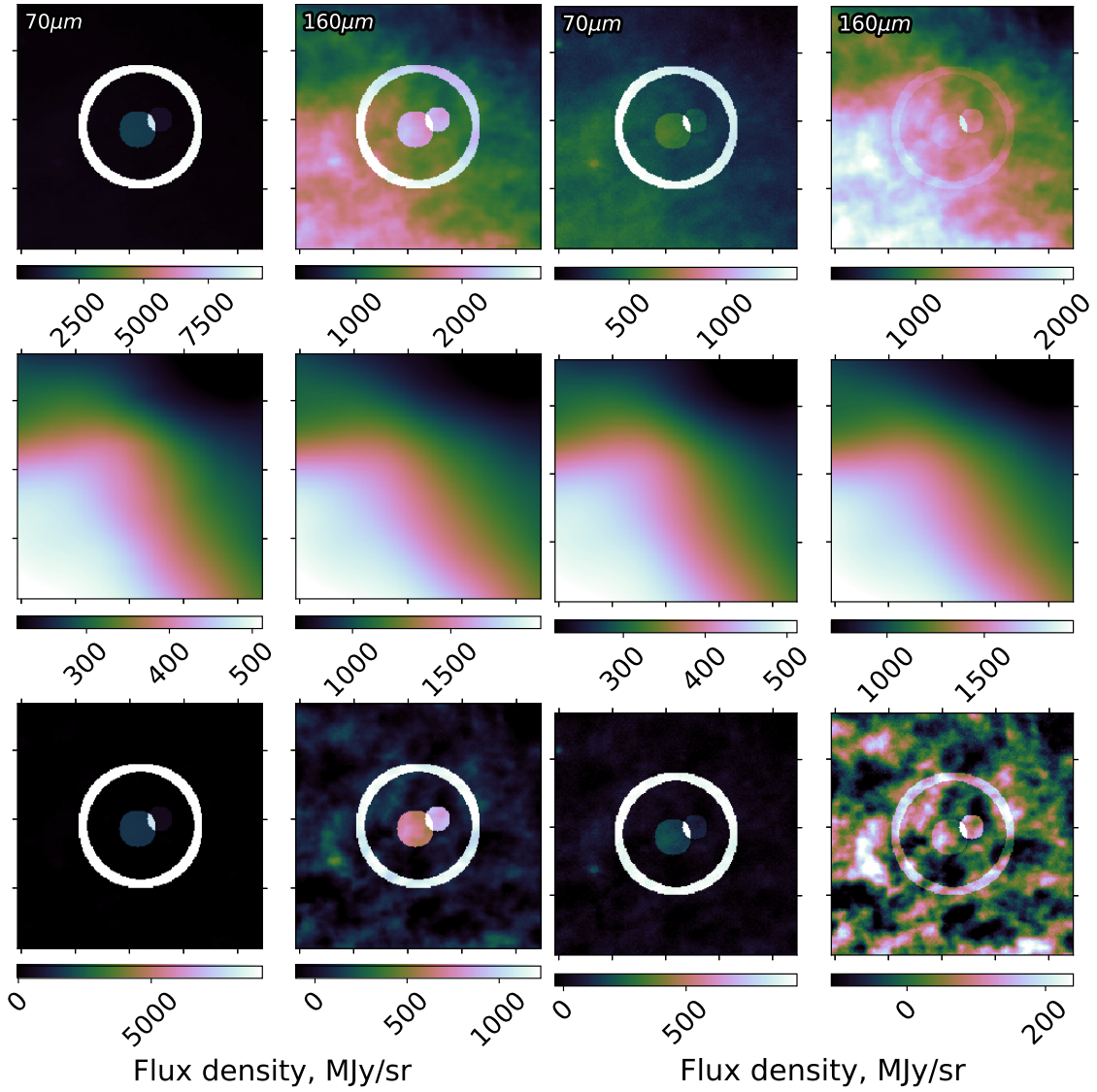

Figure 5.2: Background subtraction using the Nebuliser routine applied to the bright simulated source (left) and the less bright case (right). *Top:* images prior to background subtraction, *middle:* background estimated by Nebuliser, and *bottom:* background subtracted image.

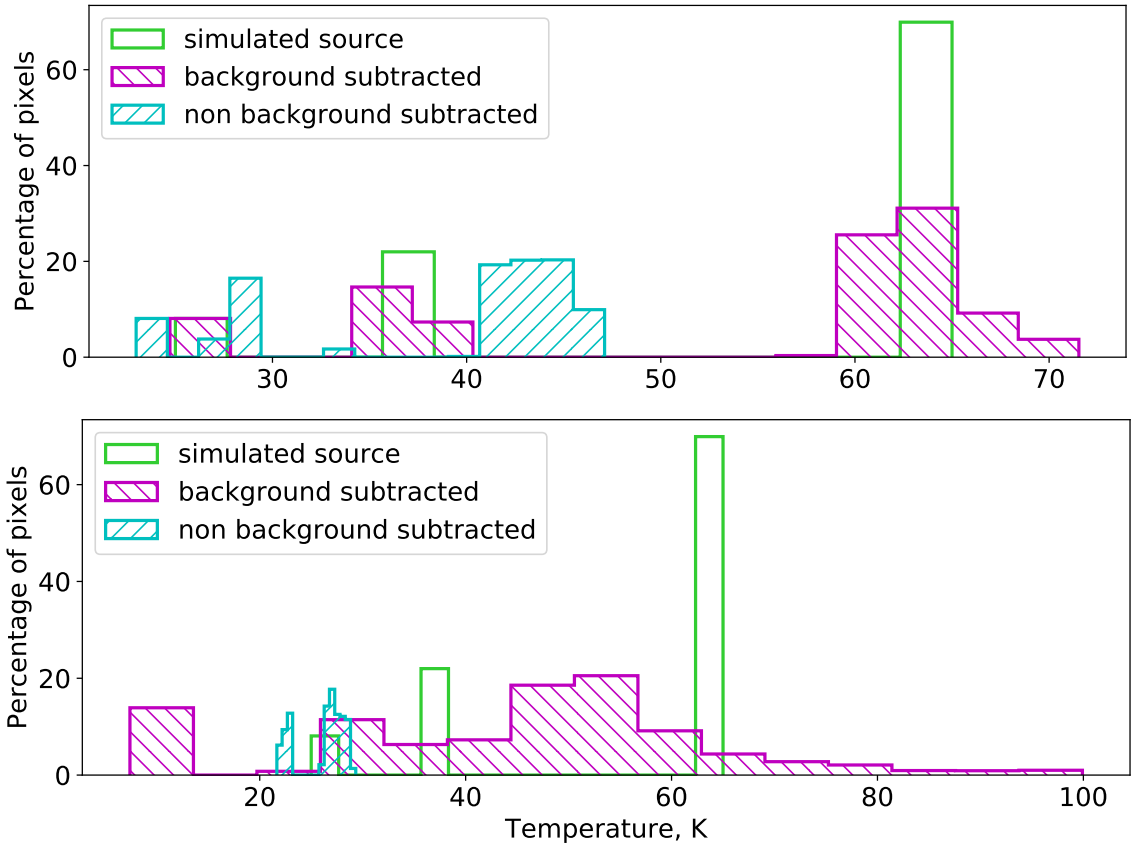

Figure 5.3: Temperatures within the simulated source in the case of a bright simulated source (*top*) and a less bright source (*bottom*). In both cases we find a distribution which is much more similar to the input when we apply a background subtraction.

Nebuliser is applied to the 70 and 160 μm images for our simulated SNR, producing the image shown in Figure 5.2, and Equation 5.1 is then used on the Nebuliser subtracted 70 and 160 µm maps.

For our bright SNR we find that the output temperature map after background subtraction accurately recovers the majority of the input temperatures across the full range of the simulated data (see Figure 5.3). An improvement is also seen for the fainter simulated SNR as we are able to identify both warm and cool dust where before we were limited to a very narrow range of cool temperatures. The resulting temperature distribution after background subtraction is wider compared with the input temperatures, as the contamination of the ISM dust in the pixels at a similar brightness level to the simulated SNR has led to a smearing out of the dust temperatures. We also see that for the faint case, the output temperature map is more sensitive to Nebuliser's modeling of large scale variations in the ISM, there are more small scale features in the output map than in the original simulation.

Many of our level 1 detected SNRs are in crowded fields and are close to or interacting with unrelated structures such as HII regions. We cannot subtract these using Nebuliser without also losing information about the SNR and our resultant temperature maps are sensitive to some contamination from such sources. This difficulty is aggravated as the ISM is bright at *Herschel* wavelengths, especially 160 – 500 µm, making some SNRs difficult to distinguish in any other than the 70 µm waveband. Consequently, we find that the Nebuliser background subtraction at 160 µm is too harsh in some regions, although this effect is much reduced compared with for example, if we were to simply subtract a constant value across the entire region.

5.1.3.1 TESTING G8.3-0.0

An example of the temperature maps derived for the SNR G8.3−0.0 before and after background subtraction is shown in Figure 5.4 to illustrate the significant effect of the dust temperature (thus leading to an overestimation of the dust mass) if the background level is not properly accounted for. Before the background level is subtracted, only a narrow range of dust temperatures are seen in the SNR ($T_d < 26$ K), whereas after subtraction dust is seen at $26 < T_d < 30$ K. See also the recent reductions of the proposed SN dust mass in the Crab Nebula due to more sophisticated measures of the background level (Nehmé et al., 2019; De Looze et al., 2019). We attempt to interpret the dust temperatures in Section 5.3.

We note that the Nebuliser routine used to subtract the background finds medium to large ISM variations, but may not subtract smaller scale complicated structure. Therefore, there may be some contamination remaining, which could act to artificially reduce the temperature of the dust believed to be associated with the SNR. For two sources (G43.3−0.2 and G349.7−0.2) we find lower dust temperatures than Koo et al. (2016) derived using the 24 – 70 µm flux ratio, this may be due to differences in the methods of analysis and/or line contamination in the 24 µm waveband. Conversely, in some regions the background may be over-subtracted where there are small scale variations, this seems to be more of an issue for the 160 µm images and this leads to hot artefacts in the maps. Next we will investigate how well we can determine dust temperatures in crowded interstellar regions, as well as attempt to quantify the effect that not correcting appropriately for the background can have on resultant SNR dust temperatures and masses.

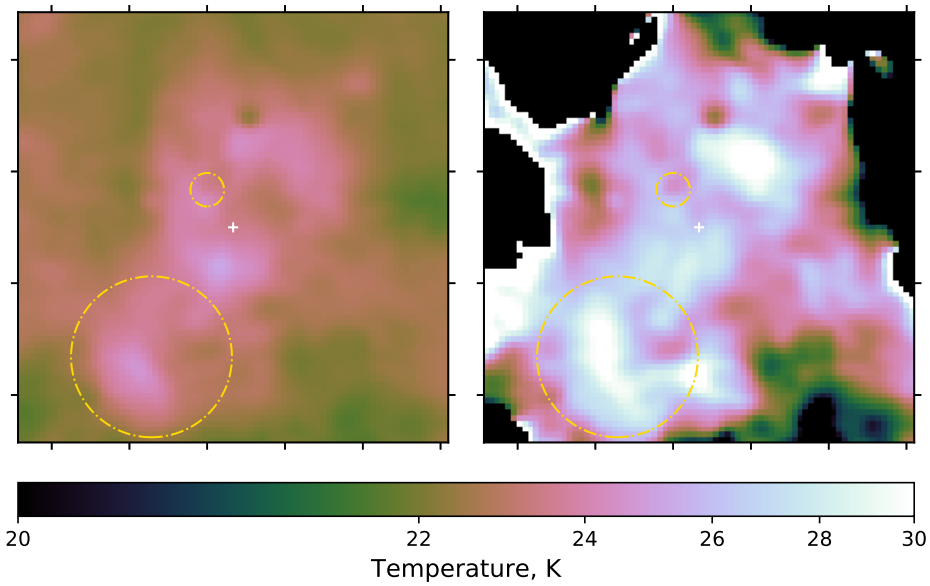

Figure 5.4: *Left:* Dust temperature map of the level 1 detected SNR G8.3−0.0 (Figure 4.3), derived using Equation 5.1 without background subtraction. *Right:* Dust temperature map derived after using Nebuliser to subtract the background. The *Herschel* images used to create the right-hand figure have been convolved to the 250 µm resolution to improve the signal. We are clearly able to identify a wider range of temperatures after applying Nebuliser background subtraction. The large and small gold circles indicate the locations of an IR bubble and a maser respectively.

5.1.4 Temperature Maps of Dust in Milky Way SNRs

The three colour images created out of the *Herschel* images shown in Section 4.1.2 and Figure B.1 reveal dusty structures and features that appear to be associated with other known SNR tracers e.g. radio, X-ray or optical emission (i.e. det = 1) or potentially related to the SN (i.e. det = 2). The colour of the dust emission in these images is, in effect, tracing the dust temperature in the environs of the SNR, however the colour scales chosen earlier are arbitrary, selected only to highlight dusty features. Here we attempt to investigate the temperature of SNR-related dust and potential heating sources using the FIR flux ratio (70 µm / 160 µm) seen by *Herschel* for the detected level 1 sources (following similar studies that used 24 µm / 70 µm flux ratios, Sankrit et al., 2010; Williams et al., 2011; Pinheiro Goncalves et al., 2011; Lakićević et al., 2015; Temim et al., 2015; Koo et al., 2016). We select this colour ratio as this should be sensitive to dust emission from grains at temperatures of $\sim 15-70$K. It should also be less affected by contamination from ionic line emission, which can account for a non-negligible proportion of the 24 μm flux (e.g. Koo et al., 2016; De Looze et al., 2019) and less affected by unrelated point

sources seen in 24 μm images. However, this ratio, and particularly the 160 μm band, may be affected by confusion with unrelated interstellar dust and line emission ([CII] 158 µm). The temperature maps are derived using the 70 and 160 µm Nebuliser subtracted maps and assuming a single temperature dust component with power law dust opacity index $\beta = 1.9$ (see C19 for more details) using equation 5.1.

We present the dust temperature maps in Figure 5.5 with individual notes discussing the map for each SNR below. We compare the dust temperature maps with multi-waveband images (by eye) to identify the source of elevated dust temperatures, which can be an indicator of heating sources such as ISM–SNR interactions. Because of the arbitrary colour scaling used in creating *Herschel* false colour images, some warm dust features may not be evident in those (Chapter 4 and Figure B.1), but may be revealed here.

G8.3−0.0: Broad molecular emission (^{12}CO), flattened radio contours, a possible OH maser, and a gamma-ray source all suggest interaction with molecular cloud to the north-west (Higashi et al., 2008; Kilpatrick et al., 2016). We detect warm dust between $\sim$ 27 and 33 K at the same location of the broad molecular lines observed by Kilpatrick et al. (2016) (their Figure 5) where it is expected that there is a SNR-MC interaction, suggesting that this is heating the dust in this region.

G11.1+0.1: We find evidence of warm dust ($\sim$ 24 – 30 K) in the region of this SNR and dust within the magenta circle in Figure 5.5 to the north is found within the radio contours. The warmest material, towards the south, does not correlate with the radio structure.

G16.4−0.5: There is warm dust ($\sim$ 23 – 28 K), the warmest of which is offset to the north-east of the 70 µm bright region, indicated by the magenta circle in Figure 5.5. The warm dust is in a similar location to radio structure although its morphology differs making it difficult to determine if the origin of the two is the same.

We do not see evidence that the *Herschel* shell around the south and western extent of the SNR has any variation in temperature compared with unrelated dust in the region.

G20.4+0.1: We find some warm dust ($\sim$ 25 – 27 K) that correlates with the radio structure, although the majority of the warm material has a different structure or is found outside of the radio contours. Anderson et al. (2011) suggested that this source may be a HII region (G20.479+0.165, Lockman, 1989).

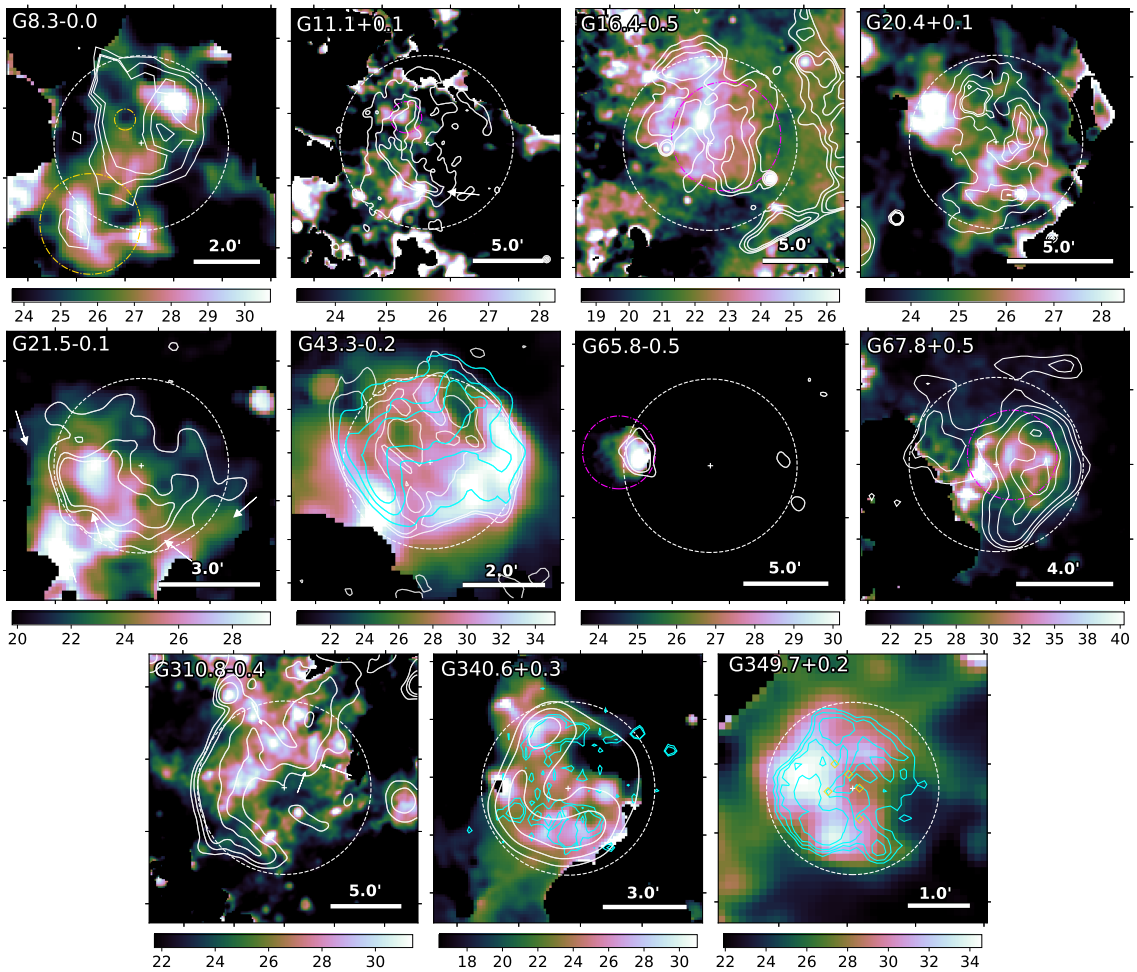

Figure 5.5: Dust temperature maps of our subset of detected level 1 sources derived using Equation 5.1. The images have been convolved to 6 arcsec to improve the signal. VLA GPS 20 cm contours (white) are overlaid onto images of G8.3−0.0, G11.1+0.1, G16.4−0.5, G20.4+0.1, G21.5−0.1, and G43.3−0.2. NVSS 1.4 GHz contours (white) are overlaid onto images of G65.8−0.5 and G67.8+0.5. MOST 843 GHz contours (white) are overlaid onto images of G310.8−0.4 and G340.6+0.3. Chandra contours (cyan) are overlaid onto the images of G43.3−0.2, G340.6+0.3, and G349.7+0.2. In some cases over-subtraction of the 160 µm background introduces hot artefacts at the edges of masked areas.

G21.5−0.1: There is evidence of warm dust ($\sim 23-30$ K) in this SNR although it does not seem to correlate with the radio structure, as shown in Figure 5.5. The warmest region within the radio contours is found in the central region, in a gap in the 160 µm structure. There is also warm dust at the edge of the south-eastern radio contours which may be swept up or shock-heated material if it is associated with the SNR.

W49B, G43.3−0.2: Numerous studies of CO, HI, shocked H_2, and MIR emission indicate that this SNR is interacting with molecular clouds (Reach et al., 2006; Zhu et al., 2014; Kilpatrick et al., 2016), although this is not completely clear as opposing studies find a lack of evidence for molecular material around the SNR (Lacey et al., 2001; Ranasinghe & Leahy, 2018b).

Our analysis supports the argument that there is some interaction as we detect warm dust (up to ~ 36 K) which coincides with the expected location of interactions to the east and south-west.

We also detect warm ($\sim 29-32$ K) dust from a filament at $\alpha = 19^{h}11^{m}07^{s}, \delta = +09°07'01''$ from which MIR colours suggest line emission from ionic shocks (Reach et al., 2006).

G65.8−0.5: We find evidence of warm dust ($\sim 24-32$ K) towards the east of the remnant, at the location of the H α structure discussed in Section 4.1.2. *Herschel* 160 – 500 µm emission was detected from a structure towards the radio centre of the SNR in Section 4.1.2, this region has temperatures between ~ 20 and 22 K.

G67.8+0.5: There is some evidence of anti-correlation between the radio contours and the dust temperatures. A warm (~ 38 K) region of dust lies in the region between two radio peaks towards the west of the remnant, as shown by the contours in Figure 5.5. There is also a peak of warm dust near the centre of the SNR which is located in a gap in the brightest radio structure. The origin of the warm dust is unclear as there are limited observations of this source. If the material is associated with the SNR it could be warm ejecta material, reverse-shocked material, or evidence of dust destruction.

We do not see evidence of warm dust at the location of optical emission to the west, where there is a potential bow shock (Sabin et al., 2013).

Kes 20A, G310.8−0.4: *Spitzer* Infrared Spectrograph (IRS) observations to the south-east suggest that this SNR has a relatively low velocity shock ($\sim 35 - 70 km\, s^{-1}$) into a low-density medium ($\sim 10^3\, cm^{-3}$) and has a distribution of dust grains that indicates shattering of grains in the shock (Andersen et al., 2011). We

do not see evidence for dust in the south-east region that is significantly warmer that the surrounding ISM. The warmest dust identified in this source is towards the north, at the location of FIR and radio structure. If this warm dust is associated with the SNR the correlation with radio could indicate shock-heated dust in this region.

G340.6+0.3: Elemental abundances indicate that ejecta dominates the X-ray bright northern shell, whereas the emission in the south is from shocked ISM (Mangano et al., 2014). We find evidence of warm dust ($\sim 25-30$ K) in the northern arc with a peak in the north-east, slightly offset from the X-ray contours, which may be warm ejecta dust. There is also warm dust in the south in a region of bright X-ray emission, although the warmest dust in this area is offset from the brightest X-ray structures. Because of the coincidence we expect that the warm dust is also shocked ISM.

G349.7+0.2: There is evidence from OH (1720 MHz) masers (Frail et al., 1996) (see the yellow diamonds in Figure 5.5) and line emission (Reynoso & Mangum, 2000; Lazendic et al., 2010) that this SNR is interacting with a coincident molecular cloud (Dubner et al., 2004). Although there is bright *Herschel* emission towards the central interacting region, our analysis suggests that the warmest dust is offset to the east.

The SNR is expanding at $\sim 710\,\mathrm{km\,s^{-1}}$ (Lazendic et al., 2005) into a medium with a density gradient, where the density is relatively low towards the west and higher towards the east. Corresponding to this gradient, we find warmer material in the eastern region where the SNR is dominated by swept-up medium (Lazendic et al., 2005), whereas towards the west we do not see evidence for SNR material that is noticeably warmer than the surrounding ISM. It is likely that the warm dust in the east of the remnant is swept-up material.

5.1.5 Dust Masses and Dust Mass Maps

Next we determine dust masses for the SNRs from this sample for which there are estimated distances in the literature. Table 5.1 shows that, even for our clearest detections, the SPIRE fluxes for our SNRs are very uncertain and we cannot confidently use these fluxes to estimate a dust mass via modified blackbody fits to the IR-submillimetre SED for these sources. Nevertheless, all of our level 1 sources are detected at 70 µm, we therefore use these maps combined with the temperature information in Figure 5.5 to estimate the dust mass within each source, giving the

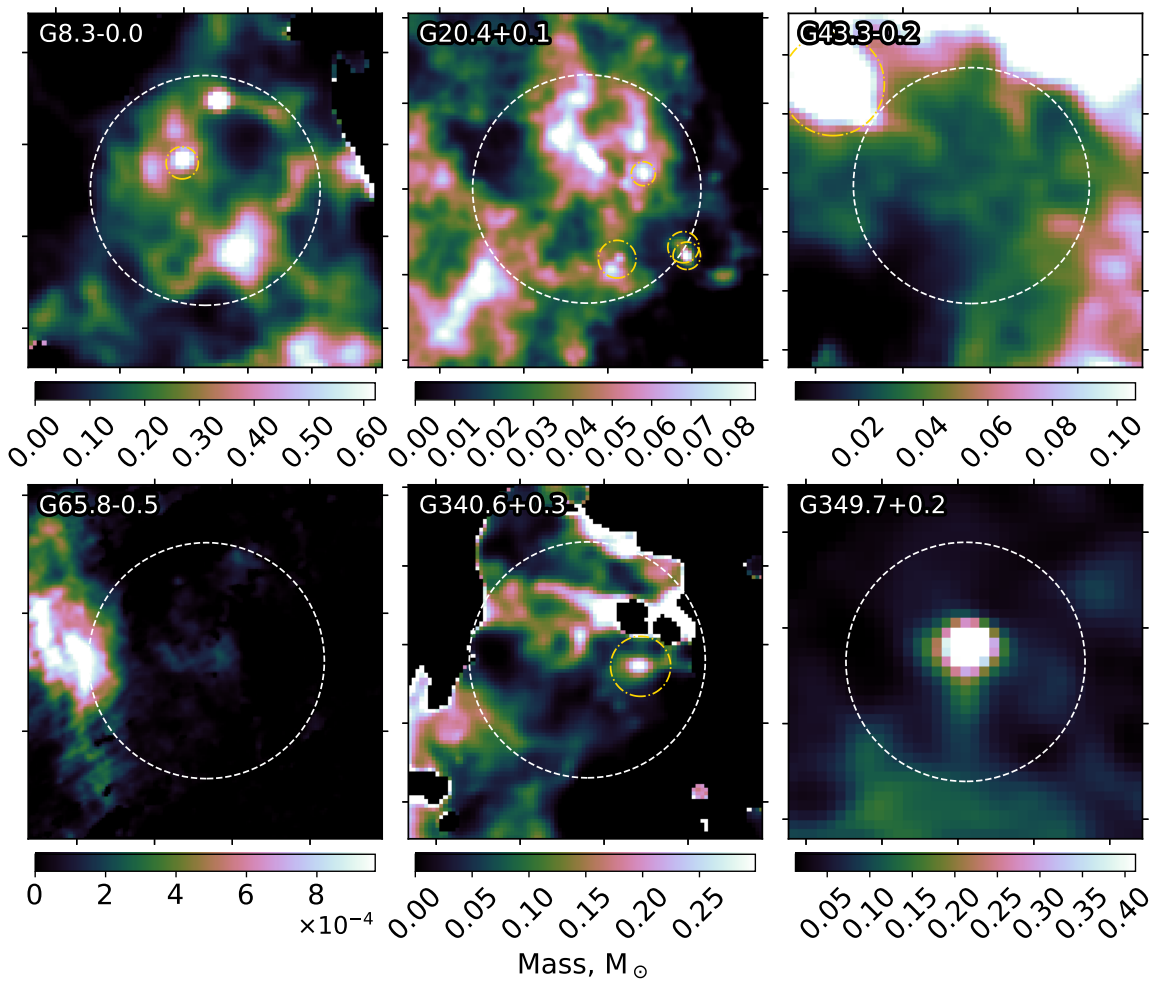

Figure 5.6: Dust mass maps for our subset of detected level 1 sources, derived using the background subtracted 70 µm flux and the temperature maps in Figure 5.5. The estimated dust mass for each SNR, as given in Table 5.2, is estimated from within the white circle for all pixels which have a 70 µm flux above a threshold level, after masking unrelated sources (shown by the gold circles).

SNR	Distance (kpc)	Dust Mass ($M_\odot$)	Refs
G8.3−0.0	16.4	340	1
G11.1+0.1			
G16.4−0.5*			
G20.4+0.1*	7.8	136	2
G21.5−0.1*			
G43.3−0.2	11.3	21.7	3
G65.8−0.5*	2.4	0.2	4
G67.8+0.5			
G310.8−0.4			
G340.6+0.3	15	138	5
G349.7+0.2	11.5	22.5	6

Table 5.2: *Sources which may be confused with a HII region (Anderson et al., 2017; Gao et al., 2019). *Distance references: 1 – Kilpatrick et al. (2016), 2 – Ranasinghe & Leahy (2018a), 3 – Ranasinghe & Leahy (2018b), 4 – Shan et al. (2018), 5 – Kothes & Dougherty (2007), 6 – Tian & Leahy (2014).*

dust maps in Figure 5.6. When estimating the mass from these sources there are two issues to resolve. First, there are large areas within the SNR with relatively small dust mass which, when summed, contribute a large mass to our final estimate. Second, in the case of G43.3−0.2 there is a region to the north of the SNR which has a low temperature (Figure 5.5) because of low 70 µm emission in this region (relative to the 160 µm flux), resulting in a large dust mass. To overcome both issues we set a 1.5 σ threshold on the 70 µm background subtracted flux, below which pixels are excluded from our dust mass estimate (lower flux thresholds are required for G43.3−0.2 and G340.6+0.3). Using the white apertures shown in Figure 5.6 we find the dust masses given in Table 5.2.

We estimate unexpectedly large dust masses for 3 of our SNRs (G8.3−0.0, G20.4+0.1, and G340.6+0.3). In two of these cases the estimated distance is extremely large; if this is overestimated it will increase our dust mass, i.e. increasing the estimated distance by a factor of 2 would increase the estimated dust mass by a factor of 4. However, we also note that closer remnants will have interacted with a smaller volume of the ISM, and consequently would have conversely swept up less dust mass as their shock front moves out. It is therefore likely that there is another factor contributing to this issue. As discussed previously, our images are highly confused and, despite careful background subtraction, there may still be contaminating ISM which acts to reduce the estimated temperatures in Figure 5.5. In the case of G8.3−0.0, increasing the temperature of each pixel by 2 K or 10 K reduces our dust mass from 340 $M_\odot$ to $\sim$190 or 35 $M_\odot$. Evidently, our dust mass

estimates are highly sensitive to small changes in the temperature and we expect that our results are greatly dependent on contaminating ISM.

Previous IRAS surveys by Arendt (1989) and Saken et al. (1992) estimated dust masses for W49B (G43.3−0.2) of 127.7 and 500 $M_\odot$ and for G349.7+0.2 of < 25.1 and 4900 $M_\odot$, which are considerably larger than those that we estimate (although we are consistent with the G349.7+0.2 mass estimated by Arendt, 1989). It is clear that background subtraction is crucial in deriving accurate dust masses and even small variations in the method of subtraction can give vastly different results. With the higher angular resolution of *Herschel* compared with IRAS we make drastic improvements in reducing the ISM contamination.

5.2 The Nature of the Centre of G351.2+0.1

In the previous Sections, we did not produce a dust temperature and mass map for the SNR G351.2+0.1 due to the large gradient in interstellar dust seen in the immediate vicinity of the SNR shell (Figure 4.14). However the inner central/radio bright region where we discovered dust emission is observed at high signal-noise in all of the *Herschel* bands. This potentially indicates the discovery of FIR emission coincident with a possible Crab-like compact object. To determine the nature of this emission across the NIR – radio regime and because of its brightness in all bands, for this source, we create a spectral energy distribution (SED) of the centre. We note that we can fit an SED for this source, as the emission in all of the *Herschel* bands observed at the location of the central radio core appear to be associated with the same source.

Photometry of the compact source from 3.6 – 350 µm (Figure 4.14) was derived using a circular aperture with diameter 1.09′ centred at $\alpha = 17^h22^m24.8^s, \delta = -36°11'06''$. In order to minimize the effect of the second dust source just to the east of the radio core (the red 'blob' in the bottom right panel of Figure 4.14), the background emission was derived using an annulus centred at the same coordinate with diameter 2.84′ and width 1.00′. Numerous point sources in the *Spitzer* bands were masked out and corrections were applied to the IRAC bands to account for the extended diffuse emission seen in the images following the instructions in the *Spitzer* IRAC handbook[3]. The *Spitzer* IRAC fluxes were dereddened following the reddening law of Indebetouw et al. (2005) where $A_{K_S} = 2.5$ mag[4].

[3] https://irsa.ipac.caltech.edu/data/SPITZER/docs/irac/iracinstrumenthandbook/29/

[4] https://irsa.ipac.caltech.edu/workspace/TMP_wYHAkz_6484/DUST/17_22_27_-36_11_00.v0001/extinction.html

NIR - FIR		Radio	
Wavelength	Flux	Frequency	Flux
µm	Jy	GHz	Jy
3.6	0.143 ± 0.022	15	0.0124 ± 0.0002
4.5	0.095 ± 0.014	5	0.0090 ± 0.0003
5.8	0.579 ± 0.087	1.5	0.0064 ± 0.0010
8.0	1.59 ± 0.24		
24	1.16 ± 0.04		
70	27.0 ± 2.7		
160	20.3 ± 2.5		
250	4.47 ± 2.63		
350	<6		

Table 5.3: Background subtracted flux measurements for the compact source at the centre of G351.2+0.1. The 350 µmflux is a 3σ upper limit. IRAC fluxes have been dereddened (Indebetouw et al., 2005) and point sources in the *Spitzer* IRAC and MIPS 24 μm images were masked out.

Errors in the fluxes were determined by combining calibration errors with the error determined in the background level. The photometry is listed in Table 5.3 alongside the VLA photometry from Becker & Helfand (1988), and the spectral energy distribution (SED) is shown in Figure 5.7. The synchrotron power law for the compact radio core is shown with slope +0.27 (Becker & Helfand, 1988). As described in Chapter 3, we fit the SED with two modified blackbodies to derive a cool dust temperature and a dust mass. We have assumed that the dust emissivity index β is kept constant at a value of 1.9. We find a best-fit (χ-squared) model with temperature 45.8 K (see also Figure 5.5) and dust mass $0.18\,\mathrm{M}_{\odot}(d/11\,\mathrm{kpc})^2$ (assuming a distance of 11 kpc from Dubner et al., 1993). We also run a monte carlo analysis by perturbing the observed fluxes within their uncertainties 1000 times and refitting the SEDs. The median SED fit from this analysis produces a cold dust component with $T_\mathrm{d} = 31.9 \pm 1.5$ K and $M_\mathrm{d} = 1.1 \pm 0.3\ \mathrm{M}_{\odot}(d/11\,\mathrm{kpc})^2$, and a hot dust component with $T_\mathrm{d} = 242.1 \pm 6.8$ K and $M_\mathrm{d} = (3.9 \pm 0.4) \times 10^{-6}\ \mathrm{M}_{\odot}(d/11\,\mathrm{kpc})^2$.

One potential issue is whether the compact source is a HII region instead of a SNR. Although the dust temperature we derive is hotter than the average values observed in HII regions (typically 15 – 30 K, Anderson et al., 2012a), we note that some HII regions have observed dust temperatures up to 40 K (Povich et al., 2007; Anderson et al., 2012b). We next compare NIR – radio colours with those observed in HII regions since different emission mechanisms should result in different predicted colours in the NIR – FIR and FIR-radio. Reach et al. (2006) suggests that the *Spitzer* IRAC colours (3.8 – 8 μm) can be used as a diagnostic between SNRs,

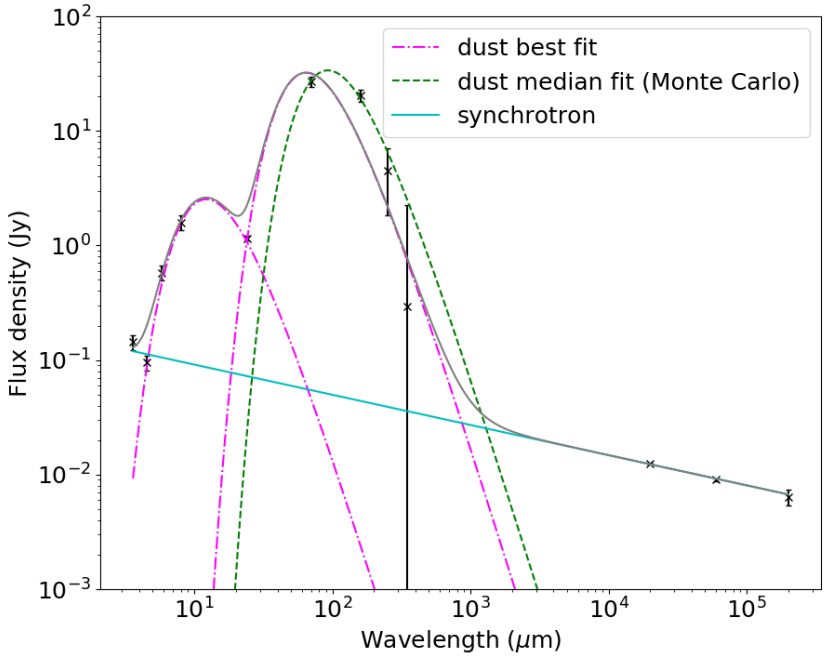

Figure 5.7: Spectral energy distibution of G351.2+0.1 from NIR-radio wavelengths. Fluxes are listed in Table 5.3. The synchrotron emission assuming a power law slope of +0.27 (Becker & Helfand, 1988) extrapolating from the VLA radio fluxes of the compact core is shown by the solid (blue) line. The best-fit (χ^2) hot and cool modified blackbody fits to the photometry are shown by the dot-dashed curves (magenta) and the combination of all emission sources is shown in the solid (grey) curve. The dotted (green) curve is the resultant median modified blackbody fit from 1000 SEDs derived by normally distributing the original observed fluxes within their errors.

the ISM (HII regions or their associated photodissociation regions, PDRs), shocked molecular gas or ionised gas as well as synchrotron sources. *Spitzer* and *Herschel* studies of HII regions suggest NIR – FIR colour plots can also be used as a diagnostic for their identification (Pinheiro Goncalves et al., 2011; Anderson et al., 2012a,b; Paladini et al., 2012). Similarly, the 8 μm and 843 MHz ratios can offer an alternative diagnostic (Cohen et al., 2007). Next we test whether the fluxes derived for G351.2+0.1 can reveal whether we are observing dust from an unrelated HII region or a SNR.

Table 5.4 shows various colours predicted or observed in HII regions in comparison to those measured for G351.2+0.1. At face value, the IR and radio colours show this source is entirely consistent with interstellar material. However there are some caveats with this. Although the IRAC colours for this source are consistent with the ISM regions in Reach et al. (2005a) (see also Table 5.4), they

are similar to that observed in the PWNe G21.5−0.9 (Zajczyk et al., 2012). Comparing with the log (F_8/F_{24}) versus log (F_{70}/F_{24}) colour plot of Pinheiro Goncalves et al. (2011) (their Figure 3), G351.2+0.1 lies along the slope of colours observed in Galactic SNRs, consistent with dust emission with a colour temperature ($T_{24/70}$) of ~ 45 K for $\beta = 2$, and well above the different trend line observed for HII regions. Although the colours are consistent with the narrow range of observed IR−FIR values found in HII regions (Paladini et al., 2012), these overlap considerably with observed values for SNRs which are observed to have much wider range of colours due to the variety of morphologies, ages, emission mechanisms in the latter. Comparing with colours for other known dusty PWNe e.g. G54.1+0.3 and the Crab Nebula (see Table 5.4), although G54.1 satisfies none of the HII diagnostic tests, the Crab does satisfy some. It is not clear how the presence of ejecta dust in SNe would affect these tests, and whether, given the wide range of properties of SNRs, it is even possible to use colours to distinguish between source types. We conclude therefore that we cannot rule out that the dust observed in the centre of G351.2 is unrelated interstellar material, but nor can we rule out a SN ejecta origin.

Colour Test	HII region test	G351.2+0.1		G54.1+0.3		Crab	
		Value	Consistent with HII?	Value	HII?	Value	HII?
$\frac{3.6}{8}\|\frac{4.5}{8}\|\frac{5.8}{8}\|I_8$ [a]	0.04|0.05|0.35|1	0.09|0.06|0.36|1	✓	..	..	..	..
$\log(F_{160}/F_{24})$ [b]	> 0.8	1.24	✓	0.10	×	0.45	×
$\log(F_{160}/F_{70})$ [b]	> -0.2	-0.12	✓	-0.5	×	-0.12	✓
$\log(F_{70}/F_{24})$ [b]	> 0.8	1.37	✓	0.6	×	0.58	×
$\log(F_{24}/F_8)$ [b]	< 1.0	-0.14	✓	1.59	×	0.52	✓
$\log(F_{24}/F_{70})$ [c]	-1.5 to -1.0	-1.37	✓	-0.58	×	-0.12	×
$F_8/S_{843\,\mathrm{MHz}}$ [d]	27 ± 10	282	?	1.4	×	0.02	×

Table 5.4: Summary of the various colour tests to resolve whether the dust source associated with the radio source observed in G351.2+0.1 originates from a HII region or a SNR. Unless specified, all the subscripts refer to the wavelength in microns. References are [a] - Reach et al. (2006), [b] - Anderson et al. (2012a), [c] - Paladini et al. (2012), [d] - Cohen et al. (2007). Also shown are the results of the same tests for the PWNe G54.1+0.3 (fluxes are taken from Temim et al. 2017 and Rho et al. 2018) and the Crab Nebula (from De Looze et al., 2019).

5.3 Interpreting the SNR Dust Temperatures: is warm dust in SNRs collisionally heated?

In Section 5.1.4 we identified warm dust in shocked regions of X-ray and radio emission, suggesting that these interactions are heating this material. We compare models of shock heating to determine the gas properties required to heat the dust to the temperatures seen in Figure 5.5. In the case of collisional dust heating, the dust temperature in X-ray emitting plasmas can be given by the following expression for $T_d \lesssim 70\,\mathrm{K}$ (Dwek et al., 1987, see also Section 1.3.4):

$$T_d^4 = \frac{(\frac{32}{\pi m_e})^{0.5} n_e (kT_{gas})^{1.5} h(a, T_{gas})}{4\sigma < Q(a, T_d) >} \tag{5.2}$$

where n_e is the electron density, a is the grain radius, T_{gas} is the gas temperature (K), $h(a, T_{gas})$ is the grain heating efficiency (~ 1 for most grain sizes), $< Q >$ is the Planck averaged dust absorption coefficient and we assume $< Q(a, T_d) >= 0.16 a T_d^{1.94}$ for graphite and silicates (Dwek & Arendt, 1992). As indicated by Dwek et al. (1987) the dust temperature provides useful constraints on the allowable combinations of gas density and temperature behind the shock.

In Figure 5.8 we consider 3 cases of electron density similar to that observed in shocked regions of core collapse SNRs (e.g. for Cas A $n_e = 16\,\mathrm{cm}^{-3}$ and $n_e = 61\,\mathrm{cm}^{-3}$ in the hot and cold components respectively, Willingale et al., 2003), and one case of a typical molecular cloud density ($n_e \sim 1000\,\mathrm{cm}^{-3}$). If the SNR dust in Figure 5.5 is collisionally heated we can rule out small grains ($a \lesssim 0.1\,\mu\mathrm{m}$) for all densities other than $1\,\mathrm{cm}^{-3}$. This would require unexpectedly cool electron gas to give the range of dust temperatures observed in our *Herschel* analysis ($\sim 25 - 40\,\mathrm{K}$) where X-ray measurements suggest that typical shocked gas (or electron) temperatures are $\gtrsim 10^6\,\mathrm{K}$ (e.g. Koo et al., 2016). For our lowest density ($n_e = 1\,\mathrm{cm}^{-3}$) the full range of SNR temperatures is available to us with grains of radius 0.5, 1.0, or 5.0 µm at reasonable gas temperatures of $T_g > 10^6\,\mathrm{K}$. Smaller grains could provide the observed results, although this is less likely as the gas temperature would be lower than expected for shocked gas. For the densest region we find that the surrounding gas must be cool ($T_g \lesssim 10^5\,\mathrm{K}$) and we must have relatively large dust grains ($a > 1\,\mu\mathrm{m}$): it is unlikely that this describes our SNRs. It is possible that these emitting dust grains are located in post-shock regions.

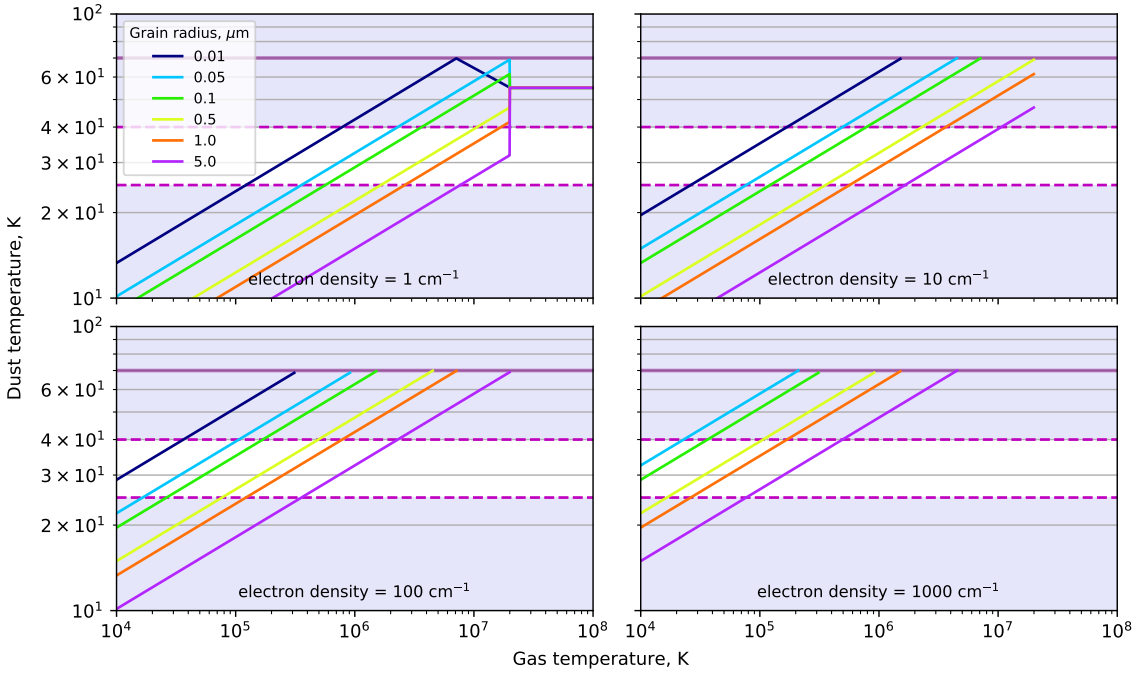

Figure 5.8: The variation of the temperature of collisionally heated dust given by Equation 5.2 assuming a range of electron densities appropriate for forward shock regions and molecular clouds. The composition of the grains is assumed to be graphite and silicate. The white region between the dashed magenta lines gives the range of temperatures observed in our SNRs in Figure 5.5. The solid purple line is at 70 K, above which this relation for collisional heating no longer applies (hence the lines end at $T_d = 70\,K$).

5.4 Conclusions

The main conclusions of this Chapter are:

- We identify warm dust in several SNRs with temperatures between $\sim$ 25 and 40 K which, if collisionally heated, indicates that there must be relatively cool shocked plasma, or the dust must be made up of large grains ($a > 1\,\mu$m). However we caution that there could still be contamination in our apertures with unrelated dust along the line of sight, which we have shown could result in dust temperatures that are biased low. We see that the largest source of uncertainty in a FIR catalogue of SNRs is the result of significant confusion with unrelated dust in the Milky Way.

- We estimate that 6 of our sample contain considerable masses of dust, although ISM contamination may bias our dust masses high.

- The FIR emission seen at the centre of G351.2+0.1 in Chapter 4 can be explained by a PWN origin (though we cannot conclusively rule out a HII region). We estimate a dust temperature and dust mass for G351.2+0.1 of 45.8 K and $M_d = 0.18$ $M_\odot$.

CHAPTER 6
A GALACTIC DUST DEVIL: THE TORNADO

'There's something here that doesn't make sense. Let's go and poke it with a stick.'

THE 11TH DOCTOR – DOCTOR WHO

In Chapter 4 we reported the detection of FIR emission from dust in the candidate supernova remnant, G357.7−0.1 (the Tornado). Here we further explore the dust content and distribution in the Tornado using Point Process Mapping PPMAP (see Chapters 1 and 3), at 8″ resolution compared to the native telescope beams of $5 - 36''$.

6.1 INTRODUCTION

Known as 'the Tornado', G357.7−0.1 (MSH 17-39) is an unusual SNR candidate at a distance of 11.8 kpc (Frail et al., 1996), comprising a 'head', 'tail', and 'eye' (Fig. 6.1). The head appears as a shell- or ring-like feature in the radio (Shaver et al., 1985), and a 'smudge' or diffuse clump with a southern peak in the X-ray, with *Suzaku* (Sawada et al., 2011) and *Chandra* (see Fig. 6.2 of Gaensler et al., 2003) respectively. A larger extended radio shell/filamentary structure exists around the head, with an elongated tail. Finally, a compact and bright radio source seen to the west of the head at $\alpha = 17^{\mathrm{h}}40^{\mathrm{m}}05.9^{\mathrm{s}}, \delta = -30^{\circ}59'00''$ (J2000) is the so-called eye of the Tornado, which is an isolated core embedded in a foreground HII region (Brogan & Goss, 2003; Burton et al., 2004), unrelated to the SNR structure.

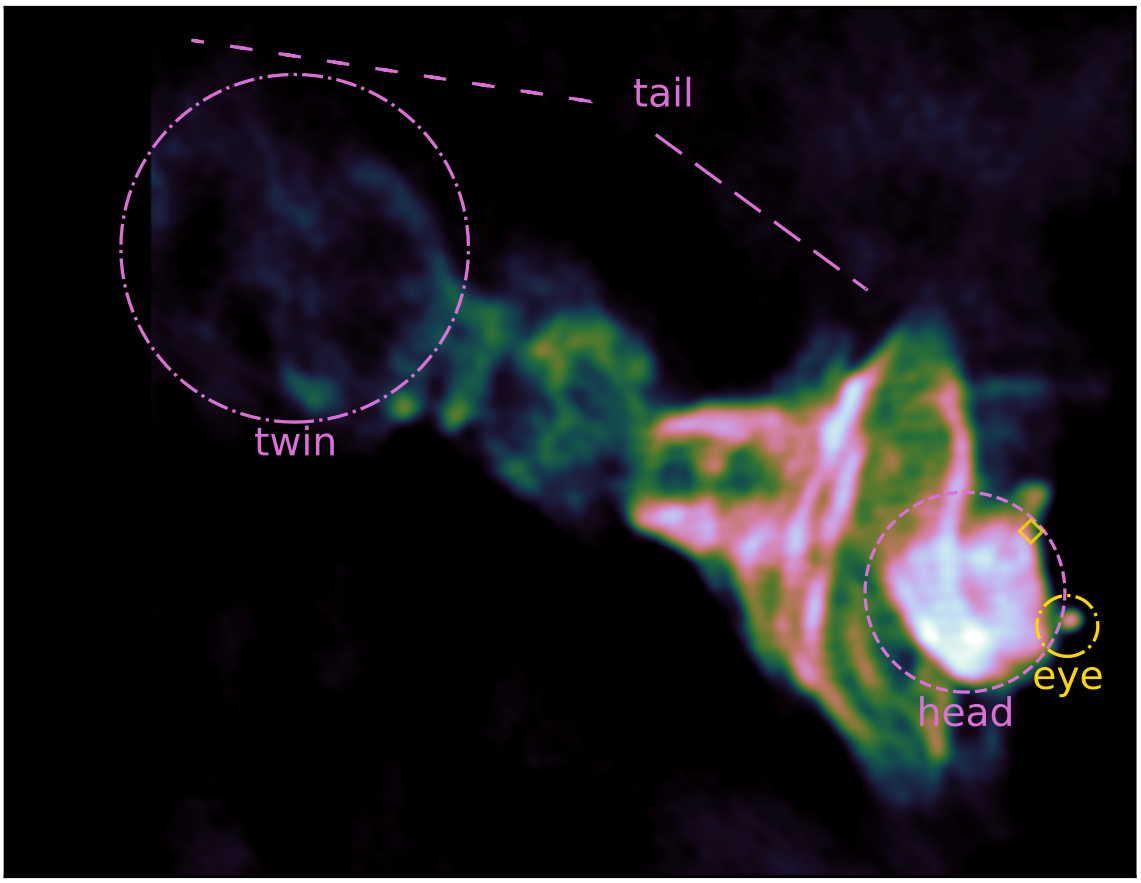

Figure 6.1: 1.4 GHz VLA continuum image of the Tornado (Brogan & Goss, 2003). The tail, head, and eye are indicated, as well as the X-ray 'twin' of the head, detected by Sawada et al. (2011). Like Gaensler et al. (2003), we define the head as the region from which both X-ray and radio emission are strongly detected. The gold diamond indicates the location of an OH (1720 MHz) maser.

Its highly unusual structure has led to various origin theories for the Tornado. From early days, the head of the Tornado has been attributed to a SNR with its radio power law index following synchrotron emission, its non-thermal radio emission, and its strong polarisation (e.g. Milne, 1979; Shaver et al., 1985; Becker & Helfand, 1985b), and later its X-ray emission power-law index (Yusef-Zadeh et al., 2003; Gaensler et al., 2003). These properties led Gaensler et al. (2003) to propose that the Tornado is a shell or mixed morphology SNR, as described by Rho & Petre (1998). The radio head of the Tornado (which is brightest in the south-west part of the 'shell' with a peak in the north-west) can be attributed to limb brightened emission due to the interaction with a molecular cloud (Gaensler et al., 2003). Indeed, shocked H_2 gas detected along the north-western edge of the head (Lazendic et al., 2004) and the presence of multiple OH masers (Frail et al., 1996; Hewitt et al.,

2008) both support this scenario. Unshocked CO emission is found from a cloud to the north-west slightly offset from shocked H_2, suggesting that there is a dense molecular cloud ($n_H \sim 10^4 - 10^6\,cm^{-3}$) which could decelerate the shock wave on this side (Lazendic et al., 2004). However, it is difficult to explain the shape of the large filamentary structures in the tail (Fig. 6.2) with a mixed morphology SNR. In this scenario, the X-ray emission from the head (detected with *Chandra*) originates from the SNR interior, i.e. interior to the limb brightened radio shell (Gaensler et al., 2003). Outside the head region, Shaver et al. (1985) suggests that the partial helical/cylindrical radio filaments could be the result of an equatorial supernova outburst, or the SN exploded at the edge of dense circumstellar shell (Gaensler et al., 2003) or a pre-existing spiral magnetic field structure (Stewart et al., 1994).

Another explanation is that the helical tail is a structure originating from the jets of an X-ray binary, as seen in the SNR W50 (Shaver et al., 1985; Helfand & Becker, 1985; Stewart et al., 1994). In that system, over the course of 20 kyr and several episodes of activity, precessing relativistic jets of the X-ray binary SS443 have shaped the SNR within which it is found (e.g. Begelman et al., 1980; Goodall et al., 2011). This has resulted in a huge nebula (208 pc across) which has a circular radio shell (with a 45 pc radius) from the expanding SNR, and lobes extending to 121.5 and 86.5 pc to the east and west respectively formed by outflows. Radio observations of the Tornado show some symmetry, with flared ends and a narrower central region (Caswell et al., 1989), and Sawada et al. (2011) suggested the presence of an X-ray 'twin' to the head at the far end. This has lead to the theory that the Tornado is an X-ray binary, with a powering source near to the centre of the radio structure, and bipolar jets which interact with ISM at either end, forming the head and its 'twin'.

However, a compact object powering the Tornado system has not yet been detected (Gaensler et al., 2003), though Sawada et al. (2011) argued that a central powering source with an active past may now be in a quiescent state and is too faint to detect in X-ray emission. Another proposed idea is that the Tornado is a pulsar wind nebula powered by a high-velocity pulsar (Shull et al., 1989), however, the spectral slope required to explain the X-ray emission is too steep (Gaensler et al., 2003). Currently, the origin of the highly unusual shaping observed in the Tornado is still under debate.

SNRs are considered to play an important role in the dust processes in the ISM, by creating freshly formed ejecta dust and destroying pre-existing interstellar dust. Indeed, dust thermal emission is widely detected in SNRs in the mid- and far-infrared regime (Dunne et al., 2003; Williams et al., 2006; Rho et al., 2008; Barlow

et al., 2010; Matsuura et al., 2011; Temim et al., 2012; Gomez et al., 2012b; De Looze et al., 2017; Temim et al., 2017; Rho et al., 2018; Chawner et al., 2019; De Looze et al., 2019). As SNRs plough through surrounding interstellar dust clouds, they form a shell-like structure, whereas ejected material is found in a compact emission source in the center of the system (Barlow et al., 2010; Indebetouw et al., 2014). In Chapter 4 we reported the discovery of thermal emission from dust in the head and tail of the Tornado (see Section 6.2), using MIR to FIR images of the region from the *Spitzer Space Telescope* (Werner et al., 2004) and the *Herschel Space Observatory* (Pilbratt et al., 2010). In this chapter we examine the unusual morphology of dust emission in the SNR candidate, the Tornado.

6.2 The Infrared View of the Tornado

6.2.1 Observations

The *Herschel* data used to discover dust emission in The Tornado is from the HiGal survey (Molinari et al., 2010b, 2016), which covers 360° in longitude and $\mid b \mid \leq 1$ and includes data from 70 – 500 μm. Data processing is described in detail in Molinari et al. (2016) and pipeline-reduced and calibration corrected fits files are available to the community via the native HIPE reduction pipeline. Zero-point calibrations for the *Herschel* SPIRE observations were already applied prior to data acquisition. The *Herschel* PACS zero-point offsets were corrected by comparing the observations to synthetic observations produced from the *Planck* foreground maps (Planck Collaboration XLVIII, 2016), and the 100 µm *IRAS* IRIS data[1]. This method is similar to that described in e.g. Bernard et al. (2010); Lombardi et al. (2014); Abreu-Vicente et al. (2016). *Spitzer* 24 µm data was available via the IRSA archive. The MIR-submm images of the Tornado are presented in Fig. 6.2 (and Fig. 6.12), where the well known features are marked with a magenta circle (the head), arrows (the tail) and a gold circle (the HII region, the eye). The tail is brightest in two prong-like structures east of the head.

Fig. 6.2 also compares the IR images with other physical tracers. We make use of the 1.4 GHz VLA radio image (with spatial resolution of $14'' \times 11''$, Brogan & Goss 2003) and X-ray data from the EPIC camera on board *XMM-Newton* (kindly provided by B. Gaensler et al. private communication), with an energy range 0.15-15 keV and spatial resolution of $6''$. As the source was only weakly detected in

[1] The zero-point corrections adopted for the G357.7-0.1 region are: 66.1 MJy/sr and 454.1 MJy/sr for 70 µm and 160 µm respectively.

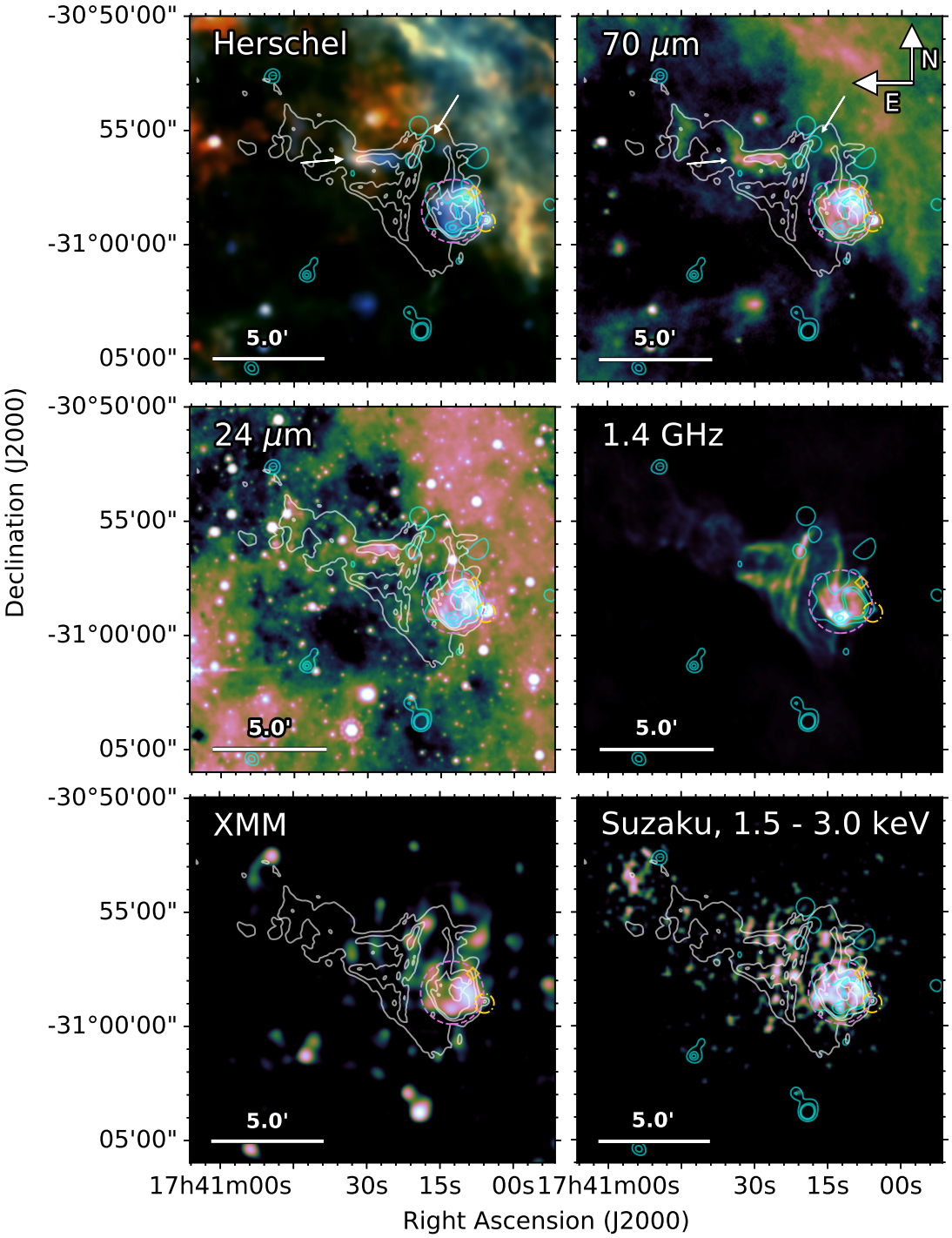

Figure 6.2: G357.7−0.1, The Tornado at FIR, radio, and X-ray - *top left: Herschel* three colour image combining the 70 (blue), 160 (green) and 250 μm (red) images, *top right: Herschel* 70 µm image, *middle left: Spitzer* MIPS 24 µm image, *middle right:* 1.4 GHz VLA image, *bottom left: XMM-Newton* X-ray image smoothed to 0.5″ pixels (kindly provided by B. Gaensler et al. private communication), and *bottom right: Suzaku* 1.5 – 3.0 keV X-ray smoothed continuum image. The white and cyan contours show the radio (1.4 GHz VLA) and X-ray emission (*XMM-Newton*) respectively. We detect dust emission across all *Herschel* wavebands from the 'head' of the Tornado, within the pink circle. We also detect FIR emission from the 'tail' of the Tornado, and from a fainter filament extending around the head, as indicated by the arrows. The gold diamond indicates the location of an OH (1720 MHz) maser.

the EPIC MOS detector, here we present data from the PN detector only. We use *XMM-Newton* rather than *Chandra* as we are only interested in the comparison of structures rather than absolute flux or spectral variations. Furthermore, the diffuse source concentrated at the south of the head previously detected with *Chandra* (Gaensler et al., 2003) is very faint and requires significant smoothing to bring out the signal; *XMM-Newton* may ultimately be more sensitive to diffuse emission given its coarse angular resolution compared to *Chandra*. X-ray observations from *Suzaku* (Sawada et al., 2011) suggest faint diffuse X-ray emission across the head of the Tornado, in close agreement to the structures observed in the *XMM-Newton* image (Fig. 6.2). We note that the distribution of X-rays as seen in the *XMM-Newton* image suggests a shell-like X-ray structure with some emission in the south which may lie interior to the shell (i.e. potentially originating from ejecta; see also the peak in the smoothed *Chandra* image of Gaensler et al., 2003).

6.2.2 Comparison of Tracers

Although this region is confused by dust in the interstellar medium (ISM) in the FIR, we detect clear emission from dust at the location of the head and tail of the SNR in all *Herschel* wavebands, as shown in Fig. 6.2 and Fig. 6.12, though the poorer resolution at 350 and 500 µm makes it more difficult to distinguish the emission from unrelated structure along the line of sight. At 70 and 160 µm, the shell-like structure is clearly seen in the head, and correlates spatially with the radio and overlaps with X-ray. This is also confirmed in the *Spitzer* 24 μm image (Fig. 6.2). The brightest peak in the MIR and FIR (to the north and north-west) is opposite to that seen in the radio emission, and is located towards the OH (1720 MHz) maser, where shock-heated H_2 is also bright (Lazendic et al., 2004). This dust feature appears confined within the radio contours, and is significantly brighter than the ambient dust seen further north-west where the interacting IS cloud is located (as traced by molecular CO emission; Lazendic et al., 2004), so there is no doubt that this is associated with the emission structures responsible for the radio and X-ray (i.e. shocked gas). The fainter southern peak in the X-ray emission correlates with two radio peaks, and the bright X-ray feature to the west coincides with the brightest 24 μm emission and fainter radio.

Outside of the head, we detect warm dust in the unrelated HII region. We also detect faint 70 µm emission that appears to correspond to one of the large radio filaments extending around the eastern side of the head. Dust emission from the tail is also seen at 24 – 160 μm. Similar to the head, we see evidence of an

anti-correlation between the radio and FIR in the tail, the FIR correlates with the upper, fainter of the two radio prongs, indicated by an arrow in Fig. 6.2. At longer *Herschel* wavelengths, we see a bright structure at the eastern end of the tail which may be associated with the Tornado, although this is difficult to distinguish from interstellar dust due to the level of confusion in this region. We do not discuss this source further.

6.3 Investigating the dust structures in the Tornado

In the previous Section, we discussed the presence of dust in the SNR G357.7-0.1, 'the Tornado' (Fig. 6.2). Here we investigate the dust properties in this source further using the point process mapping technique, PPMAP, as described in Section 1.5.2. PPMAP requires an estimate of the noise levels for each band which describes the pixel-to-pixel variation. Here, this was derived from background subtracted *Spitzer* and *Herschel* images using the standard deviation of pixels within apertures placed in quiet regions (minimal variation in foreground emission) near the source. This gives noise estimates of 2.18, 5.47, 11.87, 4.10, 1.72, and 0.48 MJy sr^{-1} for the 24, 70, 160, 250, 350, and 500 µm bands respectively, which are assumed to be uniform across the entire map.

6.3.1 Applying PPMAP to the Tornado

We initially selected 12 temperature bins centred at temperatures equally spaced in $\log(T)$ ranging from 20 to 90 K (guided by our previous analysis of SNRs in Chapter 3), and we assumed a fixed value for the dust emissivity index, $\beta = 2$, which is typical for silicate ISM dust (Planck Collaboration XXXI et al., 2016). If we were to assume a carbonaceous dust with β of 1.0 to 1.5 the estimated dust temperatures would likely be higher. As we did not find any related dust at the location of the head in any temperature bins >70 K, we re-ran the grid for temperatures ranging from 15 to 70 K.

In our first runs of PPMAP, we found that the iterative procedure did not converge to sensible fits (verified by checking the PPMAP χ^2 statistic in each band), even with hundreds of thousands of iterations. This was due to PPMAP attempting, and failing, to converge to a solution for the bright point sources, presumably stars with temperatures much higher than 90 K, in the 24 μm image (and to a lesser

extent in the 70 μm image). To resolve this, we masked the bright point sources near the Tornado (replacing their pixels with a local average level in the image) and we artificially increased the noise for the 24 μm map by a factor of 10; this effectively stops PPMAP from trying to over-fit the 24 μm band and down-weights the importance of the 24 μm in the iterative procedure. This may act to slightly reduce any dust temperatures fit by PPMAP, though in practice we found that it did not affect our results.

The Tornado is in a highly confused region due to its location close to the Galactic centre (Fig. 6.2). To determine the effect of any potential contamination from unrelated dust along the line of sight, we ran our PPMAP grid (the original 20 – 90 K run) on the Tornado without any background subtraction, and then again, after accounting for background emission. In the former scenario, the results indicate that dust structures exist in the head of the Tornado at temperatures of 20-23 K with a warmer dust component in the north-western part of the head at 26 K, where the source is believed to be interacting with a molecular cloud (Frail et al., 1996; Lazendic et al., 2004; Hewitt et al., 2008). These cold dust temperatures are very similar to general interstellar dust, and the narrow range of temperatures suggest this region is contaminated by unrelated background emission.

For PPMAP to converge in a reasonable time we must subtract the background from the maps. First we mask bright, unrelated sources as above, as well as the Tornado head and tail, and several high signal-to-noise regions to avoid overestimating the background. The images are then convolved with a 100″ FWHM Gaussian profile, providing background maps smoothed to a scale comparable to the Tornado head. The background maps are subtracted from the original zero-point calibrated maps (with the two bright sources masked). Running PPMAP with the resulting maps gives reduced-χ^2 values of 0.3, 2.0, 11.0, 9.0, 4.0, and 128.0 for 24, 70, 160, 250, 350, and 500 µm[2]. We find that the overall level of the background-subtracted images is negative, implying the method of background subtraction used is too aggressive. To account for this, we took the background-subtracted maps, estimated the mean negative offset for the whole region at each waveband (again masking the Tornado) and added this back on to the image in an attempt to bring the maps back to a zero level. Hereafter we call this the zero mean background-subtracted method. Running these images through PPMAP the

[2] These are average reduced-χ^2 estimated for the entire map at the end of the PPMAP run. As such they can be greatly influenced by variations in noise across the map, as well as regions which are not fit well, including edges (which are sampled less frequently throughout the PPMAP procedure) and areas which may be optically thick or have a temperature outside of the given range.

resulting dust temperatures and components are markedly different to the non-background-subtracted case: dust structures are observed at a wider range of temperatures (from 20 - 60 K) with the north-western dust feature peaking at 30 K. The background subtraction has resulted in the dust components in the head being attributed to warmer dust, as expected. Note that these warmer dust components correspond to the dust structures that peak in the original *Herschel* maps peaking at 70 μm. The resulting PPMAP reduced χ^2 values are 0.6, 2.2, 6.9, 11.7, 22.5 and 37.6 suggesting the overall fit is formally better than the previous case. The high χ^2 values for the longer wavebands are most likely due to underestimating the σ value, because small scale ISM variations cannot be captured by a large beam, although increasing the noise level constrains PPMAP less, giving more unreliable results across all bands.

The above tests suggest that PPMAP is sensitive to whether the background diffuse interstellar level is subtracted from the maps or not, particularly important in this case due to the high level of confusion in this region. To try and qualitatively discriminate between the tests, we created synthetic MIR-FIR observations based on the PPMAP outputs for the three scenarios above, and compared them to the original *Spitzer* and *Herschel* images. These were created from the output dust column density maps at a range of temperatures and then reversing the physical steps PPMAP uses to produce maps of flux at each wavelength, ultimately regridding the pixels and smoothing back to the resolution of the original data. This also allows us to independently check that no artefacts are introduced by PPMAP, since these would be obvious in the synthetic images. In each case, the original dust emission features seen in the head of the Tornado were recovered well in the synthetic PPMAP MIR-FIR images. Fig. 6.3 shows a comparison of the synthetic images from PPMAP versus the original data for the zero-mean-background-subtracted case. This gave the closest agreement to the original features, recovering the complex dust emission structures observed within the head (see the following Section for more information). We therefore use the PPMAP results based on this method from now on.

Finally, we note that synchrotron emission in SNRs can be a significant contributor to the FIR flux (Dunne et al., 2003; De Looze et al., 2017; Chawner et al., 2019). As this typically varies as a power law with flux $S_\nu \propto \nu^{-\alpha}$, where α is the spectral index, we can directly estimate the contribution of synchrotron emission to our FIR bands. Prior to running PPMAP we subtract the synchrotron contribution, which is estimated by extrapolating from the flux we measure from the 1.4 GHz VLA image (Becker & Helfand, 1985a; Green, 2004), assuming $\alpha = -0.63$ for the

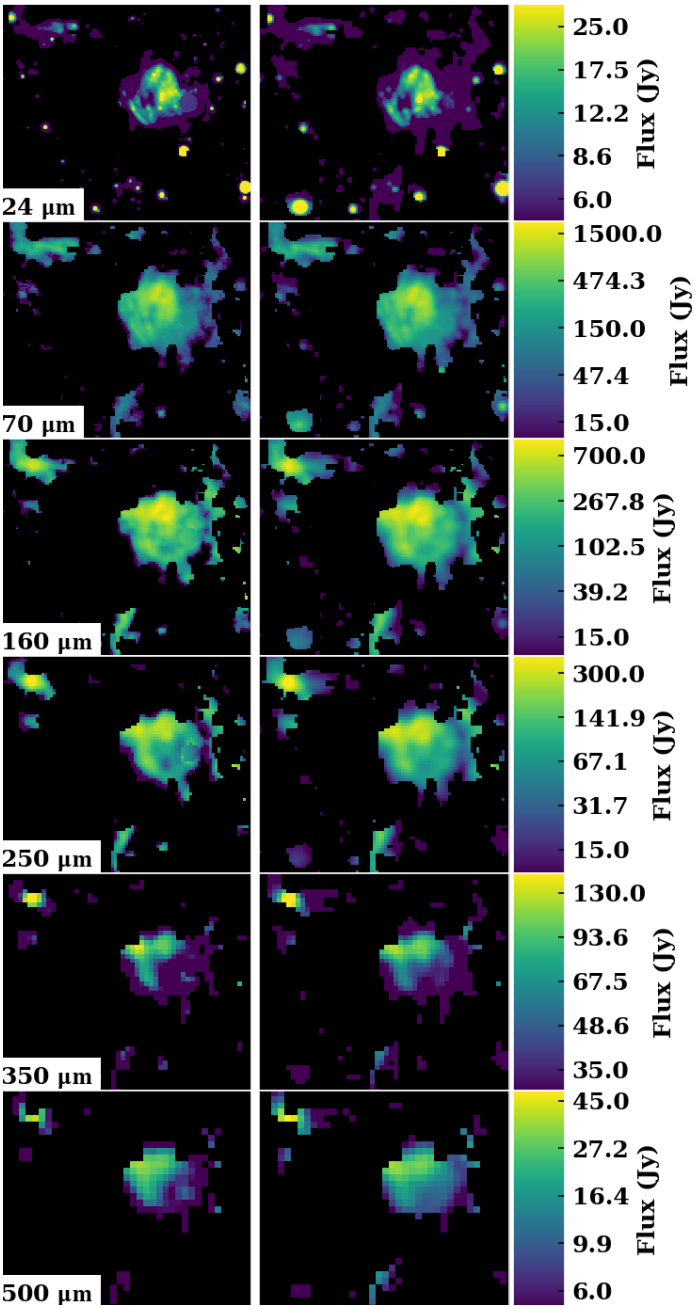

Figure 6.3: A grid comparing the original *Spitzer* and *Herschel* observations of the Tornado (*left*) with the synthetic observations (*right*) created by taking the results from PPMAP and post-processing them.

head (Law et al., 2008). We find that the synchrotron contribution to the SNR head is in the range of only 0.03 – 2.06 per cent of the total flux for our MIR–FIR wavebands in the head, as measured on the original *Herschel* maps[3], where both are measured within an aperture centred at $\alpha = 17^{h}40^{m}12.4^{s}, \delta = -30°58'31.1''$ with a $79''$ radius. We can therefore be confident that we are observing the thermal emission from dust with negligible contribution from synchrotron emission in the head.

However, the spectral index does flatten in the tail region with spectral slope varying from $-0.50 < \alpha < -0.33$ (Law et al., 2008) indicating that the tail electrons are more energetic than in the head. We therefore caution that there could be a higher contribution of synchrotron emission in the tail.

6.3.2 Results

The grid of dust mass in each temperature bin for the Tornado is shown in Fig. 6.4, assuming a distance of 12 kpc (Brogan & Goss, 2003). Fig. 6.5 shows a four colour FIR image created by combining the masses in the temperature slices at 20, 30, 40, and 61 K, and Fig. 6.6 shows the total dust mass distribution across the Tornado head. They reveal dust features observed in the *Herschel* images, but at a resolution of $\sim 8''$ compared to the native telescope beams of $5 - 36''$.

A temperature gradient is evident in both the head and tail. Cool, dense dust is found towards the north-eastern head at the location of a radio filament which extends from the head towards the northern extent of the object. The filaments outside of the head were lost in background subtraction, but this suggests that they could also contain cool, dense dust. Slightly warmer material (23 – 30 K) forms a bubble around the edge of the head and around the larger X-ray peak. In Fig. 6.6 we find that the majority of the dust mass follows this bubble shape, with a relative lack of material in the central region. Warm material (35 – 40 K) fills the central region, coincident with both the large X-ray peak and the warmest dust that we observe (53 – 61 K). It seems that the hot gas which emits the X-ray emission is heating the central region of the head, where we see warm, low density material.

[3] we note that this calculation may underestimate the synchrotron contribution to the IR fluxes since our integrated flux for the total SNR (head and tail) derived from the 1.4 GHz radio image using an aperture $\alpha = 17^{h}40^{m}29^{s}, \delta = -30°58'00''$ with a $8'$ radius, gives 80 and 70 per cent of the flux derived from the single dish measurements of Green (2004) and Law et al. (2008) respectively (scaled to the same frequency). This may, in part, explain the larger χ^2 value at 500 µm. However taking the single dish measurements would produce a maximum synchrotron contribution of 3 per cent. Indeed the biggest source of contamination in the MIR-FIR aperture measurements is the background level.

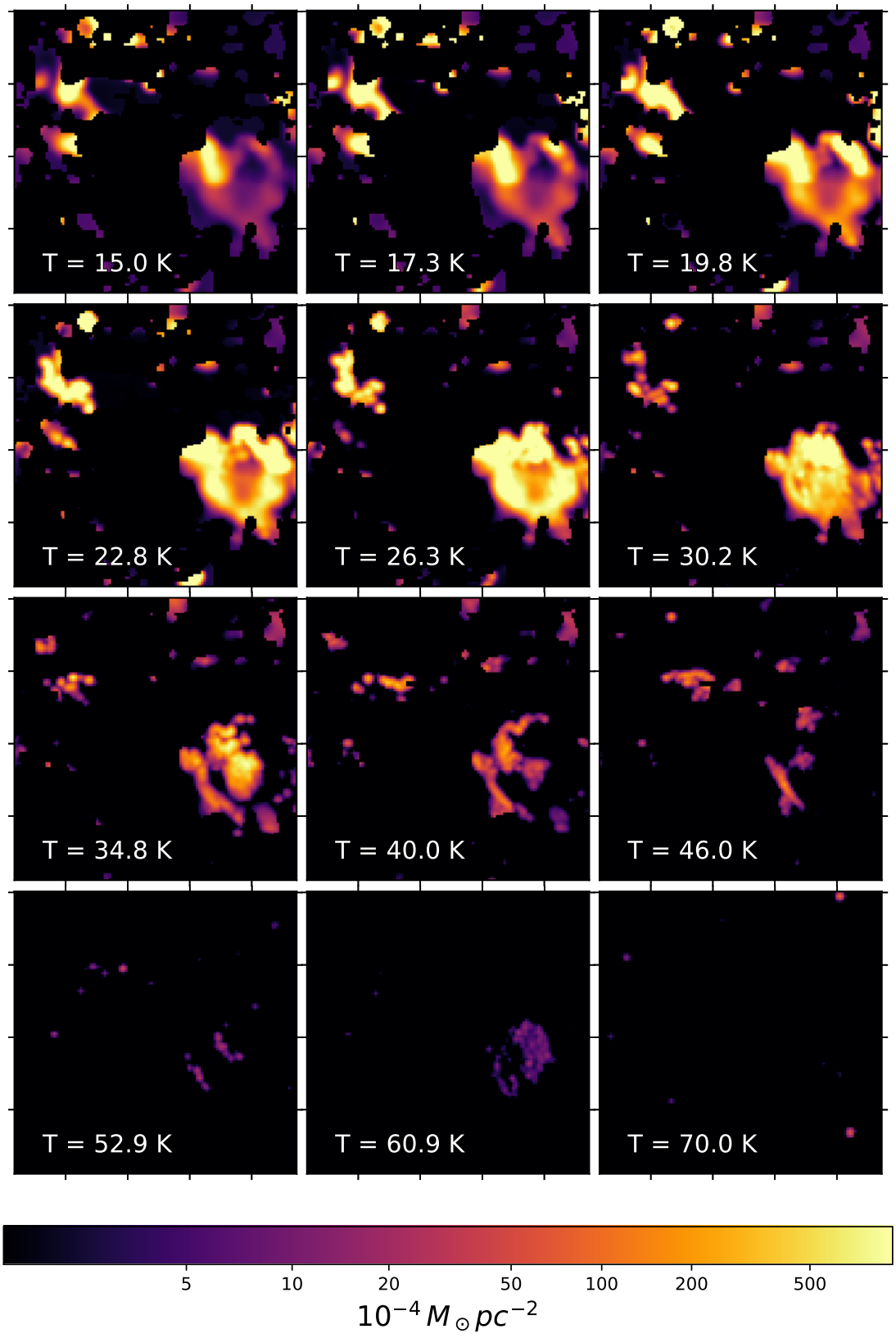

Figure 6.4: PPMAP generated maps of differential dust mass split in different temperature ranges for the Tornado. The corresponding dust temperature is indicated in the bottom-left of each panel.

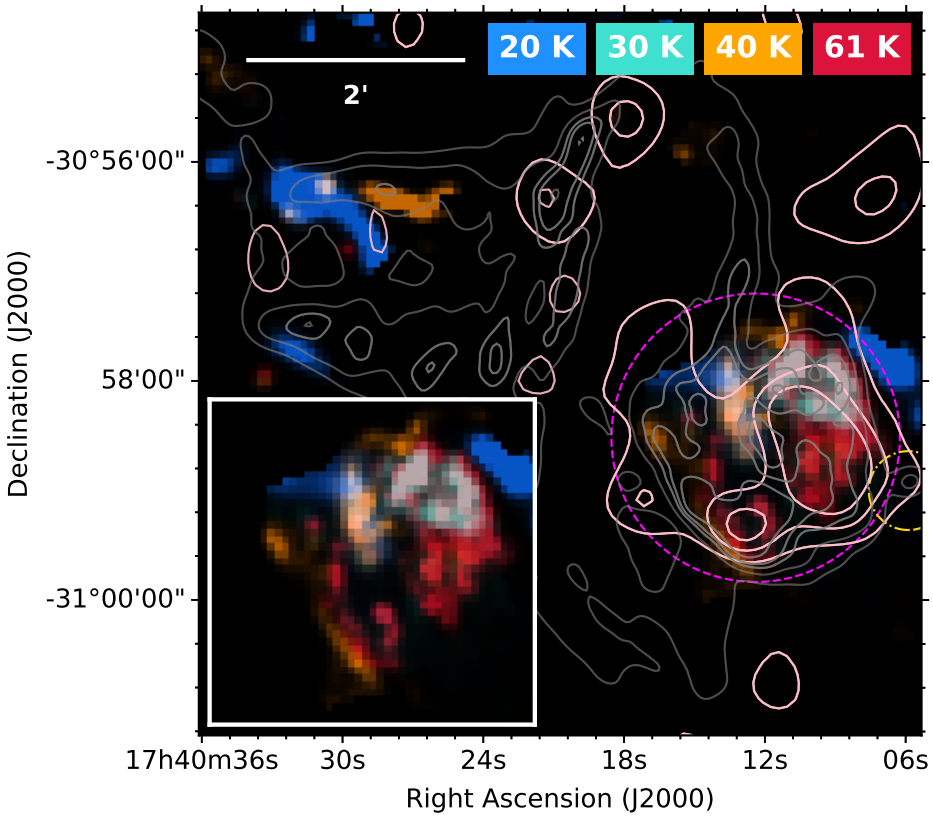

Figure 6.5: PPMAP-generated four colour map of dust mass in the Tornado created using dust temperature slices from Fig. 6.4. Colours show dust at 20 K (blue), 30 K (cyan), 40 K (gold), and 61 K (red). Overlaid contours are from the VLA 1.4 GHz (grey) and *XMM-Newton* (pink) images. The magenta dashed circle indicates the location of the head of the remnant, and is also the aperture used to derive the dust mass. The gold dash-dotted circle is the location of the eye of the Tornado (unrelated HII region).

We find a large mass of 26 – 30 K dust towards the north west where interactions with a molecular cloud may be heating the dust, as well as at the same location as the smaller region of bright X-ray emission in the south east. A filament of 35 – 46 K material sits along the eastern edge of the head, with a warm 53 K peak towards the middle, filling the radio contours at this location, as seen in Fig. 6.5. In the tail we find a large mass of cool, 15 – 20 K dust to the east, as well as slightly warmer, 23 – 30 K material which extends further north. The temperature increases towards the west, as 35 – 40 K dust fill the eastern and central contours with dense regions at the radio peaks, and 46 K material is found further west. There is some evidence of warm dust (40 – 46 K) at the X-ray and radio peak to the east of the tail, although much of this area is lost to background subtraction as it is a similar level to the surrounding ISM.

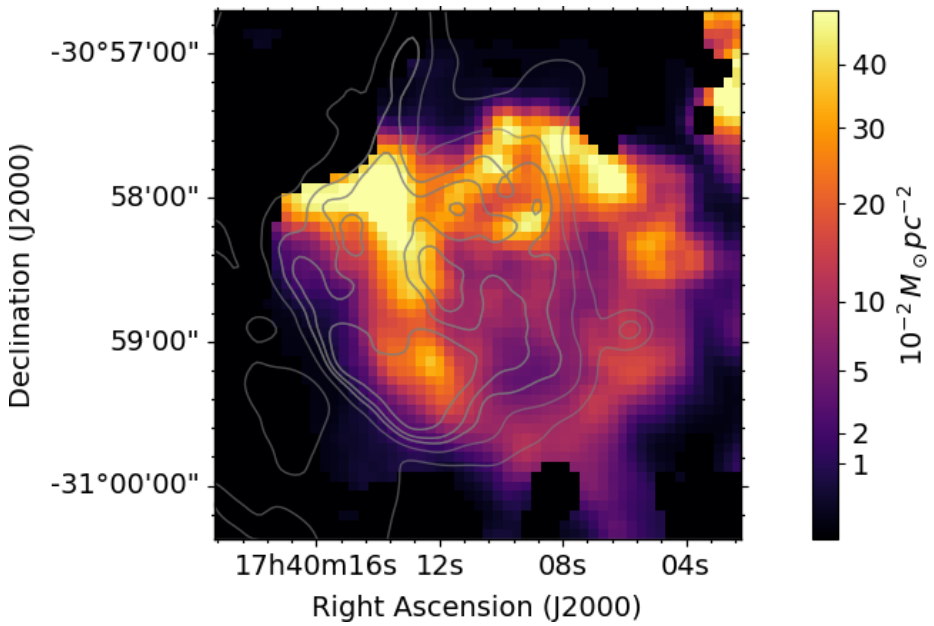

Figure 6.6: The dust mass within the Tornado head integrated across all temperature slices of Fig. 6.4, with VLA 1.4 GHz contours (grey) overlaid.

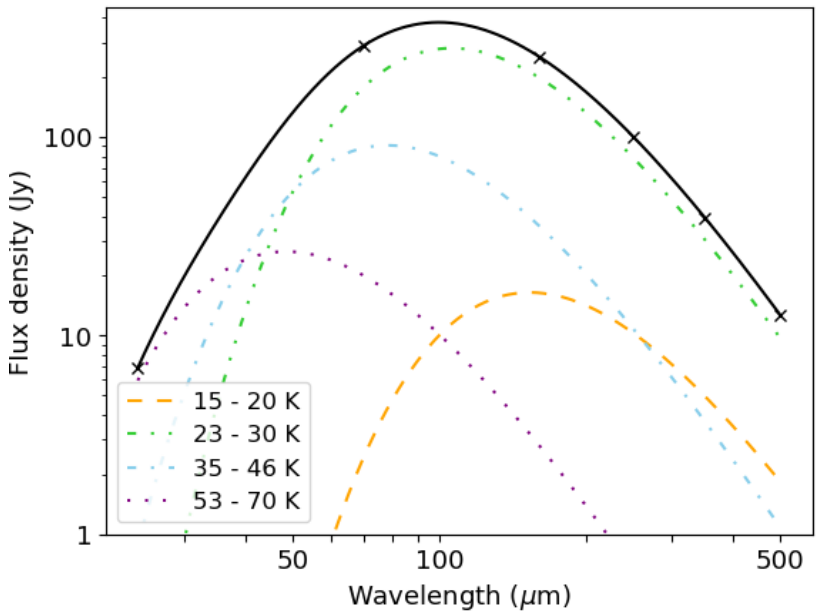

Figure 6.7: The total thermal MIR-FIR SED estimated from the PPMAP results of the head of the Tornado, within the magenta circle in Fig. 6.5, indicating how the different temperature components shown in Fig. 6.4 contribute to the thermal emission observed in the source.

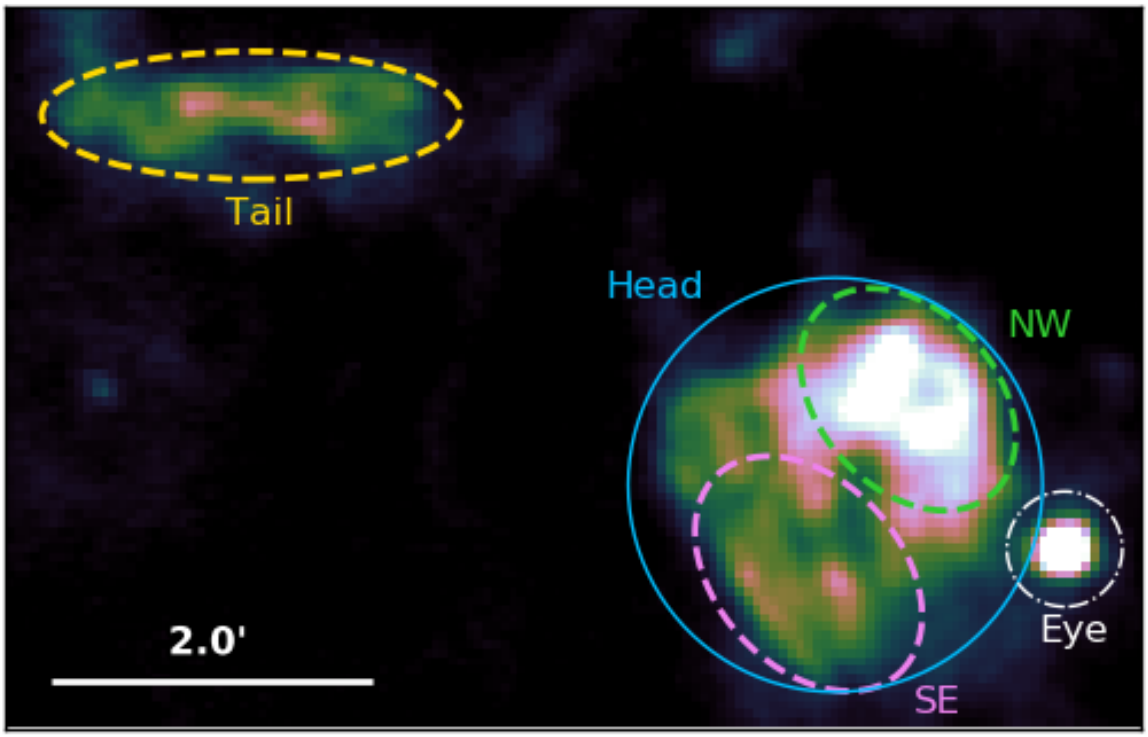

Figure 6.8: Tornado head and tail region at 70 µm. The shapes indicate regions from which we detect FIR emission and within which we compare the flux ratios in Figs. 6.9 and 6.10. These are the Tornado head (blue circle), north-western head (green dashed ellipse, south eastern head (pink dashed ellipse), Tornado tail (gold dashed ellipse), and the Tornado eye (white dash-dotted circle).

The spectral energy distribution of the head of the Tornado is shown in Fig. 6.7, broken down into the different temperature components revealed by PPMAP. We derive the total dust mass in the head of the Tornado by summing the mass within the magenta circle shown in Fig. 6.5 across the temperature grids. This gives a total dust mass for the Tornado head of 16.7 $M_\odot$ for a dust mass absorption coefficient at 300 µm of κ_{300} =0.56 $m^2\,kg^{-1}$ (James et al., 2002). If we only sum the contribution from dust structures with T_d>17 K we obtain a dust mass of 14.8 $M_\odot$, and 4.0 $M_\odot$ of mass originates from dust hotter than 30K.

6.4 The Nature of the Tornado

The nature of the Tornado is unclear as it has many confusing characteristics, with suggested candidates including an X-ray binary, a SNR, and HII region. In Section 6.3 we revealed that the Tornado contains large masses of dust, similar to the sandy whirlwind 'Dust Devils' on Earth. In this section we explore whether

the FIR emission from our own Dust Devil can give us any insight into its nature. We further examine the IR, radio, and X-ray emission to determine if it can shine any light on the different origin scenarios.

6.4.1 Properties of the Tornado

First, we study the emission colours to understand the properties of the regions from which we detect dust and how they vary across its features. Within the head, we split our analysis into two main regions of interest, as indicated by the green and magenta ellipses in Fig. 6.8 respectively: the north-west (NW), where we identified warm dust with PPMAP and where the head is thought to be interacting with a molecular cloud (Frail et al., 1996; Lazendic et al., 2004; Hewitt et al., 2008); and the south-east (SE), where there is a radio peak. Our PPMAP analysis in Section 6.3 gives estimates for the dust mass within each of these regions as $\sim 3.3 M_{\odot}$ and $\sim 2.1 M_{\odot}$ for the NW and SE respectively.

IR – radio flux ratios have been used in previous studies to identify SNRs, distinguishing them from HII regions (e.g. Whiteoak & Green, 1996). The thermally dominated emission from HII regions, with some free-free emission in the radio, gives an IR-radio ratio of $\geqslant 500$; in contrast, SNRs are dominated by synchrotron at radio frequencies and have a considerably smaller IR flux, giving an IR - radio ratio of $\leqslant 50$ (Haslam & Osborne, 1987; Furst et al., 1987; Broadbent et al., 1989). Table 6.1 shows the IR and IR – radio flux ratios from the integrated fluxes of the Tornado head. Although several of the IR flux ratios are consistent with the Tornado head being a HII region, none of the IR – radio flux ratios agree with this scenario.

In order to examine the dust emission properties of the various FIR regions of the Tornado in more detail, we follow the analysis of Pinheiro Goncalves et al. (2011) and compare IR and radio colours, including $I_{70\mu m}/I_{21\mathrm{cm}}$, $I_{24\mu m}/I_{21\mathrm{cm}}$, $I_{8\mu m}/I_{24\mu m}$ and $I_{70\mu m}/I_{24\mu m}$, for pixels within the Tornado (Figs. 6.9 and 6.10), where pixels are convolved to the lowest resolution data. For comparison we include the integrated flux of the head, the dusty region in the tail (see Fig. 6.8), the eye, and previously studied SNRs (in Figs. 6.9 and 6.10 the SNR and region names are centred on the respective flux ratios, unless indicated by an arrow).

Colour	HII region test	Tornado		G54.1+0.3		Crab	
		Value	Consistent with HII?	Value	HII?	Value	HII?
$\frac{3.6}{8}\|\frac{4.5}{8}\|\frac{5.8}{8}\|I_8$ [a]	0.04|0.05|0.35|1	0.004|0.58|0.98|1	×	..	..	..	..
$\log(F_{160}/F_{24})$ [b]	> 0.8	1.45	✓	0.10	×	0.45	×
$\log(F_{160}/F_{70})$ [b]	> -0.2	-0.09	✓	-0.5	×	-0.12	✓
$\log(F_{70}/F_{24})$ [b]	> 0.8	1.54	✓	0.6	×	0.58	×
$\log(F_{24}/F_8)$ [b]	< 1.0	-0.31	✓	1.59	×	0.52	✓
$\log(F_{24}/F_{70})$ [c]	-1.5 to -1.0	-1.54	×	-0.58	×	-0.12	×
$F_8/S_{843\,\mathrm{MHz}}$ [d]	27 ± 10	0.66	×	1.4	×	0.02	×
$F_{70}/S_{843\,\mathrm{MHz}}$ [d]	$\leqslant 50$	11.09	×				

Table 6.1: Summary of the various colour tests to resolve whether the dust associated with the Tornado head originates from a HII region or a SNR. Unless specified, all the subscripts refer to the wavelength in microns. References are [a] - Reach et al. (2006), [b] - Anderson et al. (2012a), [c] - Paladini et al. (2012), [d] - Cohen et al. (2007). Also shown are the results of the same tests for the classified (PWN) SNRs G54.1+0.3 (fluxes are taken from Temim et al. 2017 and Rho et al. 2018), and the Crab Nebula (from De Looze et al., 2019).

In Fig. 6.9 we find that the IR colours for the majority of the Tornado head pixels fall within the colour space for a SNR, and are well distinguished from the pixels within the 'eye' of the Tornado, which is a confirmed HII region with an embedded protostellar source (Burton et al., 2004). This suggests that the Tornado head is part of a SNR, rather than a HII region. Several Galactic SNRs from Pinheiro Goncalves et al. (2011) are observed to have high IR-radio flux ratios, two of which would be classified as HII regions by this test ($I_{\rm IR}/I_{\rm radio} > 500$: G21.5−0.1 and G23.6+0.3, $I_{\rm IR}/I_{\rm radio} > 50$: G10.5+0.0, G14.3+0.1, G18.6−0.2, and G20.4+0.1). Of these sources, Anderson et al. (2017) suggested that three were misidentified HII regions (G20.4, G21.5, and G23.6), which we have labelled in Figs. 6.9 and 6.10.

As shown in Fig. 6.10, Pinheiro Goncalves et al. (2011) found different trends for HII regions and SNRs when comparing their IR colours. In this colour space, we find that the Tornado falls more in line with the HII region trend. However, SNRs and HII regions inhabit much of the same colour space in Figs. 6.9 and 6.10 and there are other well known SNRs, including W49B, 3C391, and G349.7−0.2, which also lie along the HII region trend. The variation seen in these individual SNRs from the main SNR trend could instead be due to a difference in dust properties such as temperature or emissivity, possible caused by interactions with molecular clouds.

It is possible to use the IR and IR – radio colours, as in Figs. 6.9 and 6.10, to determine some of the SNR properties. Older SNRs tend to have higher IR – radio colours (e.g. Arendt, 1989), placing them towards the upper-right of the SNR colour space in Fig, 6.9. Additionally, Pinheiro Goncalves et al. (2011) found some correlation between the IR colours in Fig. 6.10 and the SNR age, suggesting that older remnants have higher 70 – 24 µm and 8 – 24 µm flux ratios. Thus, both the FIR – radio and the IR colours suggest that, if it is a SNR, the Tornado is an older remnant which has likely swept up a large mass of dust from the ISM. Pinheiro Goncalves et al. (2011) also suggested that the IR colours could give some insight into the SNR emission process. They found tentative evidence that the upper right region of the colour space in Fig. 6.10 tends to be populated by objects with molecular shock and photodissociation regions (PDRs), although they admit that this is not a secure correlation given the small sample and that the 8, 24, and 70 µm bands contain both dust emission and lines. We find that the IR flux ratios of the NW region of the Tornado Head suggests molecular emission, whereas the SE region is largely undetected at 8 µm. Given that the head is thought to be interacting with a molecular cloud in the NW this supports the relation between the 70 µm – 24 µm and 8 µm – 24 µm flux ratios and emission type.

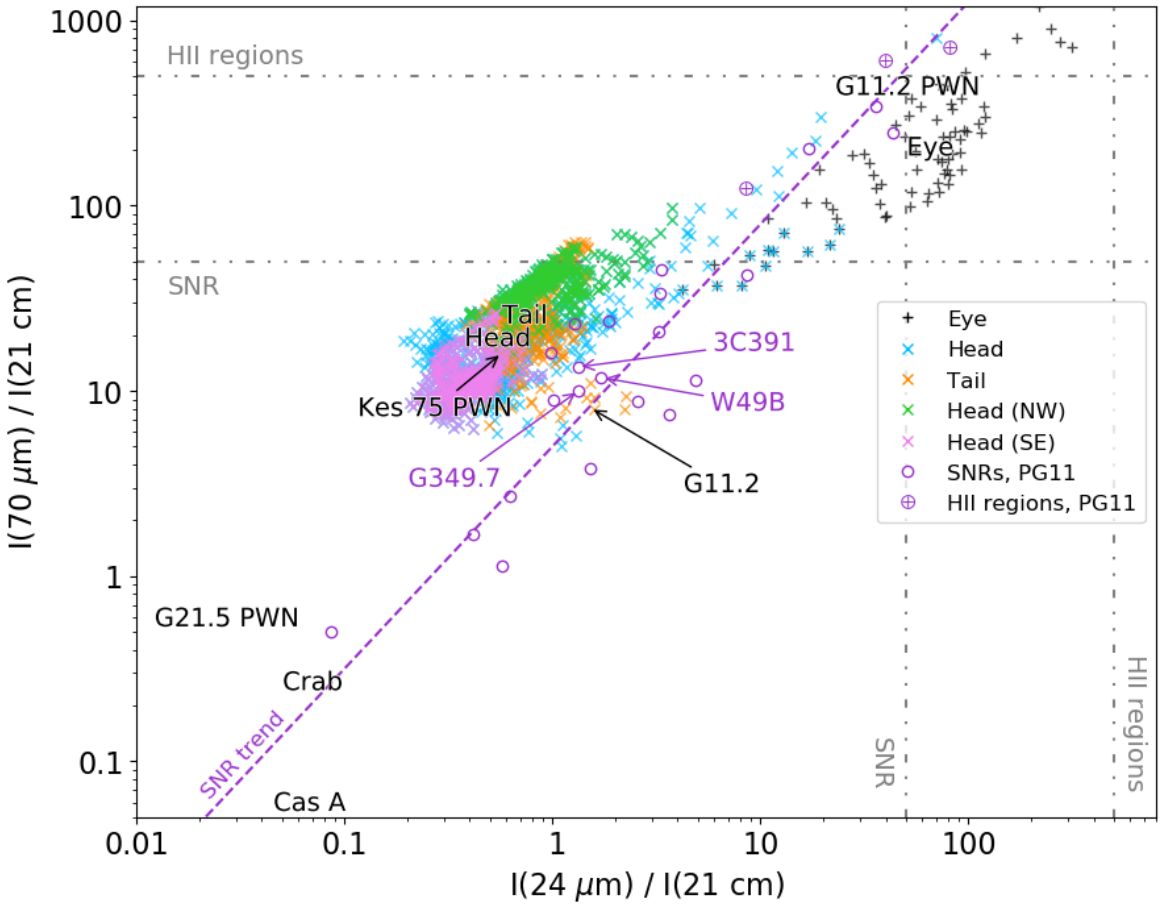

Figure 6.9: Flux ratio of individual pixels and integrated flux within the Tornado head, eye, and tail (within the circled regions in Fig. 6.8), in comparison with other SNRs and HII regions. Pixels with very low signal have been removed, where the signal divided by the subtracted background is <0.1. The fluxes for the NW and SE head, and the tail are measured from the regions indicated in Fig. 6.8. The text labels are centred on the integrated flux for the Tornado head and eye, and previously studied SNRs, estimated by De Looze et al. (Cas A and Crab; 2017, 2019) and Chapters 3 and 5 (G11.2, G21.5, G29.7 and G351.2). The grey dashed-dotted lines indicate ratios of 50 and 500, used in previous studies as diagnostics of SNRs and HII regions. The majority of the Tornado head and tail pixels fall within the SNR region, and are clearly different to the pixels within the eye, which sits very close to the HII region area of the colour space. All regions of the Tornado are found towards the upper right of the SNR regions, suggestive of an older remnant. There is a noticeable variation in the flux ratio of the NW and SE regions of the head.

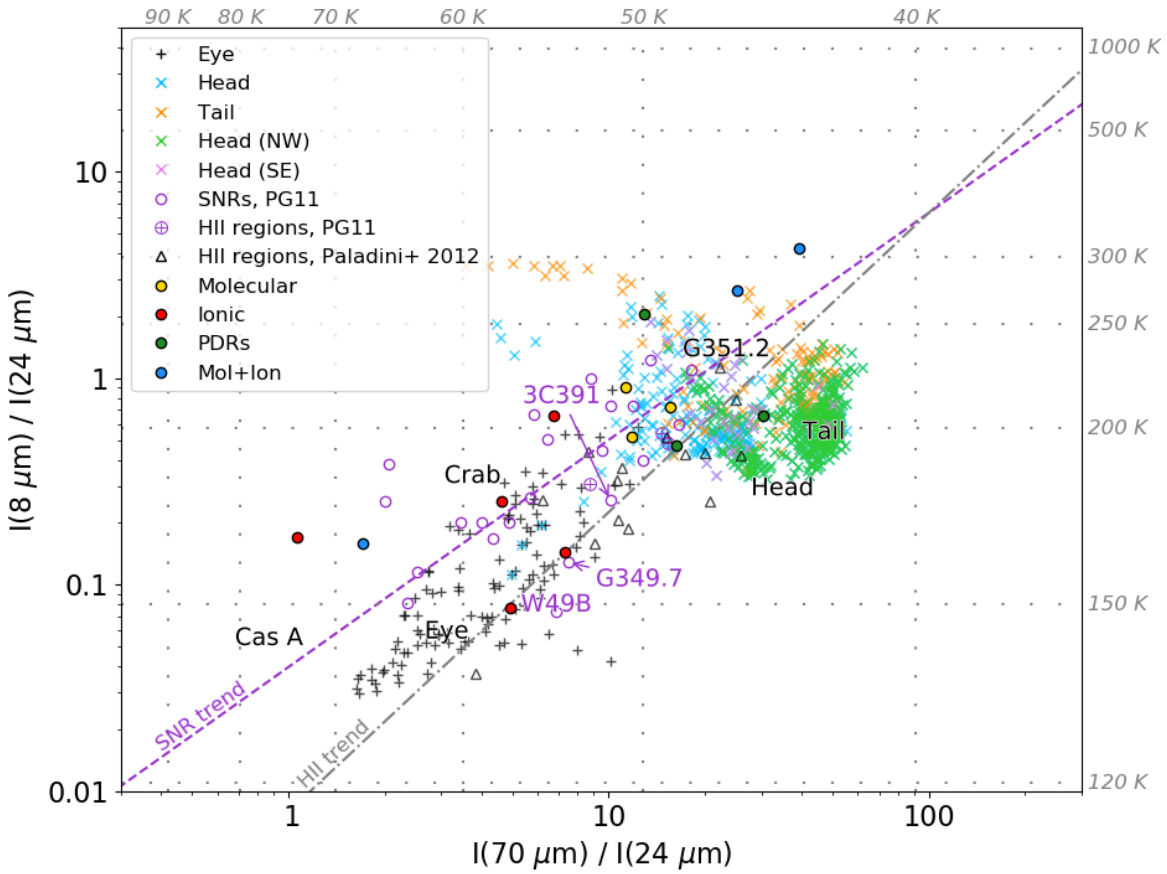

Figure 6.10: Flux ratio of individual pixels within the head, eye, and tail of the Tornado (within the circled regions in Fig. 6.8), in comparison with other SNRs and HII region. Pixels with very low signal have been removed, where the signal divided by the subtracted background is < 0.1. The fluxes for the NW and SE head, and the tail are measured from the regions indicated in Fig. 6.8. The text labels are centred on the integrated flux for the Tornado head and eye, and previously studied SNRs, estimated by De Looze et al. (Cas A and Crab; 2017, 2019) and Chapters 3 and 5 (G11.2, G21.5, and G29.7). We also include ratios for SNRs with known molecular interactions, atomic fine-structure emission, and PDRs from Pinheiro Goncalves et al. (2011). The purple dashed and the grey dash-dotted lines indicate SNR and HII region trends respectively, found by Pinheiro Goncalves et al. (2011). SNRs populate a wider area in this colour space and several Pinheiro Goncalves et al. (2011) SNR measurements lie along the HII region trend, including those highlighted in pink text. The Tornado is found towards the upper right of this colour space, suggestive of an older remnant. It is also found in a region populated mainly by SNRs with molecular interactions.

In all of the colour plots we find that the NW and SE regions (Fig.6.8) of the head are distinct and must have different emission processes. Fig. 6.9 shows a higher FIR – radio flux ratio in the NW region, suggesting an increased amount of thermal emission in the same area in which we see warm dust in Fig. 6.4: this dust may be heated through an interaction on this side.

6.4.2 What the Devil is it?

Gaensler et al. (2003) found that the X-ray emission from the head can be well explained by thermal models, rather than synchrotron emission, with a gas temperature of $kT \sim 0.6$ keV, arising from the interior of a limb-brightened radio SNR. Indeed, in Fig. 6.5 we find that the warmest dust is coincident with X-ray emission in the central region where hot gas may be heating the dust, as expected for a mixed-morphology SNR (Rho & Petre, 1998; Yusef-Zadeh et al., 2003). Sawada et al. (2011) estimated an X-ray temperature of 0.73 keV for the head. Using an X-ray temperature of 0.73 keV ($T = 8.6 \times 10^6$ K) and assuming that the Tornado nebula is an SNR, we estimate a shock velocity (V_s) and age (t) of the SNR using the radius of only the head and both the head and tail (1.3′ and 5.4′). The shock velocity is 884 km/s based on $V_s = (T/11.)^{0.5} \times 1000\,\mathrm{km\ s^{-1}}$ (Winkler & Clark, 1974). The age of the SNR ($t = 2/5\,Rs/Vs$) is therefore between 2000 and 8000 yr.

The bizarre shape of the tail is more difficult to explain with a SNR scenario. Gaensler et al. (2003) suggested that the tail could be explained by a progenitor star moving across the space whilst losing mass, which then exploded as a SN at the edge of circumstellar material (CSM; Brighenti & D'Ercole, 1994). A similar scenario has been suggested for the SNR VRO 42.05.01 (G166.0+4.3, Derlopa et al., 2020) which is much larger than the Tornado but morphologically resembles the Tornado head and surrounding filaments. When a progenitor star moves in the relatively higher density interstellar medium (ISM), the stellar motion could cause a bow shocks at the site of interaction between CSM and ISM. Bow shocks have been detected in the red-supergiants α Ori and μ Cep (Noriega-Crespo et al., 1997; Martin et al., 2007; Ueta et al., 2008; Cox et al., 2012). In the former, the bow shock has a wide opening angle, whereas the latter has a narrow-angle cylinder-type bow shock. The cylinder shape of the Tornado's tail could therefore be explained by CSM-ISM interaction. However, the CSM from red-supergiants does not emit synchrotron emission, so that the radio emission observed in the Tornado's tail would require additional energy by the SN – CSM interaction. This requires the

SN explosion itself to be highly elongated with very fast blast winds towards the east by more than by a factor of 10 to the west, which is unlikely and not supported by the hydrodynamic model (Brighenti & D'Ercole, 1994). Instead of synchrotron, the radio tail emission could be free-free; however, in that case, there should be some major heating and an obvious ionising source in the tail, which we do not see in the *Spitzer* 24 μm image (Fig. 6.2). Instead of a red-supergiant, the progenitor star could be a Wolf Rayet (WR) star, which has ionised gas in the CSM, and hence can emit free-free emission at radio wavelengths. However, the typical lifetime of a WR star is 10 – 36 kyrs (Meynet & Maeder, 2003, 2005), which is too short to form such a large scale structure while the star is moving in the local space. At a distance of 12 kpc, the furthest filament (centred at approximately $\alpha = 17^{h}40^{m}43.8^{s}, \delta = -30°55'44.9''$) is $\sim$ 25 pc from the centre of the Tornado head. This requires a progenitor to move through the ISM at speeds of approximately 1,000 km s^{-1}. Though not impossible, such a high speed motion is unlikely. It is therefore difficult to explain the Tornado's tail with past mass loss from a SN (SN-CSM interaction).

Next we investigate whether the filaments could have been formed by mass loss from a star at the location of the Tornado head. Fig. 6.11 shows the times required for material lost through the stellar wind of a progenitor to have reached the filaments (left), and typical evolutionary timescales for massive stars (right). For the stellar wind of a red supergiant to reach the distance to the furthest filament it would take between $\sim$ 156 and $\sim$ 2500 kyr for terminal wind speeds of 160 and 10 km s^{-1} respectively. Theoretical models (Ekström et al., 2012) suggest that the RSG phase lasts between $\sim$ 90 and 4000 kyr depending on the star's initial mass. In Fig 6.11 we infer the stellar wind terminal velocity for RSGs with high mass-loss rates from CO measurements (De Beck et al., 2010); some uncertainty arises as there is a dependence on the geometry of the gas (McCray, 1993). The theoretical models shown in the right-hand panel of Fig. 6.11 suggest that low mass RSGs ($M \lesssim 17\ M_{\odot}$) have lifetimes within the expected timescale needed for stellar winds to reach the distance of the furthest filament. However, intense mass-loss rates are found only towards the end of the RSG phase, making it unlikely that the filaments could be formed in this way. For a Wolf-Rayet stellar wind it would require between $\sim$ 10 and $\sim$ 36 kyr for typical terminal wind speeds between 2500 and 700 kms^{-1} to reach the furthest filament. The theoretical models shown in the right-hand panel of Fig. 6.11 indicate that the WR phase lasts a considerably longer time than required and, based on this, the filaments could have been formed by the stellar winds of a Wolf Rayet progenitor star. The winds from a Main Sequence star

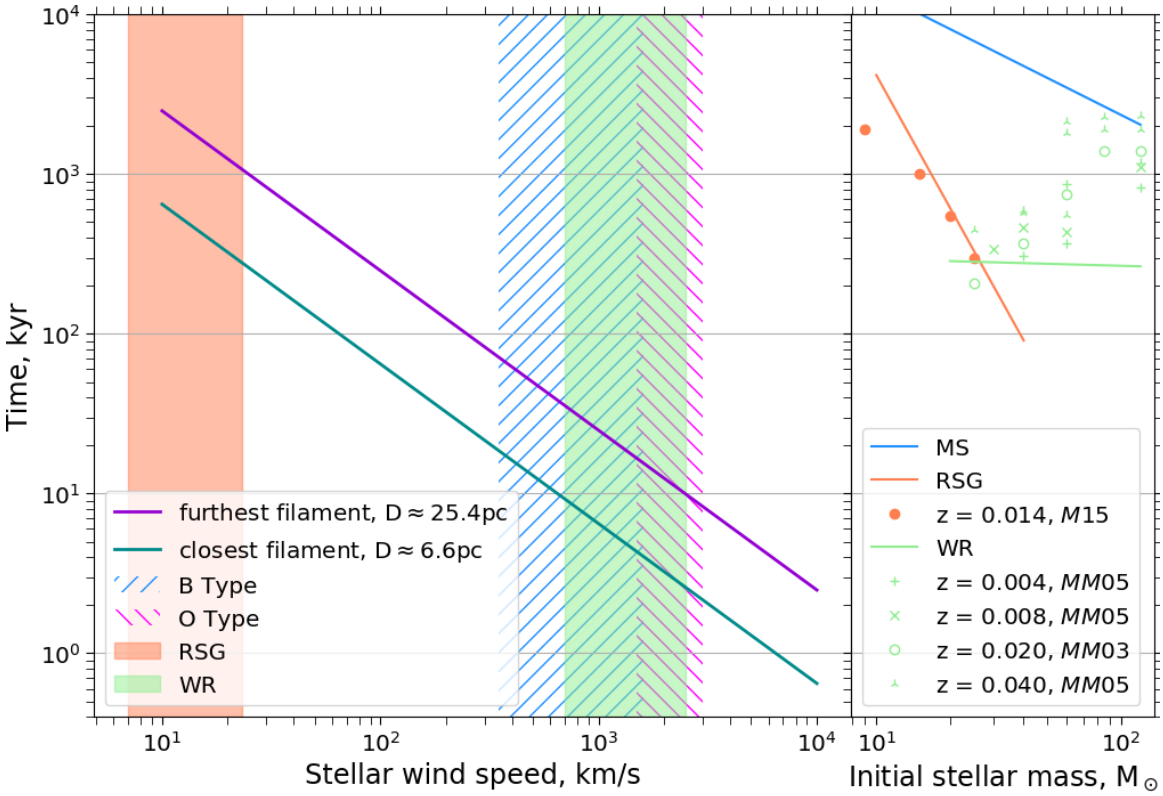

Figure 6.11: *Left:* The time required for stellar winds to reach the closest (cyan line) and furthest (purple line) radio filaments outside of the head, seen in Fig. 6.2. The shaded and hatched regions indicate typical stellar wind velocities for various massive stars (OB, Lamers et al., 1995; RSG, inferred from CO measurements by De Beck et al., 2010; WR, Hamann et al., 2019). *Right:* Typical timescales for the evolutionary phases of stars of various initial mass (solid lines: Ekström et al., 2012; Seo et al., 2018), (MM03: Meynet & Maeder, 2003, M15: Meynet et al., 2015).

would have enough time to reach the outer filament within this phase of evolution, although it is unlikely that the mass-loss would be high enough to account for forming the filaments.

Although the X-ray and radio emission from the head can be explained by thermal and synchrotron radiation from a SNR, the presence of an X-ray binary within the SNR would explain the length and the morphology of the tail in radio emission (Helfand & Becker, 1985; Stewart et al., 1994). Stewart et al. (1994) detected a spiral magnetic field around both the head and tail which they proposed could be explained by outflows from the central source dragging existing fields along the precession cone. In this instance, thermal X-ray emission at the location of the head is expected to arise from interactions between the jets and surrounding nebula, similar to that seen in the X-ray binary SS433 surrounded by a SNR W50 (Brinkmann et al., 1996; Safi-Harb & Ögelman, 1997). The radio power law index

of the central part of W50 is found to be typical for SNR (α ~0.58) (Dubner et al., 1998), while a hydrodynamic model shows that episodic jets from an X-ray binary containing a black hole compresses the SNR shell, forming a cylinder/helical shaped outflow in one direction (Goodall et al., 2011).

If the Tornado is formed by a binary system, the location of its source is controversial. In the case of the W50 – SS433 system, the high mass X-ray binary is located in the SNR, following which would place the Tornado binary within the head. However, Sawada et al. (2011) suggested that there is a *Suzaku* 1.5 – 3.0 keV band detection of a 'twin' source, opposite to where X-ray emission is already detected in the Tornado head. They propose that this originates from the interaction between the second jet of an X-ray binary system and a molecular cloud, placing any potential binary system source at the middle of the structure seen in Fig. 6.2, rather than in the head. In this case, one might expect visible emission in the IR/FIR wavelengths at the location of the 'twin' due to shocked gas/heated dust arising from jet interaction with the ISM. In the 24 µm and the *Herschel* bands there is emission towards the south-west of this region which correlates with radio structures in the tail. However, we do not see any clear evidence for an IR counterpart of the 'twin': in all *Spitzer* and *Herschel* maps, the flux at the location of the *Suzaku* peak is at a similar level to, or lower than, that of the surrounding area (see Fig. 6.13). There is some X-ray emission in the *XMM-Newton* and *Chandra* data at the location of the 'twin', although the emission does not seem correlated. However, the X-ray emission may be affected by foreground absorption, which makes association difficult to determine, and the region may peak in the 1.5 – 3.0 keV *Suzaku* band, with much lower emission of softer X-ray, making comparison between multiple bands complicated.

As there does seem to be X-ray and radio emission at the location of the 'twin' it is plausible that there is an object in this region, which may be associated with the Tornado, as suggested by Sawada et al. (2011). However, if there is emission from such an object in any of the *Spitzer* or *Herschel* bands, it is very faint and is not detected above the level of the ISM in this region (Fig. 6.13). This is unlike the head, from which there is a clear detection in the 5.8 – 500 µm bands, as well as a very bright radio structure (Fig. 6.12). It seems strange that their IR profiles are so different if the two regions have been formed by a similar process, although we cannot exclude this as a possibility. If the X-ray 'twin' head is unrelated to the Tornado, it is plausible that the location of an X-ray binary, if any, could be within the head of the Tornado, as discussed above.

Although the IR-radio emission supports a SNR origin for the Tornado head,

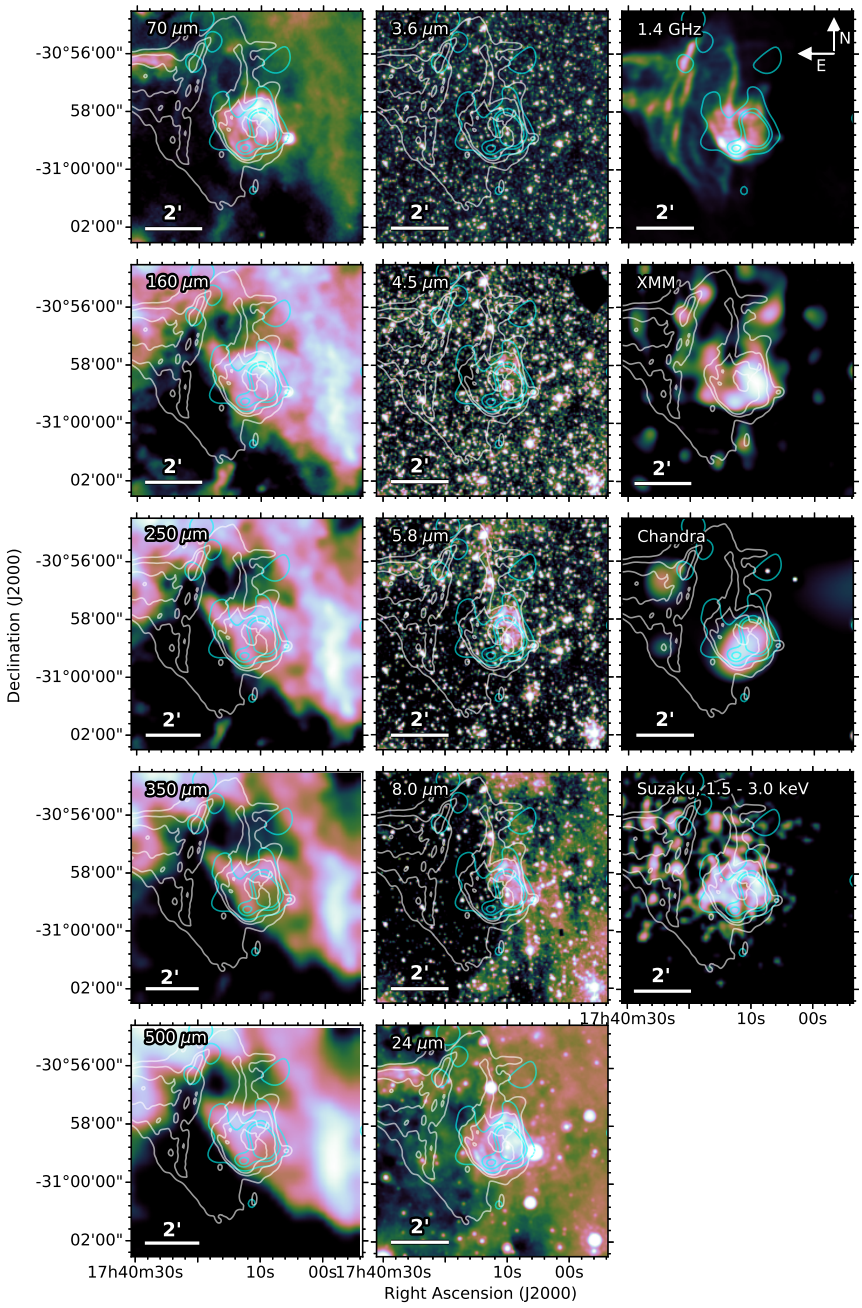

Figure 6.12: IR, radio, and X-ray view of the location of the Tornado head. *Left column: Herschel* images, *middle column: Spitzer* images, *right top:* 1.4 GHz VLA image, *right second row: XMM-Newton* X-ray image, *right third row: Chandra* X-ray image, and *right bottom: Suzaku* 1.5 – 4.0 keV X-ray image. We note that we have not applied a background subtraction or correction for vignetting as was done by Sawada et al. (2011). The white and cyan contours show the VLA 1.4 GHz and *XMM-Newton* emission respectively. There is a clear detection of emission from the head at the *Spitzer* and *Herschel* wavebands, between 5.8 and 250 μm, at 3.6, 350, and 500 μm there is emission which seems associated although it is more confused. There is a clear detection in all of the radio and X-ray images. (We use the CUBEHELIX colour scheme, Green (2011).)

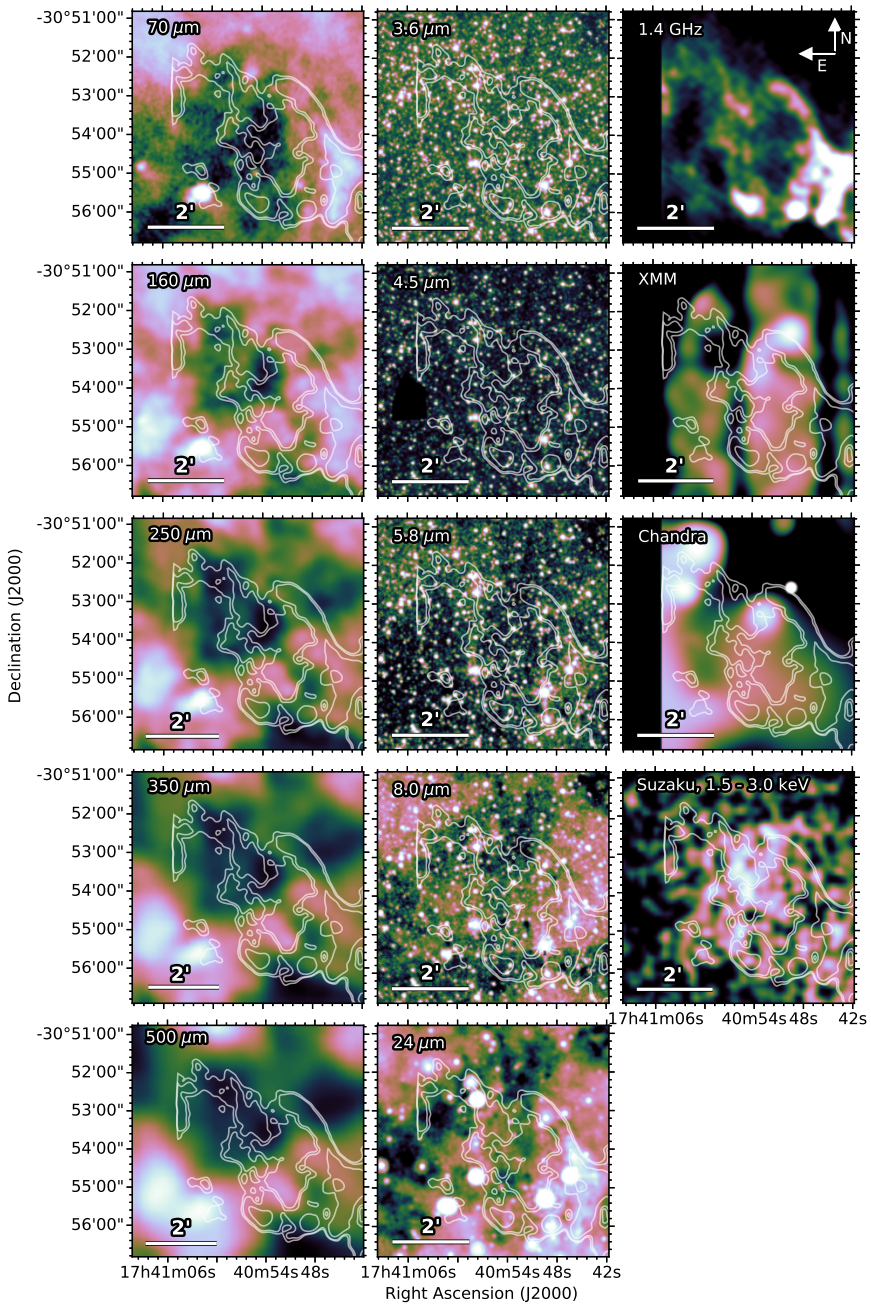

Figure 6.13: IR, radio, and X-ray view of the location of the X-ray twin, detected by Sawada et al. (2011), the scale is increased compared with the image in Fig 6.2 to enhance any features in the region. *Left column: Herschel* images, *middle column: Spitzer* images, *right top:* 1.4 GHz VLA image, *right second row: XMM-Newton* X-ray image, *right third row: Chandra* X-ray image, and *right bottom: Suzaku* 1.5 – 4.0 keV X-ray image. We note that we have not applied a background subtraction or correction for vignetting as was done by Sawada et al. (2011). The white contours show the VLA 1.4 GHz emission. In all *Herschel* and IRAC bands the flux level at the location of the twin is similar to, or lower than, that of the surrounding ISM. In all other bands there is some emission, although the morphology is not consistent with the *Suzaku* features, and at 24 μm this is fainter than much of the surrounding ISM. (We use the CUBEHELIX colour scheme, Green (2011).)

we see no clear indication that the X-ray emission from the head results from an interaction between X-ray binary jets and the surrounding nebula. However, the helical shape of the tail, and the presence of its magnetic field and synchrotron radiation, can be explained by a jet ploughing into a SNR shell, as observed in W50. Although there is no detection of a central powering source, there are cases in which the central X-ray binary may be too faint to detect at a distance of 12 kpc. Gaensler et al. (2003) suggest that this would be the case for a high-mass X-ray binary such as LS 5039 (Paredes et al., 2000), from which the luminosity may vary with orbital phase and its minimum is slightly higher than the upper limit for detection of a Tornado central source. It could also be the case that the Tornado is powered by a low mass X-ray binary in a quiescent state, having produced the observed features in a past period of prolonged activity (Sawada et al., 2011), as seen in 4U 1755–338 (Angelini & White, 2003).

6.5 Conclusion

We detect FIR emission from dust in the unusual SNR candidate the Tornado (G357.7−0.1), akin to the terrestrial sandy whirlwinds known as 'Dust Devils'. We investigate the distribution of dust in the Tornado using Point Process Mapping, PPMAP. Similar to that found in the radio emission, we find a complex morphology of dust structures at multiple temperatures within both the head and the tail of the Tornado, ranging from 20 – 60 K. In the head of the Tornado, we find warm dust in the region at which the object is thought to be interacting with a molecular cloud. We also find a filament along the SE edge coinciding with radio emission, and a cool dusty shell encapsulating hot dust near to the location of an X-ray peak. We derive a total dust mass for the head of the Tornado of 16.7 $M_{\odot}$.When considering whether the Tornado may be a SNR, we find that it is aged between 2000 and 8000 yrs and it is plausible that the estimated dust mass originates from material swept up from the ISM.

The origin of the Tornado is still unclear. We do not find clear evidence of a FIR counterpart to the Tornado 'twin' detected by Sawada et al. (2011), which was suggested to be the other end of an X-ray binary system. The FIR – radio colours in the Tornado head are consistent with a SNR origin for this structure, yet the tail is not easily explained by just the SN or a SN-CSM interaction. The tail can be explained via jets from an X-ray binary source within the nebula, similar to the W50 SNR. One useful way to distinguish between the several hypotheses put forward by various authors would be to measure the velocity of the gas motion in

the tail, if it emits in near-infrared Br α or [Fe II] for example.

Chapter 7
Conclusions and Future Work

'Aristotle said a bunch of stuff that was wrong. Galileo and Newton fixed things up. Then Einstein broke everything again. Now, we've basically got it all worked out, except for small stuff, big stuff, hot stuff, cold stuff, fast stuff, heavy stuff, dark stuff, turbulence, and the concept of time.'

Zach Weinersmith, Science: Abridged Beyond the Point of Usefulness

This thesis explores the question of whether dust can survive in SNRs and if it does, which objects are most likely to contribute to the dust content of the ISM. To address this I have studied 190 SNRs within the Galactic Plane from Green's SNR catalogue (Green, 2014), and compiled a catalogue of dusty SNRs to complement previous IR surveys by Arendt (IRAS, 1989), Saken et al. (IRAS, 1992), Reach et al. (IRAC, 2006) and Pinheiro Goncalves et al. (MIPS, 2011). In this study, SNRs are classified between Levels 1 and 4 based on the confidence of a FIR detection, following a system used by previous surveys, where a Level 1 detection is a clear detection of dust emission and Level 4 indicates a clear lack of FIR emission. Dust is detected within 39 SNRs to a Level 1 rating giving a 21 per cent detection rate, although there could be many more dusty SNRs within our sample which are too confused with the ISM to detect. Dusty SNRs within the catalogue are further

studied to determine the dust properties, with some evidence that SNe can contribute significant amounts of dust to the ISM to account for the missing mass in the dust budget. This thesis mainly relies on data from the *Herschel* survey, HiGAL (Molinari et al., 2010a, 2013, 2016), which observed FIR emission across the entire Galactic Plane ($| b | \leq 1°$).

7.1 Key Findings

7.1.1 Dusty SNR Catalogue

Inspecting Galactic SNRs with *Herschel* gives a 21 per cent Level 1 detection rate of FIR emission which, for the most part, is expected to be attributed to thermal dust emission. Of the detected dusty SNRs, 13 are from core collapse SNe and two are Type Ia remnants (the other 24 are of unknown type). There is no clear evidence that there is any ejecta dust associated with the Type Ia SNRs, and instead this is more likely to have been swept up from the ISM by the expanding SNR shell. This is consistent with previous observations of the Type Ia SNRs Tycho and Kepler (Gomez et al., 2012a), and with theoretical studies which suggest that any dust formed in Type Ia SNe is efficiently destroyed by the reverse shock (e.g. Nozawa et al., 2011).

In line with previous studies of SNRs containing dust, the highest proportion of Level 1 detections are young (<5 kyr) as these tend to be brighter and more compact, and can be identified more clearly above the level of the ISM. However, this catalogue stretches the age range of dusty Galactic remnants up to ∼100 kyr. It is expected that the dust content of the majority of Level 1 detections in this survey is most likely pre-existing material which has been swept up by the expanding SNR shell, or heated by interactions between the SNR and dense ambient material. Nevertheless, ejecta dust is detected within five SNRs: four PWNe G11.2−0.3, G21.5−0.9, G29.7−0.3 (Kes 75), and G54.1+0.3 (Temim et al., 2010; Rho et al., 2018) and a CCSNR G350.1−0.3.

7.1.2 SNR Dust Content

The dust content of the newly detected PWNe, G11.2, G21.5, and Kes 75, has been investigated via two techniques: initially fitting modified blackbody SEDs to the *Herschel* fluxes in a Monte Carlo routine, and then using PPMAP to examine the

dust in more detail at multiple temperatures. The Monte Carlo analysis gives average cold dust temperatures of $26.7^{+1.7}_{-1.3}$ K, 26.0 ± 0.7 K, and $30.7^{+11.7}_{-4.0}$ K for G11.2, G21.5, and Kes 75 respectively, and dust masses of $1.1^{+0.4}_{-0.3}\,M_\odot$, $0.12 \pm 0.02\,M_\odot$, and $0.3^{+0.4}_{-0.2}\,M_\odot$. Further analysis with PPMAP confirms the presence of cool dust structures in the three PWNe, with temperatures between 20 and 40 K and dust masses of $0.34 \pm 0.14\,M_\odot$, $0.29 \pm 0.08\,M_\odot$, $0.51 \pm 0.13\,M_\odot$ for G11.2, G21.5, and Kes 75 respectively. The disparity in the two methods is due to a combination of using different background subtraction techniques, and because PPMAP is able to trace the dust at a wide range of temperatures rather than assuming that all of the dust is at a single temperature. Regardless, both methods find significant dust masses, suggesting that SNRs containing PWNe may be important sources of cosmic dust. PPMAP is used further to study the dust emissivity index, β, and investigate whether there is any discernible difference between the properties of the PWNe dust and the surrounding ISM. Although the signal-to-noise at long wavelengths is inadequate to constrain β for G11.2 and Kes 75, there is some evidence of a variation in the dust of G21.5, for which $\beta = 1.4 \pm 0.5$ compared with the ISM where $\beta = 1.8 \pm 0.1$.

The dust within 11 other SNRs is studied using their 24 – 70 µm flux ratio. The resultant temperature maps indicate the presence of warm dust ($\sim$25 – 40 K) in all of these objects. For the sources for which there is a distance measurement, the associated dust masses are between 0.2 and $340\,M_\odot$. Some of these estimates are unexpectedly large for the mass of dust which could be produced by the SN, or swept up by the expanding shell. For SNRs located in the Galactic Plane, confusion with the ISM is the largest difficulty in accurately estimating the dust mass, as the estimated mass is highly sensitive to small changes in the temperature, which are in turn affected by contaminating ISM that reduces the average dust temperature. Thus it is likely that the largest dust masses are overestimated because of difficulty subtracting the background.

A region of dust has been detected at the centre of G351.2+0.1, radio observations of which suggest that it could be a PWN or an unrelated HII region, and in this thesis the FIR emission is studied in an attempt to ascertain its nature. SED fitting analysis gives a cool dust component with temperature and mass of 45.8 K and $0.18\,M_\odot$, and a warm component with temperature and mass of 242.1 ± 6.8 K and $(3.9 \pm 0.4) \times 10^{-6}\,M_\odot$. When considering the nature of this object, the dust temperature is higher than that of a typical HII region, although it is not unheard of, and the IR colours are consistent with either a HII region or a SNR. It is therefore possible that the dust is either unrelated interstellar material or a region of SN

ejecta with a considerable mass.

7.1.3 The Tornado SNR Candidate

In the Galactic Plane SNR survey, dust emission is detected from the aptly named Tornado SNR candidate, G357.7−0.1. Further analysis of the FIR emission with PPMAP reveals complex dust structures with temperatures between 15 and 61 K, and a total mass of 16.7 $M_\odot$.

There is noticeable variation in the IR emission across the Tornado head, with a bright peak to the north-west, where the head is expected to be interacting with dense molecular material. A study of the IR and IR – radio colours indicates a corresponding variation in dust properties across the object, implying that there is some difference in the dust properties or heating process. The properties of the Tornado head can be explained by a SNR aged between 2 and 8 kyr, which has swept large masses of dust from the surrounding, dense material. The tail of the Tornado, however, is bizarre and difficult to explain. It is unlikely that the tail was formed by a progenitor star before it exploded. The jets from an X-ray binary could form structures like those seen in the tail, and the observed emission may be explained by a jet ploughing into a SNR shell, as seen in the W50 system.

7.2 Future Work

This thesis aimed to answer the question of whether SN dust can survive to be injected into the ISM. We tackled the observational side of this complicated question, providing a larger sample of objects within which dust has been detected and measured. However, there is still much more investigation required to comprehensively determine the survival rate of ejecta dust in SNRs.

This thesis has widened the sample of SNRs analysed for their dust emission and given some insights into the types of object which could be important when considering dust formation by SNe. Analysis of G11.2−0.3, G21.5−0.9, and Kes 75 in Chapter 3 suggests that SNRs containing PWNe are important contributors of dust to the ISM. Yet, to prove their significance, or otherwise, observations of a larger sample are required. Targeted FIR observations of more PWNe could give further insight into whether there are processes within the nebulae which protect ejecta dust, and how this varies depending on the environment and SN type. There are already extensive literature studies of the Crab Nebula and Cas A.Within the Milky Way there are another 16 PWNe associated with SNRs which are outside

of the HiGAL coverage (excluding the Crab and Cas A); IR and submm observations of these would clarify the importance of PWNe in the survival of ejecta dust. The majority of FIR level 1 detections were well detected at 24 µm, with less confusion than in the longer wavebands. As such, MIRI (JWST, Bouchet et al., 2015) should be able to identify dusty PWNe, and also to resolve the dust location, given its much higher resolution at 25.5 µm compared with that of MIPS 24 µm observations. Combined with FIR images; using for example HAWC+ (40 – 300 µm, SOFIA, Harper et al., 2018), ArTéMiS (200, 350, and 450 µm, APEX Revéret et al., 2014), SCUBA2 (450 and 850 µm, JCMT, Holland et al., 2013), LABOCA (870 µm, APEX Siringo et al., 2009), and ALMA; this would give a broader sample of PWNe with FIR observations, to confirm their impact on the survival or destruction of SN dust. Additionally, as the 16 PWNe suggested are located away from the Galactic Plane, issues with confusion should be limited compared with studies in this thesis of SNRs within the Galactic Plane, allowing for greater certainty in the estimated dust mass.

In many cases it is difficult to disentangle ejecta dust and swept-up ISM within a SNR, as well as separating this from fore- and background material. This hinders our understanding of the amount, and properties, of dust formed by the SN which has thus far survived destructive processes. Indebetouw et al. (2014) and Cigan et al. (2019) have shown that, in a new era of resolved submm astronomy with ALMA, we can disentangle dusty regions to determine those which are ejecta or ISM dominated. Doing so with a larger number of SNRs would give us a greater insight into the mass of freshly formed dust, as well as that which has been processed by the reverse shock. Further spectral analysis with MIRI MRS could also help to disentangle contaminating ISM and ejecta material.

In Chapter 3 we used PPMAP to measure the dust mass of three PWNe: G11.2−0.3, G21.5−0.9, and Kes 75. However, we were unable to constrain the dust emissivity, β, which determines the Rayleigh-Jeans slope of their SED and is dependent on the dust properties, including grain size and composition. When determining the dust contribution made by SNe to the ISM, it is crucial to consider the properties of the freshly formed ejecta, as its susceptibility to destruction varies for different compositions and grain sizes. Additionally, studying variations in β across an object and in the surrounding material would further improve our ability to distinguish ejecta, processed, and ISM dust, and to scrutinize the variation in their properties. As we had limited, and highly uncertain, long wavelength data in this thesis, we were not able to constrain the Rayleigh-Jeans part of the SED, and nor therefore β. More observations of SNRs, including the three discussed, at

long wavelengths with JCMT, APEX, and ALMA would provide more detailed information about the Rayleigh-Jeans slope. This would allow us to more accurately pin down the value of β, giving a better understanding of the dust properties and it's likelihood to be injected into the ISM.

Throughout this thesis PPMAP was used to analyse the dust content of SNRs with a higher resolution than traditional SED fitting, as well as estimating the mass across a grid of temperatures. This is a powerful tool and further analysis of SNRs with it could give a great insight into the dust content and survival. In particular, PPMAP analysis of the Crab Nebula and Cas A would be interesting as the large amount of literature on these SNRs should allow a good comparison between the dust property variation and regions with known characteristics.

In Chapter 6 we discussed the properties of the Tornado SNR candidate. Further analysis of the multi-waveband data might give more of an insight into the scenario which has formed such a strange structure. In particular, we used X-ray data for a rough comparison of the location of IR emission; this could be used more effectively if the X-ray data was reduced to allow a more detailed study of the structures and likely emission processes. This could also help to determine whether the *Chandra* emission close to the location of the X-ray 'twin' is associated with the *Suzaku* detection, and therefore to reveal more about its nature. In addition to further study of the Tornado, it would be extremely interesting to study the FIR properties of the W50 – SS 433 system, which we have suggested could be analogous to the Tornado. This would both shed more light onto the comparability of the two systems, and give greater insight into the potential survival of SNR dust within such an extreme object.

7.3 Final Remarks

This thesis set out to investigate the importance of SNe to the dust budget of the ISM. By studying Galactic SNRs it was found that dust can survive, with detections of dust emission associated with SNRs as old as 100 kyr. In this search we found several interesting objects which contain large masses of dust. Although much of the dust within most of our FIR detected remnants is likely to be pre-existing, the findings of this thesis suggest that SNRs may be important contributors of dust to the ISM. There is still the question of how much dust is destroyed by SN shocks, yet there are detections of ejecta dust which has survived to a longer timescale than found in previous studies of remnants, and which, in some cases, seems to have survived the reverse shock. In particular, this work indicates that

PWNe are significant and deserving of attention in the search for dust-producing SNe. There is still more work required to determine the extent to which SNe contribute dust to the ISM and which types of objects are responsible, yet this work suggests that SNe are important in this.

Appendices

CHAPTER A
IMAGES OF THE FIRST LOOK CATALOGUE OF SNRS

In this section we present images of all of the supernova remnants in our first look sample. The border colour of each image indicates the associated detection level in this study, as given in Table 2.1, where green = level 1, orange = level 2, magenta = level 3, grey = level 4, and black = unstudied. *Herschel* images are presented in Figure A.1, and multi-wavelength images (*Herschel*, *Spitzer* IRAC, *Spitzer* MIPS, and radio) in Figure A.2.

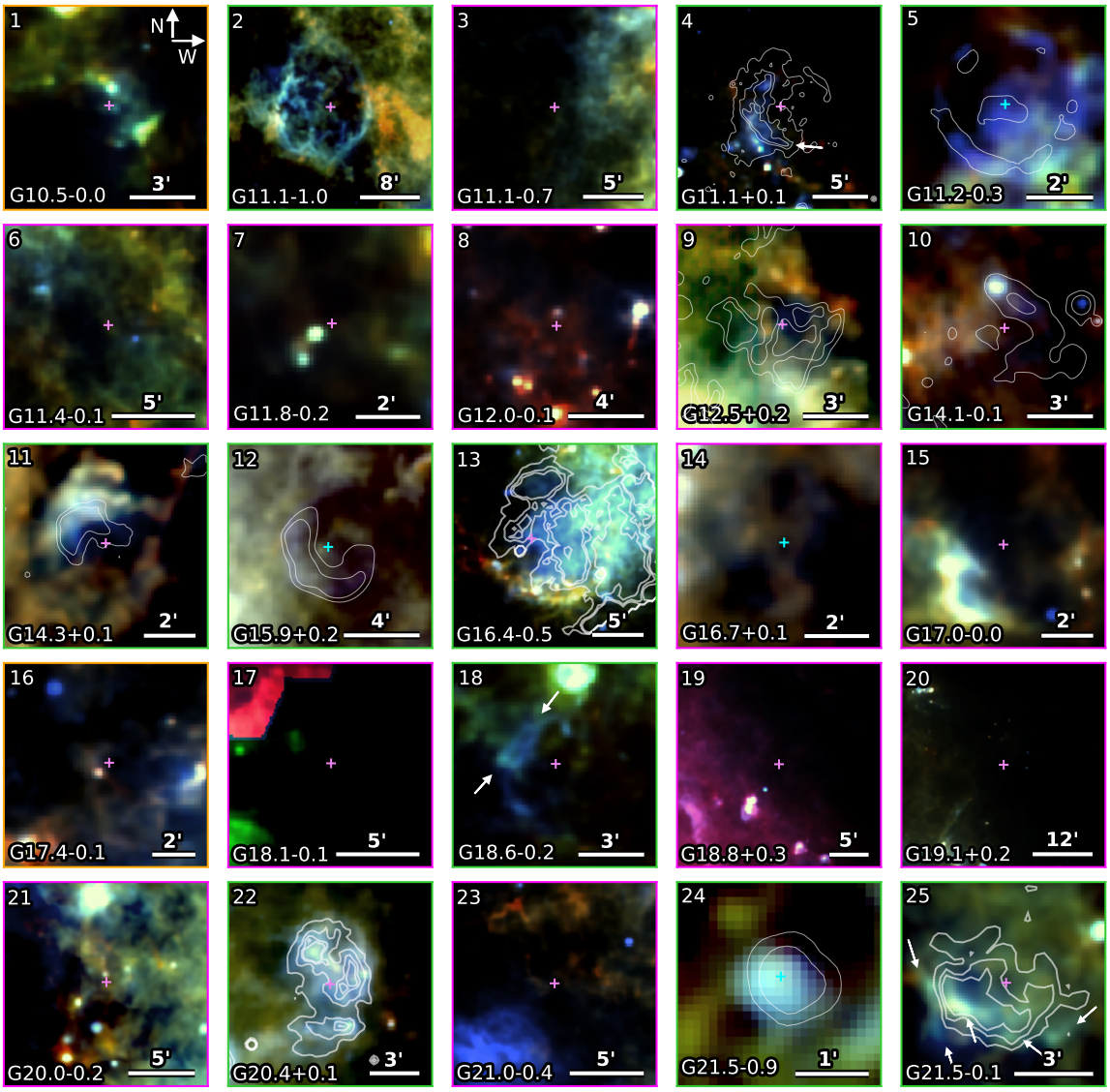

Figure A.1: *Herschel* three colour images of all of the supernova remnants in our first look sample (Chapters 2 and 3). Colours are red = 250 μm, green = 160 μm, and blue = 70 μm. Purple crosses indicate the source radio centre from Green (2014) and cyan crosses indicate the X-ray centre. Magenta diamonds indicate the location of 1720 MHz OH masers. The border colour indicates the associated detection level in this study, as given in Table 2.1, where green = level 1, orange = level 2, magenta = level 3, grey = level 4, and black = unstudied. In some panels dashed magenta circles and white arrows indicate particular FIR dust emission features associated with the SNR. X-ray contours are overlaid onto the images of G11.2−0.3 and G15.9+0.2, MIPS contours are overlaid onto G14.1−0.1, and radio contours are overlaid onto the image of G14.3+0.1.

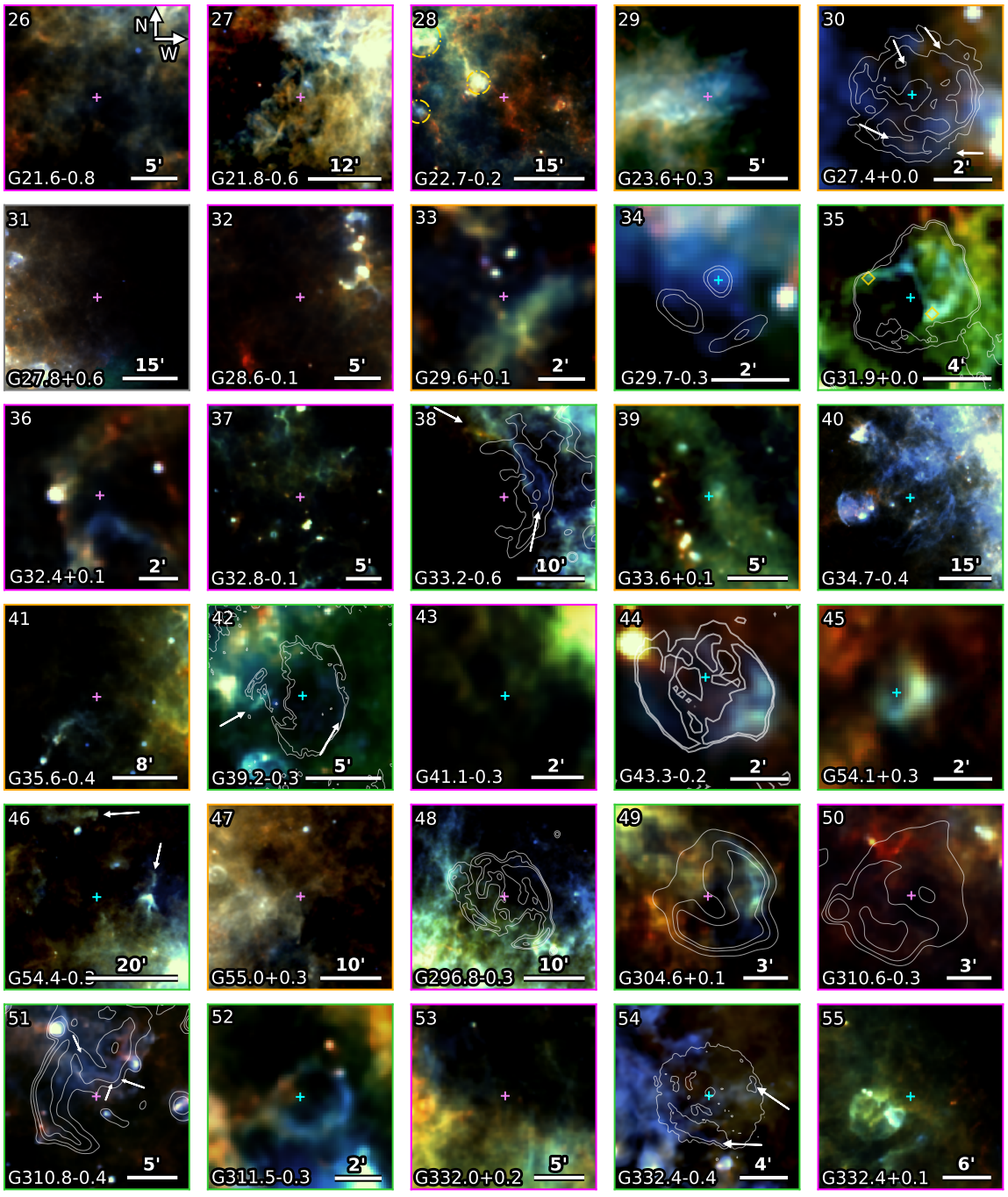

Figure A.1: Radio 20 cm contours are overlaid onto the image of G20.4+0.1, G31.9+0.0, and G33.2−0.6. X-ray contours are overlaid onto the images of G21.5−0.9, G27.4+0.0, G29.7−0.3, and G33.3+0.1.

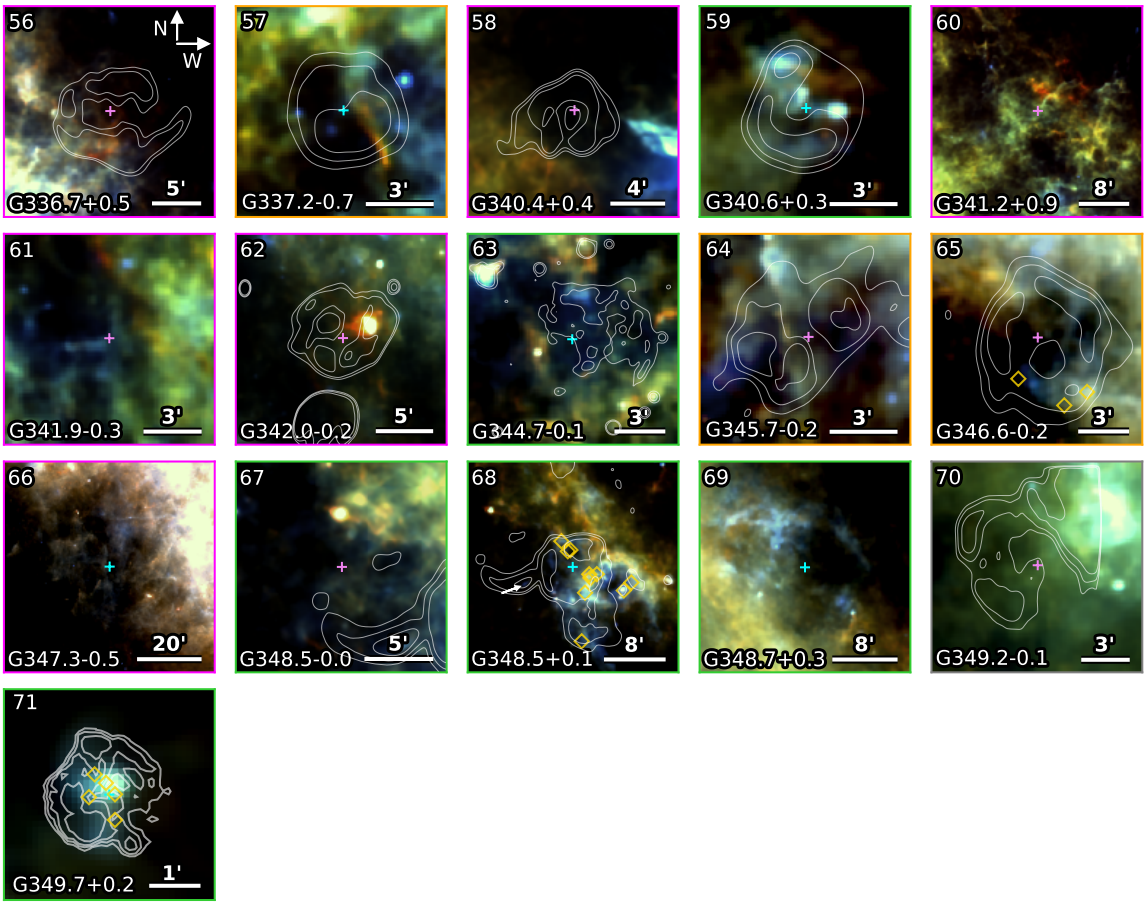

Figure A.1: Radio contours are overlaid onto the images of G39.2−0.3, G43.3−0.2, G336.7+0.5. X-ray contours are overlaid onto the image of G332.4−0.4

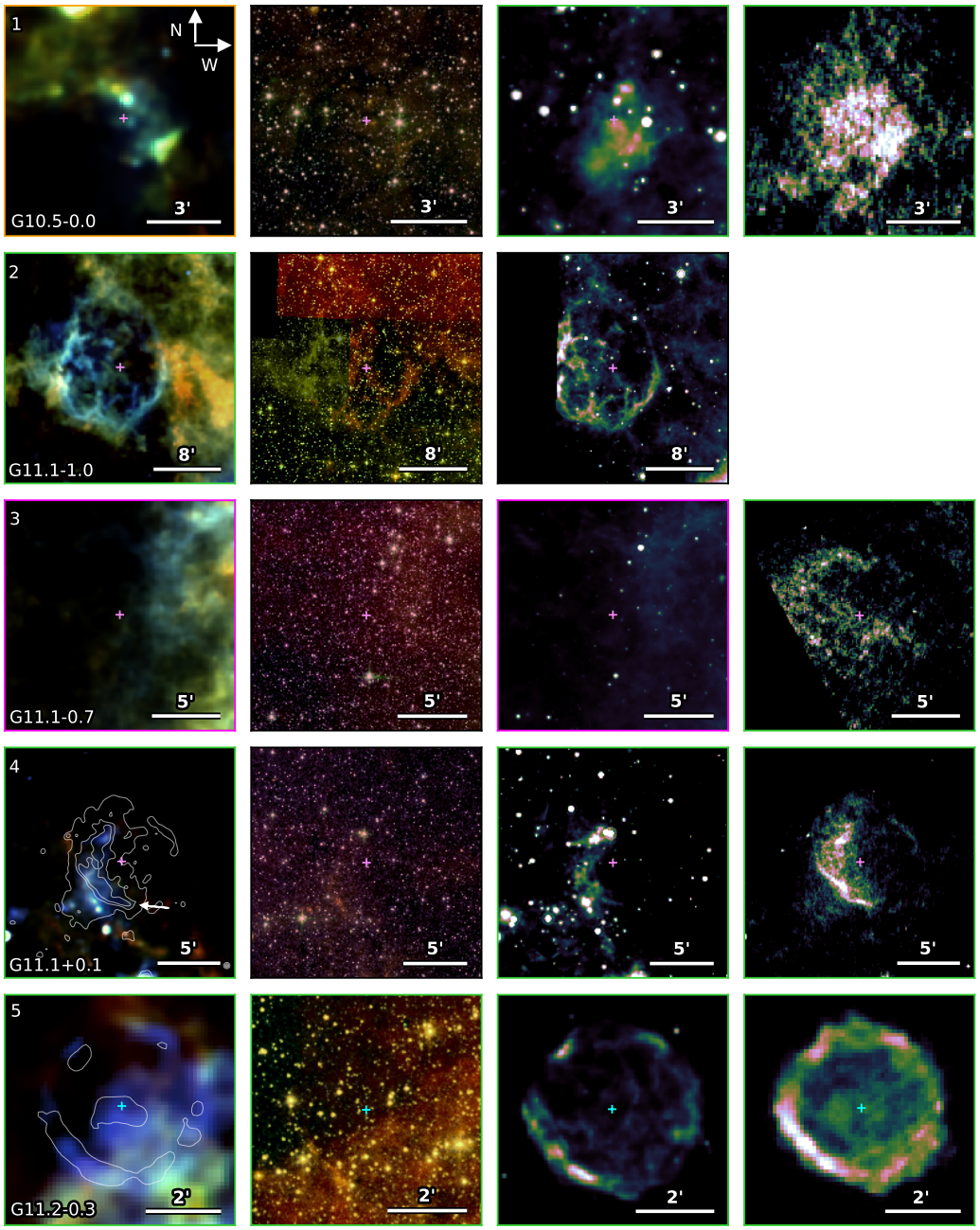

Figure A.2: Multiwavelength images of the first look catalogue *First column*: *Herschel* three colour images where colours are red = 250 μm, green = 160 μm, and blue = 70 μm. Overlaid contours are X-ray unless indicated. *Second*: *Spitzer* IRAC four colour images. *Third*: *Spitzer* MIPS 24 μm images. *Fourth*: Radio images: VLA 20 cm where $l < 48.5°$, CGPS 1420 MHz in the range $52 < l < 192°$, and MOST 0.843 GHz where $l > 255°$. The border colour indicates the detection level (Table 2.1), where green = level 1, orange = level 2, magenta = level 3, grey = level 4, and black = unstudied. This is given for this study in the first column, R06 in the second column, and PG11 in the third column. Where shown, dashed magenta circles and white arrows indicate particular FIR dust emission features associated with the SNR. The *Herschel* image of G11.2−0.3 includes X-ray contours.

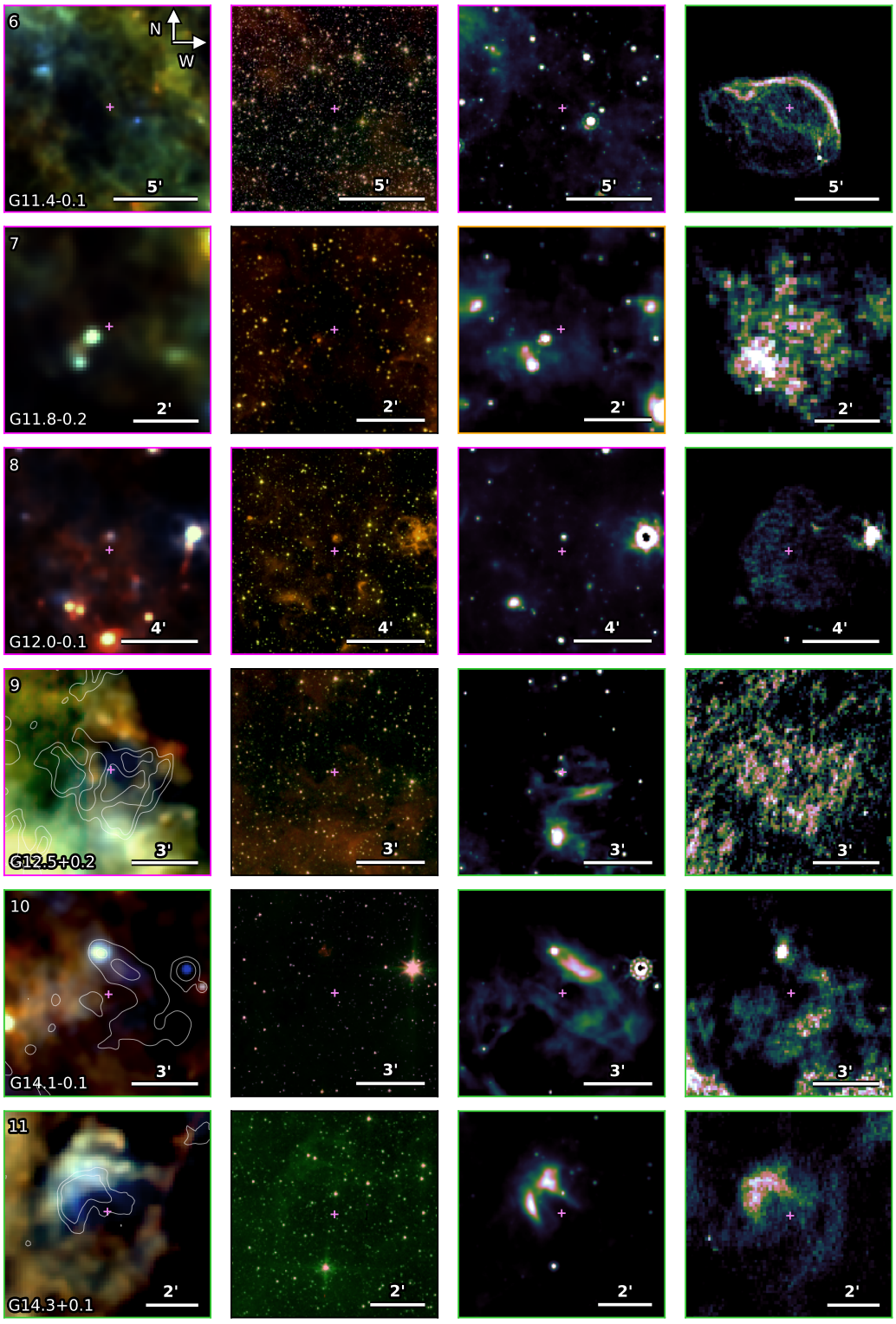

Figure A.2: MIPS 24 μm contours are overlaid onto the *Herschel* image of G14.1−0.1.

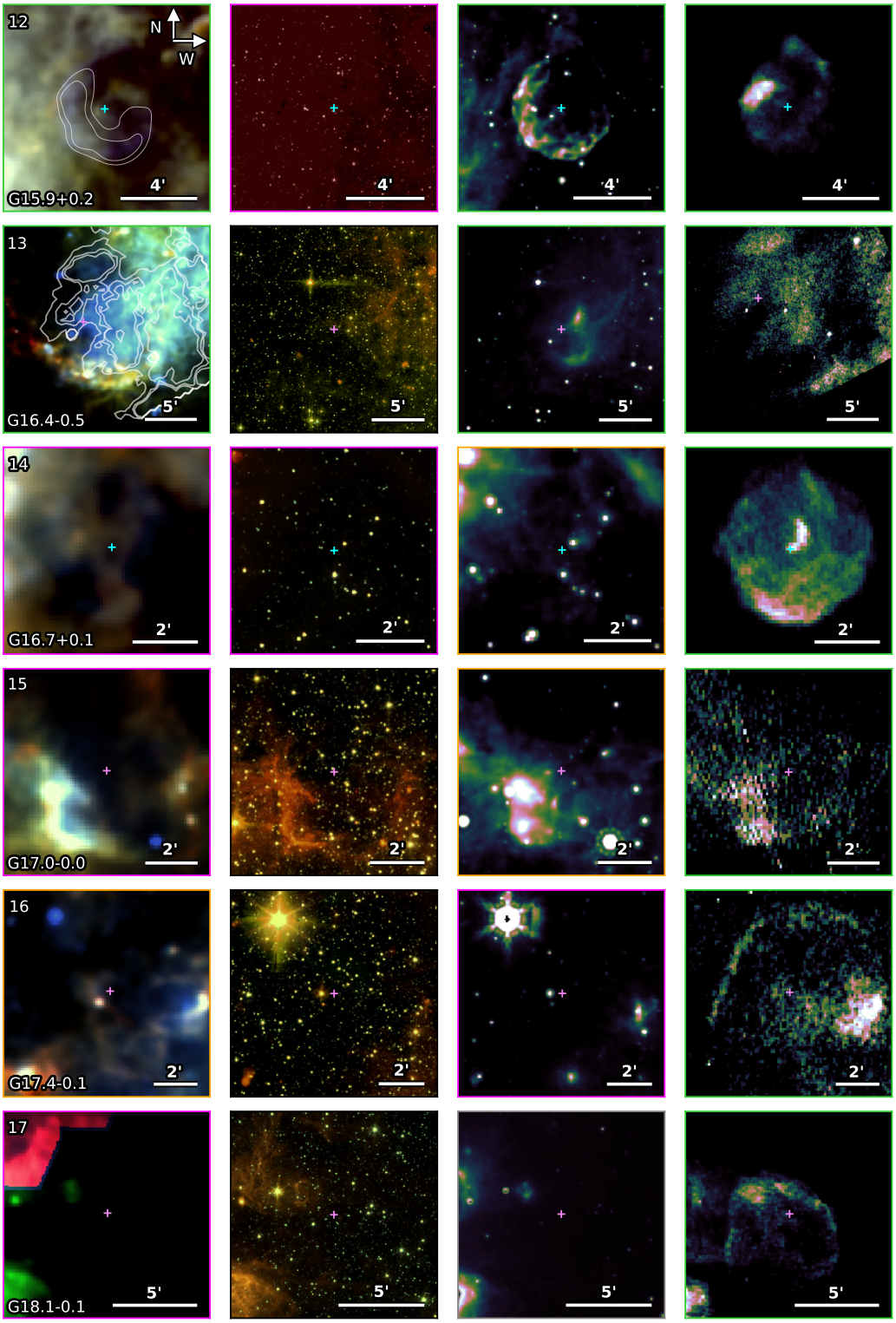

Figure A.2: Radio contours are overlaid onto the *Herschel* image of G14.3+0.1 and X-ray contours onto the *Herschel* image of G15.9+0.2.

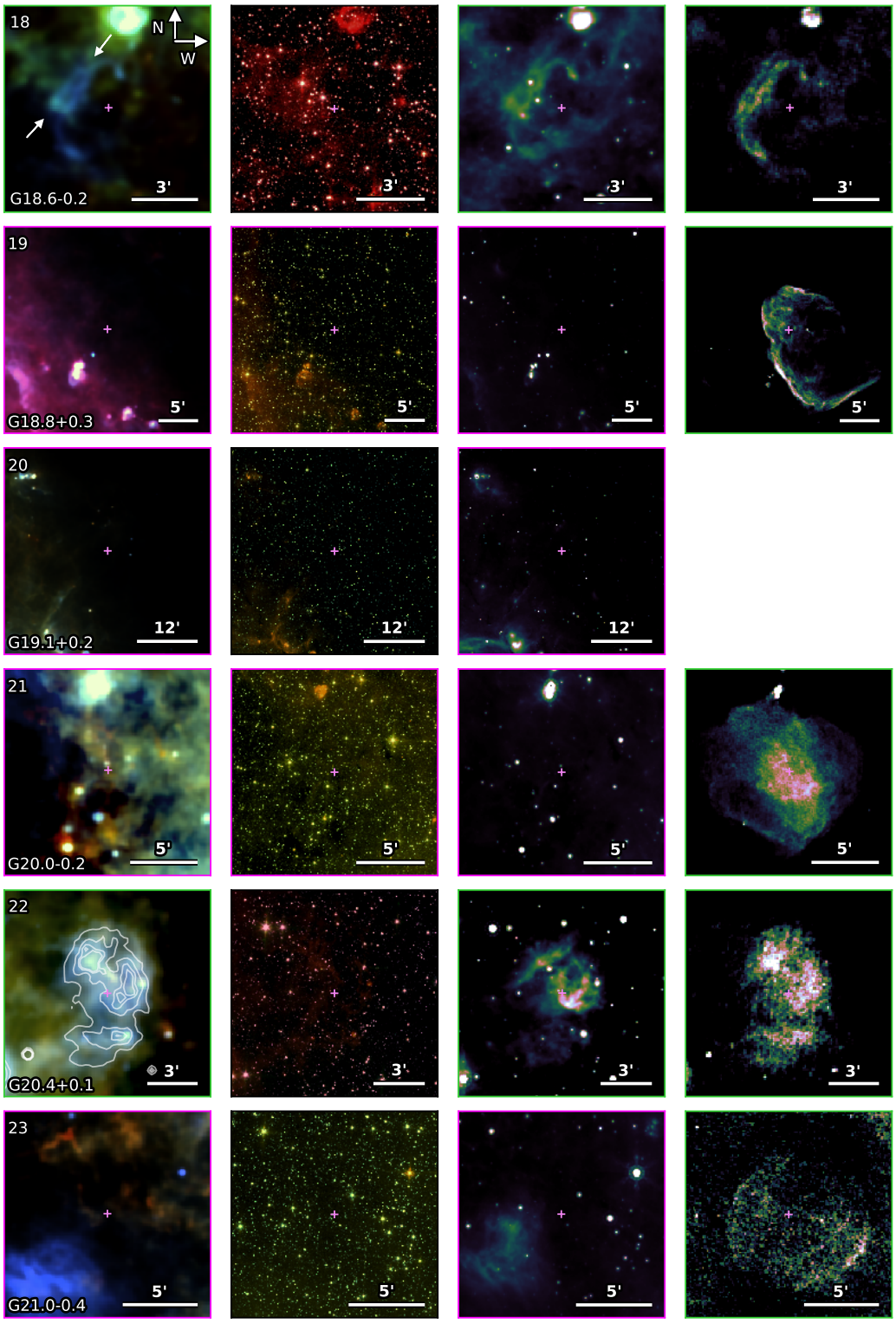

Figure A.2: - *continued.*

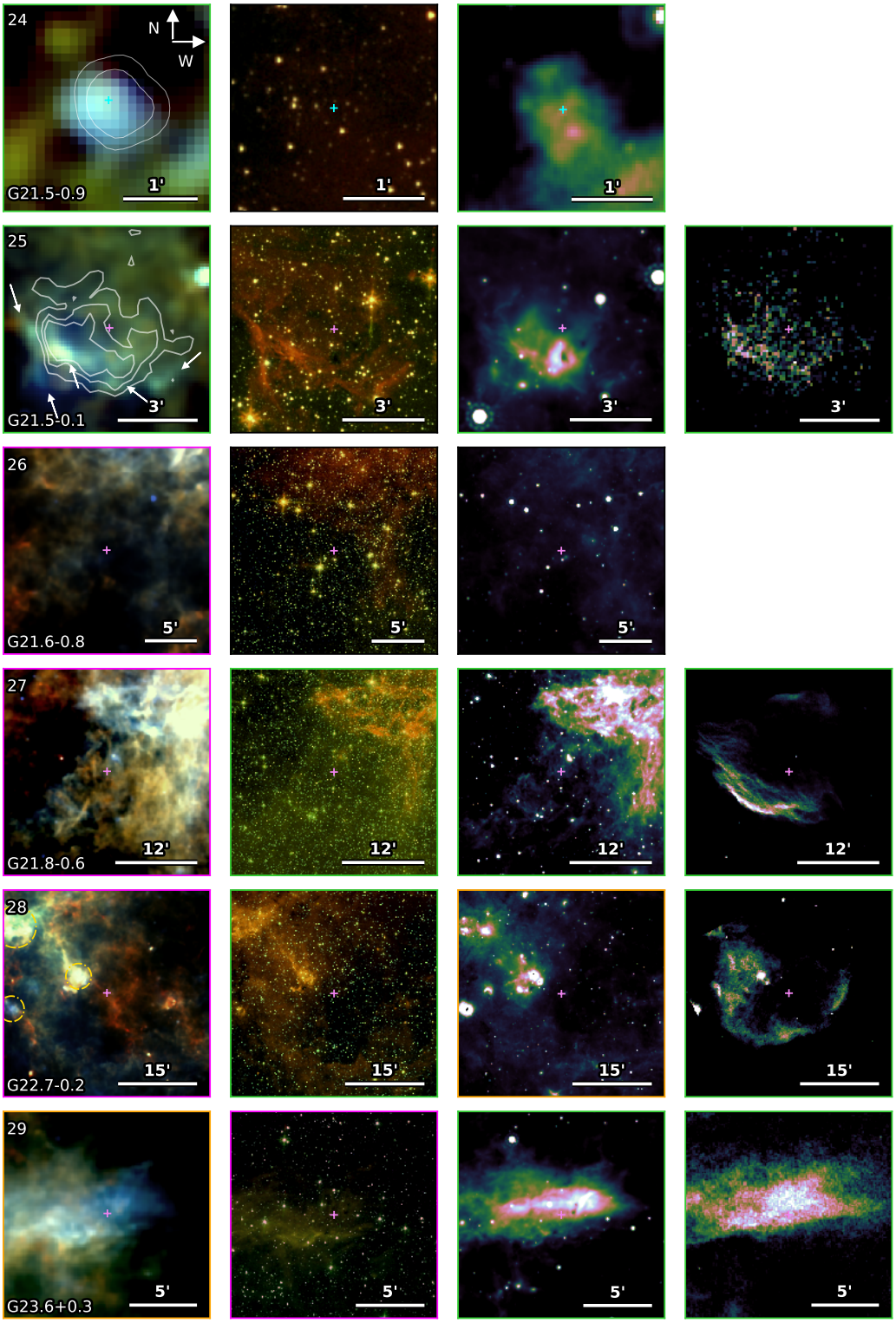

Figure A.2: Radio contours are overlaid onto the *Herschel* image of G20.4+0.1 and X-ray contours onto the *Herschel* image of G21.5−0.9.

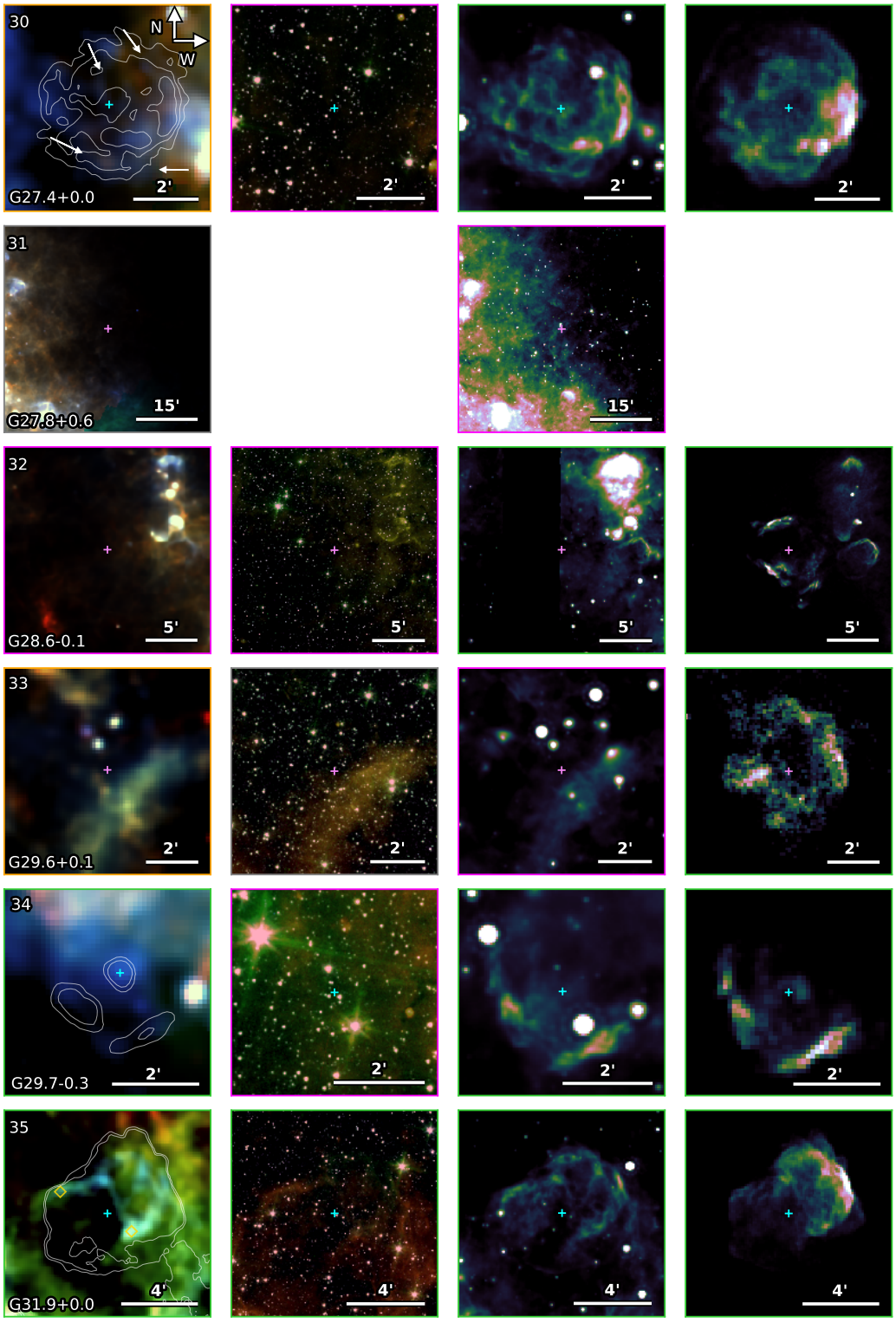

Figure A.2: X-ray contours are overlaid onto the *Herschel* image of G27.4+0.0.

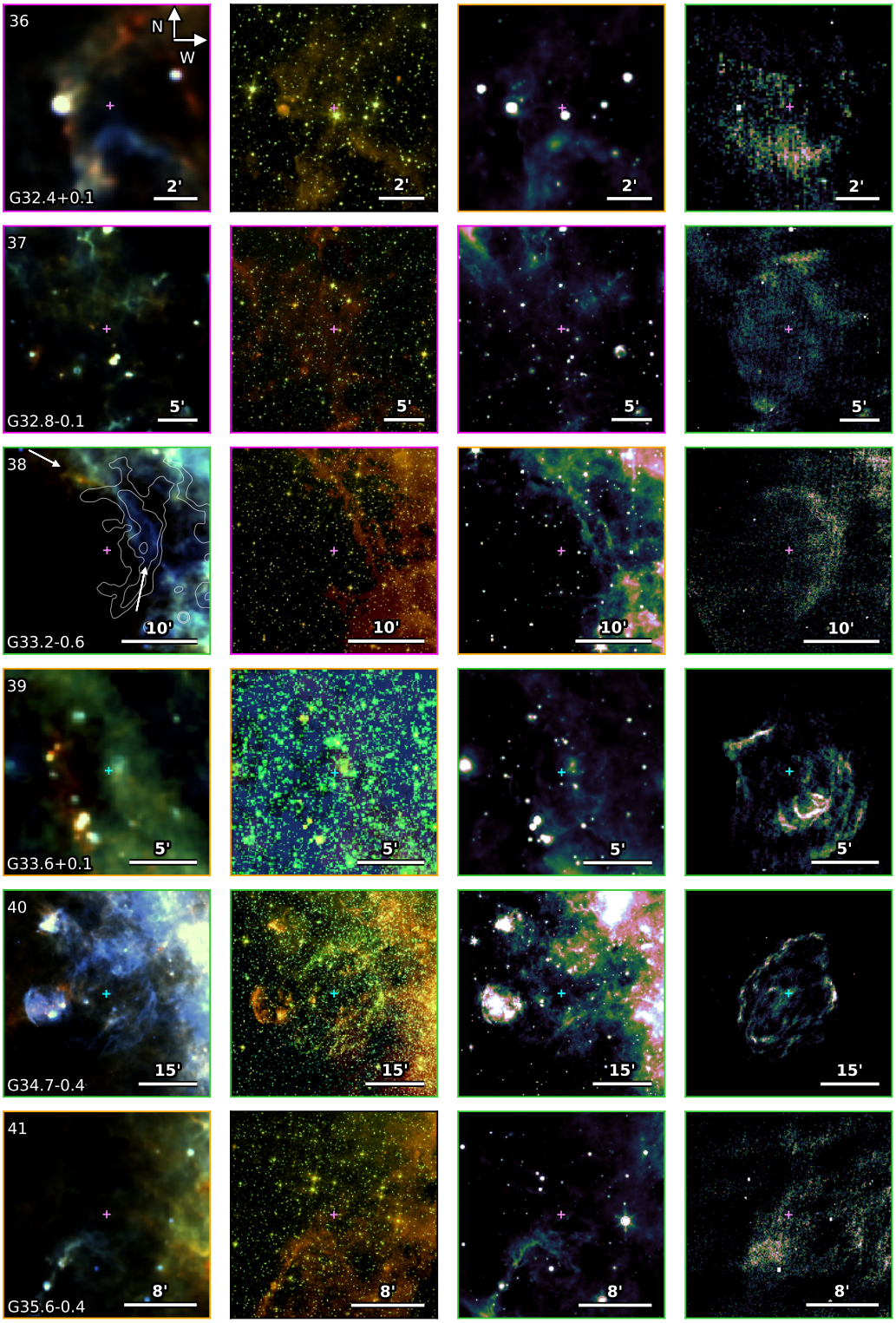

Figure A.2: X-ray contours are overlaid onto the *Herschel* image of G29.7−0.3 and radio contours onto the *Herschel* image of G31.9−0.0.

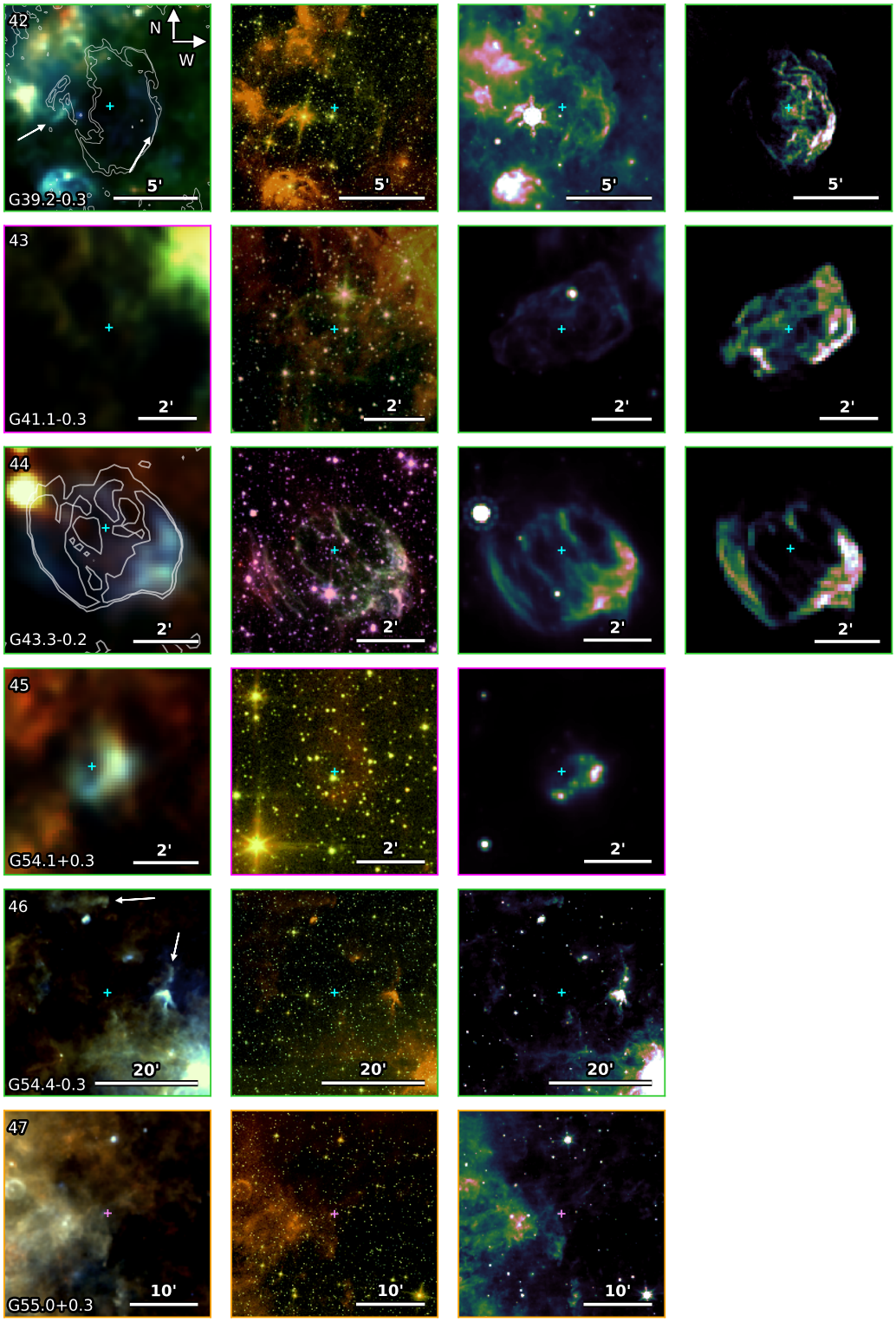

Figure A.2: Radio contours are overlaid onto the *Herschel* image of G33.2−0.6, X-ray contours onto the *Herschel* image of G33.6+0.1.

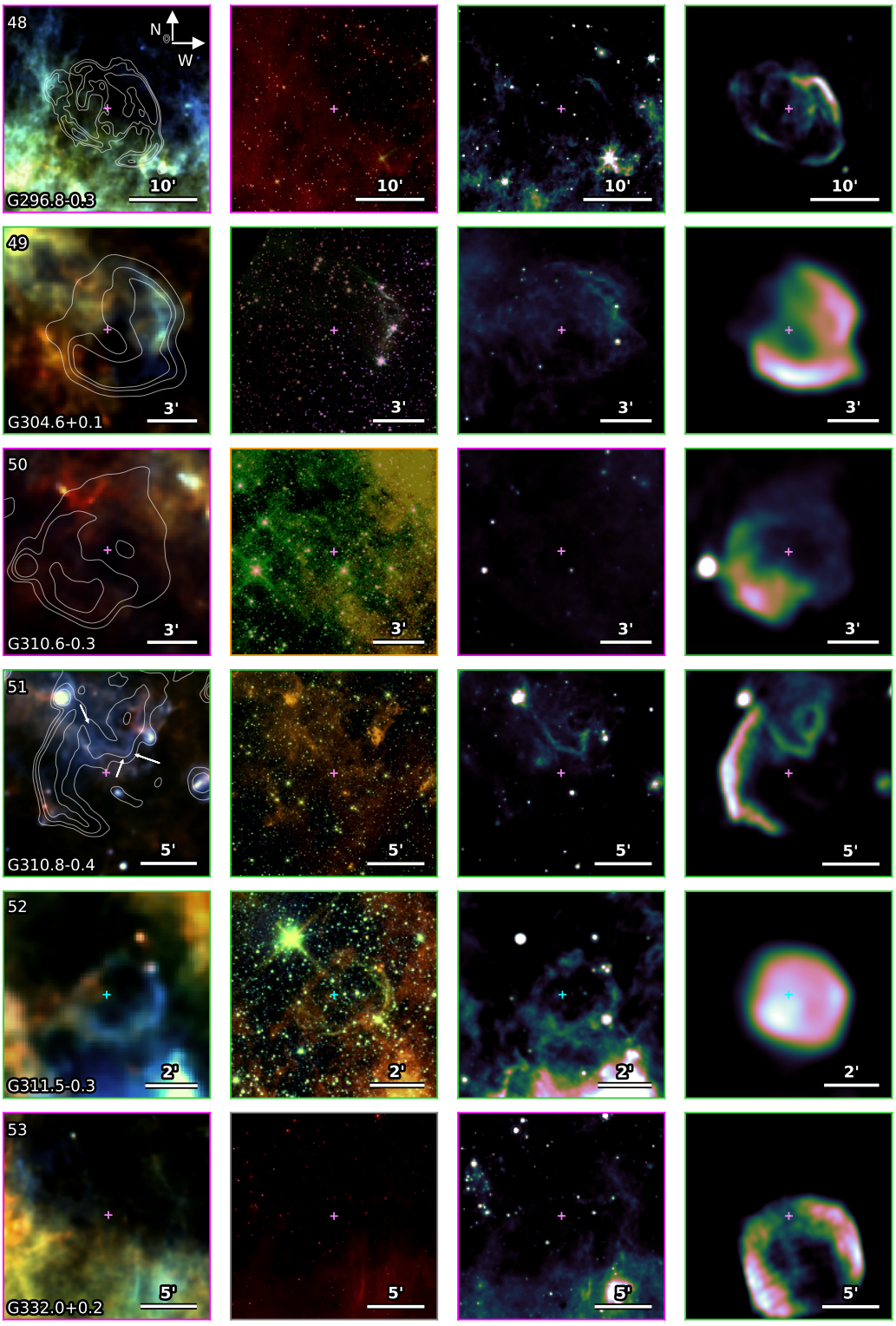

Figure A.2: Radio contours are overlaid onto the *Herschel* images of G39.2−0.3 and G43.3−0.2.

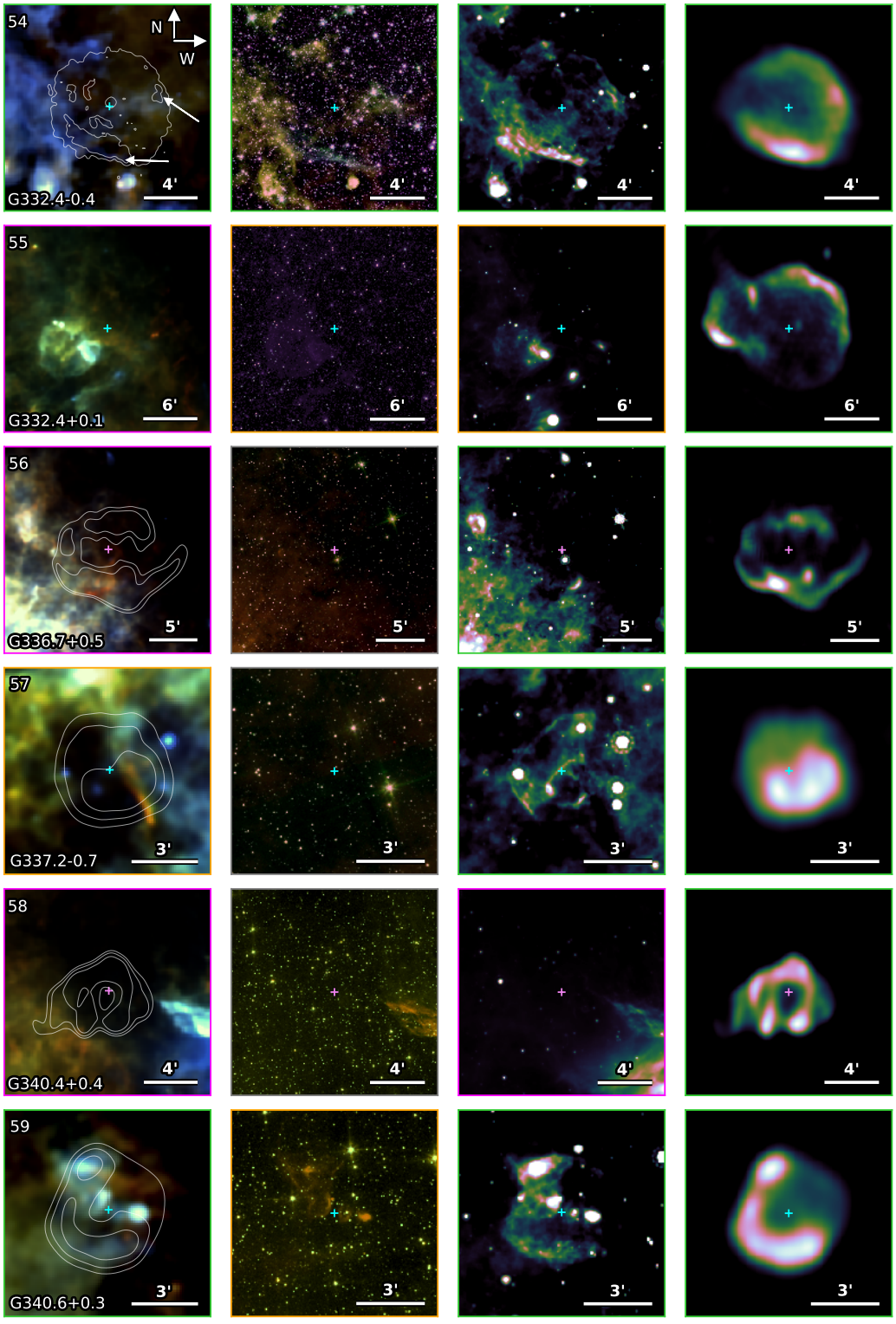

Figure A.2: Radio contours are overlaid onto the *Herschel* images of G296.8−0.3, G304.6+0.1, and G310.6−0.3.

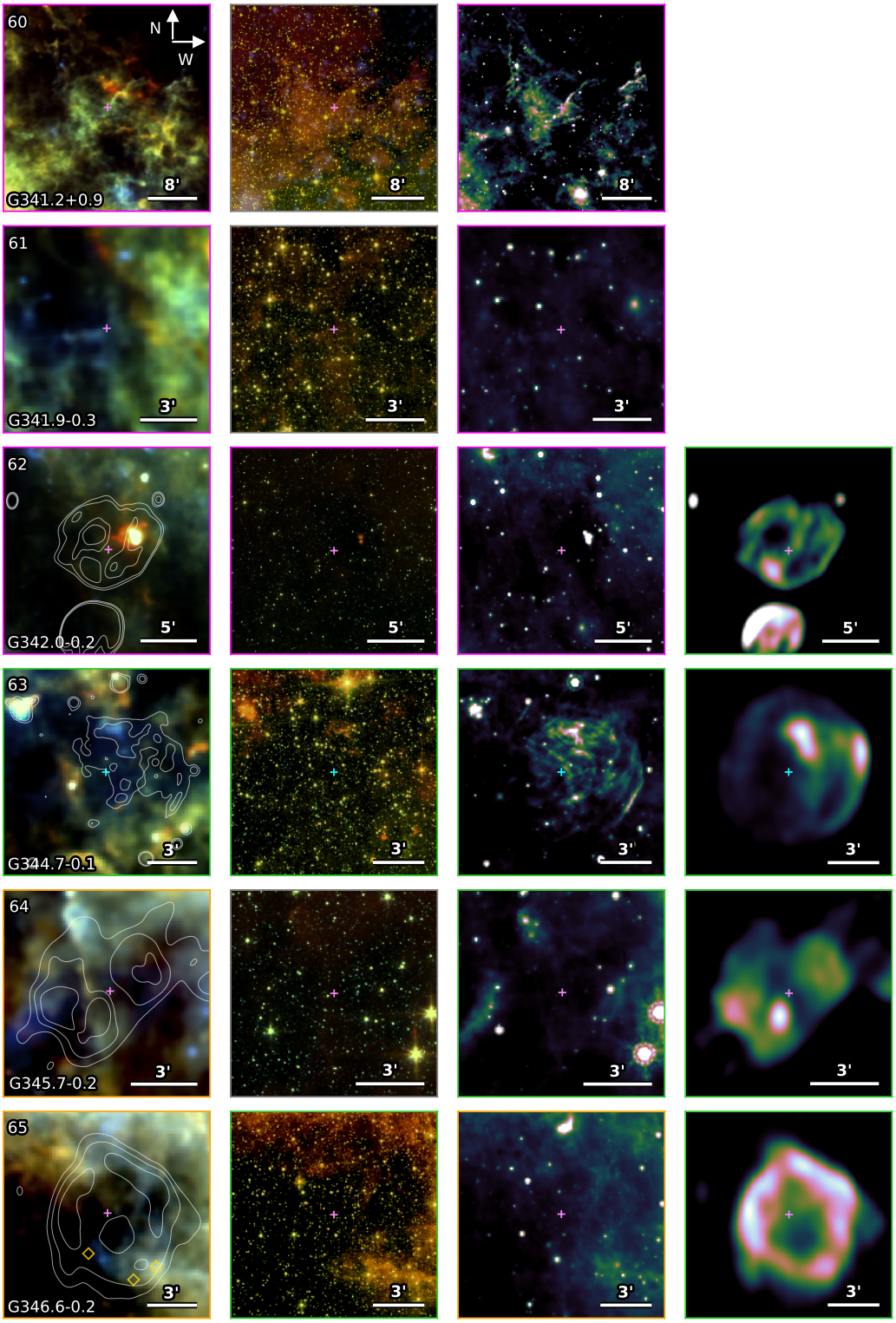

Figure A.2: Radio contours are overlaid onto the *Herschel* image of G310.8−0.4 and X-ray contours are overlaid onto the *Herschel* image of G332.4−0.4.

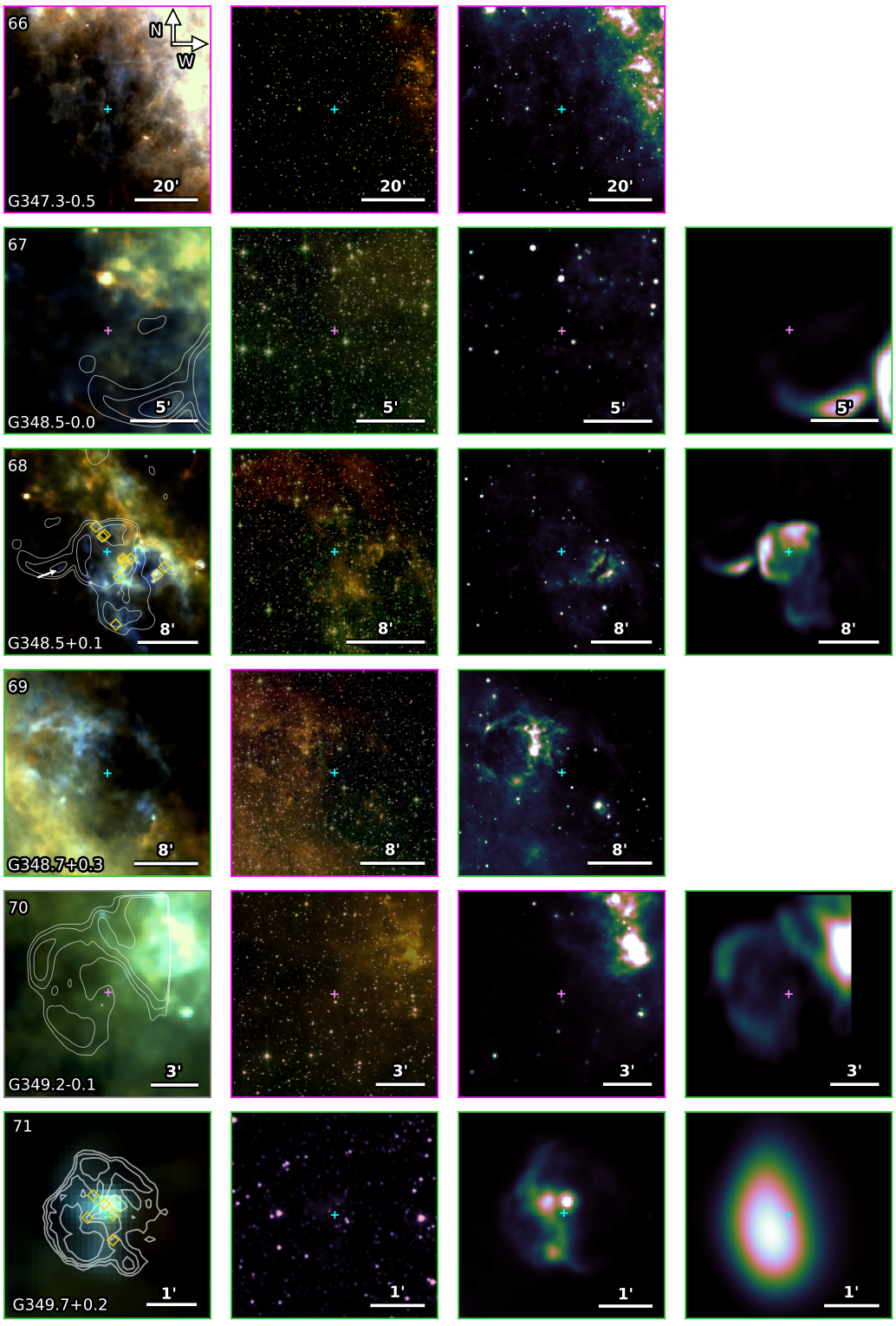

Figure A.2: Radio contours are overlaid onto the *Herschel* images of G336.7+0.5, G337.2−0.7, G340.4+0.4, and G340.6+0.3.

CHAPTER B
THE FULL GALACTIC CATALOGUE OF SNRS

B.1 GALLERY OF 190 SUPERNOVA REMNANTS OBSERVED WITH HERSCHEL

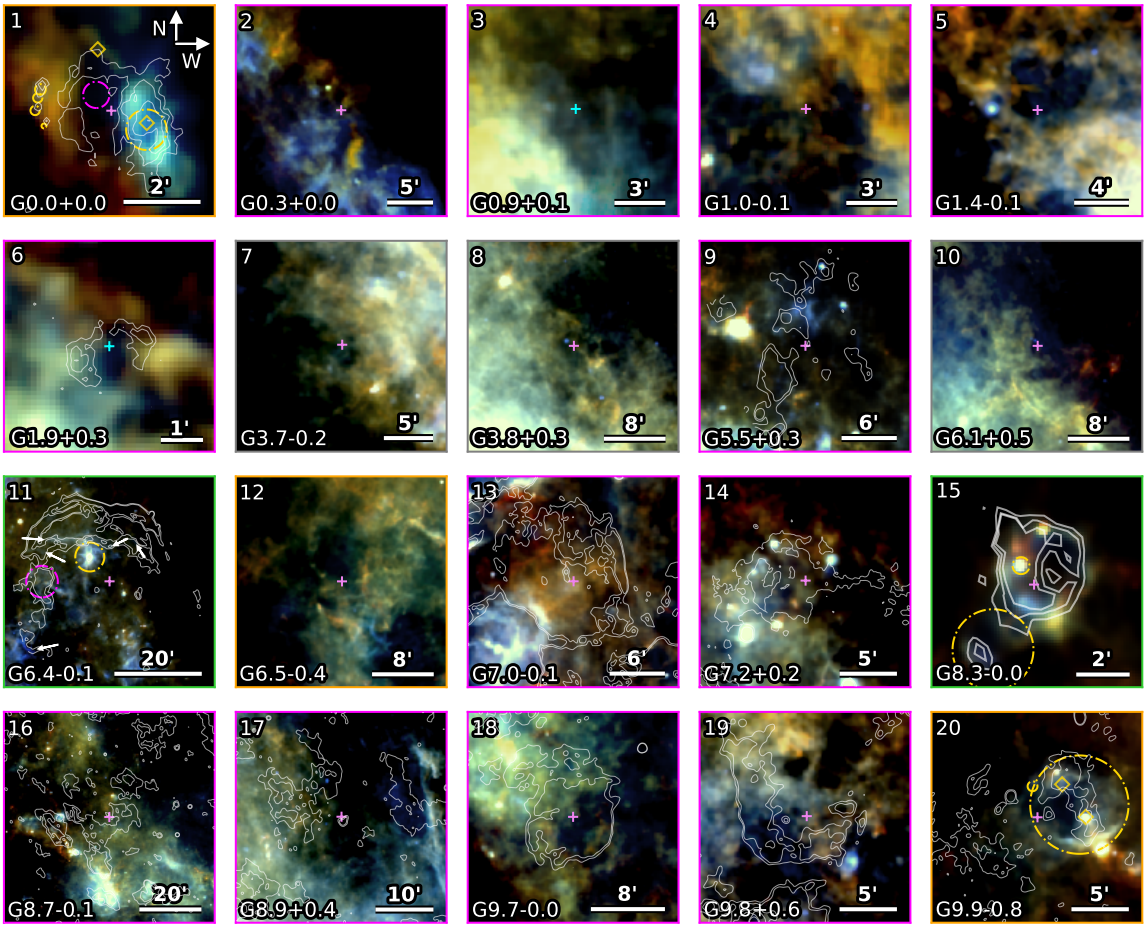

Figure B.1: *Herschel* three colour images of the locations of all supernova remnants in our sample. Colours are red = 250 μm, green = 160 μm, and blue = 70 μm. Purple crosses indicate the source radio centre from Green (2014) and cyan crosses indicate the X-ray centre. The border colour indicates the associated detection level in this study, as given in Table 2.1, where green = level 1, orange = level 2, magenta = level 3, grey = level 4, and black = unstudied. In some panels dashed magenta circles and white arrows indicate particular FIR dust emission features associated with the SNR, gold circles indicate unrelated structure such as HII regions. Overlaid onto G0.0+0.0, the gold diamonds indicate the location of the associated neutron star and Sgr A*. The gold diamonds on the image of G9.9−0.8 indicate the locations of HII regions. VLA GPS 20 cm contours overlaid onto the images of G0.0+0.0, G7.0−0.1, G7.2+0.2, G8.3−0.0, G9.7−0.0, G9.8+0.6, and G11.0−0.0; *Chandra* contours are overlaid onto G1.9+0.3 and G11.2−0.3; 90 cm contours are overlaid onto G5.5+0.3, G6.4−0.1, G8.7−0.1, G8.9+0.4, and G9.9−0.8.

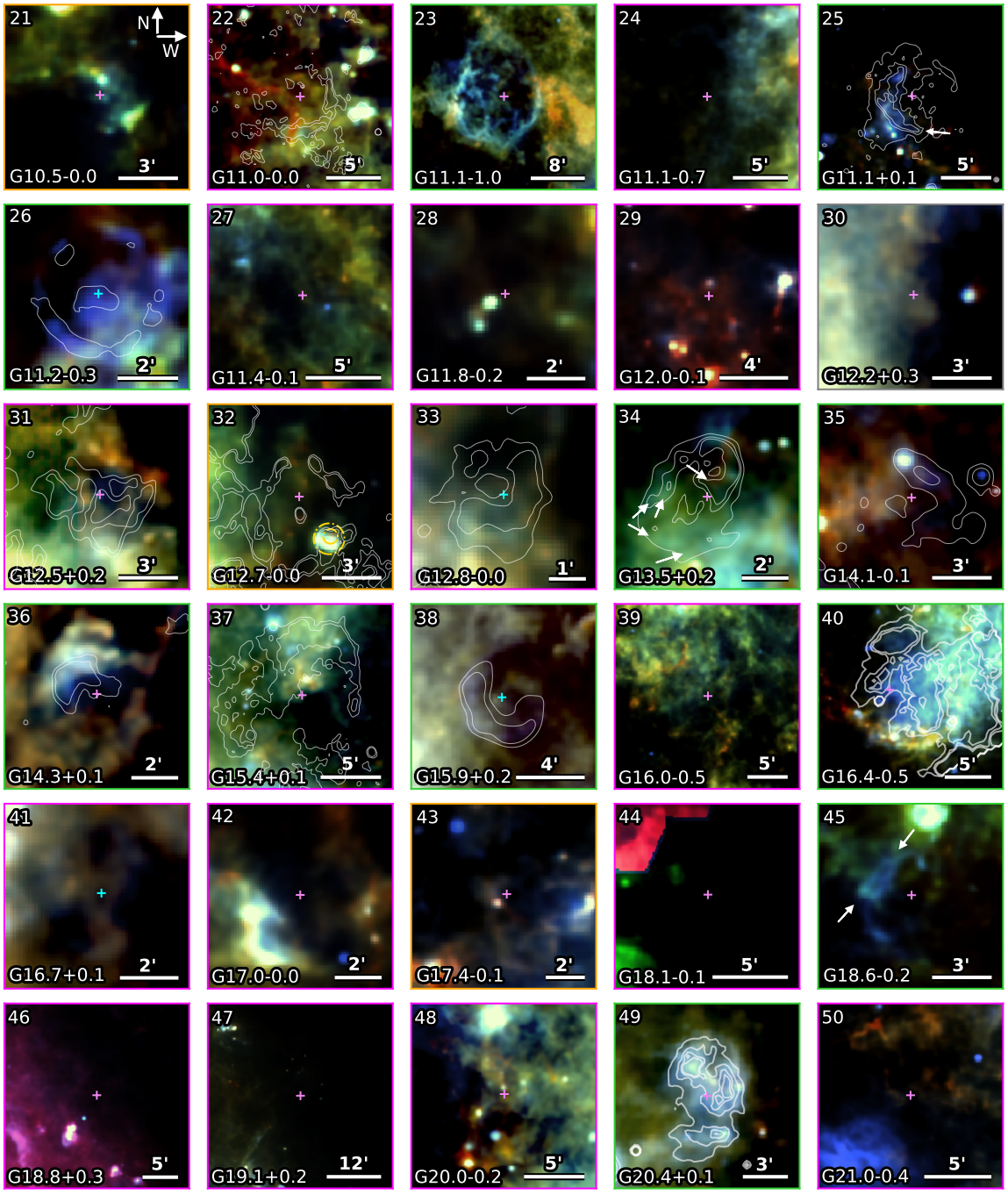

Figure B.1: VLA GPS 20 cm contours are overlaid onto G12.5+0.2, G12.7−0.0, G12.8−0.0, G13.5+0.2, G14.3+0.1, G20.4+0.1 and G24.7−0.6; VLA GPS 90 cm contours are overlaid onto G15.4+0.1; *Chandra* contours are overlaid onto G15.9+0.2, G21.5−0.9, and G27.4+0.0; MIPS 24 µm contours are overlaid onto G14.1−0.1; VGPS 21 cm contours are overlaid onto G23.3−0.3. The gold diamonds overlaid onto the image of G23.2−0.3 indicate the locations of a gamma ray source (HESS J1834−087), OH (1720 MHz) maser lines, and other maser emission.

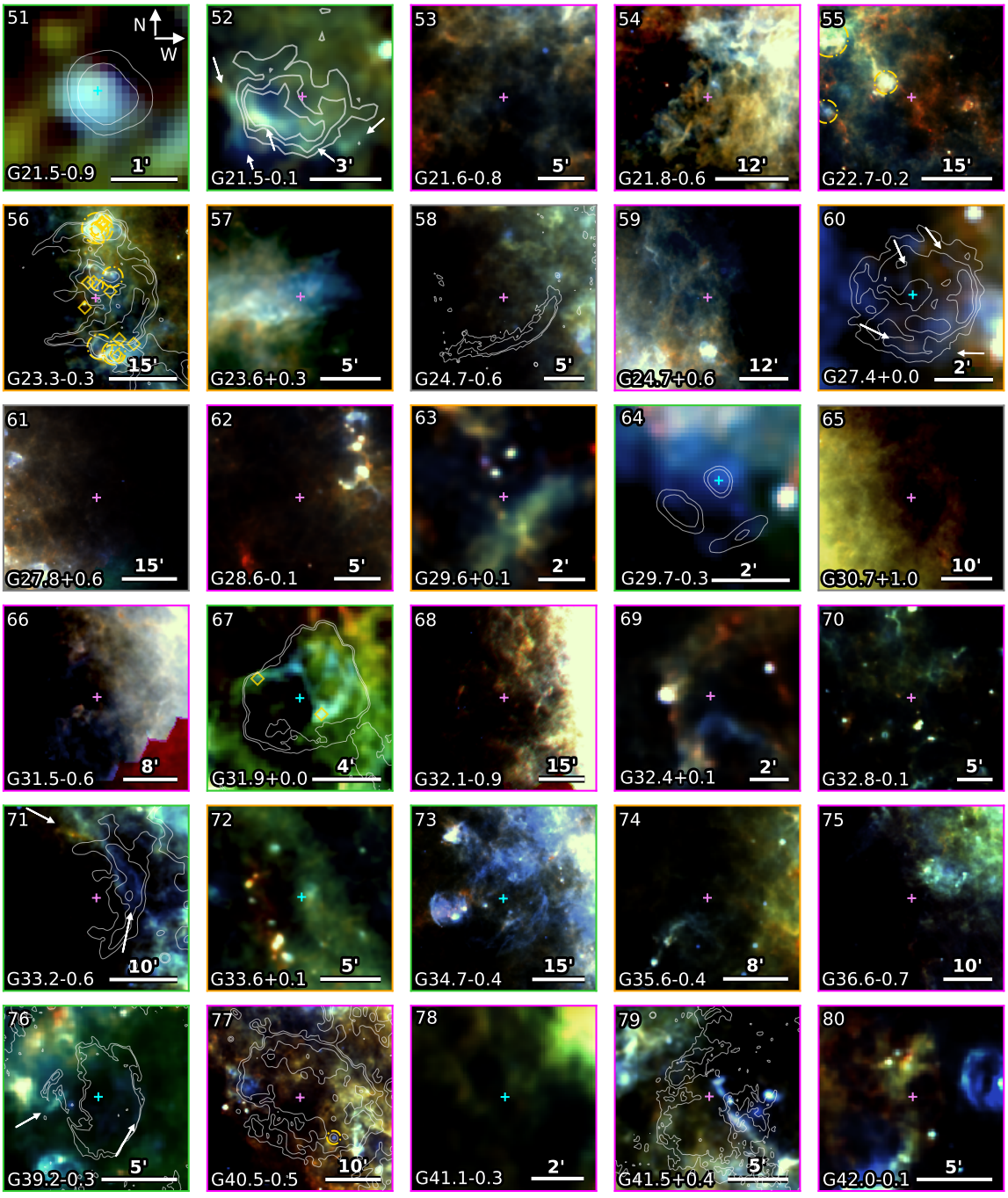

Figure B.1: *Chandra* contours are overlaid onto G29.7−0.3 and G33.6+0.1; VLA GPS 20 cm contours are overlaid onto G31.9+0.0, G33.2−0.6, G39.2−0.3, G41.5+0.4 G43.3−0.2, and G46.8−0.7; VGPS 21 cm contours are overlaid onto G40.5−0.5; NVSS 1.4 GHz contours are overlaid onto G45.7−0.4, G65.8−0.5, and G67.8+0.5.

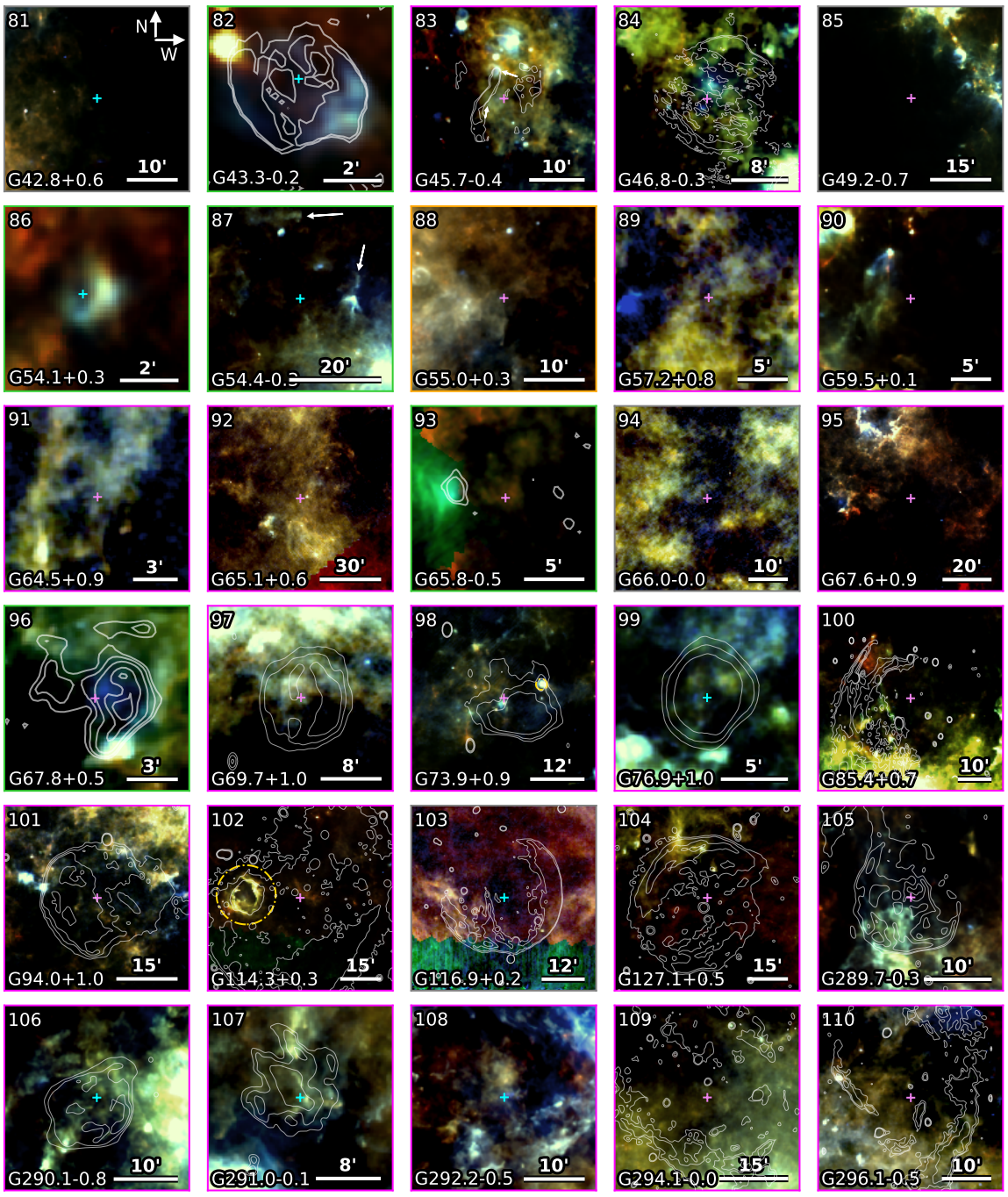

Figure B.1: Canadian Galactic Plane Survey (CGPS, 1420 MHz) contours are overlaid onto G69.7+1.0, G73.9+0.9, G76.9+1.0, G85.4+0.7, G94.0+1.0, G114.3+0.3, G116.9+0.2, and G127.1+0.5. MOST 843 MHz contours are overlaid onto G289.7−0.3, G290.1−0.8, G291.0−0.1, G294.1−0.0, G296.1−0.5, G296.8−0.3, G298.5−0.3, G298.6−0.0, G299.6−0.5, G301.4−1.0, G302.3+0.7, G304.6+0.1, and G308.1−0.7; *Chandra* contours are overlaid onto G306.3−0.9.

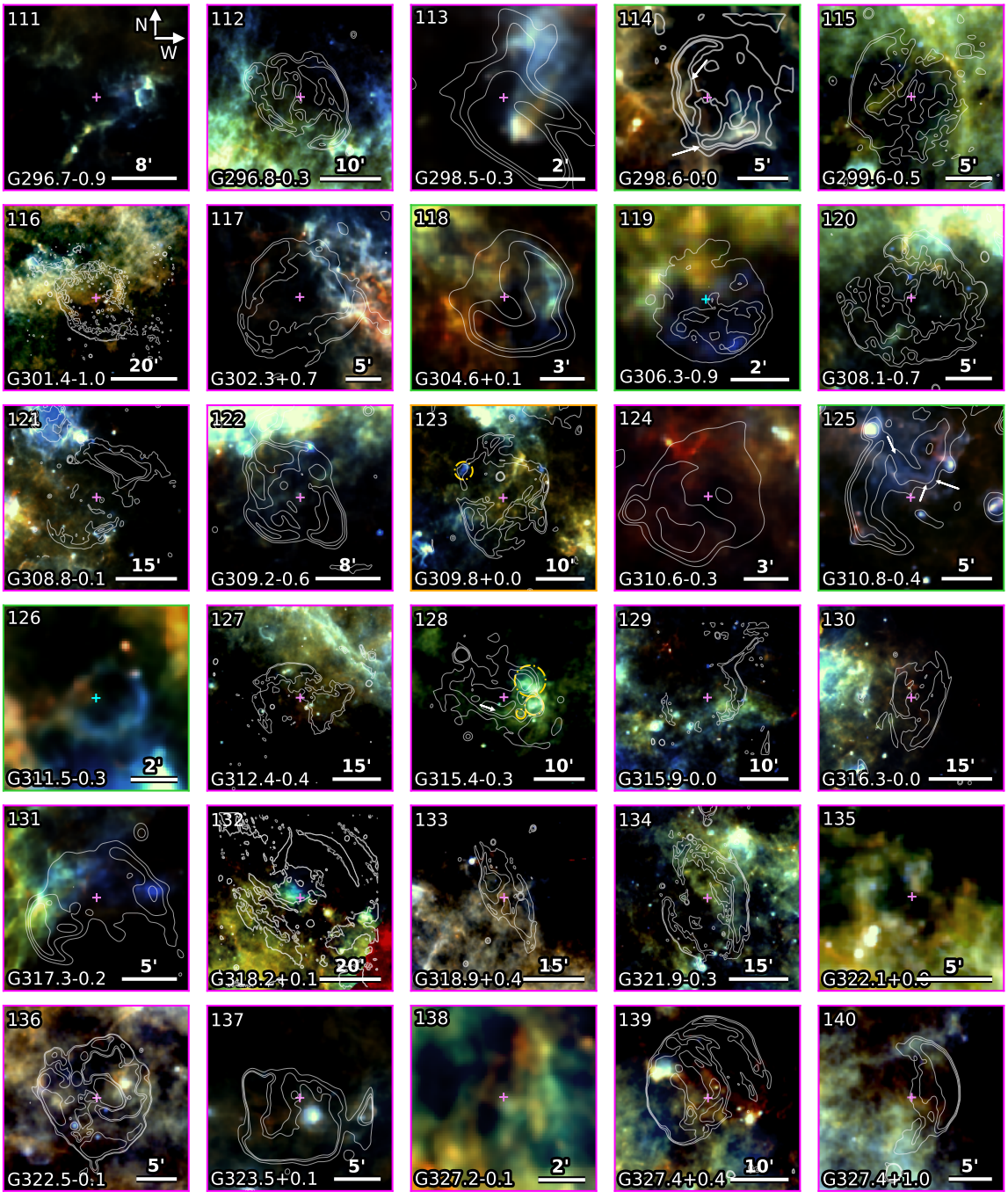

Figure B.1: *Chandra* contours are overlaid onto G332.4−0.4, all other contours are MOST 843 MHz .

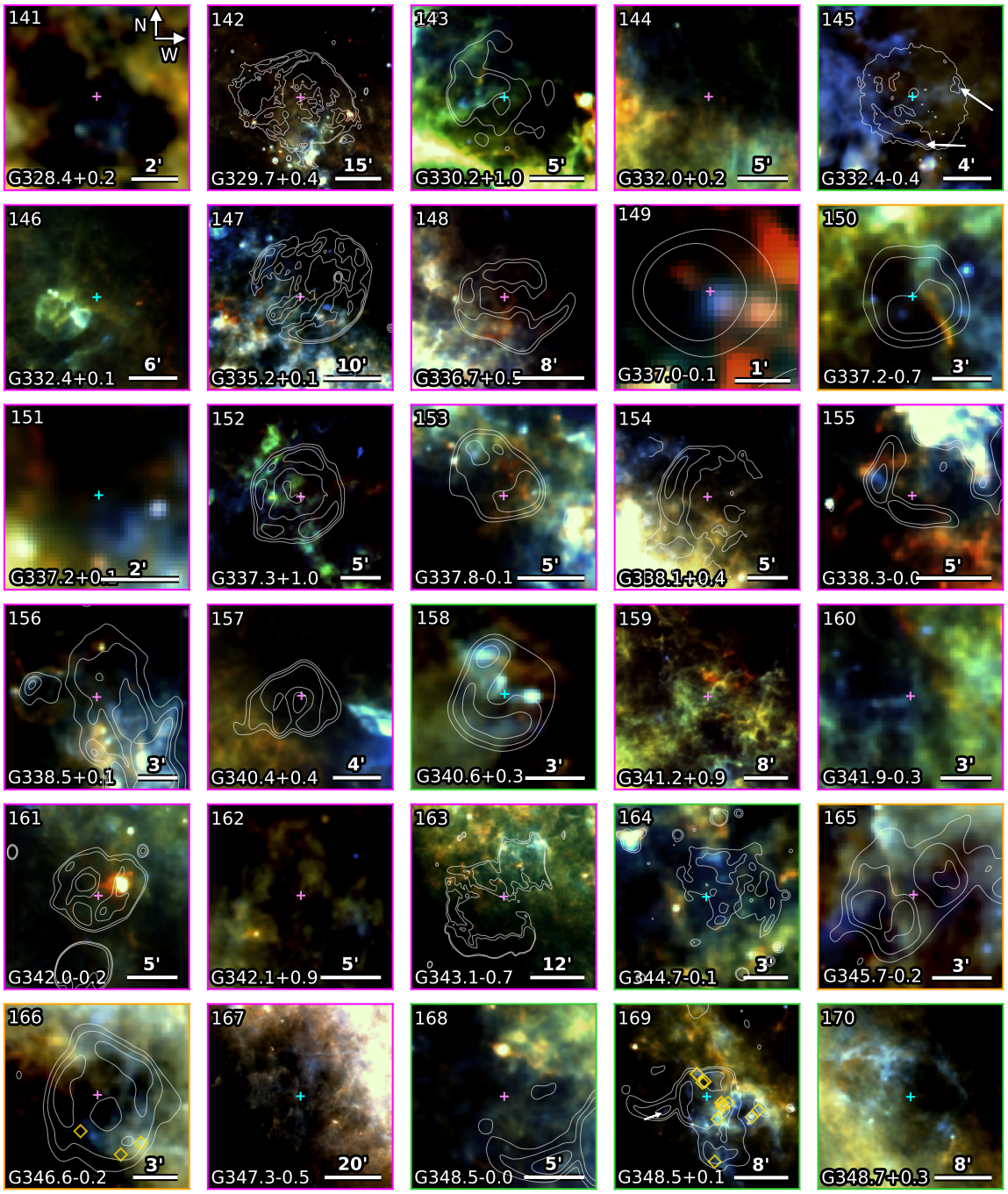

Figure B.1: MOST 843 MHz contours are overlaid onto G337.2−0.7, G342.2−0.2, G343.1−0.7, G345.7−0.2, G346.6−0.2, G348.5−0.0, G348.5+0.1, G349.2−0.1, G351.2+0.1, G351.7+0.8, G351.9−0.9, G352.7−0.1, G3541+0.1, and G354.8−0.8; MIPS 24 µm contours are overlaid onto G344.7−0.1 and G350.1−0.3; *Chandra* contours are overlaid onto G349.7+0.2. The diamonds overlaid onto the images of G350.1−0.3 and G354.1+0.1 indicate the locations of an associated neutron star and pulsar respectively. All other diamonds indicate the locations of maser emission.

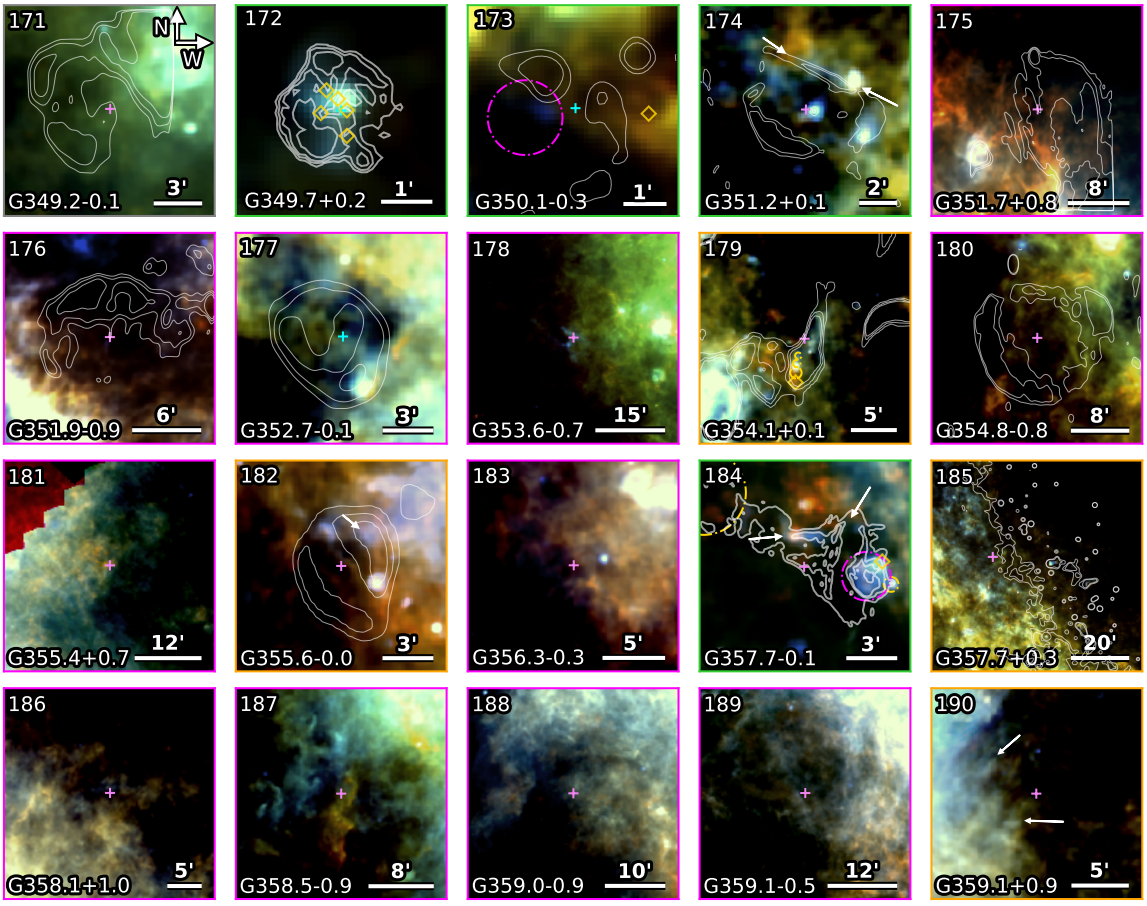

Figure B.1: MOST 843 MHz contours are overlaid onto G355.6−0.0; NVSS 1.4 GHz (white) and *Chandra* X-ray (cyan) contours are overlaid onto G357.7−0.1; MIPS 24 µm contours are overlaid onto G357.7+0.3. The gold diamond overlaid onto the images of G357.7−0.1 and G357.7+0.3 indicate the locations of an OH (1720 MHz) maser and a Mira star respectively.

B.2 Properties of the 190 Supernova Remnants

Table B.1: Supernova remnants in the Hi-GAL Survey

SNR	Name	Size [a] (arcmin)	PWN [b] (FIR)	Age (kyr)	SN Type	Hi-GAL [d]	C19 [e]	Dust features [f]	Comparison [h]	References
G0.0+0.0	Sgr A East	3.5x.25	Y (N)	9	Core collapse	2			R	1; 2; 3
G0.3+0.0		15x8				3			R	
G0.9+0.1		8	Y (N)	$2-3$	Core collapse	3			R	4
G1.0−0.1		8				3			R	1
G1.4−0.1		10				3			R	1
G1.9+0.3		1.5		~ 0.1		3			R	5; 6; 7; 8
G3.7−0.2		14x11				4			R	9
G3.8+0.3		18				4			R	9
G5.5+0.3		15x12				3			R	
G6.1+0.5		18x12				4			R	
G6.4−0.1	W28	48		10		1		Filaments	R	10; 1
G6.5−0.4		18				2			R	
G7.0−0.1		15				3			R	
G7.2+0.2		12				3			R	
G8.3−0.0		5x4				1		Shell	R	
G8.7−0.1	W30	45				3			R	1
G8.9+0.4		24				3			R	
G9.7−0.0		15x11				3			R	11; 1
G9.8−0.6		12				3			R	9
G9.9−0.8		12				2			R	
G10.5−0.0		6				2	Y		R	
G11.0−0.0		11x9				3			R	
G11.1−1.0		18x12				1	Y	Shell	OR	
G11.1−0.7		11x7				3	Y		R	
G11.1+0.1		12x10				1	Y	Western shell	R	
G11.2−0.3		4	Y (Y)	$1.4-2.4$	Type cIIb or Ibc	1	Y	Shell Central region (PWN)	RX	12
G11.4−0.1		8				3	Y		R	9
G11.8−0.2		4				3	Y			
G12.0−0.1		7	Y (N)	$0.3-3.0$	Core collapse	3	Y			13
G12.2+0.3		6x5				4			R	
G12.5+0.2		6x5				3	Y		R	

Table B.1: Supernova remnants in the Hi-GAL Survey

SNR	Name	Size [a] (arcmin)	PWN [b] (FIR)	Age (kyr)	SN Type	Hi-GAL [d]	C19 [e]	Dust features [f]	Comparison [g]	References
G12.7−0.0		6				2			R	
G12.8−0.0		3		~ 0.34	Core collapse	3			R	14; 15
G13.5+0.2		5x4				1i		Filaments	R	9
G14.1−0.1		6x5				1	Y			
G14.3+0.1		5x4				1	Y	Partial shell	R	
G15.4+0.1		15x14	Y (N)	~ 2.5	Core collapse	3			R	16; 17
G15.9+0.2		7x5		$\leqslant 2.4$	Core collapse	1	Y	Partial shell	RX	18; 19
G16.0−0.5		15x10				3			R	20
G16.4−0.5		13				1	Y	Central region	R	
G16.7+0.1		4	Y (N)	2.1	Core collapse	3	Y		R	21; 1
G17.0−0.0		5				3	Y			
G17.4−0.1		6				2	Y		R	9
G18.1−0.1		8		5		3	Y		R	22
G18.6−0.2		6	? (N)	13	Core collapse	1	Y	Outer filaments	R	23
G18.8+0.3	Kes 67	17x11		16		3	Y		R	24
G19.1+0.2		27				3	Y			
G20.0−0.2		10	Y (N)		Core collapse	3	Y		R	25; 26
G20.4+0.1		8		3.6		1	Y	Shell	R	
G21.0−0.4		9x7				3	Y		R	
G21.5−0.9		5	Y (Y)	0.87	Type IIP or Ib/Ic	1	Y	Central region (PWN)	X	26; 27
G21.5−0.1		5				1	Y	Central region	R	
G21.6−0.8		13				3	Y			28
G21.8−0.6	Kes 69	20		5		3	Y		R	29
G22.7−0.2		26	? (N)			3	Y		R	9
G23.3−0.3	W41	27		200		2			R	30; 31; 32
G23.6+0.3		10?				2	Y		R	
G24.7−0.6		15?		6.4		4			R	9
G24.7+0.6		30x15		12		3			R	33
G27.4+0.0	4C-04.7 Kes 73	4		$0.75 - 2.1$	SN IIL/b	2	Y		R	34; 35
G27.8+0.6		50x30	? (N)	$35 - 55$	Core collapse	4	Y			33; 36
G28.6−0.1		13x9		19		3	Y		R	37

Table B.1: Supernova remnants in the Hi-GAL Survey

SNR	Name	Size [a] (arcmin)	PWN [b] (FIR)	Age (kyr)	SN Type	Hi-GAL [d]	C19 [e]	Dust features [f]	Comparison [g]	References
G29.6+0.1		5		< 8		2	Y		R	38; 39
G29.7−0.3	Kes 75	3	Y (Y)	< 0.84	Type Ib/c	1	Y	Central region (PWN)	RX	39; 40
								Partial shell		
G30.7+1.0		24x18				4				9
G31.5−0.6		18?				3				9
G31.9+0.0	3C391	7x5		4		1	Y	Partial shell		41
								Northwestern radio bar		
G32.1−0.9		40?		12		3			R	42
G32.4+0.1		6				3	Y			43
G32.8−0.1	Kes 78	17		6		3	Y			44; 45
G33.2−0.6		18				1	Y	Western shell	R	9
G33.6+0.1	Kes 79	10		$4.4 - 6.7$	Type II	2	Y		R	45; 46
G34.7−0.4	W44	35x27	Y (N)	2	Core collapse	1	Y	North and western shell	R	47; 48
								Central filaments		
G35.6−0.4		15x11		2.3		2	Y		R	48; 49
G36.6−0.7		25?				3			R	
G39.2−0.3	3C396	8x6	Y (N)	7		1	Y	Western shell	R	49; 50
G40.5−0.5		22				3			R	51
G41.1−0.3	3C397	4.5x2.5		$1.35 - 1.75$	Type Ia	3	Y		R	50; 52
G41.5+0.4		10	? (N)			3			R	53
G42.0−0.1		8				3			R	
G42.8+0.6		24				4				9
G43.3−0.2	W49B	4x3		$1 - 4$	Bipolar Ib/Ic	1	Y	Fe/radio loop	R	54; 55; 56; 57
								H_2 filament		
G45.7−0.4		22				3			R	9
G46.8−0.3	(HC30)	30				3			R	58
G49.2−0.7	(W51)	30	Y (?)	30	Core collapse	4				59; 60; 61; 1
G54.1+0.3		12?	Y (Y)	2	Core collapse	1	Y	PWN southern rim		62
G54.4−0.3	(HC40)	40		95		1	Y	Outer filaments		63
G55.0+0.3		20x15?		≤ 1900		2	Y			64
G57.2+0.8		12?	? (N)			3			R	65
G59.5+0.1		15		86		3				66; 67

Table B.1: Supernova remnants in the Hi-GAL Survey

SNR	Name	Size [a] (arcmin)	PWN [b] (FIR)	Age (kyr)	SN Type	Hi-GAL [d]	C18 [e]	Dust features [f]	Comparison [g]	References
G64.5+0.9		8				3				68
G65.1+0.6		90x50	? (?)	$40 - 140$	Core collapse	3				68
G65.8−0.5		10x6?				1		Eastern structure	OR	69
G66.0−0.0		31x25?				4				
G67.6+0.9		50x45?				3		Partial shell		
G67.8+0.5		7x5				1			OR	
G69.7+0.9		16x14				3			R	9
G73.9+0.9		27				3			R	
G76.9+1.0		9	? (N)	< 40	Core collapse	3			R	70
G83.0−0.3		9x7				-				
G84.2−0.8		20x16		9		-				71
G85.4+0.7		24?			Core collapse	3			R	72
G85.9−0.6		24			Type Ia	-				72
G93.7−0.2		80				-				73
G94.0+1.0	3C434.1	30x25		7.9	Core collapse	3			R	74
G108.2−0.6		70x54				-				31
G109.1−1.0		28		14		-				75; 76
G113.0+0.2		40x17				-				77
G114.3+0.3		90x55		7.7	Core collapse	3			R	78
G116.9+0.2	CTB 1	34		13.1	Core collapse	4			R	78; 79; 80
G127.1+0.5	R5	45		$20 - 30$		3			R	81
G205.5+0.5	Monoceros Nebula	220		30		-				82; 83
G213.0−0.6		160x140				-				84
G289.7−0.3		18x14				3			R	9
G290.1−0.8	MSH 11-61A	19x14	Y (N)	50	Core collapse	3			R	85; 86
G291.0−0.1	(MSH 11-62)	15x13		~ 1.3	Core collapse	3			R	87; 88
G292.2−0.5		20x15	Y (N)	1.7	Core collapse	3			X	
G293.8+0.6		20				-				
G294.1−0.0		40				3			R	
G296.1−0.5		37x25		28	Core collapse	3			R	89; 90
G296.7−0.9		15x8				3			R	
G296.8−0.3	1156-62	20x14		$2 - 10$		3	Y		R	91

Table B.1: Supernova remnants in the Hi-GAL Survey

SNR	Name	Size [a] (arcmin)	PWN [b] (FIR)	Age (kyr)	SN Type	Hi-GAL [d]	C19 [e]	Dust features [f]	Comparison [g]	References
G298.5−0.3		5?				3			R	92
G298.6−0.0		12x9				1		Outer filaments	XR	93
G299.6−0.5		13				3			R	9
G301.4−1.0		37x23				3			R	9
G302.3+0.7		17				3			R	9
G304.6+0.1	Kes 17	8		$28-64$	Core collapse	1	Y	Western shell	R	94
G306.3−0.9		4		2.3	Type Ia	1		Inner region	XR	95; 96
G308.1−0.7		13				3			R	9
G308.8−0.1		30x20?		≤ 32.5	Core collapse	3			R	97; 98
G309.2−0.6		15x12		$0.7-4$		3			R	99
G309.8+0.0		25x19				2		Shell	R	100
G310.6−0.3	Kes 20B	8				3	Y		R	9
G310.8−0.4	Kes 20A	12				1	Y		R	101
G311.5−0.3		5		$25-42$		1	Y	Shell		102
G312.4−0.4		38		50	Core collapse	3			R	103
G315.4−0.3		24x13				3			O	9
G315.9−0.0	The Frying Pan	245x14	Y (N)	10	Core collapse	3			R	104; 105
G316.3−0.0	(MSH 14-57)	29x14				3			R	106
G317.3−0.2		11				3			R	9
G318.2+0.1		40x35				3			R	
G318.9+0.4		30x14				3			R	
G321.9−0.3		31x23				3			R	9
G322.1+0.0		8x4.5?		4.6		3			RX	107
G322.5−0.1		15				3			R	108
G323.5+0.1		13				3			R	9
G327.2−0.1		5		≤ 1.4		3				108
G327.4+0.4	Kes 27	21		2.4 or 5.3		3			R	109
G327.4+1.0		14				3			R	9
G328.4+0.2	(MSH 15-57)	5	Y (N)	10	Core collapse	3				109
G329.7+0.4		40x33				3			R	
G330.2+1.0		11		3.1	Core collapse	3			R	109; 110
G332.0+0.2		12				3	Y			

Table B.1: Supernova remnants in the Hi-GAL Survey

SNR	Name	Size [a] (arcmin)	PWN [b] (FIR)	Age (kyr)	SN Type	Hi-GAL [d]	C18 [e]	Dust features [f]	Comparison [g]	References
G332.4−0.4	RCW 103	10		2	Type IIP	1	Y	Southern arc	X	111; 112
G332.4+0.1	MSH 16-51 Kes 32	15		3		3	Y			113
G335.2+0.1		21				3			R	114
G336.7+0.5		14x10				3	Y		R	9
G337.0−0.1		21		70		3			R	115; 116
G337.2−0.7		6		0.75 − 3.5	Type Ia	2	Y		RX	117; 118
G337.2+0.1		3x2	Y (N)	1.5	Core collapse	3			R	119
G337.3+1.0	Kes 40	15x12				3			R	9
G337.8−0.1	Kes 41	9x6		3.3		3			R	120; 121
G338.1+0.4		15?				3			R	9
G338.3−0.0		8	Y (N)	6.8	Core collapse	3			R	122; 123
G338.5+0.1		9		5 − 17		3			R	124; 17
G340.4+0.4		10x7		3.1		3	Y		R	125
G340.6+0.3		6		2.6		1	Y	Shell	R	125
G341.2+0.9		22x16	Y (N)	32.6	Core collapse	3	Y			126
G341.9−0.3		7		5		3	Y			125
G342.0−0.2		12x9		11.7		3	Y		R	125; 9
G342.1+0.9		10x9				3				9
G343.1−0.7		27x21				3			R	9
G344.7−0.1		8		3	Type Ia	1	Y	North-central region	XR	127; 128
G345.7−0.2		6				2	Y		R	9
G346.6−0.2		8		47	Type Ib/Ic/II	2	Y		R	129; 1
G347.3−0.5	RX J1713.7-3946	65x55		1.59 − 2.1	Type Ib/c	3	Y			130
G348.5−0.0		10?				1	Y	Arc	R	129
G348.5+0.1	CTB37A	15?	? (N)	32 − 42		1	Y	North arc Breakout region	R	131; 129; 1
G348.7+0.3	CTB 37B	17?		5	Core collapse	1	Y	NE shell	R	132
G349.2−0.1		9x6				4	Y		R	
G349.7+0.2		2.5x2		1.8	Core collapse	1	Y	East shell	R	133; 134; 1
G350.1−0.3		4?		0.6 − 1.2	Core collapse	1		Ejecta	R	135; 136; 134

Table B.1: Supernova remnants in the Hi-GAL Survey

SNR	Name	Size [a] (arcmin)	PWN [b] (FIR)	Age (kyr)	SN Type	Hi-GAL [d]	C19 [e]	Dust features [f]	Comparison [g]	References
G351.2+0.1		7				1		North bar and centre	R	137
G351.7+0.8		18x14		≤ 68		3			R	138
G351.9−0.9		12x9				3			R	
G352.7−0.1		8x6		1.6	Type Ia	3			R	139; 140; 141
G353.6−0.7	HESS J1731-347	30		$2-6$	Core collapse	3			R	75; 142; 143
G354.1+0.1		15x3		26	Core collapse	2			R	126
G354.8−0.8		19				3			R	9
G355.4+0.7		25				3			R	
G355.6−0.0		8x6		20		2			R	9; 144
G356.3−0.3		11x7				3			R	9
G357.7−0.1	MSH 17-39 The Tornado	8x3?				1		Head and tail regions	R	1
G357.7+0.3	The Square Nebula	24		≤ 6.4		2			R	145; 1
G358.1+1.0		20				3			R	
G358.5−0.9		17				3			R	
G359.0−0.9		23				3			R	9
G359.1−0.5		24		≥ 100		3			R	1; 146
G359.1+0.9		12x11				2			R	9

[a] Radio size from Green's catalogue. [b] 'Y' indicates that a source contains an associated PWN, '?' indicates an unconfirmed PWN candidate. FIR detection of the PWN is indicated in brackets. Level of detection for each SNR is listed for the following surveys: [d] *Herschel* Hi-GAL (PACS & SPIRE, C19 (Chawner et al., 2019) and this work); '-' indicates that the source is not covered by the HiGAL survey. [e] Sources marked with 'Y' were studied by C19. [f] Location of FIR detected dust features. [g] Waveband of previous detection to which FIR structure is compared: O = optical, R = radio, X = X-ray. References for age and SN type on next page.

Table B.1 references for age and SN type:

[1]Pihlström et al., 2014, [2]Zhao et al., 2013, [3]Nynka et al., 2013, [4]Camilo et al., 2009b, [5]Carlton et al., 2011, [6]Roy & Pal, 2013, [7]Borkowski et al., 2016, [8]Zoglauer et al., 2015, [9]Case & Bhattacharya, 1998, [10]Rho & Borkowski, 2002, [11]Hewitt & Yusef-Zadeh, 2009b, [12]Borkowski et al., 2016, [13]Yamauchi et al., 2014b, [14]Halpern et al., 2012, [15]Brogan et al., 2005, [16]Castelletti et al., 2013, [17]HESS Collaboration, 2014, [18]Reynolds, 2006, [19]Klochkov et al., 2016, [20]Beaumont et al., 2011, [21]Helfand et al., 2003a, [22]Leahy et al., 2014, [23]Voisin et al., 2016, [24]Dubner et al., 1999, [25]Petriella et al., 2013, [26]Bietenholz & Bartel, 2008, [27]Bocchino et al., 2005, [28]Bietenholz et al., 2011, [29]Tian & Leahy, 2008, [30]Leahy & Tian, 2008b, [31]Tian et al., 2007b, [32]HESS Collaboration, 2015, [33]Reich & Furst, 1984, [34]Kumar et al., 2014, [35]Chevalier, 2005, [36]Misanovic et al., 2010, [37]Bamba et al., 2001, [38]Gaensler et al., 1999, [39]Leahy et al., 2008, [40]Morton et al., 2007, [41]Chen et al., 2004, [42]Folgheraiter et al., 1997, [43]Yamaguchi et al., 2004, [44]Zhou & Chen, 2011, [45]Zhou et al., 2016, [46]Sato et al., 2016, [47]Wolszczan et al., 1991, [48]Zhu et al., 2013, [49]Harrus & Slane, 1999, [50]Leahy & Ranasinghe, 2016, [51]Downes et al., 1980, [52]Yamaguchi et al., 2015, [53]Hurley et al., 1999, [54]Pye et al., 1984, [55]Smith et al., 1985, [56]Hwang et al., 2000, [57]Lopez et al., 2013, [58]Sato, 1979, [59]Koo et al., 1995, [60]Koo & Moon, 1997, [61]Green et al., 1997, [62]Bocchino et al., 2010, [63]Park et al., 2013, [64]Matthews et al., 1998, [65]Surnis et al., 2016, [66]Billot et al., 2010, [67]Xu & Wang, 2012, [68]Tian & Leahy, 2006, [69]Shan et al., 2018, [70]Arzoumanian et al., 2011, [71]Leahy & Green, 2012, [72]Jackson et al., 2008, [73]Uyaniker et al., 2002, [74]Jeong et al., 2013, [75]Tian et al., 2010, [76]Sasaki et al., 2013, [77]Kothes et al., 2005, [78]Yar-Uyaniker et al., 2004, [79]Lazendic & Slane, 2006, [80]Pannuti et al., 2010, [81]Leahy & Tian, 2006, [82]Odegard, 1986, [83]Leahy et al., 1986, [84]Reich et al., 2003, [85]Reynoso et al., 2006, [86]Kamitsukasa et al., 2015, [87]Moffett et al., 2002, [88]Slane et al., 2012, [89]Castro et al., 2011, [90]Gök & Sezer, 2012, [91]Gaensler et al., 1998, [92]Hwang & Markert, 1994, [93]Bamba et al., 2016, [94]Combi et al., 2010b, [95]Reynolds et al., 2013, [96]Combi et al., 2016, [97]Caswell et al., 1992, [98]Kaspi et al., 1992, [99]Rakowski et al., 2001, [100]Caswell et al., 1980, [101]Andersen et al., 2011, [102]Pannuti et al., 2014b, [103]Doherty et al., 2003, [104]Camilo et al., 2009a, [105]Ng et al., 2012, [106]Caswell et al., 1975, [107]Heinz et al., 2013, [108]Whiteoak, 1992, [109]McClure-Griffiths et al., 2001, [110]Torii et al., 2006, [111]Nugent et al., 1984, [112]Frank et al., 2015, [113]Vink, 2004, [114]Kaspi et al., 1996, [115]Sarma et al., 1997, [116]Castro et al., 2013, [117]Rakowski et al., 2006, [118]Takata et al., 2016, [119]Combi et al., 2005, [120]Combi et al., 2008, [121]Zhang et al., 2015, [122]Lemiere et al., 2009, [123]Gotthelf et al., 2014, [124]Kothes & Dougherty, 2007, [125]Caswell et al., 1983a, [126]Frail et al., 1994, [127]Giacani et al., 2011, [128]Yamaguchi et al., 2012, [129]Pannuti et al., 2014b, [130]Tsuji & Uchiyama, 2016, [131]Tian & Leahy, 2012, [132]HESS Collaboration, 2008a, [133]Tian & Leahy, 2014, [134]Yasumi et al., 2014, [135]Gaensler et al., 2008, [136]Lovchinsky et al., 2011, [137]Dubner et al., 1993, [138]Tian et al., 2007a, [139]Giacani et al., 2009, [140]Pannuti et al., 2014a, [141]Sezer & Gök, 2014, [142]HESS Collaboration, 2011, [143]Acero et al., 2015, [144]Minami et al., 2013, [145]Phillips & Marquez-Lugo, 2010, [146]HESS Collaboration, 2008b.

CHAPTER C
CHECKING PPMAP OUTPUT

C.1 PPMAP FLUX CHECK

PPMAP fluxes are estimated from the dust mass in each temperature slice, assuming a distance to The Tornado of 6 kpc. Initially the mass and therefore the flux within an aperture with radius of 0.021° is found for each temperature slice. The aperture size was chosen to encapsulate the majority of the Tornado head and exclude the HII region to the west of the head. For comparison the flux was measured in the same from the and *Spitzer* maps (24 µm – 500 µm). As shown in Figure C.1, it was found that the PPMAP flux estimates were significantly underestimated compared with those from the flux maps. There are a number of factors which could have affected our flux estimates:

- the background level may have been underestimated when measuring the source flux from the flux maps;
- our lower limit on the PPMAP temperature range may have been too high, therefore excluding a large mass of dust at the coolest temperatures;
- when measuring from the flux maps the aperture may have included some contribution from the HII region to the west of the head.

The first stage is to check that the background level had not been underestimated. To do this the aperture photometry is completed with three different methods of background subtraction:

- an annulus is placed around the source within inner and outer radii of 0.0318° and 0.0404° respectively where the average value gives the background level to be subtracted from the measured source flux;

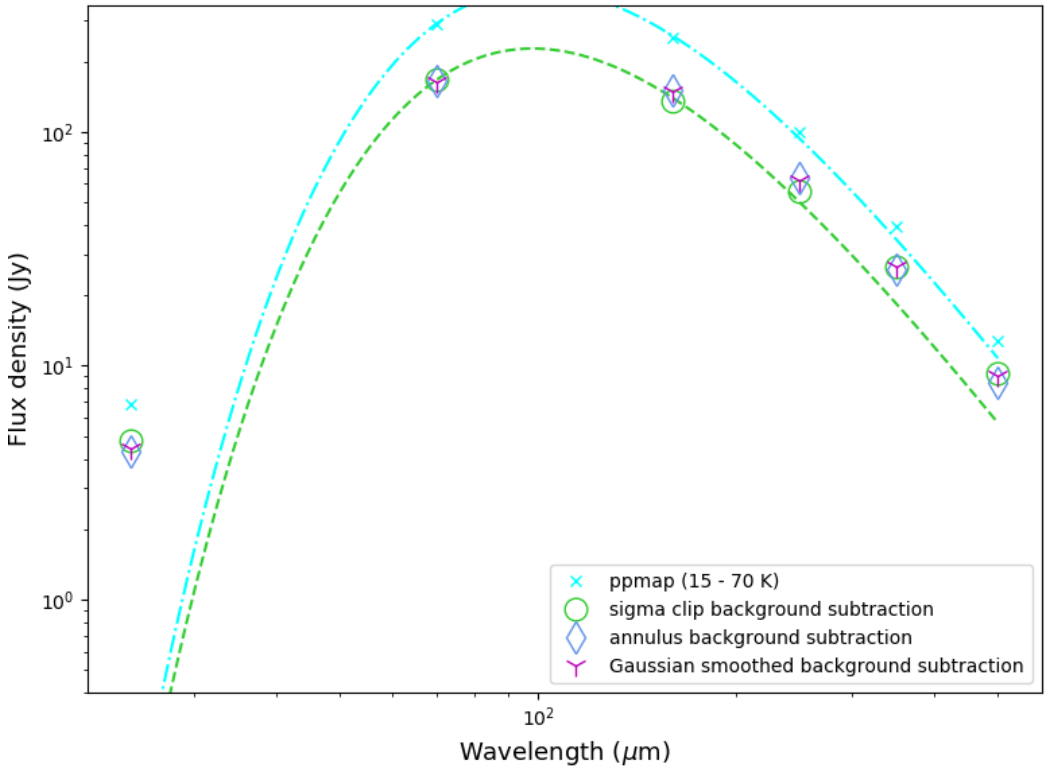

Figure C.1: The flux from the Tornado head estimated by PPMAP and by aperture photometry. There is a large inconsistency between the PPMAP and aperture photometry fluxes. Three methods are used to estimate the background level which all give consistent results. Varying the limits of the PPMAP temperature range alters the PPMAP fluxes slightly but cannot reduce the inconsistency significantly.

- the Tornado head is masked, and the remaining map sigma clipped, the average value of the resultant map is used for a background level and subtracted from the measured source flux;
- the Tornado head is masked and filled with linearly interpolated background emission, then the full map is smoothed with a Gaussian kernel with FWHM of 100″ giving a smooth estimate of the local background emission, which is subtracted from the flux maps.

As shown in Figure C.1 in all three cases the estimated background level is roughly consistent and does not reduce the difference in the PPMAP and aperture photometry fluxes.

After ruling out that the flux inconsistency is caused by a variation in the estimated background level, we reduce the lower bound of the PPMAP temperature grid. We find that this gives a slightly greater flux for all of the wavebands other than 24 µm although this is not enough to account for the difference with the

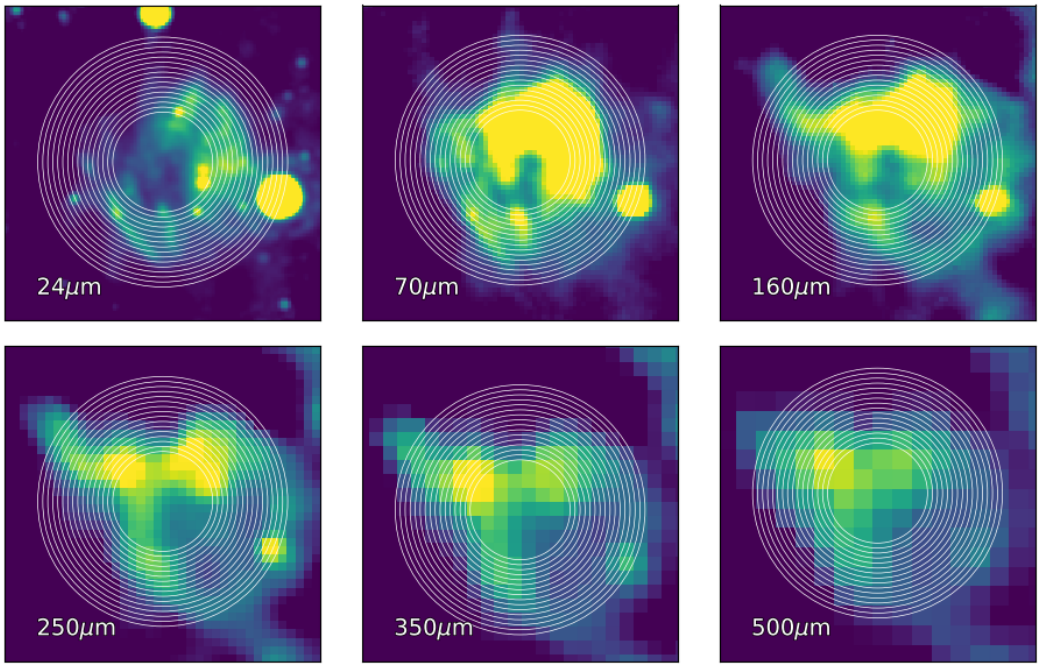

Figure C.2: Flux maps of the Tornado head with a Gaussian smoothed background subtracted. The rings indicate the apertures used to find the fluxes shown in Figure C.3, which have radii between 0.01° and 0.026° increasing in steps of 0.001°.

aperture photometry fluxes, as shown in Figure C.1.

Next, we investigate whether the issue may be due to the size of the aperture. We vary the aperture radius between 0.01° and 0.026° in steps of 0.001° whilst keeping the aperture centred at the same location, as shown in Figure C.2, and remeasure the source flux within. As seen in Figure C.3, the measured flux is only consistent with the PPMAP fluxes for some of the smallest apertures at 24 and 70 µm. These small apertures exclude large parts of the Tornado head and it is not expected that this accurately represents the flux of the source and we can rule out that the flux inconsistency is caused by an oversized aperture including any contribution from the HII region.

Finally, it may be that the issue is caused during the PPMAP run. The reduced χ^2 for each band is above 100, suggesting that PPMAP is unable to converge effectively to a solution. To account for this we first try increasing the number of iterations and determining the local noise level more effectively, both of which have little effect. As there are bright point sources in the 24 and 70 µm images it may be that PPMAP overfits these points and fails to converge on the region of interest. We artificially increase the 24 µm noise by a factor of ∼10 and mask the bright sources, replacing them with average values form background pixels. This prevents PPMAP from overfitting the 24 µm flux, which is not necessarily important to constrain the

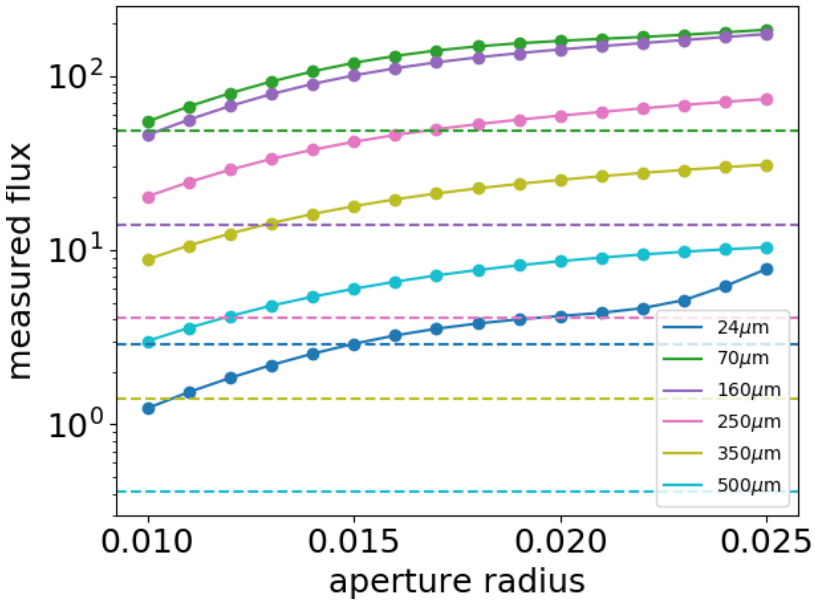

Figure C.3: The flux measured by aperture photometry when varying the aperture radius. The PPMAP flux only intersects the aperture photometry flux for the 24 and 70 µm wavebands, and only for the smaller apertures. In these cases some of the brightest parts of the Tornado head have been excluded from the aperture (see Figure C.2) and this result does not represent the source flux.

dust mass and may be contaminated by line emission or emission from warm dust. Doing this gives us PPMAP results which match the fluxes estimated with aperture photometry.

BIBLIOGRAPHY

'The more that you read, the more things you will know. The more that you learn, the more places you'll go.'

DR SEUSS

Abreu-Vicente J., Ragan S., Kainulainen J., Henning T., Beuther H., Johnston K., 2016, A&A, 590, A131

Acero F., Renaud M., Ballet J., Hewitt J. W., Rousseau R., Tanaka T., 2015, A&A, 580, A74

Aguirre J. E. et al., 2011, ApJS, 192

Andersen M., Rho J., Reach W. T., Hewitt J. W., Bernard J. P., 2011, ApJ, 742, 7

Anderson L. D., Bania T. M., Balser D. S., Rood R. T., 2011, ApJS, 194

Anderson L. D. et al., 2017, A&A

Anderson L. D., Zavagno A., Barlow M. J., García-Lario P., Noriega-Crespo A., 2012a, Distinguishing between HII regions and planetary nebulae with Hi-GAL, WISE, MIPSGAL, and GLIMPSE

Anderson L. D. et al., 2012b, A&A, 542

Angelini L., White N. E., 2003, ApJ, 586, L71

Arendt R. G., 1989, ApJS, 70, 181

Arendt R. G., Dwek E., Moseley S. H., 1999, ApJ, 521, 234

Arendt R. G. et al., 2011, ApJ, 734, 54

Arikawa Y., Tatematsu K., Sekimoto Y., Takahashi T., 1999, PASJ, 51, L7

Arzoumanian Z., Gotthelf E. V., Ransom S. M., Kothes R., Landecker T. L., 2011, ApJ, 739

Baade W., Zwicky F., 1934, PNAS, 20, 259

Balog Z. et al., 2014, Exp. Astron, 37, 129

Bamba A., Sawada M., Nakano Y., Terada Y., Hewitt J., Petre R., Angelini L., 2016, PASJ, 68, S51

Bamba A., Ueno M., Koyama K., Yamauchi S., 2001, PASJ, 53, 21

Barbon R., Ciatti F., Rosino L., 1979, A&A, 72, 287

Barlow M. J. et al., 2010, A&A, 518, L138

Barnard E., 1907, ApJ, 25, 218

Beaumont C. N., Williams J. P., Goodman A. A., 2011, AJ, 741

Becker R. H., Helfand D. J., 1984, ApJ, 283, 154

Becker R. H., Helfand D. J., 1985a, Nature, 313, 115

Becker R. H., Helfand D. J., 1985b, ApJ, 297, L25

Becker R. H., Helfand D. J., 1988, AJ, 95, 883

Beeston R. A. et al., 2018, MNRAS, 479, 1077

Begelman M. C., Sarazin C. L., Hatchett S. P., McKee C. F., Arons J., 1980, ApJ, 238, 722

Bendo G. J. et al., 2013, MNRAS, 433, 3062

Benjamin R. A. et al., 2003, PASP, 115, 953

Bernard J. P. et al., 2010, A&A, 518, L88

Bertoldi F., Carilli C. L., Cox P., Fan X., Strauss M. A., Beelen A., Omont A., Zylka R., 2003, A&A, 406, L55

Bevan A. et al., 2019, MNRAS, 485, 5192

Bianchi S., Schneider R., 2007, MNRAS, 378, 973

Bietenholz M. F., Bartel N., 2008, MNRAS, 386, 1411

Bietenholz M. F., Matheson H., Safi-Harb S., Brogan C., Bartel N., 2011, MNRAS, 412, 1221

Billot N., Noriega-Crespo A., Carey S., Guieu S., Shenoy S., Paladini R., Latter W., 2010, ApJ, 712, 797

Biscaro C., Cherchneff I., 2014, A&A, 564, A25

Biscaro C., Cherchneff I., 2016, A&A, 132, 1

Blandford R. D., Ostriker J. P., 1978, ApJ, 221, L29

Bocchino F., Bandiera R., Gelfand J., 2010, A&A, 71, 1

Bocchino F., van der Swaluw E., Chevalier R., Bandiera R., 2005, A&A, 442, 539

Bocchio M., Jones A. P., Slavin J. D., 2014, A&A, 570, A32

Bocchio M., Marassi S., Schneider R., Bianchi S., Limongi M., Chieffi A., 2016, A&A, 587, A157

Bock D. C. J., Gaensler B. M., 2005, ApJ, 626, 343

Bond J., Arnett W., Carr B., 1984, ApJ, 280, 825

Borkowski K. J., Reynolds S. P., Roberts M. S. E., 2016, ApJ, 819, 160

Boselli A., Lequeux J., Gavazzi G., 2002, A&A, 384, 33

Bouchet P. et al., 2015, PASP, 127, 612

Bowen G. H., 1988, ApJ, 329, 299

Braun R., Gull S. F., Perley R. A., 1987, Nature, 327, 395

Brighenti F., D'Ercole A., 1994, MNRAS, 270, 65

Brinkmann W., Aschenbach B., Kawai N., 1996, A&A, 312, 306

Broadbent A., Haslam C., Osborne J. L., 1989, MNRAS, 237, 381

Brogan C., Goss W., 2003, AJ, 272

Brogan C. L., Devine K. E., Lazio T. J., Kassim N. E., Tam C., Brisken W. F., Dyer K. K., Roberts M. S. E., 2004, ApJ, 127, 355

Brogan C. L., Gaensler B. M., Gelfand J. D., Lazendic J. S., Lazio T. J. W., Kassim N. E., McClure-Griffiths N. M., 2005, ApJ, 629, L105

Brogan C. L., Gelfand J. D., Gaensler B. M., Kassim N. E., Lazio T. J., 2006, ApJ, 639, 5

Burton M. G., Lazendic J. S., Yusef-Zadeh F., Wardle M., 2004, MNRAS, 348, 638

Camilo F., Lorimer D. R., Bhat N. D. R., Gotthelf E. V., Halpern J. P., Wang Q. D., Lu F. J., Mirabal N., 2002, ApJ, 574, 5

Camilo F., Ng C. Y., Gaensler B. M., Ransom S. M., Chatterjee S., Reynolds J., Sarkissian J., 2009a, ApJ, 703, 55

Camilo F., Ransom S. M., Gaensler B. M., Lorimer D. R., 2009b, ApJ, 700, 34

Camilo F., Ransom S. M., Gaensler B. M., Slane P. O., Lorimer D. R., Reynolds J., Manchester R. N., Murray S. S., 2006, ApJ, 637, 11

Carey S. J. et al., 2009, PASP, 121, 76

Carlton A. K., Borkowski K. J., Reynolds S. P., Hwang U., Petre R., Green D. A., Krishnamurthy K., Willett R., 2011, ApJ Letters, 737, 18

Carter L. M., Dickel J. R., Bomans D. J., 1997, PASP, 109, 990

Case G. L., Bhattacharya D., 1998, ApJ, 504, 761

Castelletti G., Supan L., Dubner G., Joshi B., Surnis M., 2013, A&A, 557, L15

Castro D., Slane P., Carlton A., Figueroa-Feliciano E., 2013, ApJ, 774

Castro D., Slane P. O., Gaensler B. M., Hughes J. P., Patnaude D. J., 2011, ApJ, 734, 86

Caswell J. L., Haynes R. F., Milne D. K., Wellington K. J., 1980, MNRAS, 190, 881

Caswell J. L., Haynes R. F., Milne D. K., Wellington K. J., 1983a, MNRAS, 203, 595

Caswell J. L., Haynes R. F., Milne D. K., Wellington K. J., Smith R., 1983b, PASA, 5, 227

Caswell J. L., Kesteven M. J., Bedding T. R., Turtle A. J., 1989, PASA, 8, 184

Caswell J. L., Kesteven M. J., Stewart R. T., Milne D. K., Haynes R. F., 1992, ApJ, 399, L151

Caswell J. L., Murray J. D., Roger R. S., Cole D. J., Cooke D. J., 1975, A&A, 45, 239

Chapin E. L. et al., 2009, MNRAS, 398, 1793

Chatzopoulos E., Wheeler J. C., 2012, ApJ, 748

Chawner H. et al., 2020, MNRAS, 493, 2706

Chawner H. et al., 2019, MNRAS, 483, 70

Chen Y., Su Y., Slane P. O., Wang Q. D., 2004, ApJ, 616, 27

Cherchneff I., Dwek E., 2009, ApJ, 703, 642

Cherchneff I., Lilly S., 2008, ApJ, 683, L123

Chevalier R. A., 1998, MemSAI, 69, 977

Chevalier R. a., 2005, ApJ, 619, 839

Cigan P. et al., 2019, ApJ, 886, 51

Cioffi D. F., McKee C. F., Bertschinger E., 1988, ApJ, 334, 252

Clark C. J. et al., 2019, MNRAS, 489, 5256

Clark C. J., Schofield S. P., Gomez H. L., Davies J. I., 2016, MNRAS, 459, 1646

Clemens M. S. et al., 2013, MNRAS, 433, 695

Cohen M. et al., 2007, MNRAS, 374, 979

Combi J. A. et al., 2010a, A&A, 522, A50

Combi J. A., Albacete Colombo J. F., Martí J., 2008, A&A, 28, L25

Combi J. A. et al., 2010b, A&A, 523, A76

Combi J. A., Benaglia P., Romero G. E., Sugizaki M., 2005, A&A, 431, L9

Combi J. A., García F., Suárez A. E., Luque-Escamilla P. L., Paron S., Miceli M., 2016, A&A, 592, 8

Cox N. L. et al., 2012, A&A, 537

Cruciani A. et al., 2016, MNRAS, 459, 4224

Davidson K., Fesen R. A., 1985, ARA&A, 23, 119

De Beck E., Decin L., de Koter A., Justtanont K., Verhoelst T., Kemper F., Menten K. M., 2010, A&A, 523, A18

De Graauw T. et al., 2010, A&A, 518, L6

De Looze I. et al., 2019, MNRAS, 488, 164

De Looze I. et al., 2017, MNRAS, 465, 3309

De Vis P. et al., 2017, MNRAS, 471, 1743

De Vis P. et al., 2019, A&A, 623, 1

Dell'Agli F., García-Hernández D. A., Schneider R., Ventura P., La Franca F., Valiante R., Marini E., Di Criscienzo M., 2017, MNRAS, 467, 4431

Dell'Agli F., Ventura P., Schneider R., di Criscienzo M., García-Hernández D. A., Rossi C., Brocato E., 2015, MNRAS, 447, 2992

Dempsey J. T., Thomas H. S., Currie M. J., 2013, ApJS, 209, 8

Derlopa S., Boumis P., Chiotellis A., Steffen W., Akras S., 2020, MNRAS

Di Carlo E. et al., 2008, ApJ, 684, 471

Di Criscienzo M. et al., 2013, MNRAS, 433, 313

Diehl R. et al., 2006, Nature, 439, 45

Doherty M., Johnston S., Greeb A. J., Roberts M. S., Romani R. W., Gaensler B. M., Crawford F., 2003, MNRAS, 339, 1048

Dole H. et al., 2006, A&A, 451, 417

Douvion T., Lagage P. O., Pantin E., 2001, A&A, 593, 589

Downes A. J. B., Pauls T., Salter C. J., 1980, A&A, 92, 46

Dragicevich P. M., Blair D. G., Burman R. R., 1999, MNRAS, 302, 693

Draine B., 2003, ARA&A, 41, 241

Draine B. T., 1981, ApJ, 245, 880

Draine B. T., Lee H. M., 1984, ApJ, 285, 89

Driver S. P. et al., 2016, MNRAS, 455, 3911

Dubner G., Giacani E., 2015, A&A Review, 23

Dubner G., Giacani E., Reynoso E., 1999, AJ, 118, 930

Dubner G., Giacani E., Reynoso E., Parón S., 2004, A&A, 426, 201

Dubner G. M., Giacani E. B., Goss W. M., Moffett D. A., Holdaway M., 1996, ApJ, 111, 1304

Dubner G. M., Holdaway M., Goss W. M., Mirabel I. F., 1998, AJ, 116, 1842

Dubner G. M., Moffett D. A., Goss W. M., Winkler P. F., 1993, AJ, 105, 2251

Dunne L., Eales S., Edmunds M., Ivison R., Alexander P., Clements D. L., 2000, MNRAS, 315, 115

Dunne L., Eales S., Ivison R., Morgan H., Edmunds M., 2003, Nature, 424, 285

Dunne L., Eales S. A., 2001, MNRAS, 327, 697

Dunne L. et al., 2011, MNRAS, 417, 1510

Dunne L. et al., 2009, MNRAS, 394, 1307

Dwek E., 1998, ApJ, 501, 643

Dwek E., Arendt R. G., 1992, ARA&A, 30, 11

Dwek E., Arendt R. G., 2015, ApJ, 810, 75

Dwek E., Cherchneff I., 2011, ApJ, 727

Dwek E., Dinerstein H. L., Gillett F. C., Hauser M. G., Rice W. L., 1987, ApJ, 315, 571

Dwek E., Galliano F., Jones A. P., 2007, ApJ, 662, 927

Eales S. et al., 2012, ApJ, 761

Ekström S. et al., 2012, A&A, 537

Elias J. H., Matthews K., Neugebauer G., Persson S. E., 1985, ApJ, 296, 379

Elmhamdi A., Danziger I. J., Cappellaro E., Della Valle M., Gouiffes C., Phillips M. M., Turatto M., 2004, A&A, 426, 963

Engelbracht C. W. et al., 2007, PASP, 119, 994

Ercolano B., Barlow M. J., Sugerman B. E., 2007, MNRAS, 375, 753

Fazio G. G. et al., 2004, ApJS, 154, 10

Feder J., Russell K. C., Lothe J., Pound G. M., 1966, AIP, 15, 111

Fixsen D. J., Dwek E., Mather J. C., Bennett C. L., Shafer R. A., 1998, ApJ, 508, 123

Folgheraiter E. L., Warwick R. S., Watson M. G., Koyama K., 1997, MNRAS, 292, 365

Fowler W. A., Hoyle F., 1964, ApJS, 9, 201

Frail D. A., Goss W. M., Whiteoak J. B. Z., 1994, AJ, 437, 23

Frail D. A., Reynoso E., Giacani E., Green A., Otrupcek R., 1996, AJ, 111, 1651

Frank K. A., Burrows D. N., Park S., 2015, AJ, 810, 113

Froebrich D. et al., 2015, MNRAS, 454, 2586

Furst E., Reich W., Sofue Y., 1987, A&A SS, 71, 63

Gaensler B. M., Fogel J. K. J., Slane P. O., Miller J. M., Wijnands R., Eikenberry S. S., Lewin W. H. G., 2003, ApJ, 594, L35

Gaensler B. M., Gotthelf E. V., Vasisht G., 1999, ApJ, 526, L37

Gaensler B. M., Manchester R. N., Green A. J., 1998, MNRAS, 296, 813

Gaensler B. M., Slane P. O., 2006, ARA{&}A, 44, 1

Gaensler B. M. et al., 2008, ApJ, 680, L37

Gall C., Andersen A. C., Hjorth J., 2011a, A&A, 528, A13

Gall C., Andersen A. C., Hjorth J., 2011b, A&A, 528, 1

Gall C., Hjorth J., Andersen A. C., 2011c, A&A Review, 19

Gall C. et al., 2014, Nature, 511, 326

Gao X. Y., Reich P., Hou L. G., Reich W., Han J. L., 2019, A&A, 623, 1

Ghavamian P., Williams B. J., 2016, ApJ, 831, 188

Giacani E., Smith M. J. S., Dubner G., Loiseau N., 2011, A&A, 531, A138

Giacani E., Smith M. J. S., Dubner G., Loiseau N., Castelletti G., Paron S., 2009, A&A, 507, 841

Giacani E. B., Dubner G. M., Kassim N. E., Frail D. a., Goss W. M., Winkler P. F., Williams B. F., 1997, AJ, 113, 1379

Gilman R. C., 1969, ApJ, 155, L185

Glatzel W., Fricke K., El Eid M., 1985, A&A, 149, 413

Gök F., Sezer A., 2012, MNRAS, 419, 1603

Goldreich P., Ward W. R., 1973, ApJ, 183, 1051

Gomez H. L. et al., 2012a, MNRAS, 420, 3557

Gomez H. L. et al., 2012b, ApJ, 760, 96

Goodall P. T., Alouani-Bibi F., Blundell K. M., 2011, MNRAS, 414, 2838

Goss W. M., Schwarz U. J., van Gorkom J. H., Ekers R. D., 1985, MNRAS, 215, 69

Goss W. M., Shaver P. A., Skellern D. J., Watkinson A., 1979, A&A, 78, 75

Gotthelf E. V. et al., 2014, ApJ, 788, 1

Gould R. J., Salpeter E. E., 1963, ApJ, 138, 393

Gray A., 1994a, MNRAS, 270, 847

Gray A. D., 1994b, MNRAS, 270, 835

Green A. J., Frail D. A., Goss W. M., Otrupcek R., 1997, ApJ, 114, 2058

Green D. A., 2004, BASI, 32, 335

Green D. A., 2009, MNRAS, 399, 177

Green D. A., 2011, BASI, 39, 289

Green D. A., 2014, BASI, 42, 47

Green D. A., 2015, MNRAS, 454, 1517

Green D. A., 2019, J A&A, 40

Green D. A., Dewdney P. E., 1992, MNRAS, 254, 686

Green J. A. et al., 2010, MNRAS, 417, 1964

Greisen E. W., 2003, in Astrophysics and Space Science Library, Vol. 285, Information Handling in Astronomy - Historical Vistas, Springer, Dordrecht

Griffin M. et al., 2010, A&A, 518, L3

Hakobyan A. A. et al., 2017, MNRAS, 471, 1390

Hakobyan A. A. et al., 2016, MNRAS, 456, 2848

Halpern J. P., Gotthelf E. V., 2010, ApJ, 710, 941

Halpern J. P., Gotthelf E. V., Camilo F., 2012, ApJ Letters, 753, 10

Hamann W.-R. et al., 2019, A&A, 625, A57

Harper D. A. et al., 2018, JAI, 7, 1

Harrus I. M., Slane P. O., 1999, ApJ, 516, 811

Hashimoto M., Iwamoto K., Nomoto K., 1993, ApJ Letters, 414, L105

Haslam C. G., Osborne J. L., 1987, Nature, 327, 211

Heger A., Woosley S. E., 2002, ApJ, 567, 532

Heinz S. et al., 2013, ApJ, 779

Helfand D. J., Agueros M. A., Gotthelf E. V., 2003a, ApJ, 592, 941

Helfand D. J., Becker R. H., 1985, Nature, 313, 118

Helfand D. J., Becker R. H., White R. L., Fallon A., Tuttle S., 2006, AJ, 131, 2525

Helfand D. J., Collins B. F., Gotthelf E. V., 2003b, ApJ, 582, 783

Helfand D. J., Velusamy T., Becker R. H., Lockman F. J., 1989, ApJ, 341, 151

Herschel W., 1811, PTRSL, 101, 269

HESS Collaboration, 2008a, A&A, 836, 829

HESS Collaboration, 2008b, A&A, 517, 509

HESS Collaboration, 2008c, A&A, 477, 353

HESS Collaboration, 2011, A&A, 531, A81

HESS Collaboration, 2014, ApJ Letters, 794, 2

HESS Collaboration, 2015, A&A, 574, A27

Hester J. J., 2008, ARA{&}A, 46, 127

Hester J. J. et al., 1996, ApJ, 456, 225

Hewish A., Bell S. J., Pilkington J. D. H., Scott P. F., Collins R. A., 1968, Nature, 217, 709

Hewitt J. W., Yusef-Zadeh F., 2009a, ApJ, 694, 16

Hewitt J. W., Yusef-Zadeh F., 2009b, ApJ, 694, 16

Hewitt J. W., YusefâĂŘZadeh F., Wardle M., 2008, ApJ, 683, 189

Higashi Y. et al., 2008, ApJ, 683, 957

Hildebrand R. H., 1983, QJRAS, 24, 267

Höfner S., Andersen A. C., 2007, A&A, 465, L39

Höfner S., Jørgensen U. G., Loidl R., Aringer B., 1998, A&A, 340, 497

Höfner S., Olofsson H., 2018, A&A Review, 26, 1

Holland W. S. et al., 2013, MNRAS, 430, 2513

Houck J. R. et al., 2004, ApJS, 5487, 62

Howard A. D., 2020, PhD thesis, Cardiff University

Hoyle F., Fowler W. A., 1960, ApJ, 132, 565

Hunter J. D., 2007, Computing in Science and Engineering, 9, 90

Hurley K. et al., 1999, ApJ, 510, L111

Hwang U., Markert T. H., 1994, ApJ, 431, 819

Hwang U., Petre R., Hughes J. P., 2000, ApJ, 532, 970

Iben I. J., Tutukov A. V., 1984, ApJS, 54, 335

Indebetouw R. et al., 2005, ApJ, 619, 931

Indebetouw R. et al., 2014, ApJ Letters, 782, L2

Irwin M., 2010, UKIRT Newsletter, 26, 14

Ishihara D. et al., 2010, A&A, 521, L61

Jackson J. M. et al., 2006, ApJS, 163, 145

Jackson M. S., Safi-Harb S., Kothes R., Foster T., 2008, ApJ, 674, 936

James A., Dunne L., Eales S., Edmunds M. G., 2002, MNRAS, 335, 753

Janka H.-T., 2012, ARNPS, 62, 407

Jeong I. G., Koo B. C., Cho W. K., Kramer C., Stutzki J., Byun D. Y., 2013, ApJ, 770

Jones A. P., Tielens A. G. G. M., Hollenbach D. J., 1996, ApJ, 469, 740

Jones A. P., Tielens A. G. G. M., Hollenbach D. J., McKee C. F., 1997, AIP Conference Proceedings, 402, 19

Jones L. R., Smith A., Angelini L., 1993, MNRAS, 265, 631

Junkes N., Furst E., Reich W., 1992, A&A, 261, 289

Kamitsukasa F., Koyama K., Uchida H., Nakajima H., Hayashida K., Mori K., Katsuda S., Tsunemi H., 2015, PASJ, 67, 161

Kankare E. et al., 2014, A&A, 572, A75

Kapteyn J. C., 1909, ApJ, 29, 46

Karakas A., Lattanzio J. C., 2007, PASA, 24, 103

Kaspi V. M., Manchester R. N., Johnston S., Lyne A. G., D'Amico N., 1992, ApJ, 399, L155

Kaspi V. M., Manchester R. N., Johnston S., Lyne A. G., D'Amico N., 1996, AJ, 111, 2028

Kaspi V. M., Roberts M. E., Vasisht G., Gotthelf E. V., Pivovaroff M., Kawai N., 2001, ApJ, 560, 371

Kassim N. E., Weiler K. W., Baum S. A., 1991, ApJ, 374, 212

Kennel C. F., Coronitti F. V., 1984, ApJ, 283, 694

Keohane J. W., Reach W. T., Rho J., Jarrett T. H., 2007, ApJ, 654, 938

Kessler M. F., Habing H. J., 1996, A&A, 315, L27

Kilpatrick C. D., Bieging J. H., Rieke G. H., 2016, ApJ, 816, 1

Kim S.-H., Martin P., 1994, ApJ, 431, 783

Kim S.-H., Martin P. G., Hendry P. D., 1994, ApJ, 422, 164

Kirchschlager F., Schmidt F. D., Barlow M. J., Fogerty E. L., Bevan A., Priestley F. D., 2019, MNRAS, 489, 4465

Klochkov D., Suleimanov V., Sasaki M., Santangelo A., 2016, A&A, 12, 8

Koo B.-C., Kim K.-T., Seward F. D., 1995, ApJ, 447, 211

Koo B.-C., Lee J.-J., Jeong I.-G., Seok J. Y., Kim H.-J., 2016, ApJ, 821, 20

Koo B.-C. et al., 2008, ApJ, 673, 225

Koo B.-c., Moon D., Lee H., Lee J.-j., Matthews K., 2007, ApJ, 657, 308

Koo B.-C., Moon D.-S., 1997, ApJ, 485, 263

Kothes R., Dougherty S. M., 2007, A&A, 1000, 993

Kothes R., Reich W., 2001, A&A, 372, 627

Kothes R., UyanÄśker B., Reid R. I., 2005, A&A, 444, 871

Kozasa T., Hasegawa H., Nomoto K., 1991, A&A, 249, 474

Kozasa T., Nozawa T., Tominaga N., Umeda H., Maeda K., Nomoto K., 2009, in Cosmic Dust - Near and Far ASP Conference Series, Vol. 414

Krause O., Birkmann S. M., Rieke G. H., Lemke D., Klaas U., Hines D. C., Gordon K. D., 2004, Letters to Nature, 432, 596

Kumar H. S., Safi-Harb S., Slane P. O., Gotthelf E. V., 2014, ApJ, 781, 41

Lacey C. K., Lazio T. J. W., Kassim N. E., Duric N., Briggs D., Dyer K. K., 2001, ApJ, 559, 954

Lakićević M. et al., 2015, ApJ, 799, 50

Lamers H. J. G. L. M., Snow T. P., Lindholm D. M., 1995, ApJ, 455, 269

Large M. I., Vaughan A. E., Wielebinski R., 1968, Nature, 220, 753

Lau R. M., Herter T. L., Morris M. R., Li Z., Adams J. D., 2015, Science, 348, 413

Law C. J., Cotton W. D., Maddalena R. J., 2008, ApJS, 177, 255

Lazendic J. S., Slane P. O., 2006, ApJ, 647, 350

Lazendic J. S., Slane P. O., Hughes J. P., Chen Y., Dame T. M., 2005, ApJ, 618, 733

Lazendic J. S., Wardle M., Burton M. G., Yusef-Zadeh F., Green A. J., Whiteoak J. B., 2004, MNRAS, 354, 393

Lazendic J. S., Wardle M., Whiteoak J. B., Burton M. G., Green A. J., 2010, MNRAS, 409, 371

Leahy D., Green K., Tian W., 2014, MNRAS, 438, 1813

Leahy D., Naranan S., Singh K., 1986, MNRAS, 220, 501

Leahy D., Tian W., 2006, A&A, 257, 251

Leahy D. A., Green K. S., 2012, ApJ, 760, 4

Leahy D. A., Ranasinghe S., 2016, ApJ, 817, 74

Leahy D. A., Tian W., Wang Q. D., 2008, ApJ, 136, 1477

Leahy D. A., Tian W. W., 2008a, A&A, 480, L25

Leahy D. A., Tian W. W., 2008b, AJ, 135, 167

Lemiere A., Slane P., Gaensler B. M., Murray S., 2009, ApJ, 706, 1269

Li W., Chornock R., Leaman J., Filippenko A. V., Poznanski D., Wang X., Ganeshalingam M., Mannucci F., 2011, MNRAS, 412, 1473

Lockman F. J., 1989, ApJS, 71, 469

Lombardi M., Bouy H., Alves J., Lada C. J., 2014, A&A, 566, A45

Lopez L. A., Ramirez-Ruiz E., Castro D., Pearson S., 2013, ApJ, 764, 1

Lovchinsky I., Slane P., Gaensler B. M., Hughes J. P., Ng C. Y., Lazendic J. S., Gelfand J. D., Brogan C. L., 2011, ApJ, 731

Lovelace R. B. E., Sutton J. M., Craft H. D., 1968, International Astronomical Union Circular, 2113, 1

Macalpine G. M., Satterfield T. J., 2008, ApJ, 136, 2152

Maeda Y. et al., 2002, ApJ, 570, 671

Mancini M., Schneider R., Graziani L., Valiante R., Dayal P., Maio U., Ciardi B., Hunt L. K., 2015, MNRAS Letters, 451, L70

Mangano V., Burrows D. N., Park S., Shea T. K., 2014, in AAS/High Energy Astrophysics Division #14, p. 120.05

Marigo P., Bressan A., Chiosi C., 1996, A&A, 313, 545

Marsh K. A., Whitworth A. P., Lomax O., 2015, MNRAS, 454, 4282

Marsh K. A. et al., 2017, MNRAS, 471, 2730

Marsh K. A., Whitworth A. P., Smith M. W. L., Lomax O., Eales S. A., 2018, MNRAS, 480, 3052

Martin D. C. et al., 2007, Nature, 448, 780

Mathis J. S., Rumpl W., Nordsieck K. H., 1977, ApJ, 217, 425

Matsuura M., 2017, in Handbook of Supernovae, Alsabti A., Murdin P., eds., Springer, Cham, p. 2125

Matsuura M. et al., 2009, MNRAS, 396, 918

Matsuura M. et al., 2015, ApJ, 800, 50

Matsuura M. et al., 2011, Science, 333, 1258

Matsuura M., Woods P. M., Owen P. J., 2013, MNRAS, 429, 2527

Matthews B. C., Wallace B. J., Taylor A. R., 1998, ApJ, 20, 312

Mattsson L. et al., 2014, MNRAS, 444, 797

McClure-Griffiths N. M., Green a. J., Dickey J. M., Gaensler B. M., Haynes R. F., Wieringa M. H., 2001, ApJ, 551, 394

McCray R., 1993, ARA&A, 31, 175

Mckee C. F., 1974, ApJ, 335

McKinney W., 2010, PPSC, 51

Mennella V. M., Rucato J. R. B., Olangeli L. C., Alumbo P. P., Otundi A. R., Ussoletti E. B., 1998, ApJ, 496, 1058

Meynet G. et al., 2015, A&A, 575, 1

Meynet G., Maeder A., 2003, A&A, 404, 975

Meynet G., Maeder A., 2005, A&A, 429, 581

Micelotta E. R., Dwek E., Slavin J. D., 2016, A&A, 590, A65

Micelotta E. R., Matsuura M., Sarangi A., 2018, Space Science Reviews, 214

Michałowski M. J., 2015, A&A, 80, 1

Michałowski M. J., Murphy E. J., Hjorth J., Watson D., Gall C., Dunlop J. S., 2010, A&A, 522, A15

Millard J. S. et al., 2020, MNRAS, 494, 293

Milne D., 1979, AJP, 32, 83

Minami S., Ota N., Yamauchi S., Koyama K., 2013, PASJ, 65

Minkowski R., 1941, PASP, 53, 224

Misanovic Z., Kargaltsev O., Pavlov G. G., 2010, ApJ, 725, 931

Miyaji S., Nomoto K., 1987, ApJ, 318, 307

Miyaji S., Nomoto K., Yokoi K., Sugimoto D., 1980, PASJ, 32, 303

Moffett D., Gaensler B., Green A., Slane P., Harrus I., Dodson R., 2002, in ASP Conf. Series 271, Vol. 271, p. 221

Moffett D. A., Reynolds S. P., 1994, ApJ, 437, 705

Molinari S. et al., 2016, A&A, 591

Molinari S. et al., 2010a, PASP, 122, 314

Molinari S. et al., 2010b, PASP, 122, 314

Molinari S. et al., 2013, A&A, 518, L100

Moon D.-S., Koo B.-C., Lee H.-G., Matthews K., Lee J.-J., Pyo T.-S., Seok J. Y., Hayashi M., 2009, ApJ, 703, L81

Morgan H. L., Edmunds M. G., 2003, MNRAS, 343, 427

Morsi H. W., Reich W., 1987, A&A SS, 69, 533

Morton T. D., Slane P., Borkowski K. J., Reynolds S. P., Helfand D. J., Gaensler B. M., Hughes J. P., 2007, AJ, 667, 219

Murakami H. et al., 2007, PASJ, 59, 369

Nath B. B., Laskar T., Shull J. M., 2008, ApJ, 682, 1055

Nehmé C., Kassounian S., Sauvage M., 2019, Experimental Astronomy, 48, 1

Ng C. Y., Bucciantini N., Gaensler B. M., Camilo F., Chatterjee S., Bouchard A., 2012, ApJ, 746, 1

Nomoto K., 1980, SSR, 27, 563570

Nomoto K., 1982a, ApJ, 253, 798

Nomoto K., 1982b, ApJ, 257, 780

Nomoto K., 1984, ApJ, 277, 791

Nomoto K., 1987, ApJ, 322, 206

Nomoto K., Iwamoto K., Kishimoto N., 1997, Science, 276, 1378

Nomoto K., Tominaga N., Blinnikov S. I., 2014, AIP Conference Proceedings, 1594, 258

Noriega-Crespo A., Ven Buren D., Cao Y., Dgani R., 1997, AJ, 117, 837

Nozawa T., Kozasa T., Habe A., Dwek E., Umeda H., Tominaga N., Maeda K., Nomoto K., 2007, ApJ, 666, 955

Nozawa T., Kozasa T., Tominaga N., Maeda K., Umeda H., Nomoto K., Krause O., 2010, ApJ, 713, 356

Nozawa T. et al., 2008, ApJ, 684, 1343

Nozawa T., Kozasa T., Umeda H., Maeda K., Nomoto K., 2003, ApJ, 598, 785

Nozawa T., Maeda K., Kozasa T., Tanaka M., Nomoto K., Umeda H., 2011, ApJ, 736, 45

Nozawa T., Yoon S. C., Maeda K., Kozasa T., Nomoto K., Langer N., 2014, ApJ Letters, 787, 1

Nugent J. J., Pravdo S. H., Garmire G. P., Becker R. H., Tuohy I. R., Winkler P. F., 1984, ApJ, 284, 612

Nynka M. et al., 2013, ApJ Letters, 778, 1

Ober W., El Eid M., Fricke K., 1983, A&A, 119, 61

Odegard N., 1986, ApJ, 301, 813

Oliphant T. E., 2006, A guide to NumPy. Trelgol Publishing USA

Oliva E., Moorwood A. F. M., Danziger I. J., 1990, A&A, 240, 453

Oliva E., Moorwood A. F. M., Drapatz S., Lutz D., Sturm E., 1999, A&A, 343, 943

Omand C. M., Kashiyama K., Murase K., 2019, MNRAS, 484, 5468

Ostriker J., Silk J., 1973, ApJ, 184, L113

Otsuka M. et al., 2010, A&A, 518, 2

Owen P. J., Barlow M. J., 2015, ApJ, 801, 141

Paladini R. et al., 2012, ApJ, 760

Pannuti T. G., Kargaltsev O., Napier J. P., Brehm D., 2014a, ApJ, 782

Pannuti T. G., Rho J., Borkowski K. J., Cameron P. B., 2010, AJ, 140, 1787

Pannuti T. G., Rho J., Heinke C. O., Moffitt W. P., 2014b, AJ, 147, 55

Paredes J. M., Marti J., Ribó M., Massi M., 2000, Science, 288, 2340

Park G. et al., 2013, ApJ, 777, 14

Paron S., Giacani E., Rubio M., Dubner G., 2011, A&A, 530, A25

Patnaik A., Hunt G., Salter C., Shaver P., Velusamy T., 1990, A&A, 232, 467

Petriella A., Paron S. A., Giacani E. B., 2013, A&A, 554, A73

Phillips J. P., Marquez-Lugo R. A., 2010, MNRAS, 409, 701

Phillips J. P., Ramos-Larios G., Perez-Grana J. A., 2009, MNRAS, 397, 1215

Pihlström Y. M., Sjouwerman L. O., Frail D. A., Claussen M. J., Mesler R. A., McEwen B. C., 2014, AJ, 147

Pilbratt G. L. et al., 2010, A&A, 518, L1

Pinheiro Goncalves D. et al., 2011, AJ, 142, 42

Planck Collaboration XIV, 2014, A&A, 564, A45

Planck Collaboration XLVIII, 2016, A&A, 596

Planck Collaboration XXXI et al., 2016, A&A, 586, A134

Plank Collaboration XXIX, 2016, A&A, 586, A132

Poelarends A. J. T., Herwig F., Langer N., Heger A., 2008, ApJ, 675, 614

Poglitsch A. et al., 2010, A&A, 518, L2

Popping G., Somerville R. S., Trager S. C., 2014, MNRAS, 442, 2398

Povich M. S. et al., 2007, ApJ, 660, 346

Priestley F. D., Barlow M. J., De Looze I., 2019, MNRAS, 485, 440

Puget J.-L., Abergel A., Bernard J.-P., Boulanger F., Burton W., Desert F.-X., Hartmann D., 1996, A&A, 308, L5

Purcell C. R. et al., 2012, MNRAS, 426, 1972

Pye J. P., Becker R. H., Seward F. D., Thomas N., 1984, MNRAS, 207, 649

Rakavy G., Shaviv G., 1967, ApJ, 148, 803

Rakowski C. E., Badenes C., Gaensler B. M., Gelfand J. D., Hughes J. P., Slane P. O., 2006, ApJ, 646, 982

Rakowski C. E., Hughes J. P., Slane P. O., 2001, ApJ, 548, 258

Ranasinghe S., Leahy D. A., 2018a, MNRAS, 477, 2243

Ranasinghe S., Leahy D. A., 2018b, AJ, 155, 204

Rea N., Borghese A., Esposito P., Zelati F. C., Bachetti M., Israel G. L., Luca A. D., 2016, ApJ Letters, 828, L13

Reach W. T. et al., 2005a, PASP, 117, 978

Reach W. T., Rho J., Jarrett T. H., 2005b, ApJ, 618, 297

Reach W. T. et al., 2006, AJ, 131, 1479

Rees M. J., Gunn J. E., 1974, MNRAS, 167, 1

Reich W., Furst E., 1984, A&A SS, 57, 165

Reich W., Zhang X., Furst E., 2003, A&A, 408, 961

Revéret V. et al., 2014, in SPIE, Vol. 9153, Millimeter, Submillimeter, and Far-Infrared Detectors and Instrumentation for Astronomy VII, p. 915305

Reynolds M. T. et al., 2013, ApJ, 766, 112

Reynolds S. P., 2006, ApJ, 652, L45

Reynolds S. P., Chevalier R. A., 1984, ApJ, 278, 630

Reynoso E. M., Green A. J., Johnston S., Giacani E. B., Goss W. M., 2004, PASA, 21, 82

Reynoso E. M., Johnston S., Green A. J., Koribalski B. S., 2006, MNRAS, 369, 416

Reynoso E. M., Mangum J. G., 2000, ApJ, 20, 874

Rho J., Borkowski K. J., 2002, ApJ, 575, 44

Rho J. et al., 2018, MNRAS, 479, 5101

Rho J. et al., 2017, ApJ, 834, 19

Rho J. et al., 2008, ApJ, 673, 271

Rho J., Petre R., 1998, ApJ, 503, L167

Rho J., Petre R., Schlegel E. M., Hester J. J., 1994, ApJ, 430, 757

Rieke G. H. et al., 2004, ApJS, 154, 25

Rowlands K., Gomez H. L., Dunne L., Aragón-Salamanca A., Dye S., Maddox S., da Cunha E., van der Werf P., 2014, MNRAS, 441, 1040

Roy S., Pal S., 2013, PIAU, 9, 197

Sabin L. et al., 2013, MNRAS, 431, 279

Safi-Harb S., Ögelman H., 1997, ApJ, 483, 868

Saken J. M., Fesen R. A., Shull M. J., 1992, ApJS, 81, 715

Salpeter E. E., 1974, ApJ, 193, 579

Salter C. J., Emerson D. T., Steppe H., Thum C., 1989a, A&A, 225, 167

Salter C. J. et al., 1989b, ApJ, 338, 171

Sankrit R. et al., 2010, ApJ, 712, 1092

Sarangi A., Cherchneff I., 2015, A&A, 575, A95

Sarangi A., Matsuura M., Micelotta E. R., 2018, Space Science Reviews, 214

Sarma A., Goss W., Green A., Frail D. A., 1997, ApJ, 483, 335

Sasaki M., Plucinsky P. P., Gaetz T. J., Bocchino F., 2013, A&A, 552, A45

Sato F., 1979, ApL, 20, 43

Sato T., Koyama K., Lee S. H., Takahashi T., 2016, PASJ, 68, S81

Sawada M., Go Tsuru T., Koyama K., Oka T., 2011, PASJ, 63, S849

Scannapieco E., Madau P., Woosley S., Heger A., Ferrara A., 2005, ApJ, 633, 1031

Schneider R., Valiante R., Ventura P., Dell'Agli F., Criscienzo M. D., Hirashita H., Kemper F., 2014, MNRAS, 442, 1440

Schuller F. et al., 2009, A&A, 504, 415

Sedov L. I., 1959, Similarity and Dimensional Methods in Mechanics

Seo J., Kang H., Ryu D., 2018, JKAS, 51, 37

Sezer A., Gök F., 2014, ApJ, 790, 5

Sezer A., Gök F., Hudaverdi M., Ercan E. N., 2011, MNRAS, 417, 1387

Shan S. S., Zhu H., Tian W. W., Zhang M. F., Zhang H. Y., Wu D., Yang A. Y., 2018, ApJS, 238, 35

Shaver P. A., Salter C. J., Patnaik A., van Gorkom J. H., Hunt G. C., 1985, Nature, 313, 113

Shull M. J., Fesen R. A., Saken J. M., 1989, ApJ, 346, 860

Siess L., 2007, EAS Publications Series, 19, 103

Silvia D. W., Smith B. D., Michael Shull J., 2010, ApJ, 715, 1575

Simpson R. J. et al., 2012, MNRAS, 424, 2442

Siringo G. et al., 2009, A&A, 497, 945

Sjouwerman L. O., Pihlström Y. M., Fish V. L., 2010, ApJ Letters, 739, L111

Slane P., Chen Y., Lazendic J. S., Hughes J. P., 2002, ApJ, 580, 904

Slane P. et al., 2012, ApJ, 749, 131

Smith A., Jones L. R., Peacock A., Pye J. P., 1985, ApJ, 296, 469

Smith D. J. et al., 2013, MNRAS, 436, 2435

Smith M. W. et al., 2012a, ApJ, 756

Smith N., Silverman J. M., Filippenko A. V., Cooper M. C., Matheson T., Bian F., Weiner B. J., Comerford J. M., 2012b, AJ, 143, 17

Staelin D. H., Reifenstein E. C., 1968, Science, 162, 1481 LP

Stewart R. T., Haynes R. F., Gray A. D., Reich W., 1994, ApJ, 432, L39

Straniero O., Chieffi A., Limongi M., Busso M., Gallino R., Arlandini C., 1997, ApJ, 478, 332

Struve F. G. W., 1847, Etudes d'Astronomie Stellaire: Sur la voie lactee et sur la distance des etoiles fixes

Stupar M., Parker Q. A., 2011, MNRAS, 414, 2282

Su Y., Chen Y., Yang J., Koo B.-c., Zhou X., Jeong I.-g., Zhang C.-g., 2009, ApJ, 694, 376

Sugizaki M., Mitsuda K., Kaneda H., Matszaki K., Yamauchi S., Koyama K., 2001, ApJS, 134, 77

Surnis M. P., Joshi B. C., Maan Y., Krishnakumar M. A., Manoharan P. K., Naidu A., 2016, ApJ, 826, 184

Sutherland P. G., Wheeler J. C., 1984, ApJ, 280, 282

Takata A., Nobukawa M., Uchida H., Tsuru T. G., Tanaka T., Koyama K., 2016, PASJ, 68, S31

Tam C., Roberts M. S. E., 2003, ApJ, 598, L27

Tawara Y., Yamauchi S., Awaki H., Kii T., Koyama K., Nagase F., 1988, in Physics of Neutron Stars and Black Holes, pp. 71–74

Taylor A. R. et al., 2003, AJ, 125, 3145

Taylor G., 1950, PRSA, 201, 159

Taylor J. H., Manchester R. N., Lyne A. G., 1993, ApJS, 88, 529

Temim T., Dwek E., Arendt R. G., Borkowski K. J., Reynolds S. P., Slane P., Gelfand J. D., Raymond J. C., 2017, ApJ, 836, 129

Temim T., Dwek E., Tchernyshyov K., Boyer M. L., Meixner M., Gall C., Roman-Duval J., 2015, ApJ, 799, 158

Temim T., Slane P., Reynolds S. P., Raymond J. C., Borkowski K. J., 2010, ApJ, 710, 309

Temim T., Sonneborn G., Dwek E., Arendt R. G., Gehrz R. D., Slane P., Roellig T. L., 2012, ApJ, 753, 72

The L. S. et al., 2006, A&A, 450, 1037

The Astropy Collaboration et al., 2018, AJ, 156

The Astropy Collaboration et al., 2013, A&A, 558, A33

Tian W. W., Haverkorn M., Zhang H. Y., 2007a, MNRAS, 378, 1283

Tian W. W., Leahy D. A., 2006, A&A, 455, 1053

Tian W. W., Leahy D. A., 2008, MNRAS, 58, 54

Tian W. W., Leahy D. A., 2012, MNRAS, 421, 2593

Tian W. W., Leahy D. A., 2014, ApJ, 783, L2

Tian W. W., Leahy D. A., Li D., 2010, MNRAS: Letters, 404, L1

Tian W. W., Li Z., Leahy D. A., Wang Q. D., 2007b, ApJ, 657, L25

Tielens A. G. G. M., Allamandola L. J., 1987, Composition, Structure, and Chemistry of Interstellar Dust

Todini P., Ferrara A., 2001, MNRAS, 325, 726

Torii K., Tsunemi H., Dotani T., Mitsuda K., 1997, AJ, 489, L145

Torii K., Uchida H., Hasuike K., Tsunemi H., Yamaguchi Y., Shibata S., 2006, PASJ, 58, 11

Townsley L. K., Broos P. S., Garmire G. P., Anderson G. E., Feigelson E. D., Naylor T., Povich M. S., 2018, ApJS, 235, 43

Traficante A. et al., 2011, MNRAS, 416, 2932

Truelove J. K., McKee C. F., 1999, ApJS, 120, 299

Trumpler R. J., 1930, Lick Observatory Bulletin, 420, 154

Tsuboi M., Miyazaki A., Uehara K., 2015, PASJ, 67, 109 1

Tsuji N., Uchiyama Y., 2016, PASJ, 68, 1

Tuohy I. R., Garmire G. P., 1980, ApJ, 239, L107

Turatto M., 2003, in Supernovae and Gamma-Ray Bursters, Weiler K., ed., Vol. 598, pp. 21–36

Ueta T. et al., 2008, PASJ, 60, 407

Umeda H., Nomoto K., 2002, ApJ, 565, 385

Uyaniker B., Kothes R., Brunt C., 2002, ApJ, 565, 1022

Valiante R., Schneider R., Bianchi S., Andersen A. C., 2009, MNRAS, 397, 1661

van den Bergh S., 1991, Physics Reports, 204, 385

van den Bergh S., 1993, Comments on Astrophysics, 17, 125

van der Swaluw E., Achterberg A., Gallant Y. A., 1998, MemSAI, 69, 1017

van der Swaluw E., Achterberg A., Gallant Y. A., Downes T. P., Keppens R., 2003, A&A, 397, 913

van der Swaluw E., Achterberg A., Gallant Y. A., Toth G., 2001, A&A, 380, 309

van der Swaluw E., Downes T. P., Keegan R., 2004, A&A, 420, 937

Van Der Walt S., Colbert S. C., Varoquaux G., 2011, Computing in Science \& Engineering, 13, 22

Vasisht G., Aoki T., Dotani T., Kulkarni S. R., Nagase F., 1996, ApJ, 456, L59

Vasisht G., Gotthelf E. V., Torii K., Gaensler B. M., 2000, ApJ, 542, L49

Veneziani M. et al., 2013, A&A, 549, A130

Ventura P. et al., 2012, MNRAS, 424, 2345

Ventura P., Dell'agli F., Schneider R., Di criscienzo M., Rossi C., La franca F., Gallerani S., Valiante R., 2014, MNRAS, 439, 977

Vink J., 2004, ApJ, 604, 7

Virtanen P. et al., 2020, Nature Methods, 17, 261

Voisin F., Rowell G., Burton M. G., Walsh A., Fukui Y., Aharonian F., 2016, MNRAS, 458, 2813

Watson D., Christensen L., Knudsen K. K., Richard J., Gallazzi A., Michłowski M. J., 2015, Nature, 519, 327

Weaver T. A., Woosley S. E., 1980, AIPC, 63, 15

Webbink R. F., 1984, ApJ, 277, 355

Werner M. W. et al., 2004, ApJS, 154, 1

Wesson R., Barlow M. J., Matsuura M., Ercolano B., 2014, MNRAS, 446, 2089

Wheeler J. C., Harkness R. P., 1990, Rep. Prog. Phys., 53, 1467

Whelan J., Iben I. J., 1973, ApJ, 186, 1007

Whiteoak J. B., Green A. J., 1996, A&A SS, 118, 329

Whiteoak J. B. Z., 1992, MNRAS, 256, 121

Whittet D. C. B., 1992, Dust in the galactic environment, Tayler R. J., White R. E., eds. CRC press

Williams B. J. et al., 2006, ApJ, 652, L33

Williams B. J. et al., 2011, ApJ, 729

Willingale R., Bleeker J. A., Van der Heyden K. J., Kaastra J. S., 2003, Astronomy and Astrophysics, 398, 1021

Winkler P. F. J., Clark G. W., 1974, ApJ, 191, L67

Wolszczan A., Cordes J. M., Dewey R. J., 1991, ApJ, 372, L99

Woltjer L., 1972, ARA&A, 10, 129

Wooden D. H. et al., 1993, ApJS, 88, 477

Woosley S. E., 2017, ApJ, 836, 244

Woosley S. E., Blinnikov S., Heger A., 2007, Nature, 450, 390

Woosley S. E., Heger A., 2015, in Very Massive Stars in the Local Universe, Vink J. S., ed., Vol. 412, Astrophysics and Space Science Library, pp. 199–225

Woosly S. E., Weaver T. A., 1994, ApJ, 423, 371

Wootten A., 1981, ApJ, 245, 105

Xu J. L., Wang J. J., 2012, A&A, 543, A24

Yamaguchi H. et al., 2015, ApJ, 801, L31

Yamaguchi H., Tanaka M., Maeda K., Slane P. O., Foster A., Smith R. K., Katsuda S., Yoshii R., 2012, ApJ, 749, 137

Yamaguchi H., Ueno M., Koyama K., Bamba A., Yamauchi S., 2004, PASJ, 56, 1059

Yamauchi S., Bamba A., Koyama K., 2014a, PASJ, 66, 20

Yamauchi S., Minami S., Ota N., Koyama K., 2014b, ASJ, 66, 1

Yamauchi S., Ueno M., Koyama K., Bamba A., 2005, PASJ, 57, 459

Yar-Uyaniker A., Uyaniker B., Kothes R., 2004, ApJ, 616, 247

Yasumi M., Nobukawa M., Nakashima S., Uchida H., Sugawara R., Tsuru T. G., Tanaka T., Koyama K., 2014, PASJ, 66, 1

Yoshida T., Umeda H., Maeda K., Ishii T., 2016, MNRAS, 457, 351

Yusef-Zadeh F., Goss W., 1999, ApJ, 527, 172

Yusef-Zadeh F., Melia F., Wardle M., 2000, Science, 287, 85

Yusef-Zadeh F., Morris M., 1987, ApJ, 320, 545

Yusef-Zadeh F., Wardle M., Rho J., Sakano M., 2003, ApJ, 585, 319

Zajczyk A. et al., 2012, A&A, 542

Zhang G. Y., Chen Y., Su Y., Zhou X., Pannuti T. G., Zhou P., 2015, ApJ, 799

Zhao J. H., Morris M. R., Goss W. M., 2013, ApJ, 777, 1

Zhou P., Chen Y., 2011, ApJ, 743, 4

Zhou P., Chen Y., Safi-Harb S., Zhou X., Sun M., Zhang Z.-Y., Zhang G.-y., 2016, ApJ, 831

Zhou P., Safi-Harb S., Chen Y., Zhang X., Jiang B., Ferrand G., 2014, ApJ, 791, 87

Zhu H., Tian W. W., Torres D. F., Pedaletti G., Su H. Q., 2013, ApJ, 775, 95

Zhu H., Tian W. W., Zuo P., 2014, ApJ, 793

Zhukovska S., Henning T., 2013, A&A, 555, 1

Zoglauer A. et al., 2015, ApJ, 798, 4

'She felt confident that with a great deal of practice and effort, she would succeed in the end.'

ROALD DAHL, MATILDA